

Modelling and Reconstruction of Whole Body parametric maps in PET-MRI Pharmacological imaging *Modélisation et reconstruction de images paramétrique corps-entier en imagerie pharmacologique TEP-IRM*

Thèse de doctorat de l'université Paris-Saclay

École doctorale n°575, Electrical, Optical, Bio: physics and engineering
(EOBE)

Spécialité de doctorat : Imagerie et physique médicale
Unité de recherche : Laboratoire d'Imagerie Biomédicale Multimodale Paris Saclay,
CEA, CNRS, Inserm
Référent : Faculté des sciences d'Orsay

Thèse présentée et soutenue à Orsay, le 31/08/2021, par

Zacharias CHALAMPALAKIS

Composition du Jury

Marie POIRIER-QUINOT

Professeure, Université Paris-Saclay

Présidente

Alexandre BOUSSE

Maître de conférences (HDR), Université de
Bretagne Occidentale

Rapporteur & Examinateur

Denis MARIANO GOULART

Professeur, Université de Montpellier

Rapporteur & Examinateur

Johan NUYTS

Professeur, KU/UZ Leuven

Examinateur

Fotis KOTASIDIS

Chercheur, GE Healthcare

Examinateur

Direction de la thèse

Claude COMTAT

Ingénieur chercheur, CEA

Directeur

Simon STUTE

Ingénieur de recherche hospitalier, CHU Nantes

Co-encadrant

Dedication

Acknowledgements

Contents

Résumé de thèse	xiii
Introduction	xxv
I Theory and Methods	1
1 Positron Emission Tomography	3
1.1 Historical Perspective	3
1.2 Fundamental physics of PET	4
1.3 PET Systems	6
1.4 Hybrid PET Systems	14
1.5 Whole Body PET: Static Imaging	16
1.6 Whole Body PET: Dynamic Imaging	18
1.7 Advancements on extended A-FOV PET systems	19
2 Pharmacokinetics	21
2.1 Principles of pharmacokinetic modelling	21
2.2 One-tissue compartment model	22
2.3 Two-tissue compartment model	23
2.4 Gjedde-Patlak linearisation method	25
2.5 Spectral analysis method	26
2.6 IsotoPK pharmacological study	28
3 PET image reconstruction	31
3.1 Projection and back-projection process	31
3.2 Formulation of the system model	34
3.3 Formulation of the objective function	35

3.4 Maximum Likelihood - Expectation Maximisation	36
3.5 Dynamic reconstruction	37
4 CASToR	43
4.1 Datafile	44
4.2 Geometry	45
4.3 Dynamic aspects	45
4.4 Multi-bed reconstruction	47
II Contributions	49
5 Multi-bed Dynamic Whole-Body PET: Acquisition Optimization	51
5.1 Introduction	51
5.2 Methods & Results	52
5.3 Comparison of protocols	59
5.4 Discussion	60
5.5 Conclusion	62
6 Dynamic Reconstruction Implementation and Application to a Patlak Simulation Study	63
6.1 Introduction	64
6.2 Methods	65
6.3 Results	76
6.4 Discussion	85
6.5 Conclusion	90
7 Extension of Dynamic Reconstruction to Multi-Bed Reconstruction	93
7.1 Introduction	93
7.2 Methods	94
7.3 Results	100
7.4 Discussion	107
7.5 Conclusion	110
8 Dynamic Reconstruction Using the Spectral Model and Adaptive Residual Modelling	111
8.1 Introduction	112
8.2 Methods	113
8.3 Results	115

8.4 Discussion	117
8.5 Conclusion	120
Bibliography	125
Appendices	141
A Multi-bed Dynamic Whole Body PET: Data exportation and processing	143
B Simulation Study Supplementary material	147
C Direct multi-bed dynamic reconstruction: Supplementary material	149
Secondary Contributions	155

List of Figures

1	Courbe de tête (taux de détections en fonction du temps) de l'étude du primate acquis montrant les phases DSB et DWB de l'acquisition et les trois positions du lit DWB.	xvi
2	Vues de projection d'intensité maximale des images TEP reconstruites de l'étude primate, pour les deux phases de l'acquisition.	xvi
3	Simulation: Courbes de compromis entre le bruit et le biais du thalamus (gauche) et du cortex (droite) pour les reconstructions 4D des données du protocole DWB-1. Métriques basées sur les VOI (haut) et sur les voxels (bas).	xviii
4	Données réelles: Rapport contraste/bruit (gauche) et SD du foie par rapport à la moyenne des VOI de la tumeur (droite) pour les reconstructions 3D et 4D.	xix
5	Données réelles: Les images paramétriques K_i (avec filtrage Gaussien à 5mm) de SB et DWB rejouent des ensembles de données provenant de reconstructions 3D et 4D à des valeurs SD appariées sur le foie.	xix
6	Courbes d'activité temporelle moyenne des VOI pour la reconstruction spectrale 3D et 4D. Régions VOI indiquées qui sont incluses dans l'acquisition DSB et DWB.	xxi
7	K_1 estimé à partir de la reconstruction spectrale 4D pour les régions VOI incluses dans les acquisitions DSB et DWB, présentées pour les balayages <i>CTRL</i> et <i>RIF</i>	xxii
1.1	Illustration of the described interactions. (A) No interaction resulting in transmission of photon. (B) Photoelectric absorption from inner shell electron, resulting in its ejection and followed by an inner electron transition and characteristic X-Ray emission. (C) Elastic (Rayleigh) scattering conserving the energy of the photons but resulting in small angle change in direction. (D) Compton scattering with outer shell electron resulting to change of energy and direction of incident photon.	5
1.2	Example illustration of PMT based block detector diagram and their placement within a PET ring (Adapted from www.radiologycafe.com)	7

1.3	Representation of different types of detected coincidence events.	9
1.4	Example illustration of LORs for 2D acquisition mode using direct and cross planes (left) and 3D acquisition mode (right) for an 8 ring scanner with 15 axial slices.	10
1.5	Example of 2D and 3D axial sensitivity profiles, with and without maximum ring difference limits, for a scanner with 45 crystal rings which provide 45 direct and 44 cross-planes.	10
1.6	Schematic of the GE Signa hybrid PET-MR system, comprising of detector module units (bottom) in a ring formation within the MR RF body coil (top).	15
1.7	Relative axial sensitivity of individual beds (top) and combined sensitivity profile (bottom) for approximately 50% overlap for the Signa PET/MR.	17
1.8	Relative axial sensitivity of 5 bed positions with decreasing overlap for the Signa PET/MR. . .	18
1.9	Combinations of overlap and number of beds for static (A&B) and dynamic whole-body imaging(C). Relative axial sensitivity is shown in shades of red, with bed start (—) and end (----) positions.	18
2.1	Representation of compartments and exchanges rates for 1TCM (top) and 2TCM (bottom) . .	23
2.2	Example measured arterial input function $C_P(t)$ and modelled PV input function (using $k_g=0.5 \text{ min}^{-1}$) (left). Combination of arterial and PV input function to provide $C_H(t)$, assuming a 25/75 ratio (right).	29
4.1	Example of Customizable and Advanced Software for Tomographic Reconstruction (CASToR) abstraction design for the projection component.	44
5.1	Coronal MIP projections of 7 volunteer control DWB scans with overlay of axial bed start (—) and end (----) location.	54
5.2	Coronal MIP projections of 7 volunteer rif DWB scans with overlay of axial bed start (—) and end (----) location.	54
5.3	Box plots of intra-bed delays dl_{bed} of the IsotoPK DWB protocol used in practice.	55
5.4	Box plots of delay between WB Sweeps dl_{Sweep} of the IsotoPK DWB protocol used in practice. .	55
5.5	MRAC acquisitions of NHP study showing the planned bed positions of the two acquisition phases, with overlay of axial bed start (—) and end (----) location.	57
5.6	Head curve (prompts rate against time) of the acquired NHP study data in a single list-mode file using the fully-automated protocol.	58
5.7	Head curve (prompts rate against time) of the acquired NHP study showing the DSB and DWB phases of the acquisition and the three DWB bed positions.	58

5.8	Coronal MIP views of the NHP study's reconstructed PET images, for the two phases of the acquisition, with overlay of axial bed start (—) and end (----) location.	59
5.9	NHP study's image derived input function using information from multiple bed positions.	59
6.1	CASToR framework for dynamic reconstructions.	66
6.2	Dynamic whole-body acquisition protocols considered for simulation.	69
6.3	Fourth dynamic whole-body acquisition protocol considered for simulation, which includes an initial dynamic single bed phase centred over considered bed position.	70
6.4	Real data MIP SUV image (A) and the drawn VOI (B).	76
6.5	Simulation: Eroded thalamus (left) and Cortex (right) noise versus bias trade-off curves for 3D and 4D Patlak reconstructions. VOI based metrics (top row) and voxel-based metrics (bottom row).	77
6.6	Simulation: Eroded thalamus (left) and Cortex (right) noise versus bias trade-off curves for 4D reconstructions of DWB-1 protocol data. VOI based metrics (top row) and voxel-based metrics (bottom row).	79
6.7	Simulation: Eroded thalamus (left) and Cortex (right) noise versus bias trade-off curves for 4D reconstructions, with MLEM and NNLS nested optimization. VOI based metrics (top row) and voxel-based metrics (bottom row).	80
6.8	Simulation: Eroded thalamus (left) and Cortex (right) noise versus bias trade-off curves for 4D reconstructions of the simulated DWB protocol data. VOI based metrics (top row) and voxel-based metrics (bottom row).	81
6.9	Real Data: Contrast to Noise ratio (left) and liver SD vs. VOI mean of the tumour (right) for 3D and 4D reconstructions without TOF information.	82
6.10	Real Data: Contrast to Noise ratio (left) and liver SD vs. VOI mean of the tumour (right) for 3D and 4D reconstructions using TOF information.	83
6.11	Real Data: Parametric K_i images (with 5mm Gaussian Filtering) from SB and DWB replay datasets from 3D and 4D reconstructions, using TOF information, at matched SD values over the liver.	83
6.12	Simulation single noise realisation of DWB-1 data: Contrast to Noise ratio (left) and white matter SD vs. eroded thalamus K_i mean for 3D and 4D reconstructions.	84
6.13	Single slice through parametric K_i images of one noise replicate (with 3mm Gaussian Filtering) (top) and their corresponding Bias images (over noise replicates) (bottom) from SB and DWB data 3D and 4D reconstructions at matched RMS CoV in the eroded thalamus.	84

6.14 Simulation: Eroded thalamus (left) and Cortex (right) noise versus bias trade-off curves for K_1 parametric imaging from 4D spectral reconstructions of the simulated DWB-1 protocol data. VOI based metrics (top row) and voxel-based metrics (bottom row)	86
6.15 Simulation: Eroded thalamus (left) and Cortex (right) noise versus bias trade-off curves for K_1 parametric imaging from 4D spectral reconstructions of the simulated SB and DWB-4 protocol data. VOI based metrics (top row) and voxel-based metrics (bottom row)	87
6.16 Single slice through parametric K_1^* images of one noise replicate (with 3mm Gaussian Filtering) (top) and their corresponding Bias images (over noise replicates) (bottom) from SB and DWB data, for 4D Spectral reconstructions at matched RMS CoV in the eroded thalamus.	88
7.1 Axial slice number vs time for an example three bed positions DWB acquisition. Central axial slices (left) and slices at the overlapping regions (right) considered for the result framing.	95
7.2 Axial slice number vs time for an example three bed positions DWB acquisition, including an initial DSB phase of 180 s.	95
7.3 Example three frame images from a three bed DWB acquisition (NHP study of chapter 5)	97
7.4 Example three frame sensitivity images from a three bed positions DWB acquisition.	97
7.5 Planned DSB and DWB bed positions shown on coronal MRAC image, with bed start (—) and end (----) positions.	99
7.6 Coronal MIP image of 3D reconstruction (4it28sub) of a single frame from the DSB acquisition on the <i>CTRL</i> scan	101
7.7 Coronal MIP images of 3D reconstructions (4it28sub) of a single frame per bed position from the first whole-body pass of the DWB acquisition on the <i>CTRL</i> scan.	101
7.8 MIP image of a single frame from 4D reconstruction (15it28sub) of the <i>CTRL</i> scan	102
7.9 MIP image of the first whole-body pass frames from 4D reconstruction (15it28sub) of the <i>CTRL</i> scan.	102
7.10 VOI mean time activity curves for 3D and 4D spectral reconstruction. VOI regions shown which are included in both DSB and DWB acquisition.	104
7.11 VOI mean time activity curves for 3D and 4D spectral reconstruction. VOI regions shown which are covered only by the DWB acquisition, whose start time is designated with a vertical dotted line.	105
7.12 VOI mean time activity curves for 4D spectral reconstructions, with and without the use of DSB data. VOI regions shown are included in both DSB and DWB acquisitions.	106
7.13 K_1 MIP images from the 4D spectral reconstruction using both DSB and DWB acquisitions, shown for the <i>CTRL</i> and <i>RIF</i> scan.	107

7.14 K_1^* values as estimated from the 4D spectral reconstruction for VOI regions included in both DSB and DWB acquisitions , shown for the <i>CTRL</i> and <i>R/F</i> scan	107
7.15 K_1^* values as estimated from the 4D spectral reconstruction for VOI regions included in both DSB and DWB acquisitions , shown for the <i>CTRL</i> and <i>R/F</i> scan	108
8.1 Coronal view of activity distribution from the evaluated reconstructions (frames of 41.2 to 44.1 minutes post injection). Difference images are also shown for selected cases against the 3D reconstruction.	115
8.2 Average and standard deviation time curves of the liver and bladder VOIs, for the comparison of 3D to 4D reconstruction results as well as 4D reconstruction with residual modelling using different number of residual basis functions.	117
8.3 Average and standard deviation time curves of the dome of the liver the whole liver and bladder VOIs, for the comparison of 4D reconstruction with residual modelling with and without temporal filtering of residuals.	118
8.4 Fraction map of K_j and modelled residuals g_{jf} of the residual model 4D-ResidMod-3RBF-Tempfilt at iteration 75.	118
8.5 Standard deviation of VOIs for regions in the whole-body, for all evaluated reconstructions. . .	119

List of Tables

1.1	Commonly used radioisotopes and their relevant characteristics for PET imaging.	5
5.1	Framing of IsotoPK DWB protocol.	53
6.1	Evaluated reconstruction parameters.	74
6.2	Additional reconstructions characteristics.	74
6.3	θ_{VOI}^{GT} and true K_i values for the simulated acquisition protocols (min^{-1}).	75
6.4	Average reconstruction times for 1 full iteration (28 subsets) over DWB-1 data using CASToR.	79
7.1	VOIs used for evaluation of DWB scans.	100
A.1	Details of Whole Body Sweeps of IsotoPK DWB protocol.	144

Résumé de thèse

Introduction

La tomographie par émission de positons (TEP) est passée, dans les dernières décennies, d'un outil utilisé principalement dans les applications de recherche à un outil d'imagerie clinique qui a un rôle majeur dans de nombreuses applications cliniques et applications de recherche clinique [1]. En combinaison avec plusieurs radiotraceurs disponibles, qui permettent à l'imagerie TEP de cibler et de recueillir des informations sur la fonction au niveau moléculaire, la TEP peut fournir des informations uniques sur les biomarqueurs. La nature non invasive de l'imagerie TEP, combinée à son potentiel de reproductibilité entièrement quantitative et fiable des informations sur les biomarqueurs, sont des aspects très importants qui la rendent désirable dans le cadre de la médecine de précision [1, 2]. La plupart des applications cliniques actuelles de la TEP se concentrent sur l'imagerie statique et des mesures qualitatives et semi-quantitatives. Mais la TEP a la capacité de fournir des paramètres biologiquement pertinents entièrement quantitatifs, en surveillant la cinétique du traceur et le comportement dynamique avec un balayage dynamique sur une période de temps. Ces informations peuvent être utilisées pour générer des images paramétriques qui décomposent les informations en paramètres de modèles qui guident le comportement dynamique. Ceux-ci peuvent être utilisés pour identifier les différentes régions qui contribuent à un comportement différent d'absorption du traceur et peuvent être liés à des différences dans la fonction sous-jacente et la pathophysiologie, avec une applicabilité dans la recherche et les futures applications cliniques.

La majorité des scanners cliniques offrent un champ de vision axial (Axial Field of View; A-FOV) limité, entre 15 et 26 cm [3]. En imagerie statique, la couverture du corps entier est obtenue en combinant plusieurs positions du lit à différents emplacements axiaux pour étendre le champ de vision effectif [4], ou par un mouvement axial continu du lit (Continuous Bed Movement; CBM) [5]. De même, pour réaliser une imagerie dynamique sur l'ensemble du corps, des protocoles dynamique du corps entier (Dynamic Whole Body; DWB) ont été développés, qui utilisent de multiples passages répétés sur le corps entier [6–8]. Mais ces protocoles d'acquisition posent des défis qui proviennent des lacunes temporelles résultantes dans les

données dynamiques acquises de toute position de lit donnée. Ces écarts sont introduits à chaque position du lit par le temps consacré à l'imagerie d'autres positions du lit et par les retards du système de scanner dus au temps nécessaire pour déplacer le lit dans la direction axiale et préparer l'acquisition de la position suivante du lit. Mais cette acquisition résulte en une forte réduction à la fois des nombre de détections totaux collectés pour chaque position lit et de la fréquence d'échantillonnage temporel. En outre, l'acquisition d'informations sur les changements temporels rapides dans la phase initiale de l'étude dynamique est compromise, car ces changements ne sont pas échantillonnés de manière adéquate pour toutes les positions du lit. Par conséquent, les estimations des paramètres à partir d'acquisitions TEP dynamiques du corps entier sont potentiellement compromises par les limitations ci-dessus dans leur précision et leur exactitude. La génération d'images paramétriques à partir de données dynamiques nécessite l'ajustement du modèle dynamique d'intérêt sur les courbes d'activité temporelle (Time activity curve; TAC) pour chaque voxel de l'image. En raison de la mauvaise statistique et du bruit élevé associés aux mesures de TAC au niveau du voxel, qui sont encore dégradés par les protocoles d'acquisition DWB, les estimations d'images paramétriques peuvent être fortement erronées par le bruit et potentiellement biaisées. L'objectif principal de cette thèse était d'explorer l'optimisation de l'acquisition et les nouvelles stratégies de reconstruction pour améliorer les cartes paramétriques du corps entier.

Les contributions peuvent être séparées en trois parties. La première partie se concentre sur l'optimisation du protocole DWB sur un scanner clinique TEP/IRM, visant à réduire les écarts temporels des acquisitions DWB et à augmenter les comptes collectés ainsi que la fréquence d'échantillonnage. La deuxième partie se concentre sur l'utilisation d'algorithmes de reconstruction dynamique pour améliorer l'imagerie paramétrique de la TEP , en utilisant des données simulées et réelles. La troisième et dernière partie est consacrée à l'application des algorithmes de reconstruction dynamique évalués sur des données réelles d'une première étude pharmacocinétique chez l'homme appelée IsotoPK [9], afin de fournir une régularisation temporelle des cartes d'activité et de générer des cartes paramétriques pertinentes pour cette étude. Dans cette application à des données DWB réelles, des considérations supplémentaires ont été faites pour tenir compte des erreurs de modélisation dans la reconstruction en utilisant des modèles résiduels adaptatifs dans la boucle de reconstruction.

Contributions

TEP dynamique multi-lits pour le corps entier : Optimisation de l'acquisition

Dans ce chapitre, nous examinons les résultats des performances d'acquisition d'un protocole DWB mis en œuvre sur le scanner Signa TEP/IRM dans le cadre de l'étude pharmacocinétique IsotoPK [9], en termes de

délais et d'écart temporels qui en résultent. Nous décrivons ensuite le développement et la mise en œuvre d'un protocole expérimental entièrement automatisé pour l'imagerie DWB qui a été conçu dans le but de réduire les délais d'acquisition et de permettre une plus grande flexibilité sur l'acquisition. Cette protocole a été conçu dans le but de réduire ces délais en automatisant entièrement le processus d'acquisition et en enregistrant en continu les informations TEP dans un seul fichier en mode liste pour toutes les positions du lit pendant toute la durée de l'étude DWB. En utilisant une telle stratégie d'acquisition, les délais entre les positions du lit et les balayages WB ont été réduits au temps pris par le seul mouvement physique de la table du scanner. La performance du protocole d'acquisition expérimental nouvellement développé a été testée sur une étude de un primate non humain et les résultats ont été comparés au protocole utilisé dans l'étude IsotoPK.

En utilisant les informations temporelles des données TEP brutes IsotoPK extraites de 7 examens de sujets, les délais moyens de ce protocole DWB à 5 positions de lit ont fourni un délai intra-lit moyen de 5,69 s (95%CI : 5,63-5,75) et un délai moyen entre les balayages WB de 26,17 s (95%CI : 26,13-26,22).

Après des tests initiaux à l'aide de fantômes, le protocole DWB automatisé a été testé sur une étude Non-Human Primate (NHP) utilisant un nouveau traceur ¹⁸F-Crizotinib. Le examen a été effectué avec l'utilisation de 3 positions de lit, pour un total de 28 passages de WB. La figure 5.7 montre les 260 premières secondes de la courbe de acquisition des données enregistrées en mode liste, avec les phases et les positions du lit superposées. Celles-ci montrent la phase initiale de lit unique dynamique (Dynamic Single Bed; DSB) qui a été conduite centrée sur le cerveau pendant une durée de 90 s, suivie par les premières acquisitions de passes WB de trois positions de lit. L'estimation des délais (écart temporels) pour cette étude utilisant le protocole d'acquisition automatisé a été faite en utilisant les informations enregistrées. Les résultats ont montré un délai moyen intra-lit de 3,77 s (95%CI : 3,62-3,91) et un délai moyen entre les balayages de 4,6 s (95%CI : 4,53-4,67). Pour faire une comparaison entre le protocole IsotoPK de 5 positions de lit et le protocole automatisé qui a été testé en utilisant 3 positions de lit, le temps de retard entre les balayages de cette étude a été estimé en utilisant une approximation à 7,66 s.

L'utilisation du protocole entièrement automatisé a permis de réduire considérablement les délais, tout en simplifiant l'acquisition des ensembles de données DWB par une automatisation complète. Ces réductions des délais peuvent se traduire par une amélioration des statistiques d'acquisition ainsi que par un balayage temporel plus rapide, ce qui peut être essentiel dans les premières phases de l'acquisition du DWB. De considérations supplémentaires sur les vitesses de table admissibles pour la sécurité et le confort des patients doivent être faites avant d'utiliser ce protocole sur des sujets humains.

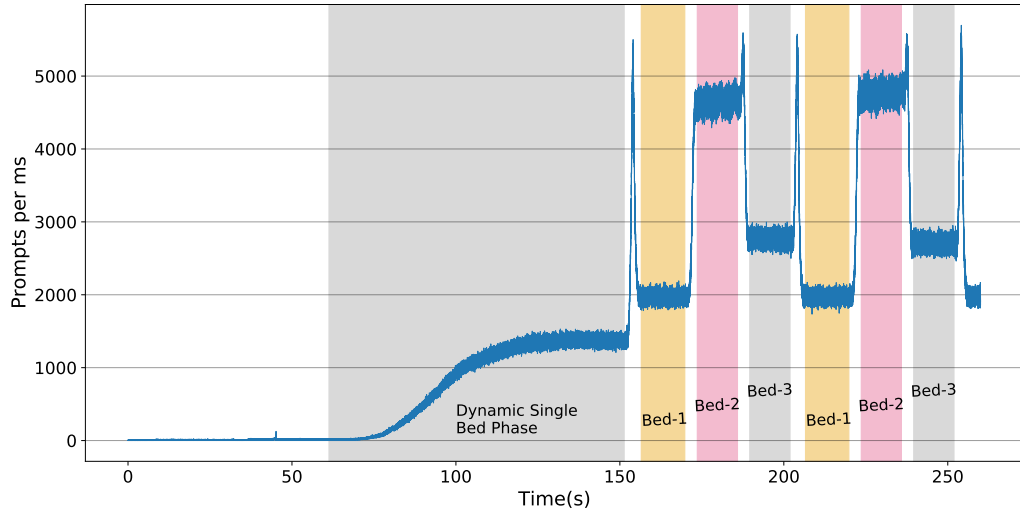


Figure 1: Courbe de tête (taux de détections en fonction du temps) de l'étude du primate acquis montrant les phases DSB et DWB de l'acquisition et les trois positions du lit DWB.

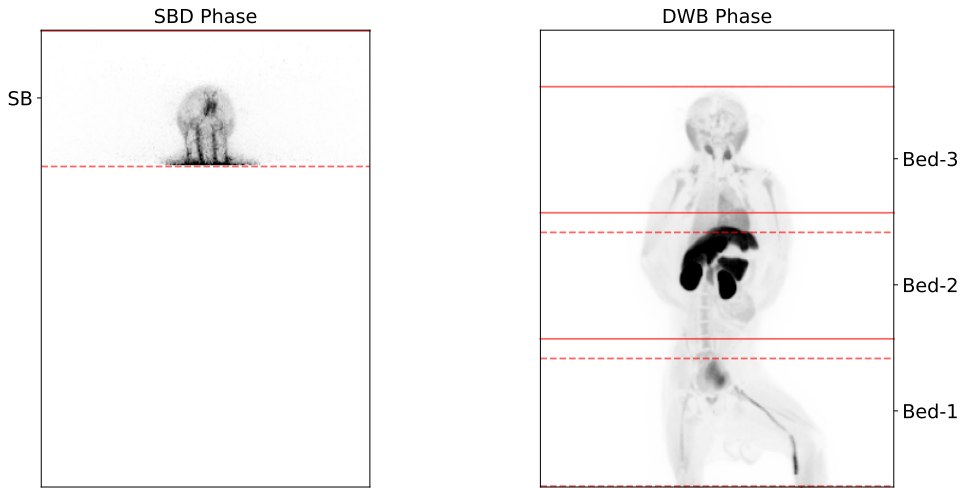


Figure 2: Vues de projection d'intensité maximale des images TEP reconstruites de l'étude primate, pour les deux phases de l'acquisition.

Reconstruction dynamique de données DWB: Une étude de simulation

La génération d'images paramétriques à partir de données dynamiques peut être un défi lorsqu'elle est appliquée à des données DWB. En raison de la mauvaise statistique et du bruit élevé associés aux mesures de TAC au niveau du voxel, en particulier pour les acquisitions DWB, les estimations d'images paramétriques peuvent être fortement erronées par le bruit et potentiellement biaisées. L'utilisation de la reconstruction dynamique directe a été proposée pour améliorer cette tâche en utilisant des modèles dynamiques directement dans la reconstruction. Ces techniques permettent une modélisation plus précise du bruit des données TEP brutes dans le processus de reconstruction et peuvent améliorer le bruit des images paramétriques et réduire le biais [10]. Dans ce chapitre, nous décrivons l'implémentation d'algorithme de reconstruction dy-

namique au sein de la plateforme open source de reconstruction entièrement quantitative CASToR [11], qui a été réalisée dans le cadre de ce projet. Nous évaluons ensuite les performances des algorithmes de reconstruction dynamique à l'aide de simulations pour l'imagerie DWB TEP au fluorodésoxyglucose ($[^{18}\text{F}]\text{FDG}$), pour différents modèles dynamiques et pour différents protocoles d'acquisition en DWB. Les simulations ont été réalisées à l'aide du fantôme cérébral numérique Zubal [12]. Les résultats ont finalement été démontrés dans une étude TEP dynamique réelle. L'évaluation a porté spécifiquement sur l'imagerie paramétrique Patlak K_i et l'utilisation du modèle Patlak Patlak1985 et de l'analyse spectrale Cunningham1993 pour la reconstruction dynamique. Le modèle d'analyse spectrale a été utilisé avec trois ensembles différents de nombres de fonctions de base (17, 9 et 6). Le modèle de Patlak n'est valable que pour les données après que les conditions d'état stationnaire sont atteintes ($t > t_{ss} \approx 15\text{min}$), alors que le modèle spectral peut s'adapter à toutes les données dynamiques. Afin de comparer plus étroitement les deux modèles pour la reconstruction 4D, des comparaisons ont été faites en utilisant le modèle spectral avec toutes les données dynamiques ainsi qu'avec les données dynamiques après t_{ss} (reconstructions marquées avec $t > t_{ss}$).

Les résultats de la comparaison entre la reconstruction dynamique (4D) et la reconstruction image par image (3D, suivie d'une modélisation cinétique post-reconstruction) ont été effectués pour deux régions du fantôme cérébral. Les comparaisons ont été effectuées en utilisant des mesures au niveau du VOI et du voxel (respectivement %Bias vs %CoV et %RMS Bias vs %RMS CoV). Ces résultats sont présentés dans la figure 6.6. Les résultats montrent que la reconstruction dynamique utilisant le modèle de Patlak (4D Patlak) sur les données DWB peut fournir des résultats proches de ceux des protocoles à lit unique sans lacunes temporelles dans leurs données. En outre, la reconstruction 4D Patlak a fourni une gamme plus courte de valeurs de biais avec des itérations croissantes par rapport à la reconstruction 3D. La reconstruction dynamique avec le modèle spectral (4D Spectral) a fourni des résultats encore meilleurs que la reconstruction Patlak 4D des données DWB et la reconstruction 3D des données dynamiques à lit unique. La reconstruction spectrale 4D, utilisant 9 fonctions de base, a permis d'obtenir un compromis optimal entre une faible variance/bruit et un faible biais. La reconstruction spectrale 4D utilisant des données $t > t_{ss}$ a donné lieu à un comportement similaire en termes de variance et de bruit à celui de la reconstruction Patlak 4D, avec des caractéristiques de biais légèrement inférieures sur certaines régions par rapport à la reconstruction Patlak.

Les résultats appliqués à l'ensemble de données réelles, qui ont été répertoriées pour émuler le cadrage et les écarts d'acquisition du DWB, ont montré que le rapport contraste/bruit (CNR) le plus élevé sur une tumeur dans les poumons a été obtenu par les reconstructions 4D Spectral, suivies par la reconstruction Patlak 4D. Les deux méthodes de reconstruction dynamique ont fourni un rapport contraste/bruit plus faible que la reconstruction 3D effectuée sur des données DWB ou des données dynamiques à lit unique sans lacunes.

Une évaluation du bruit paramétrique de l'image dans le foie a montré un comportement similaire pour toutes les reconstructions 4D, avec un bruit plus faible que la reconstruction 3D des mêmes données DWB mais plus élevé que la reconstruction 3D des données dynamiques à lit unique. Les images paramétriques K_i issues des reconstructions 3D et 4D des données réelles aux itérations avec des valeurs SD du foie correspondantes sont présentées dans la figure 6.11. En conclusion, nous avons montré que la reconstruction

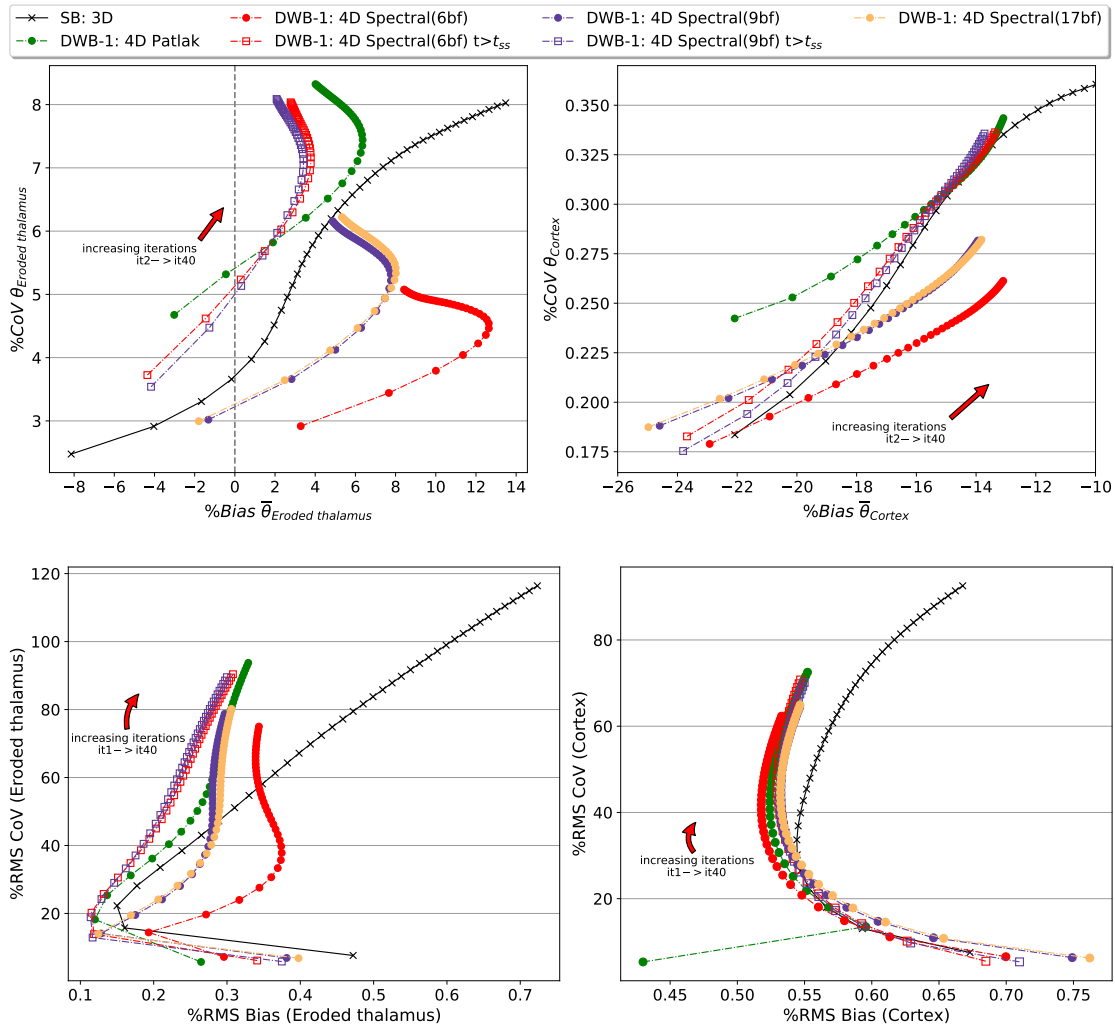


Figure 3: Simulation: Courbes de compromis entre le bruit et le biais du thalamus (gauche) et du cortex (droite) pour les reconstructions 4D des données du protocole DWB-1. Métriques basées sur les VOI (haut) et sur les voxels (bas).

dynamique 4D est nécessaire en imagerie paramétrique DWB pour obtenir une quantification précise et stable. Pour l'imagerie paramétrique FDG Patlak K_i , nous avons montré des résultats de reconstruction dynamique directe Patlak avec des valeurs de bruit et de biais comparables à l'imagerie paramétrique basée sur la reconstruction 3D à partir d'études dynamiques à lit unique. L'utilisation du modèle spectral dans la reconstruction a permis une meilleure utilisation des données dynamiques et une réduction supplémentaire

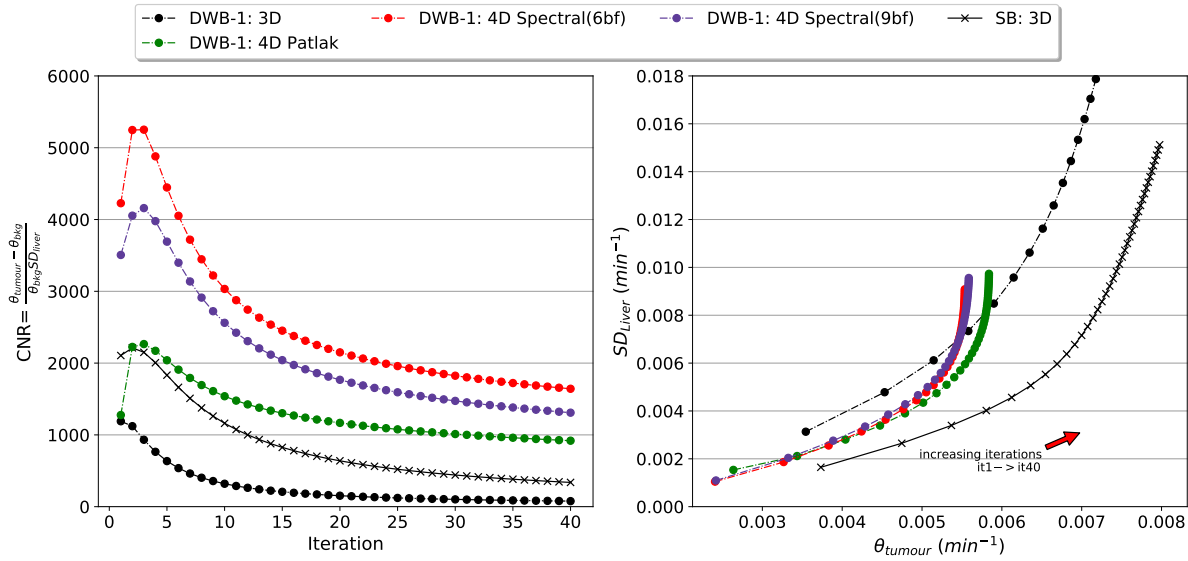


Figure 4: Données réelles: Rapport contraste/bruit (gauche) et SD du foie par rapport à la moyenne des VOI de la tumeur (droite) pour les reconstructions 3D et 4D.

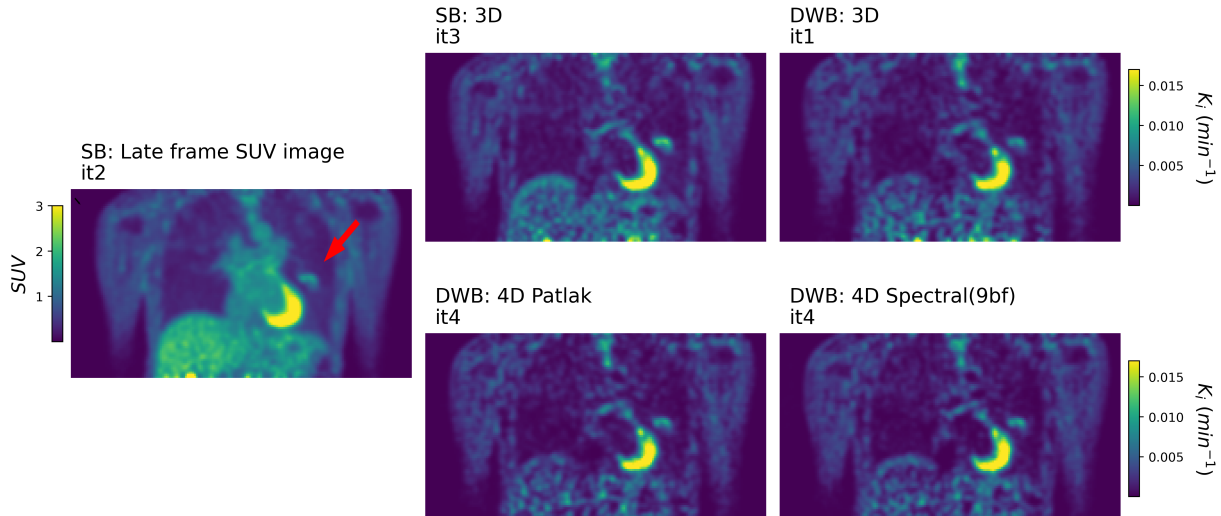


Figure 5: Données réelles: Les images paramétriques K_i (avec filtrage Gaussien à 5mm) de SB et DWB rejouent des ensembles de données provenant de reconstructions 3D et 4D à des valeurs SD appariées sur le foie.

du bruit par rapport à la reconstruction dynamique de Patlak. Dans l'ensemble, l'utilisation de la reconstruction dynamique 4D pour l'imagerie paramétrique DWB offre des propriétés souhaitables qui permettent la transition de les études dynamiques à lit unique et les pratiques courantes d'imagerie paramétrique par reconstruction 3D sans perte de qualité d'image et avec des avantages supplémentaires pour la précision des images paramétriques.

Reconstruction dynamique de données DWB : Application d'une étude pharmacocinétique réelle

Dans ce chapitre, nous décrivons la mise en œuvre des algorithmes de reconstruction dynamique développés précédemment dans un cadre de reconstruction dynamique directe multi-lits au sein de CASToR. Cette approche directe permet d'utiliser toutes les données TEP acquises avec des informations temporelles précises dans une seule boucle de reconstruction, tout en permettant l'utilisation de la reconstruction dynamique directe pour des protocoles d'acquisition DWB plus flexibles et complexes.

Le cadre développé a été appliqué sur des données DWB réelles, qui ont été acquises dans le cadre de l'étude pharmacocinétique IsotoPK [9]. Le protocole d'acquisition de cette étude commence par une acquisition dynamique à lit unique (Dynamic Single Bed; DSB) de 180 s centrée sur le foie, suivie d'une acquisition DWB de 15 passages WB, pour une durée totale d'une heure. L'étude est réalisée sur des volontaires sains, avec une injection d'un nouveau traceur [¹¹C]Glyburide, pour étudier la distribution et la fonction des transporteurs de solutés (SLC) dans la pharmacocinétique des médicaments. Deux scans sont réalisés par volontaire en un seul jour, respectivement sans et avec l'utilisation de l'inhibiteur (rifampicine), appelés scans *CTRL* et *RIF*. Des reconstructions dynamiques ont été réalisées avec le modèle spectral et ont été évaluées par rapport à une reconstruction 3D régulière utilisant les données de la courbe temps-activité (TAC) sur les volumes d'intérêt (VOI). Enfin, les reconstructions du modèle spectral ont été utilisées pour générer des images paramétriques K_1 . Comme les estimations de K_1 sont sensibles aux informations dynamiques initiales, qui, pour ce protocole, n'étaient disponibles que pour les emplacements couverts par l'acquisition DSB, les images paramétriques K_1 générées n'ont été utilisées que pour l'évaluation des VOI couverts par cette seule acquisition. En outre, la correction de la fraction du sang a été ignorée pour l'imagerie de K_1 afin d'éviter l'induction d'un bruit excessif par l'application de cette correction au niveau du voxel ; les images paramétriques estimées de K_1 de substitution (symbolisées par K_1^*) sont donc présentées.

Les résultats de l'analyse VOI, donnés dans la figure 7.10 pour le scan *CTRL*, ont montré une bonne concordance des TAC entre la reconstruction 3D et spectrale 4D. Les images paramétriques de K_1^* issues de la reconstruction spectrale 4D sont présentées dans la figure 7.14 pour les scans du même sujet, avec et sans injection de l'inhibiteur. En outre, nous présentons dans ce chapitre la mise en œuvre et les résultats des tests d'un algorithme de reconstruction dynamique innovant avec la modélisation résiduelle adaptative pour détecter et corriger toute écart du modèle dynamique. Ces sont particulièrement importantes pour la reconstruction dynamique, car le processus de mise à jour tomographique est lié au modèle dynamique et les erreurs d'ajustement du modèle dynamique peuvent se propager spatialement à d'autres régions. Dans l'étude IsotoPK, la principale erreur concernée était le processus de remplissage de la vessie qui était mal modélisé par le modèle spectral. Nos résultats utilisant la modélisation résiduelle adaptative

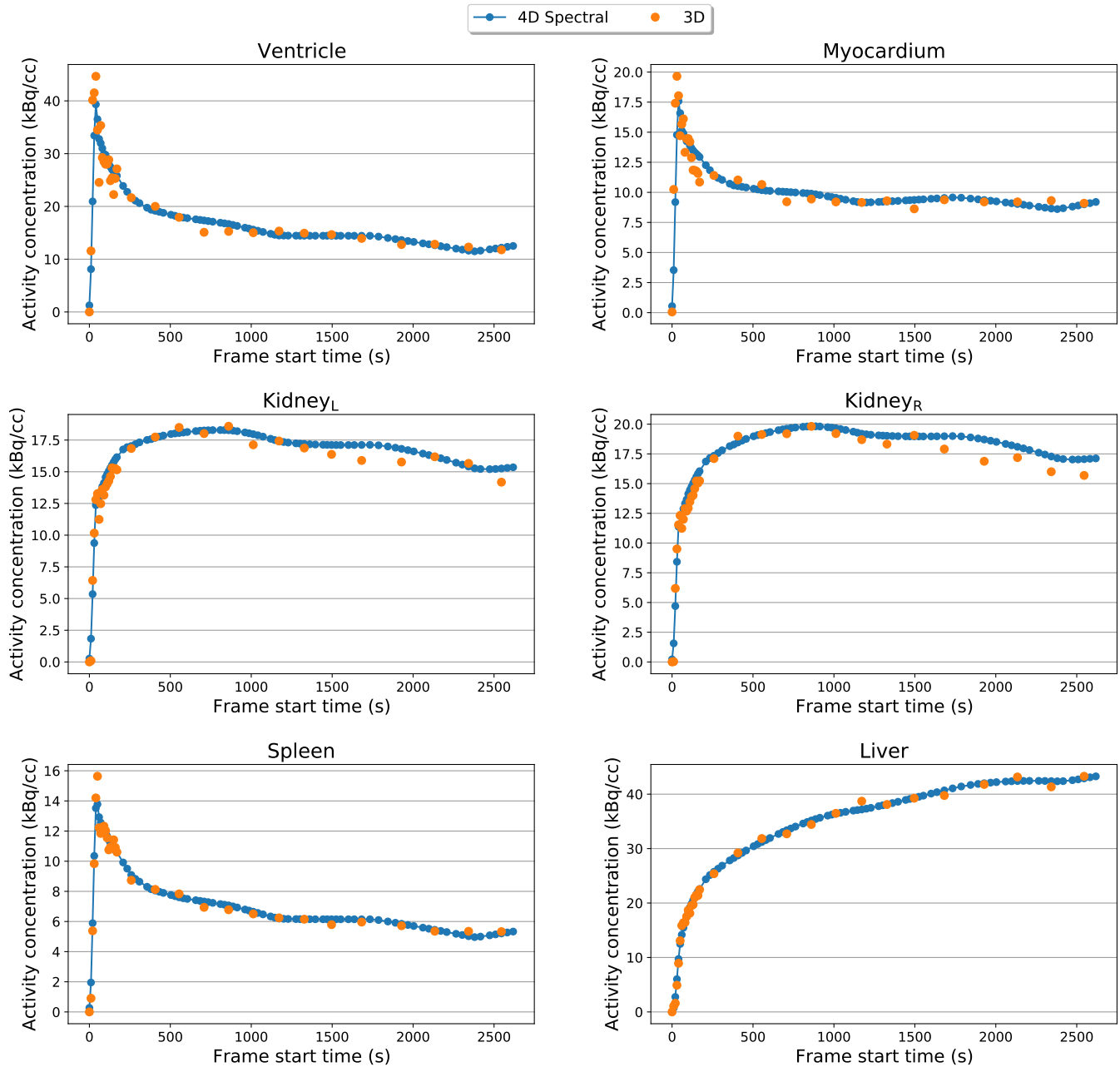


Figure 6: Courbes d'activité temporelle moyenne des VOI pour la reconstruction spectrale 3D et 4D. Régions VOI indiquées qui sont incluses dans l'acquisition DSB et DWB.

dans la reconstruction dynamique ont montré des améliorations significatives dans le TAC de la vessie, où l'algorithme adaptatif a réussi à détecter et à corriger le processus de remplissage, au prix d'un bruit d'image supplémentaire sur toutes les régions. Les résultats optimaux ont été obtenus avec une combinaison de filtrage spatial et temporel dans le traitement des données résiduelles avant la modélisation résiduelle, en termes de sélectivité de l'algorithme et de niveaux de bruit ajouté.

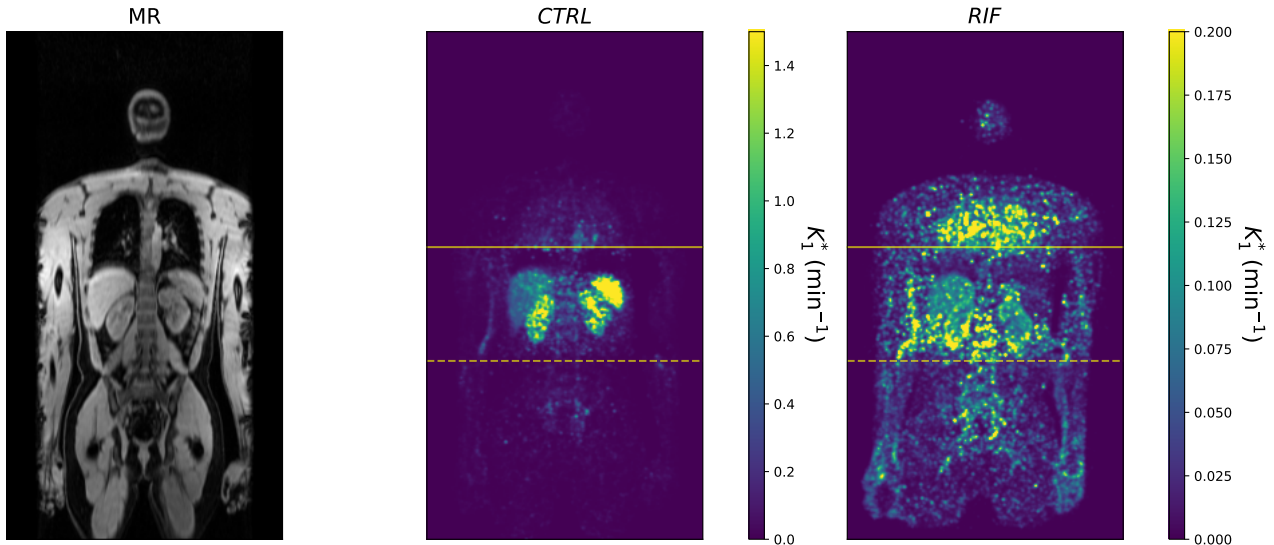


Figure 7: K_1 estimé à partir de la reconstruction spectrale 4D pour les régions VOI incluses dans les acquisitions DSB et DWB, présentées pour les balayages *CTRL* et *RIF*.

Conclusions et perspectives

L'imagerie TEP dynamique sur le corps entier a le potentiel d'augmenter la valeur de l'imagerie TEP, en permettant d'étendre au corps entier l'imagerie TEP et paramétrique entièrement quantitative. Dans le processus de transition des études dynamiques à lit unique aux études DWB à lits multiples, il y a une perte considérable de statistiques de données TEP et de fréquence d'échantillonnage. La reconstruction dynamique peut faciliter cette transition en compensant la perte de qualité de l'image et en offrant des avantages supplémentaires pour la précision des images paramétriques. Il est possible de réduire davantage le bruit de l'image en optimisant le protocole d'acquisition ou en utilisant des modes d'acquisition améliorés pour l'imagerie DWB, comme la acquisition CBM.

Nous avons montré avec succès qu'avec l'utilisation du modèle d'analyse spectrale, l'utilisation de toutes les données dynamiques dans une reconstruction unique et l'utilisation de la modélisation résiduelle adaptative, un algorithme générique de reconstruction dynamique peut être appliqué pour pratiquement tous les types d'acquisitions DWB. Cette reconstruction fournit une régularisation temporelle sur les estimations d'activité et permettant la génération de certaines images paramétriques lorsque celles-ci sont pertinentes pour l'étude.

Plusieurs aspects liés à l'estimation des types de mouvements complexes présentés pendant la durée typique d'une étude DWB, que ils doivent être pris en compte dans la reconstruction dynamique pour garantir une imagerie sans erreur et sans artefact. Récemment, avec le développement de nouveaux scanners à FOV étendu [13, 14] et de scanners corps total [15], il y a un regain d'intérêt pour résoudre ces problèmes

pour l'imagerie dynamique du corps entier. Bien que les scanners à A-FOV étendu puissent certainement bénéficier de l'estimation des images paramétriques de la DWB, en particulier celles sensibles à la cinétique rapide précoce après l'injection, leur disponibilité dans les environnements cliniques sera un sujet de préoccupation pendant au moins un certain temps. Les processus dynamiques plus lents peuvent encore être échantillonnés efficacement sur l'ensemble du corps avec les scanners actuels et les protocoles de DWB multi-lits, tels que ceux récemment introduits dans certains scanners commerciaux [16], qui peuvent être plus rentables et plus facilement accessibles dans les environnements cliniques. Nous nous attendons donc à ce que le regain d'intérêt pour l'imagerie paramétrique du corps entier et l'imagerie quantitative complète se traduise par des avancées qui bénéficieront à l'imagerie DWB pour les scanners de tous les A-FOV et pour différents protocoles d'acquisition.

Introduction

Positron Emission Tomography (PET) has grown over a period of multiple decades from a tool used infrequently and primarily limited to research applications into a clinical imaging tool that plays a major role in many clinical practices and applications. In combination with multiple available radiotracers, the compounds that enable PET imaging to target and gather information of function at the molecular level, PET can provide unique biomarker information. The non-invasive nature of PET imaging, in combination with its potential for fully quantitative and reliable reproducibility of biomarker information, are some very important aspects that make it desirable in the delivery of precision medicine. Precision medicine is defined as an approach for disease treatment and prevention that takes into account individual variability in genes, environment, and lifestyle for each person. PET can play a vital role towards wider adoption of precision medicine due to its potential in the delivery of unique biomarker information [2].

Engineering advancements over the last decades have led to the development of highly efficient PET systems and in the creation of hybrid imaging systems, notably the PET/CT and PET/MR systems. The clinical need for multi-modality information has led to the fast adoption of such hybrid systems in clinical practice, with “one-stop-shop” protocols providing multi-modality information in single imaging sessions. Finally, hybrid systems have enabled the use of imaging information in “synergy”, to provide new and superior information on the underlying function and anatomy [17].

Despite PET’s great success in clinical integration and applicability, the use of the modality and the main focus of many years of development have been concentrated on static imaging and qualitative or semi-quantitative measures. These have been driven mainly by applications in oncology, where these measures have so far been deemed sufficient in clinical pathways of cancer patients. At the same time, the ability of PET to provide fully quantitative measures of the biological functions under study has been reserved for research orientated applications and developments of new tracers or study of human physiology. But recently, the increasing focus on precision medicine has led to renewed attention to PET’s dynamic capabilities, for quantification of biologically relevant parameters by monitoring tracer kinetics and dynamic behaviour. These quantitative capabilities of PET are expected to be at the centre of future developments and clinical

research for the next decade [1, 18].

Problemata

The majority of the current clinical applications of PET can be found in oncology, where imaging information over the Whole Body (WB) is needed to detect and characterise the primary and metastatic disease. Whole body information is also desirable for many current and potential future applications of dynamic PET, which can result in fully quantitative measures and biomarkers information over the whole body. Beyond the use of such information for precision oncology, it can be used to study the kinetics of drugs distribution and function over the whole body. This information can be used, while considering the human body as a single system, in the study of interactions and signalling between organs of the body to investigate complex physiology and pathology interactions [1, 19].

A major limitation in the acquisition of the required PET data over the whole body is the limited axial field of view (A-FOV) of the majority of current clinical systems. The majority of the PET systems provide an axial coverage between 15 and 26 cm [3]. In practice, whole-body coverage is achieved using multiple bed positions at different axial locations to provide the desired axial coverage [4], or via continuous axial bed motion (CBM) during the acquisition [5]. Both acquisition strategies can be extended for Dynamic Whole Body (DWB) acquisition, by use of multiple repeated whole-body passes [6–8]. Recently these DWB protocols have been integrated within commercial PET systems [16]. These acquisition protocols pose challenges that arise from the resulting temporal gaps in the acquired dynamic data of any given bed position. These gaps are introduced at each bed position by the time spent on imaging other bed positions and by scanner system delays due to the time required to translate the bed in the axial direction and prepare for the acquisition of the next WB pass. The result is a sharp reduction in both total counts collected for each axial location as well as in temporal sampling frequency. Furthermore, acquisition of information from fast temporal changes in the early phase of the dynamic study is compromised, as those are not sampled adequately for all bed positions. Consequently, parameter estimates from dynamic whole-body PET acquisitions are potentially compromised by the above limitations in the acquisition, degrading their precision and accuracy.

Recently, scanners with increased A-FOV have been developed, offering increased sensitivity and substantially more or total-body coverage, that enables synchronous dynamic imaging of the whole body without the need of multiple bed positions and the associated issues with temporal gaps [13–15]. These systems are currently found in very few pilot PET centres around the world and are not widely adopted in clinics yet. Since the first Total-Body scanner came online there has been an increased focus in the research for clinical applications of such systems, one of which is the use for dynamic whole-body imaging. As such the

research interest in this field is expected to increase in the next years, with a particular focus on clinical utility as well as practical aspects of ease-of-use and cost-effectiveness.

Challenges and Contributions

PET dynamic data can be used to extract kinetic parameters over regions of interest or on the voxel level, with the latter being used to create parametric images of the applied dynamic model. Parametric images can provide information that is helpful in identifying and separating out different regions that exhibit different dynamic behaviour, without imposing predefined Volumes Of Interest (VOIs) in the analysis [20]. One of the major challenges in dynamic whole-body acquisitions using multiple whole-body passes is the estimation of accurate parametric images. Generation of parametric images from dynamic data requires fitting of the dynamic model of interest on time activity curves (TAC) for every voxel in the image. But due to the poor statistics and high noise associated with TAC measurements at the voxel level, which are further degraded by DWB acquisition protocols, parametric image estimates can be heavily corrupted by noise and potentially biased. The main objective of this thesis was to explore acquisition optimization and novel reconstruction strategies for the improvement of whole-body parametric maps. The contributions can be separated into two major parts. The first part A) is focused on optimization of the DWB protocol on a clinical PET/MR scanner, aiming at the reduction of temporal gaps in the DWB acquisition and increase of collected counts as well as an increase of sampling frequency. The second part B) is focused on the improvement in the use of acquired DWB PET data by exploiting dynamic reconstruction algorithms. As part of this PhD project, various dynamic reconstruction algorithms were implemented in the open source reconstruction platform CASToR, for use with simulated and real data acquired from clinical scanners. An innovative approach for direct multi-bed dynamic reconstruction was developed and applied on real DWB data, for the direct reconstruction of parametric images and temporal regularisation of the reconstructed activity image data.

HYBRID-ITN

This PhD project was funded and conducted within the Healthcare Yearns for Bright Researchers for Imaging Data (HYBRID) Innovative Training Network (ITN). This is an industrial and academic ITN, funded by the European Union's Horizon 2020 research and innovation programme under the Marie Skłodowska-Curie grant agreement No 764458. The aim of the HYBRID group is to advance and fully exploit the potential of integrated, dual-modality and multi-parametric imaging offered by multi-modality hybrid imaging. Quantitative and parametric imaging is at the centre of focus of the group.

The main challenges that were addressed by the group define the three main work packages of the programme:

- WP2: Data collection

The aim of the data collection group is to address challenges of multi-modality data acquisition and image reconstruction for the reliable formation of parametric and multi-parametric images.

- WB3: Data processing

The aim of the data processing group is to explore and improve on methods of extracting information using multi-parametric imaging and multiple parameters.

- WB4: Clinical translation

The aim of this group is to explore integration techniques of multi-parametric imaging into clinical use-case scenarios.

This PhD project was conducted as part of the data collection group WP2 (project WP2.4). The planned direction of the project was defined towards expanding computation and use of fully-quantitative parametric maps in PET to whole-body datasets. Specifically, the direction of the project was set towards the development of clinically viable schemes for parametric whole-body PET/MR imaging for improved characterisation of oncological diseases throughout the body. The carried out project focused on general methodological advancements for whole-body parametric imaging, with applications on real data focusing on whole-body pharmacological studies rather than clinical studies in oncology due to the limited availability of clinical whole-body data.

Specific tasks and goals have been pre-defined by the ITN, to be delivered throughout the project in the form of reports of deliverables and milestones. Those are not included in the thesis manuscript explicitly but many of them form part of the contributions.

Secondments between the partner organisations were also planned within the HYBRID network. The aim of secondments is for the participating PhD students to learn from practices in other organisation and engage in multi-centre research projects. Two academic and one industrial secondment was planned for each student. In this project, secondments were planned with the University Medical Center Groningen (UMCG), the Medical University of Vienna (MUW) and with General Electric Healthcare (GEHC). Additionally, the secondment of a student from King's College London (KCL) was organised to take place in our centre. The secondment with the student from KCL and the secondment to MUW resulted in collaboration projects, whose work has resulted in two publications. These are attached at the end of this manuscript in the **Secondary Contributions** section.

- GEHC: Waukesha, WI (3 weeks)

The secondment was planned at the main factory facility which hosts the research and development team of GE's PET/MR systems. The purpose of the secondment was to conduct research for the

development of a fully automated dynamic whole-body acquisition protocol for the Signa PET/MR system. In addition this secondment served as an experience of research and development in the industrial setup.

- GEHC: Zürich (1 week)

The secondment with GE also took part at the University hospital of Zürich, where research and testing is performed for clinical applications of dynamic PET imaging, in order to get an insight into the clinical implementation of dynamic PET protocols.

- UMCG (2 weeks)

This secondment was planned in order to gain experience in PET kinetic modelling for research studies and explore uses of analysis methods that could be used for this PhD project.

- MUW (2 weeks)

The initial purpose of this secondment was to make use of advanced reconstruction techniques developed for this PhD project to a cohort of epilepsy dynamic PET dataset at MUW for generation of parametric images. Due to the pandemic, the majority of the secondment was conducted remotely. The collaboration project was slightly adapted to be performed by distance and focused more on motion correction aspects for dynamic brain PET.

Apart from the secondments, the HYBRID network conducted many meetings (approximately twice a year) where all the ITN partners would come together and discuss progress. These meetings served substantially in exchange of ideas and guidance on individual research projects as well as in forming of collaborations.

Organization of the manuscript

The manuscript is organised into two major parts. **Part I** outlines the methodologies involved in this project that are necessary for the understanding of the work carried out in this project. It is separated into four chapters which cover PET physics, pharmacokinetics, PET image reconstruction theory and implementations in custom software respectively. **Part II** of the manuscript provides the contributions made in this thesis in the form of four chapters.

Chapter 5 describes the development of a custom fully-automated protocol for dynamic whole body imaging on the Signa PET/MR and shows results from the use of this protocol on a NHP scan.

Chapter 6 describes the development and implementation of dynamic reconstruction methods within an open-source reconstruction software, which were subsequently used in this project, for dynamic single bed studies. The rest of the chapter outlines in detail an extensive simulation study conducted for the evaluation

of the developed reconstruction methods for DWB Patlak parametric imaging. This simulation study was presented at the **IEEE/MIC** 2019 conference and submitted for publication to the **Physics in Medicine & Biology** journal.

Chapter 7 presents the development of a direct multi-bed dynamic reconstruction method, as an extension of the developments presented in chapter 6 for use with all dynamic bed data from DWB studies. In this chapter we present the application of this direct multi-bed reconstruction method to dynamic whole body data from a first in man pharmacological study conducted at our centre. The results of this application in the pharmacological study were presented at the **European Association of Nuclear Medicine** 2020 conference.

Chapter 8 presents work conducted for the application of an adaptive modelling method for dynamic reconstruction and its application on whole body dynamic data from the pharmacological study presented in the previous chapter. The results of the application were presented at the **IEEE/MIC** 2020 conference.

A Conclusions and Prospects section is provided at the end of **Part II**, summarising the contributions in the context of the aims of this PhD project and of clinical utility of findings. Future prospects and aspects that need to be addressed further as also discussed.

Appendices with supplementary material relating to the presented work are also provided.

Secondary contributions made in collaboration projects as part of the ITN programme are provided at the end of the manuscript in the **Secondary Contributions** section.

Part I

Theory and Methods

Chapter 1

Positron Emission Tomography

This section covers aspects of the main principles of Positron Emission Tomography (PET) and serves as a brief introduction to the notions that are necessary for the description of the work carried out in this thesis. It is not an exhaustive review of the processes involved in PET imaging. Readers can find more basic principles explained in detail in the textbooks which are frequently referenced in this chapter.

1.1 Historical Perspective

The main principles of a PET imaging system were developed and demonstrated with a working scanner prototype in the late 1970s by Ter-Pogossian et al. [21] and Phelps et al. [22]. The main concept of their prototype, which forms the basis of PET devices, was the placement of detectors in a circular formation around the imaged object and the detection of annihilation photon pairs which serves as "Electronic" collimation. This principle of "Electronic" collimation makes PET imaging superior to single photon based imaging devices still until today as it does not require a physical collimator which considerably reduces the sensitivity, as in Single-photon Emission Computed Tomography (SPECT) imaging systems. Early PET systems were limited due to the cost and engineering limitations to an axial coverage of a few axial planes and were mostly used in brain imaging. Development of scanner models with a larger diameter and larger axial Field of View (FOV) enabled use for imaging of other organs than the brain [23]. The expanded FOV along with the capability of achieving whole-body coverage by use of shifted axial acquisitions [24] (multiple axial bed positions to achieve whole-body coverage) have established the use of PET in oncology [25] and driven many more technological developments towards higher sensitivity for improved small lesion detectability and reduction of scan time [26].

1.2 Fundamental physics of PET

1.2.1 Positron emission

As its name suggests, PET is an imaging method based on positron emission. Positron emission is a spontaneous process that happens as part of the β^+ decay process of radionuclides. Radionuclides are comprised of atoms with excess energy that decay to stable forms via routes that result in the emission of radiation. The rate at which a radionuclide undergoes decay depends on its characteristic half-life $T_{1/2}$. This is defined as the time taken for half of the nuclei of a specific radionuclide to decay. The rate of decay at any time t is defined as the activity $A(t)$, measured in Becquerels (Bq), which changes over time according to

$$A(t) = A_0 e^{-\lambda t}, \quad (1.1)$$

where A_0 is the activity at reference time $t_0 = 0$ and λ is the decay constant, for which

$$\lambda = \frac{\ln(2)}{T_{1/2}}. \quad (1.2)$$

The β^+ decay process results in the emission of a positron (e^+) particle and a neutrino (ν). The positron is given part of the excess radioisotope energy in the form of kinetic energy, which when emitted within a material is gradually lost from continuous interactions with other atoms of the material until the positron approaches close to a rest. During this period the positron follows a tortuous random path. The positron range can be defined for a sufficiently large number of emissions as either the FWHM or the mean of the distribution of distances between the emission and annihilation positions. The positron range value will depend on the positrons energy spectrum and the interacting material properties. After most of its kinetic energy has been expended, the positron rapidly interacts with an electron and annihilates. This interaction results in the conversion of the two particles into two photons of 511 keV which are emitted in almost opposite directions ($\sim 180^\circ$). Due to the non-zero kinetic energy during the annihilation, the excess energy results in a small acollinearity of the photon pair. For *in vivo* [^{18}F]-Fluorodeoxyglucose (FDG) imaging, a common radiolabeled tracer used in PET oncology applications, it has been shown that the FWHM acollinearity is approximately 0.54° [27]. A list of positron emitting radionuclides which are commonly used in PET imaging is given in table 1.1 along with relevant characteristics for PET imaging.

1.2.2 Interactions with matter

The mean range of positrons from commonly used PET radionuclides is in the order of a few millimetres within tissue and almost all positrons are annihilated within the body. On the other hand, the 511 keV photons

Table 1.1: Commonly used radioisotopes and their relevant characteristics for PET imaging [28].

Radionuclide	Half-life	e^+ maximum energy (MeV)	Mean range in water (mm)
^{15}O	2 min	1.732	3.0
^{13}N	10.0 min	1.199	1.8
^{11}C	20.4 min	0.96	1.2
^{18}F	110 min	0.634	0.6
^{68}Ga	67.8 min	1.899	2.9
^{64}Cu	12.7 h	0.653	0.7
^{89}Zr	78.4 h	0.902	1.3

have fewer chances of interacting within the body and a large fraction of them will exit the imaged object without interacting.

The two most probable interactions for photons of 511 keV in tissue are photoelectric absorption and Compton scattering. In photoelectric absorption, the photon is completely absorbed while interacting with an atomic electron of the inner shell, to which it provides all of its energy. In Compton scattering, the photon interacts with an atomic electron of an outer shell, to which it passes part of its energy. This scattering process results in a change of direction and reduction of the energy of the original photon, while the loosely bound electron is ejected from the interacting atom. Between the two processes, the Compton effect is the dominant interaction for 511 keV photons in tissue. Elastic scattering (Rayleigh scattering) is another interacting process in which no loss of energy occurs and the direction of the incident photon is changed by a relatively small angle. This interaction is more dominant in lower energies than 511 keV photons.

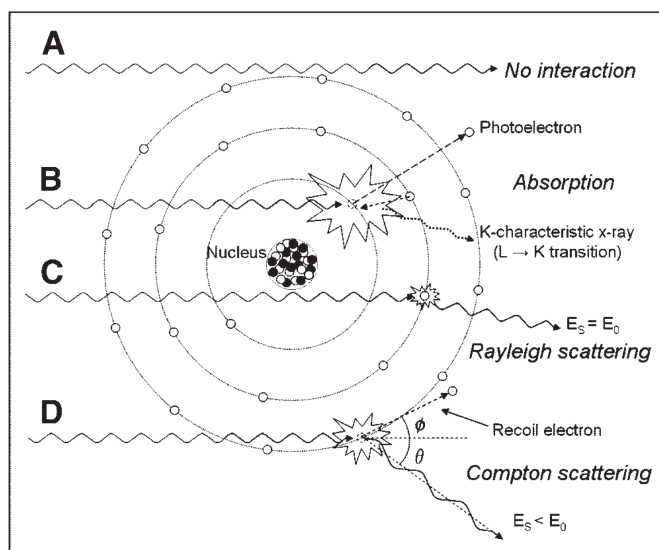


Figure 1.1: Illustration of the described interactions. (A) No interaction resulting in transmission of photon. (B) Photoelectric absorption from inner shell electron, resulting in its ejection and followed by an inner electron transition and characteristic X-Ray emission. (C) Elastic (Rayleigh) scattering conserving the energy of the photons but resulting in small angle change in direction. (D) Compton scattering with outer shell electron resulting to change of energy and direction of incident photon. Adapted from Seibert *et al.* [29].

1.2.3 Attenuation

Knowledge of the probabilities for the interaction of 511 keV photons in a material can be used to calculate a precise attenuation factor that can be applied at the macroscopic level. Given a well collimated photon beam of intensity I_0 , the intensity I_x at depth x within the material (along the direction of the beam) will be reduced due to interactions with the material according to Beer-Lambert's law

$$I_x = I_0 e^{-\mu x} , \quad (1.3)$$

where μ is the linear attenuation coefficient (in cm^{-1}). This factor accounts for all possible interactions, whether absorption or scattering, and its value depends on the material properties and the energy of the photons. In water its value for 511 keV photons is 0.096 cm^{-1} [30].

1.3 PET Systems

1.3.1 PET Detectors

The goal of a PET imaging system is to stop and detect the annihilation photon pairs and record information that can be used to estimate the annihilation event's position. The basic component for the detection of annihilation gammas is the scintillation crystal. These are inorganic crystals that emit light (lower energy photons) upon interaction with the gammas. The amount of produced light is proportional to the energy deposited by the gamma interactions and can be used to deduce energy information of the interaction. Photosensitive detectors are coupled with the crystals to capture the produced light and output an electronic signal that can be digitally registered. Traditionally Photomultiplier Tubes (PMTs) are used in most PET systems, while some more recent systems make use of Silicon Photomultipliers (SiPMs). Depending on their mode of operation SiPMs can allow for better efficiency and response speed and can be used in conditions where PMTs could not, such as within the MR field of PET-MR hybrid systems. More details on SiPM integration in PET/MR are given in section 1.4.2. The most common configuration of the PET detectors is within a block or module configuration, where a smaller number of photosensitive detectors to crystals is used. An example of a single crystal block to 4 PMTs is shown in figure 1.2 for PMT based scanners. The crystals are partially cut into segments to reduce lateral dispersion of light and improve localisation of detection by the PMTs. In the example of figure 1.2 the crystal is cut in a 6×6 configuration.

The blocks or modules are placed in ring configurations that provide full 360° of coverage in the transaxial direction. Multiple rings are often placed adjacent to each other to increase axial coverage and solid angle coverage which provides increased detection sensitivity.

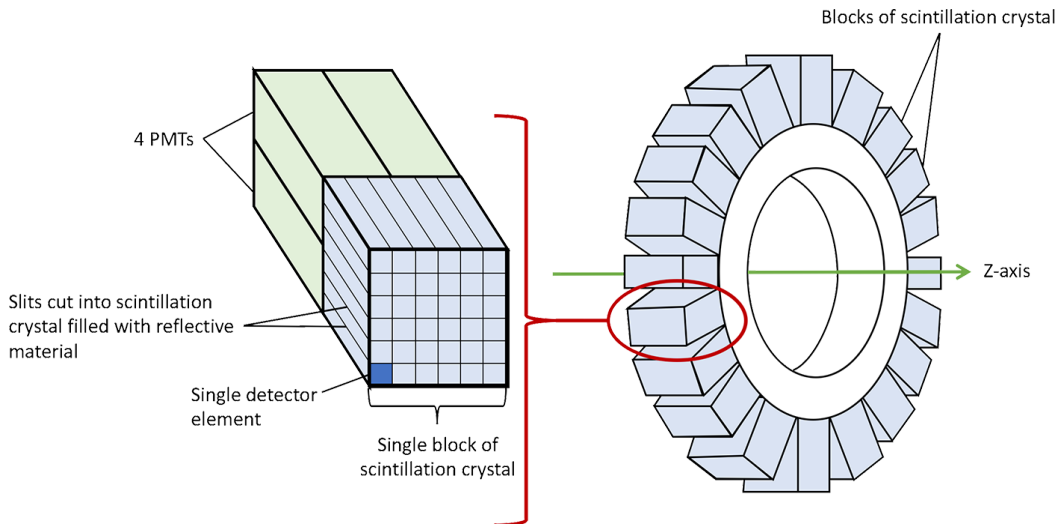


Figure 1.2: Example illustration of PMT based block detector diagram and their placement within a PET ring (Adapted from www.radiologycafe.com)

1.3.2 PET Data coincidence sorting

Individual events recorded by the detectors are called *single* events. In PET, detection of annihilation events requires the detection of both annihilation generated photons. To identify these photons, the detection system makes use of "coincidence detection". Pairs of single events detected within a predefined timing window are assumed to be photons originating from a single annihilation which are defined as *prompt coincidence events*. The line connecting the two detectors that record the coincident event is defined as the Line of Response (LOR).

Improved timing resolution of detector systems has enabled further information of the annihilation point to be made by capturing the detector arrival difference of the two annihilation photons. This difference can help localise the point on the LOR where the annihilation took place, within some range of uncertainty defined by the detector timing resolution. This capability of PET is referred to as *time-of-flight* (TOF). This information, collected for each coincidence event, can then be used within the image reconstruction process for improved results, as it will be shortly described in chapter 3.

Unfortunately not all coincidence events recorded within the coincidence window will always be originating from the same annihilation event and be detected without interacting within the body. Apart from true coincidences, they could also be one of the following listed type of events. Some of these type of events are illustrated in figure 1.3.

- **Random event**

As the rate of single events increases the chances of photons originating from different annihilation events being detected within the coincidence timing window are also increasing. In this case, the

system will record coincidence events that are not correlated. These events are referred to as random events. The rate of random events is directly proportional to the size of the timing window and to the square of the activity in the scanner. These events are uncorrelated to the imaged object and hence degrade the acquired data and subsequently image quality and quantification. The expected rate of random coincidences can be estimated using the rates of single events or using delayed coincidence windows. These estimations are then pre-processed and subsequently applied as corrections in the image reconstruction process.

- **Scatter events**

As described scattering of the annihilation gammas results in changes to its energy and direction of travel. Subsequent detection of scattered gammas results in mispositioned LORs that also degrade the data, image quality and quantification. Because scattered gammas have lower energy than 511 keV, they can be rejected by applying a low energy threshold in the detectors. But due to energy resolution limitations, this threshold is set low enough to best avoid rejection of true coincidence events while still filtering a reasonable amount of scattered events. To correct for the remaining events that are being recorded as true coincidences, special scatter simulation algorithms are employed to estimate the amount of scatter coincidences in the data and account for it during the image reconstruction process [31, 32].

- **Multiple events**

Multiple single events (more than two) can be recorded within the coincidence timing window in which case they are referred to as multiple events. As these cannot be used to resolve LORs, they are either rejected completely or in some cases processed further to deduce which pair of single events are more likely to be true coincidences, using techniques that vary between scanner models and manufacturers.

- **Delayed event**

As described above, an estimation of randoms can be made using an additional detection channel to capture coincidences with a delay of several times the duration of the coincidence window. These events are considered uncorrelated and serve as a direct measurement of randoms. Specific variance reduction techniques are then applied on these randoms estimations before being used as corrections in reconstruction, to avoid inducing additional noise in the data [33].

- **Prompt event**

True, random and scatter events that meet the acceptance criteria for coincidence detection are indistinguishable at the time of detection and recorded as valid coincidence events. They are referred to as prompt events. These are pre-corrected or used directly in the reconstruction process along with the corrections, depending on the use of either analytical or statistical reconstruction methods respectively.

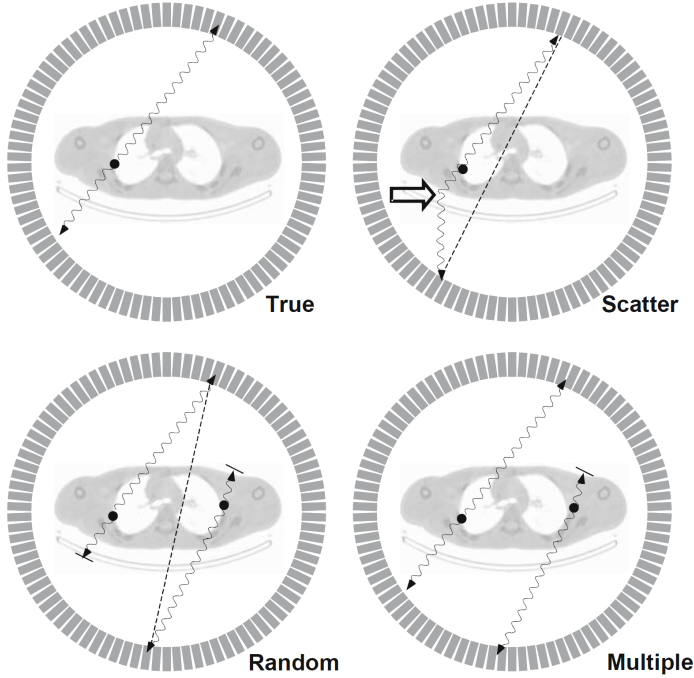


Figure 1.3: Representation of different types of detected coincidence events. Adapted from Bailey *et al.* [33].

1.3.3 PET acquisition

As described the ring formation of PET detectors is the dominant geometry used in PET systems. Using multiple rings results in the increase of Axial Field of View (A-FOV), solid angle coverage and possible combinations of detectors meaning a higher number of LORs. But early multi ring systems were making use of 2D acquisition, where only direct and cross-plane ring coincidences were allowed. This was enforced using tungsten septa between rings, as seen in figure 1.4.

With evolving detector and electronics technology, 3D acquisition became possible and is now the standard acquisition mode. 3D acquisition offers the same data as 2D acquisition and also includes all the oblique LORs data resulting in an increase of sensitivity (4 to 6 times) [34]. The use of oblique views leads to non-uniform sensitivity profiles in the axial direction due to the higher number of LORs closer to the centre of the A-FOV, with the maximum sensitivity at the centre and a minimum at the edges of the A-FOV. A comparison between the 2D and 3D sensitivity profiles is shown as an example in figure 1.5. In addition to more coincidence events, the higher sensitivity and acceptance of single events result in an increase of randoms and scatter events, which in addition may now be originating from activity outside the A-FOV of the system.

In 3D mode the maximum angle of events accepted in the axial direction can sometimes be limited by enforcing a maximum ring difference permitted LORs. This results in a uniform axial sensitivity profile at a

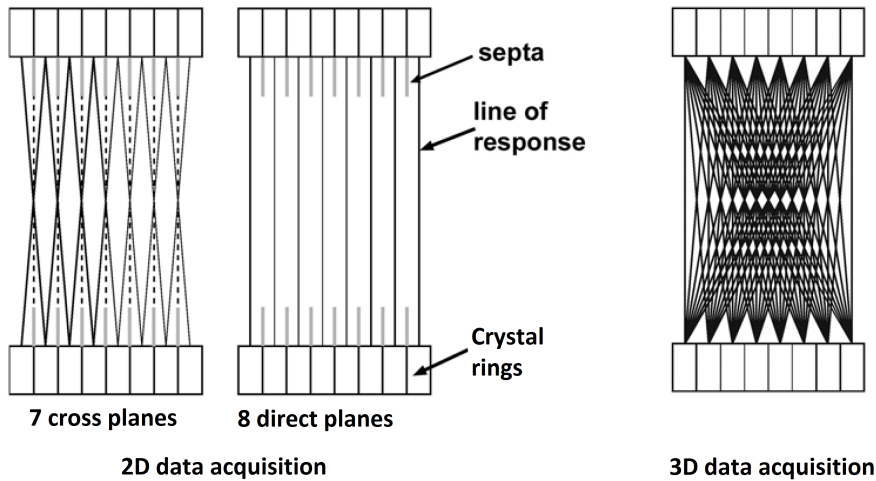


Figure 1.4: Example illustration of LORs for 2D acquisition mode using direct and cross planes (left) and 3D acquisition mode (right) for an 8 ring scanner with 15 axial slices. Adapted from Cherry S. and Magnus D. [35]

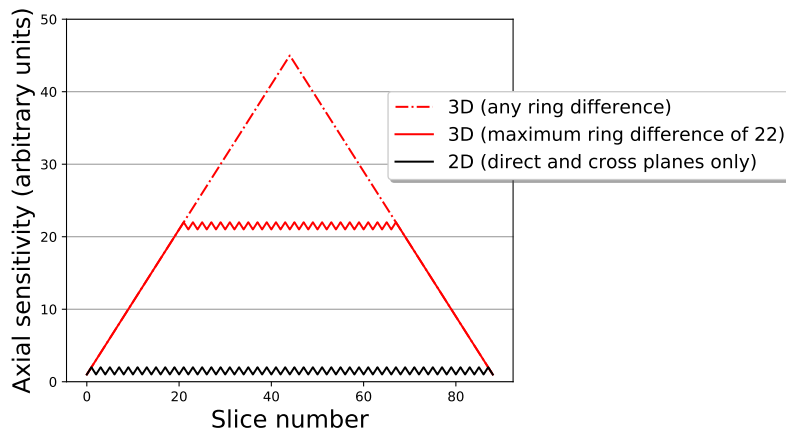


Figure 1.5: Example of 2D and 3D axial sensitivity profiles, with and without maximum ring difference limits, for a scanner with 45 crystal rings which provide 45 direct and 44 cross-planes.

central region of the A-FOV, as seen in figure 1.5.

1.3.4 Storage of PET coincidence events

The recorded coincidence data are stored digitally to allow post processing and reconstruction of image data. The different methods for storing the data can result in different storage requirements, allow or not allow for specific event information to be stored and even necessitate different reconstruction techniques.

- **List Mode**

In the simplest form coincidence events can be stored in a binary file as a stream of events by the order of their detection. This format follows naturally the detection process and allows for multiple detector information to be included in each event. A time tag is normally included in the data stream every

millisecond. The minimum information recorded per event is the detector pair IDs. Any additional information such as time-of-flight, detection energy, etc. can also be included with each event. For time-of-flight the data can include exact arrival time differences, to make best use of the information in post processing or reconstruction methods. The use of list-mode files is practical for dynamic studies as they naturally include all dynamic information and can take less storage space than the other alternative formats described below. List-mode data can be binned into the formats described below before reconstruction or used directly with list-mode reconstruction algorithms.

- **Histogram**

Coincidence events per detector pair (LOR) can be summed together and stored into a single entry. The total number of entries will be equal to the total number of detector pairs. These entries make up a histogram, where effectively all the events have been histogrammed into the detector pairs. No timing information is preserved and hence multiple histograms are required if data are recorded dynamically, in a predefined temporal binning. This format can result in smaller files for static imaging compared to list-mode, but in the case of dynamic imaging it frequently results in a much larger total size of files as multiple detector pair entries are empty (zero) for some time frames. Furthermore, if time-of-flight information is also available, separate histograms need to be created for each time-of-flight bin (discretization of the TOF resolution), which further increases the zero entries and storage requirements. Compression is possible in both axial and transaxial direction of the data, which is referred to as axial compression (or span) and angular compression (or mashing) respectively [34]. These are employed by some scanner manufacturers to counteract the increasing size of histograms from increasing scanner resolution and better TOF resolution. The compression strength is chosen as a trade-off of file size and degrading image quality properties [36].

- **Sinogram**

Sinograms are representations of the data in projections through the process of projection using a transformation such as the Radon or X-Ray transform [37]. Each pixel of the sinogram represents the integral of events over a specific line through the image space. The name "sinogram" comes from the fact that a point source (off-centred) is represented as a sine wave in the sinogram. The use of sinograms is inherited from other tomographic imaging methods where data are acquired as projections. Sinograms are used with analytical reconstruction methods, shortly described in chapter 3, which require the projection space to be fully and uniformly sampled.

As in this project we did not make use of analytical reconstruction algorithms, we have not described the formation and use of sinograms in detail. In the project, we made use of both real data from clinical PET scanners and simulated data from analytical simulations. For real data we made use of the list-mode data

format, to reduce file size and allow for flexibility in the treatment of the data, while for simulations we used the histogram data format as we were limited to that by the nature of analytical simulations. It is important to note that clinical PET systems are performing reconstructions using histograms or sinograms and although they can record data in list-mode format, they always re-bin the data to histograms or sinograms before performing a reconstruction. By contrast in this project, we made use of list-mode reconstruction algorithms when using list-mode datasets.

1.3.5 PET Corrections and Quantification

PET has always been used as a quantitative imaging method, providing image values that relate to radioactivity concentration. This is an important requirement for semi-quantitative and quantitative interpretations of the imaged data, with quantitative measures being at the foreground on this thesis project. But accurate quantification of images requires corrections that need to be considered before and during the reconstruction process. The main corrections needed for quantifiable PET are outlined here.

- **Randoms correction**

As discussed previously, random events in the data are estimated using delayed coincidence detection or by measurements of single event rates between detectors. For most clinical scanner manufacturers and for list-mode data these are normally provided in the same stream of data, with delay events recorded similarly to prompts and with single event rates recorded for every predefined time interval (for example every second) for each detector or detector block. Similarly, for histogram data, a separate histogram of random events is provided. A histogram per frame (time bin) is required for multiple frame datasets, for randoms as well as for prompt events. In the reconstruction software used in this projects, CASToR [11], the corrections are provided for each event LOR or histogram bin within the raw dataset file. Furthermore, randoms corrections in CASToR are provided in rates (s^{-1}) which is a more natural format to use with list-mode data reconstruction and dynamic datasets.

- **Scatter correction**

As described previously, a certain amount of the annihilation gammas will scatter with the atoms of the travelling medium via Compton scattering, which results in changes of energy and direction of the gammas. Even after the energy filtering applied on the detectors, an amount of those scattered gammas will be detected and recorded as coincidence events that degrade the PET data and affect image quality and quantification. The most commonly used approach to account for scatter in clinical scanners is the use of the Single Scatter Simulation algorithm [31] to estimate scatter. These simulations are based on an initial activity distribution estimate from the uncorrected PET data and knowledge of the probability of scattering. Scatter estimates, similar to random estimates, are then used as ad-

ditive corrections within statistical reconstruction methods. Again, in CASToR these are provided as rates (s^{-1}).

- **Normalisation**

Sensitivity between LORs will differ due to detector and geometric efficiencies effects. Normalisation coefficients for each LOR are estimated using measurements and modelling of the normalisation components and are subsequently used in reconstruction to correct for these efficiencies.

- **Dead-time correction**

After every detection event, a certain amount of time is required for sub-systems involved in the detection to become ready for detection again and so interaction events occurring during that recovery time will not be registered. As the number of interactions increases at higher imaged activities, the proportion of events not registered is also increasing. The result is a non-linear system response for different levels of imaged activities. This effect is corrected using dead-time correction which is applied by the use of lookup tables that relate single rates to dead-time factors in addition to real-time dead-time monitoring measurements.

- **Attenuation correction**

Absorption or scatter interactions within the body results in loss of gammas detection. Even if only one of the two annihilation gammas is lost the result is a non registered event. The probability of attenuation depends on the total probability of interaction within a LOR and is independent of the annihilation position within that line. This enables the estimation of attenuation factors for each LOR within the body by use of transmission measurements, either with radioactive sources or X-rays sources. For these measurements earlier scanners made use of positron or single gamma sources to estimate attenuation while most modern clinical systems make use of Computed Tomography (CT) or Magnetic Resonance (MR) scans to estimate attenuation factors.

- **Calibration Factor**

Subsequently, after all other corrections have been applied there is a need for a global calibration factor to relate the estimated number of true events to activity concentration. PET systems are calibrated against a reference source to obtain such factors.

- **Decay correction**

Finally, measurements need to be corrected for decay of the imaged radionuclide for the duration of the acquisition and for decay-correction to a reference time. For static imaging, the reference time is chosen to be the imaging start time, while for dynamic acquisitions the reference time is commonly chosen to be the time of tracer injection.

1.4 Hybrid PET Systems

1.4.1 PET-CT

As described above attenuation correction is essential for quantitative PET imaging. Early PET systems made use of external radioactive sources to acquire a transmission scan. Some of the drawbacks of these methods were that transmission scans would contribute to an increase of image noise on PET images and that transmission scan acquisition was increasing the total duration of the examination. As PET imaging became more frequently used in clinical applications, the need for fusion of PET images with CT images became apparent, firstly for the clinical value by complementary PET functional images to CT anatomical images and secondly for aiding in attenuation correction and anatomical localisation. These needs led to the development of the first hybrid PET systems, with the first PET/CT system being introduced in the late 1990s [38]. The first PET/CT was able to acquire a whole body PET/CT scan, using multiple bed positions as it will be described later in this chapter, within an hour with precisely co-registered CT and PET images that were acquired close in time [39]. The CT scan was used in PET attenuation correction via scaling of attenuation coefficients (μ) to account for the energy difference between CT X-rays and annihilation photons [30]. PET/CT eliminated the need for radioactive source transmission scans and the problems with excessive noise associated with these relatively poor quality transmission images.

1.4.2 PET-MR

MRI provides anatomical images with higher soft-tissue contrast than CT imaging. The option of different acquisitions sequences can allow for different types of soft-tissue contrast, which can also extend to dynamic and parametric MR imaging applications [17] and also to functional MRI [40]. The fusion of PET and MR was technically challenging due to interference between the two systems [41]. Initial PET and MR clinical workflows and systems made use of separate PET and MR or PET/CT and MR scanners to scan the patient using a single bed to transfer the patient from one scanner to the other and minimise patient misalignment [42, 43].

The use of PMT based detectors for synchronous PET/MR imaging was only possible using long optical fibres that shifted the detection of events by the PMTs at a safe distance away from the centre of the magnetic field [44, 45]. Later advancements in PET detector technology allowed for Avalanche photodiodes (APD) and silicon photomultipliers (SiPM) based detectors, which led to the development of PET inserts [40] for MR and the development of fully integrated PET-MR systems that perform synchronous acquisitions [46–48]. There are currently two PET/MR integrated systems by commercial manufacturers, the Siemens mMR and the GE Signa. In this project, we relied on access and real PET data from a GE Signa PET/MR that

is available in our centre. But we also made use of Siemens mMR data in a collaboration project with the Medical University of Vienna that is described in the Secondary Contributions section at the end of this manuscript.

The Signa PET/MR scanner was designed based on an existing 3 Tesla MR scanner (3T MR750w MR scanner) that was modified to accommodate the PET detector ring. The ring comprises of 28 transverse modules (seen in figure 1.6) with 720 scintillator crystals per module. Those are coupled with SiPM detector modules, which are capable of capturing TOF information. A schematic of the modules and their integration in the system ring is shown in figure 1.6. The PET ring configuration results to 45 crystal rings which provide a total of 89 slices and an A-FOV coverage of approximately 25 cm with a slice thickness of 2.78 mm. Details on the system characteristics and evaluation of performance can be found in the work of Grant *et al* [47].

It is interesting to note that the latest GE PET/CT systems make use of similar detector configuration and type which provide similar performance for PET imaging [49].

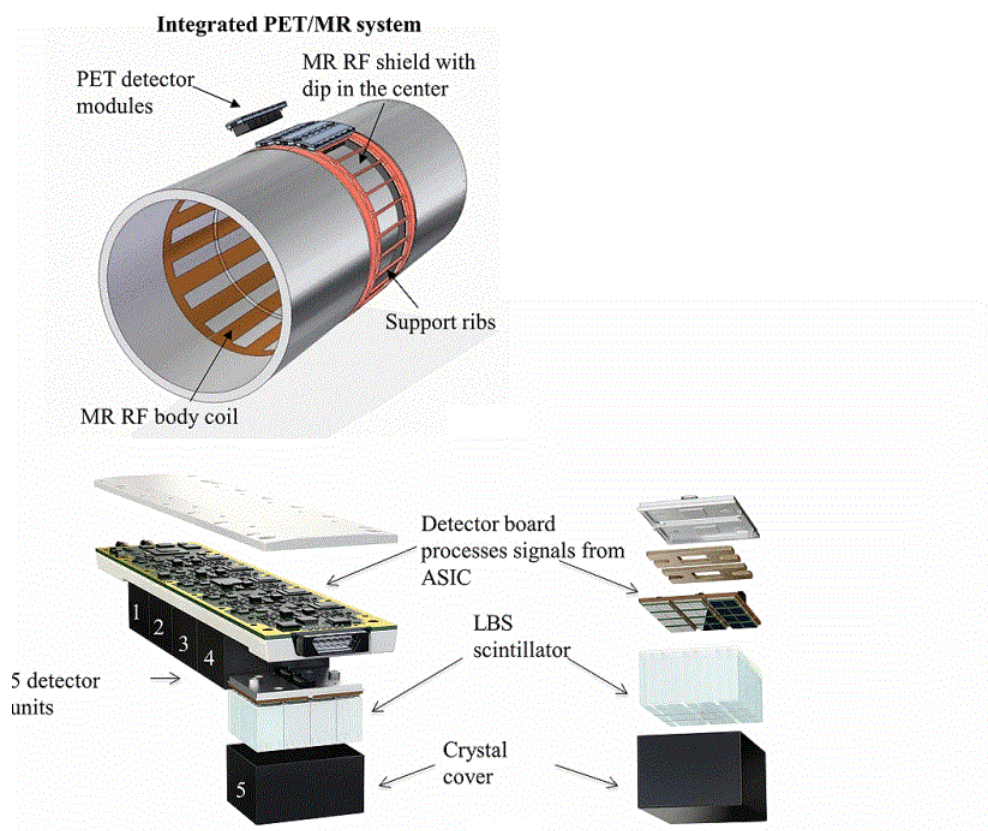


Figure 1.6: Schematic of the GE Signa hybrid PET-MR system, comprising of detector module units (bottom) in a ring formation within the MR RF body coil (top) [48].

1.5 Whole Body PET: Static Imaging

For many clinical applications, as for example in oncology, PET imaging over the whole body is essential for the detection and characterisation of primary and metastatic disease. Developments in PET detectors technology and reduction of production costs have resulted in increasing axial length of PET scanners using additional detector rings, with currently widespread clinical models offering between 15 to 26 cm of axial coverage [3]. In practice for static imaging whole-body coverage is achieved using multiple bed positions. The first suggestion and optimization work in extending the effective A-FOV of PET scans using multiple bed positions was made by Dahlbom *et al.* [24]. This work was made on PET systems operated in 2D mode, where a bed displacement of approximately equal to the system's A-FOV was used to increase the acquisition's effective A-FOV. As systems became capable of acquiring in 3D mode, offering increased sensitivity but resulting in axial varying sensitivity profiles, different strategies were needed for multi-bed acquisitions. The two methods suggested and developed are the *Step and Shoot* (SS) [4] and the *Continuous Bed Motion* (CBM) [5] acquisition methods.

1.5.1 Step and Shoot

The SS method makes use of multiple bed positions that are partially overlapped in the axial direction to increase the sensitivity of the acquisition at the edges of adjacent beds, by combining data of adjacent beds over the overlapping region as shown in figure 1.7. One way of combining the multi-bed datasets is to reconstruct each bed individually, displace the reconstructed images according to their axial location and combine them using weighted averaging [4]. This method has prevailed in clinical PET systems that use the SS acquisition method, as it does not require additional considerations in the reconstruction process of each bed and the combination of bed images can be performed post-reconstruction. Alternatively, the axial displacement of each bed raw dataset can be performed during the projection and back-projection process in iterative reconstruction, which then directly results in the reconstruction of the whole-body image [50]. Use of the overlap data in iterative reconstruction can potentially result in improved noise characteristics at the overlapping regions, as the full sampled statistics over these regions are combined prior to each image update [50, 51]. The axial sensitivity profile for the Signa PET-MR system is shown in figure 1.7. The system makes use of all (44) ring differences in the acquisition and reconstructions, which results in the shown axial sensitivity profile. Using this profile, multi-bed acquisition resulting in a uniform axial sensitivity profile requires overlap of 44 slices ($\sim 50\%$ of A-FOV). The amount of overlap used depends on the needs for uniformity in axial sensitivity and reconstructed image noise. This in term will also depend on the used reconstruction type and the activity distribution of the imaged subject [4]. For standard clinical scanning at the Signa PET-MR an overlap of $\sim 27\%$ is used by default, to balance between sensitivity uniformity and

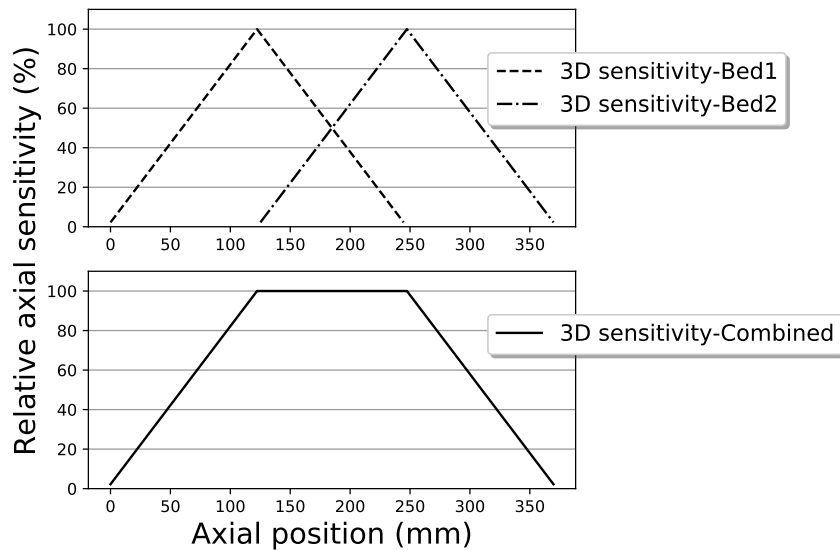


Figure 1.7: Relative axial sensitivity of individual beds (top) and combined sensitivity profile (bottom) for approximately 50% overlap for the Signa PET/MR.

examination time for standard WB examinations. The trade-off is made between the effective A-FOV and the total acquisition time, with the latter being of practical importance for patient comfort and high throughput. In addition, the acquisition time per bed is also an important parameter that affects this trade-off. For example, newer and higher sensitivity scanners can enable shorter scanning per bed for the same image quality, which allows for increased overlapping and improved axial sensitivity uniformity at the same total scan time. Examples of three overlapping options and the provided coverage for the Signa PET/MR are shown in figure 1.8 and 1.9 respectively. Many clinical WB protocols actually require imaging of approximately half the length of the body, from head to thighs, which can be accommodated with 5 or 6 bed positions on the Signa PET/MR. When full body coverage is required the number of beds is increased to 9 or 10.

1.5.2 Continuous Bed Motion

Continuous Bed Motion was proposed as an extension of step and shoot acquisition performed with small steps, to provide uniform axial sensitivity profiles [52, 53]. In clinical CBM acquisition protocols, the bed positional information is stored in list-mode during the examination and the data are sorted after or during the examination in histograms or sinograms (referred as "chunks") before reconstruction. The velocity of the bed movement can be adjusted depending on the amount of desired collected statistics, similar to the acquisition time per bed in SS acquisitions. In recent systems, the bed velocity can also be varied within an examination according to the needs and distribution of the imaged activity [5]. Beyond the potential technical gains, CBM protocols have also been shown to aid in patient comfort during examination [54].

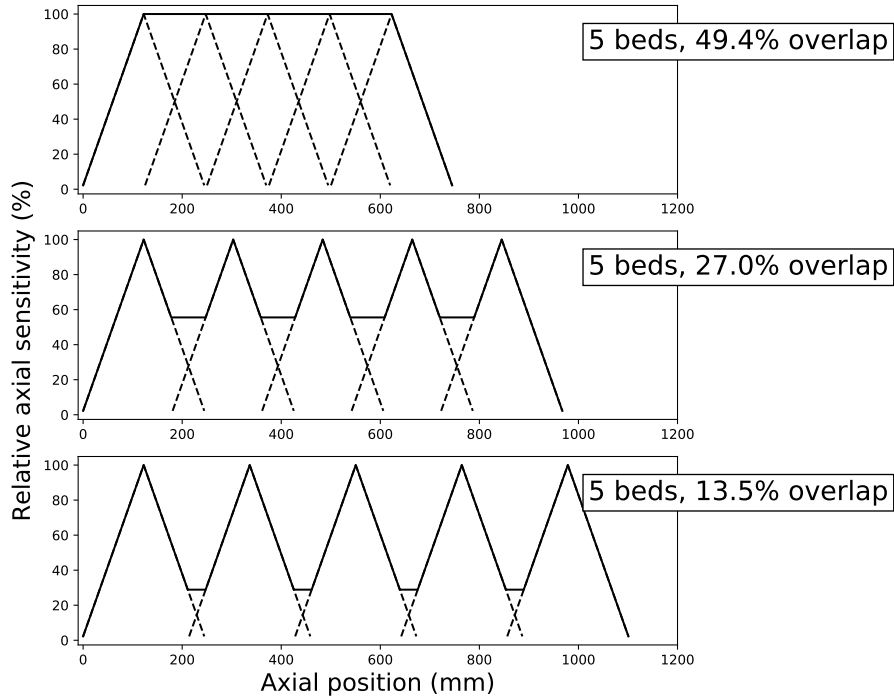


Figure 1.8: Relative axial sensitivity of 5 bed positions with decreasing overlap for the Signa PET/MR.

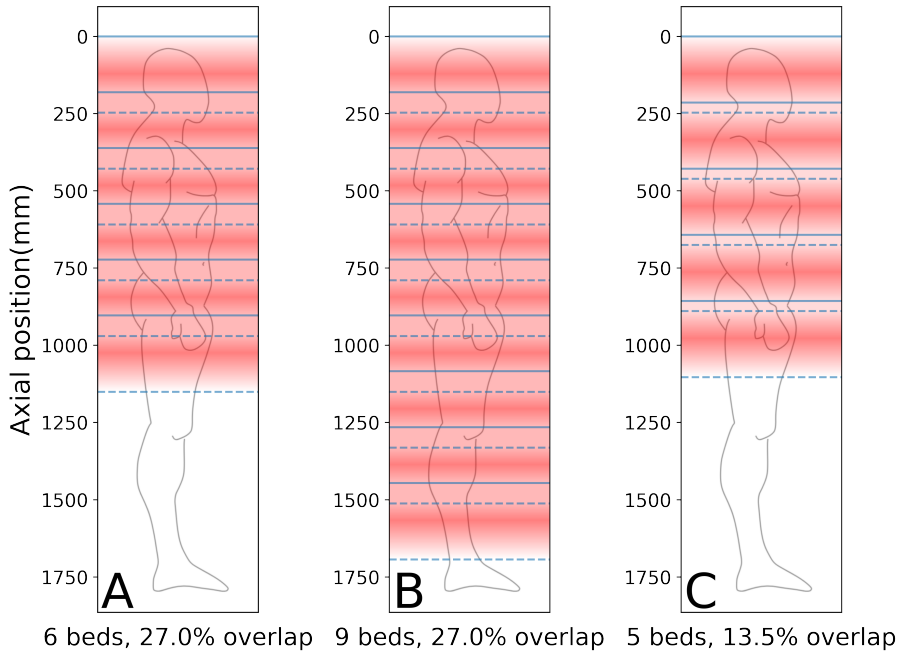


Figure 1.9: Combinations of overlap and number of beds for static (A&B) and dynamic whole-body imaging(C). Relative axial sensitivity is shown in shades of red, with bed start (—) and end (----) positions.

1.6 Whole Body PET: Dynamic Imaging

As outlined in the introduction, clinical and research applications can benefit from DWB PET information. In clinical applications, DWB data can be used to construct fully quantitative parametric images for diagnosis

and response monitoring of disease and pathology over the whole body. In research, DWB information can enable studying of the whole body organism and interactions between different tissues, organs or compartments [1, 19].

Although recent advancements in PET have led to the development of PET/CT systems with increased A-FOV, with approximately half [13, 14] or even total-body axial coverage [15], the majority of clinical PET systems in use are limited in the range from 15 to 26 cm [3]. Based on the same principles and methods used in static WB PET imaging, DWB protocols have been developed with the use of repeating whole-body passes (often referred to as "sweeps"). These protocols can be implemented using SS acquisition, as proposed in the original work on multi-bed DWB protocols by Karakatsanis *et al.* [6, 7], or as later proposed using CBM [16, 55]. Such protocols are nowadays implemented in commercial PET/CT systems [16] and it has been shown that their use in clinical practice is feasible [56, 57]. Their uses in clinical imaging is an ongoing active area of research.

The transition from single-bed to multi-bed dynamic acquisition poses some considerable limitations in acquisition counts and sampling frequency. The immediate effect of the transition is the introduction of temporal gaps in the acquired data of any given bed position. These are introduced at each bed position by the time spent on imaging other bed positions and by scanner system delays due to the time required to move the bed to the next position and prepare for the next acquisition. These gaps cause a significant reduction in the sensitivity of the acquisition, with fewer total counts collected for each axial location when compared to single bed dynamic acquisitions. Furthermore, estimation of fast temporal changes in tracer uptake is compromised as the early time points of the acquisition are not fully sampled for all beds. Finally, the established clinical protocols that make use of image derived input function (IDIF) to ease integration in clinical practice further sacrifice imaging time in the study's early phase, which is spent in acquiring fast frames over a single bed location, during a Dynamic Single Bed (DSB) phase, centred over the heart and the aorta [7, 16]. These limitations pose considerable problems on consequent parameter estimation and to a greater extent in parametric imaging performed using data from these protocols over the whole-body. These issues are addressed further in **Part II** of this thesis manuscript.

1.7 Advancements on extended A-FOV PET systems

Longer axial coverage has been a desirable characteristic for PET imaging systems, but limitations in technology and costs made it possible only during recent years. As described in recent review articles, earlier attempts to make scanners beyond the 15-26 cm of A-FOV were successfully but at the time only for prototypes and limited by cost and hardware capabilities [3, 58]. Recently the EXPLORER consortium led to the

development of scanners with 70 cm and 194 cm A-FOV [13, 59]. The adopted term for scanners that can encompass the whole-body is *Total-body* (TP) PET. More recently, a 106cm A-FOV PET-CT scanner was made commercially available by Siemens [14].

The increase in A-FOV offers many potential benefits for clinical and research applications [19]. Many of the direct clinical applications of such systems are envisioned for standard of care imaging using considerably lesser injected activity, improved image quality and detection limits of lesions, faster throughput etc. Early imaging applications have shown considerable potential towards these aspirations [60, 61]. Beyond standard of care, many research opportunities arise from the availability of high sensitivity combined with synchronous imaging of the whole body. Particular for dynamic imaging over the whole-body early applications have shown the feasibility of whole-body parametric imaging [62–64], study of fast kinetics including joint estimations of input function [65, 66] as well as whole-body parametric imaging with much lesser injected activity [67]. Comparisons on methodology and challenges for DWB imaging using regular scanners and extended A-FOV scanners are discussed further in the discussion and conclusion sections of this manuscript.

Chapter 2

Pharmacokinetics

PET makes use of positron-emitting radionuclides for the study of biochemical and physiological processes *in vivo*. The molecules of interest for the processes under study are labelled with a radionuclide and then introduced in the body. The PET imaging system provides information about the distribution of the labelled molecules *in vivo* over time and can be used to deduce information about the underlying process kinetics.

2.1 Principles of pharmacokinetic modelling

Pharmacokinetics refers to the study of absorption, distribution, metabolism and excretion of drugs in living systems. The study of pharmacokinetics is based on measurements of the concentration of drugs and their metabolites in tissues over time. Pharmacokinetic models describe the transport and binding rates of tracer from local concentration differences across boundaries, that can be either physical (such as a membrane or an organ outline) or conceptual boundaries as for example between bound and unbound tracer. These boundaries define separate compartments with distinct activity concentration which form the basis of pharmacokinetic models, also referred to as compartmental models.

The three key assumptions underlying compartmental modelling are:

- The concentration of the PET tracer is not high enough to influence the physiological processes and endogenous molecular interactions under study.
- That all physiological processes and interactions are in constant state for the duration of the PET study.
- The assumption that tracer concentration is instantly uniform in all compartments of the model.

By common convention in pharmacokinetic modelling, the first compartment is the arterial plasma pool from where the tracer distributes to tissues. The concentration of tracer in the arterial plasma $C_P(t)$ over time t is measured or deduced from population studies and applied to the model, as an input function that powers the system. If the tracer is metabolised during the study, this process needs to be modelled using metabolite measurements. Only the concentration of parent tracer can be used as input function in quantitative analysis of the tracer kinetics. By convention in dynamic PET studies conducted under a single session, the time point $t_0 = 0$ is set to be the tracer injection time.

Compartmental models behave according to a set of first-order ordinary differential equations, which means that the change of concentration in one compartment is a linear function of the concentrations of all compartments. This linearity establishes that the measured tissue activity concentration will be the convolution of the input function with the impulse response function (IRF) of the system, which is described by the compartmental model and its parameters. As such the tissue activity concentration $C_T(t)$ can be modelled as

$$C_T(t) = C_P(t) * \text{IRF}(t), \quad (2.1)$$

where $*$ is the convolution operator.

When a measurement of activity concentration is made with PET, the measurement will include the underlying tissue activity and activity from the intravascular blood in this tissue. The proportion of tissue volume occupied by intravascular blood V_B is commonly referred to as blood fraction. The measured activity concentration C_{PET} can be expressed as

$$C_{PET}(t) = (1 - V_B)C_T(t) + V_B C_B(t), \quad (2.2)$$

where C_B is the total blood activity concentration. Measurements of the arterial plasma to total blood ratio can be made to relate between $C_B(t)$ and $C_P(t)$. For the tracers of interest in this PhD project, the ratio of the two concentrations is assumed to be constant with time and to be $C_B(t) = rC_P(t)$.

2.2 One-tissue compartment model

As the simplest model, the one-tissue compartment model (1TCM) can be described using two constant rates for the input and output of tracer from the tissue, K_1 and k_2 respectively. A representation can be seen in figure 2.1.

The rate of change of the activity concentration in tissue C_T will depend on the metabolite corrected arterial plasma input function C_P and the activity concentration in tissue, described by the differential equa-

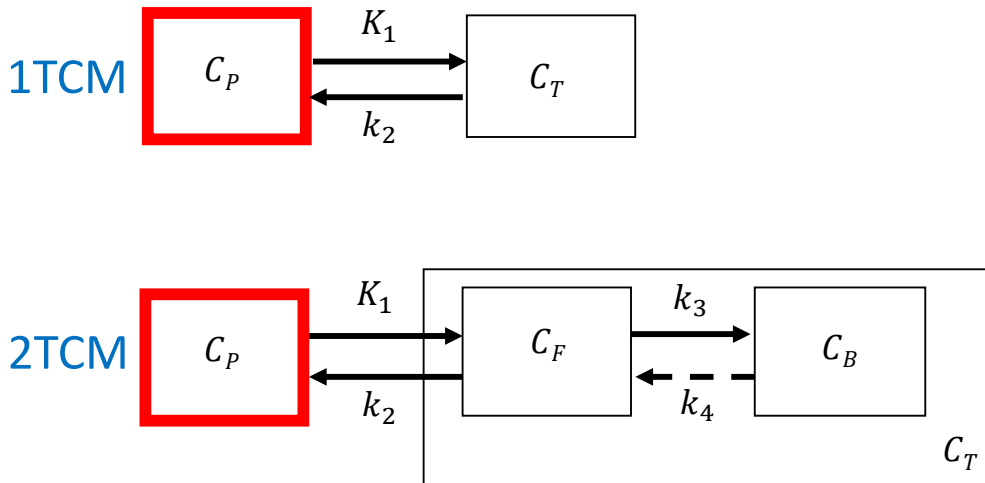


Figure 2.1: Representation of compartments and exchanges rates for 1TCM (top) and 2TCM (bottom)

tion 2.3.

$$\frac{dC_T(t)}{dt} = K_1 C_P(t) - k_2 C_T(t) \quad (2.3)$$

$$C_T(t) = K_1 e^{-k_2 t} * C_P(t) \quad (2.4)$$

$$C_{PET}(t) = K_1 e^{-k_2 t} * C_P(t)(1 - V_B) + C_B(t)V_B \quad (2.5)$$

Equation 2.4 is the solution of the differential equation 2.3, which becomes 2.5 for the PET measurement that includes the fractional blood volume.

2.3 Two-tissue compartment model

The two-tissue compartment model (2TCM) is a commonly used model as it describes the behaviour of ^{18}F -Fluorodeoxyglucose (^{18}F -FDG), which is commonly used tracer in clinical and research PET protocols. The separation into two tissue compartments is made to distinguish between free and trapped (bound) tracer, represented as $C_F(t)$ and $C_B(t)$ respectively, with the trapping caused by the tracer being metabolised in the

cells by mitochondria. The set of differential equations describing the 2TCM is shown in equations 2.6.

$$\frac{d}{dt}C_F(t) = K_1 C_A(t) - (k_2 + k_3)C_F(t) + k_4 C_B(t) \quad (2.6a)$$

$$\frac{d}{dt}C_B(t) = k_3 C_F(t) - k_4 C_B(t) \quad (2.6b)$$

The pathway of tracer from the trapped to the free state, via the process of dephosphorylation, is commonly considered negligible for the duration of common PET studies. With the assumption of $k_4 = 0$ the two differential equations in 2.6 simplify to the system 2.7 which when solved results in equation 2.8.

$$\frac{d}{dt}C_F(t) = K_1 C_A(t) - (k_2 + k_3)C_F(t) \quad (2.7a)$$

$$\frac{d}{dt}C_B(t) = k_3 C_F(t) \quad (2.7b)$$

$$C_T(t) = C_F(t) + C_B(t) = K_1(e^{-(k_2+k_3)t} + \frac{k_3}{k_2+k_3}(1 - e^{-(k_2+k_3)t})) * C_P(t) \quad (2.8)$$

The parameters K_1 , k_2 and k_3 , which are referred to as micro-parameters, can be estimated by fitting equation 2.8 on measured Time Activity Curve (TAC) data.

A parameter of interest for clinical studies is the influx rate constant K_i , given by equation 2.9. This is considered as a macro-parameter of the system and can be understood as the proportion of flux K_1 that results in trapped tracer.

$$K_i = \frac{K_1 k_3}{k_2 + k_3}. \quad (2.9)$$

The influx of FDG is proportional to the influx of glucose, also referred as the glucose metabolic rate MR_{glu} . The proportionality constant is called the lumped constant LC and along with the concentration of blood glucose C_P^{glu} can be used to express

$$MR_{glu} = K_i \left(\frac{C_P^{glu}}{LC} \right) \quad (2.10)$$

2.4 Gjedde-Patlak linearisation method

Direction estimation of model micro-parameters, such as those of equation 2.8, requires non-linear fitting optimization procedures. These are commonly time consuming and their estimations are heavily susceptible to noise. For parametric imaging, where the model estimation has to be performed for every voxel of the image, estimation of micro-parameters is commonly avoided due to the poor statistics and high noise associated with TAC measurements at the voxel level. Linearisation methods allow for transformation of the measured data, to enable use of linear least-square fitting procedures for estimation of model macro-parameters, under certain assumptions. Furthermore, these methods reduce the number of parameters to be estimated, thus reducing the variability of estimates and sensitivity to noise.

With the assumption of irreversible tracer behaviour the Gjedde-Patlak method has been developed, described by Gjedde [68] and Patlak *et al.* [69]. The proposed transformation is

$$\frac{C_T(t)}{C_P(t)} = K_i \frac{\int_0^t C_P(\tau) d\tau}{C_P(t)} + V_\alpha, \quad t > t_{ss}, \quad (2.11)$$

where K_i is the steady state trapping rate and V_α the apparent volume of distribution. The transformation is valid for time points t after steady state conditions are achieved at time t_{ss} . Steady state conditions are achieved when the reversible compartments are in steady-state equilibrium with the plasma blood compartment.

The Gjedde-Patlak linearisation method referred to simpler as *Patlak model*, is commonly used with the 2TCM model for FDG, under the assumption of $k_4 = 0$. In this case, the Patlak model parameters can be related to micro-parameters using equation 2.9 and

$$V_\alpha = \frac{K_1 k_2}{(k_2 + k_3)^2}. \quad (2.12)$$

With the assumption of $C_B(t) = rC_P(t)$, we can substitute equation 2.11 into equation 2.2 and describe the observed activity $C_{PET}(t)$ using the Patlak model as

$$\frac{C_{PET}(t)}{C_P(t)} = \underbrace{(1 - V_B)K_i}_{\theta_1} \frac{\int_0^t C_P(\tau) d\tau}{C_P(t)} + \underbrace{(V_\alpha(1 - V_B) + rV_B)}_{\theta_2}, \quad (2.13)$$

where the Patlak slope θ_1 and the Patlak intercept θ_2 are the model parameters that can be estimated from TAC measurements of $C_{PET}(t)$.

A limitation in the use of the Patlak model using equation 2.13 is that V_B is not necessarily known a priori

and Patlak analysis can not distinguish between K_i and $(1 - V_B)$. In many applications, V_B is assumed to be small (≤ 0.05) and neglected, but it can be a cause for systematic errors. In the applications of the Patlak model in this project, we will refer to the slope θ_1 as the Patlak K_i value, which is the value of interest that is commonly used in practice with Patlak analysis.

2.5 Spectral analysis method

The Spectral analysis method was originally introduced by Cunningham et al. [70]. The method is based on the general form of the solutions of compartmental models and describes the generic behaviour of any compartmental system as a positively weighted sum of decaying exponential functions with decay rates β which describe the exchange between compartments, convolved with an input function.

The spectral analysis model for $C_T(t)$ can be expressed using M functions as

$$C_T(t) = \sum_{b=0}^{M-1} \phi_b e^{-\beta_b t} * C_P(t), \quad (2.14)$$

where ϕ_b are the model coefficients (constrained to positive values) for the exponential functions with decay rates β_b that describe the exchange between compartments.

The advantage of this methodology is that it can be used to fit on TAC data, with few assumptions on the underlying kinetics. Additionally, it can be used to deduce information of the underlying kinetics using the basis pursuit strategy proposed by Gunn et al. [71]. Macro-parameters of the underlying model can also be deduced using the spectral analysis fitted model. Tracer delivery to tissue K_1 can be estimated directly with

$$K_1 = \sum_{b=0}^{M-1} \phi_b. \quad (2.15)$$

For reversible kinetics, the parameters can be used to deduce the volume of distribution V_D as

$$V_D = \sum_{b=0}^{M-1} \frac{\phi_b}{\beta_b}. \quad (2.16)$$

For irreversible kinetics, a parameter of the model is used to account for the trapping rate K_i . In this work we use parameter ϕ_0 to describe irreversible trapping, with its respective exponential decay rate set to zero

$\beta_0 = 0$. With this assumption the model becomes

$$C_T(t) = \phi_0 * C_P(t) + \sum_{b=1}^{M-1} \phi_b e^{-\beta_b t} * C_P(t), \quad (2.17)$$

for which $K_i = \phi_0$.

Finally, to model the observed activity $C_{PET}(t)$ using the spectral analysis model, we can substitute equation 2.14 into equation 2.2 and assume again that $C_B(t) = rC_P(t)$ to get

$$C_{PET}(t) = (1 - V_B) \sum_{b=0}^{M-1} \phi_b e^{-\beta_b t} * C_P(t) + rV_B C_P(t). \quad (2.18)$$

If we account for the parameter $(1 - V_B)$ into the weights ϕ_b , the equation can be written in short as

$$C_{PET}(t) = \sum_{b=0}^M \phi_b e^{-\beta_b t} * C_P(t), \quad (2.19)$$

for which $\beta_M \rightarrow \infty$ and $\phi_M = rV_B$. When fitted on measured $C_{PET}(t)$ data, the spectral model in equation 2.19 can be used to deduce K_1 , and either V_D or K_i respectively for reversible or irreversible tracers behaviour, using

$$K_1 = \frac{\sum_{b=0}^{M-1} \phi_b}{1 - V_B} \quad (2.20a)$$

$$V_D = \sum_{b=0}^{M-1} \frac{\phi_b}{\beta_b(1 - V_B)} \quad (2.20b)$$

$$K_i = \frac{\phi_0}{1 - V_B}. \quad (2.20c)$$

2.5.1 Choice of spectral rates

On equation 2.19 the spectral rates $\beta_1 \dots \beta_{M-1}$ are used to describe the exchange between compartments. These are set to cover the range of expected underlying kinetics and are commonly logarithmically spaced within that range [71]. As a rule of thumb, the lower limit of the range can be set to $\beta_1 = 1/(3T_{end})$ where T_{end} is the total time of the PET study, and the upper limit of the range can be set to $\beta_{M-1} = 3/T_{in}$ where T_{in} is the duration of the first frame of the study [72].

In spectral analysis, the number of the spectral parameters used is empirically set in the 10^2 order of magnitude. This relatively large number allows for clear separation of the underlying exchange rates, for deduction of models of the underlying behaviour. For use with dynamic reconstruction a smaller number of parameters is used, ideally less than the number of time bins (frames) of the data, which is still adequate to model the PET measurements while maintaining low image noise.

2.6 IsotoPK pharmacological study

Traditionally it has been assumed that passive diffusion is the main mechanism controlling drug delivery to tissues. But it is now recognised that the presence of membrane transporters at blood-tissue interfaces suggests that transporters also play an important role in drug pharmacokinetics. DWB imaging studies can play an important role in the study of transporter distribution and function in regards to drug delivery to tissues over the body [73]. To this purpose, a novel PET tracer has been developed using Glyburide (glibenclamide, GLB) labelled with ^{11}C . Glyburide is a drug used for treatment of diabetes and targets many transporters of the Solute Carrier O (SLCO) family [74, 75]. Preliminary pre-clinical studies have indicated that these transporters are expressed mainly in the liver and the kidneys [74].

A first in man study, named *IsotoPK*, was designed and is being conducted in our centre for the study of the distribution of these transporters in healthy volunteers [9]. The study is conducted on the Signa PET/MR, using a Dynamic Whole Body (DWB) acquisition protocol, with two acquisitions per volunteer to study the distribution without and with the administration of an inhibitor substance prior to PET imaging. Arterial blood samples for deduction of an input function and metabolite analysis are collected manually during the duration of each scan.

Data from this study are presented in chapter 7, showing examples of distribution of the tracer on an example volunteer. The use of the data in this project was made with a focus on methodological aspects for whole-body parametric imaging, but the developed methodology will be used in the future after all volunteer data have been collected to evaluate its findings. Initial results on three volunteers have shown that Glyburide is very slowly metabolised and therefore did not require metabolites to be accounted for in PET analysis, since their impact on PET quantification would be minimal. Findings also showed strong binding of tracer with plasma ($\geq 90\%$). Predominant uptake of the tracer was seen in the liver and also the kidneys. Lower uptake was observed in the spleen, the aorta wall and the pancreas. At all other tissues, no strong tracer uptake was seen.

Data coming from this protocol were used in this thesis. The IsotoPK study was the first DWB protocol to be conducted on the Signa PET/MR.

2.6.1 PET analysis in the liver

One of the unique characteristics of the liver, in regards to pharmacokinetic modelling, is that it is supplied with blood via two routes. The hepatic artery (HA) accounts for approximately 25% of the blood supply in the liver, while the portal vein (PV) accounts for the rest 75% [76]. The portal vein delivers blood that has been filtered mainly by the gastrointestinal tract, a process that alters the characteristics of the portal vein input function. Studies on pigs and non-invasive studies on humans have produced methods to model the PV input function as a dispersion of the arterial input function [77], which can be modelled using

$$C_{PV}(t) = k_g e^{-k_g t} * C_P(t). \quad (2.21)$$

With knowledge of the k_g dispersion value and ratio between PV and HA input, the liver input function $C_H(t)$ can be then modelled as

$$C_H(t) = 0.75 \cdot C_{PV}(t) + 0.25 \cdot C_P(t). \quad (2.22)$$

An toy example demonstration of the two components of $C_H(t)$ is shown in figure 2.2.

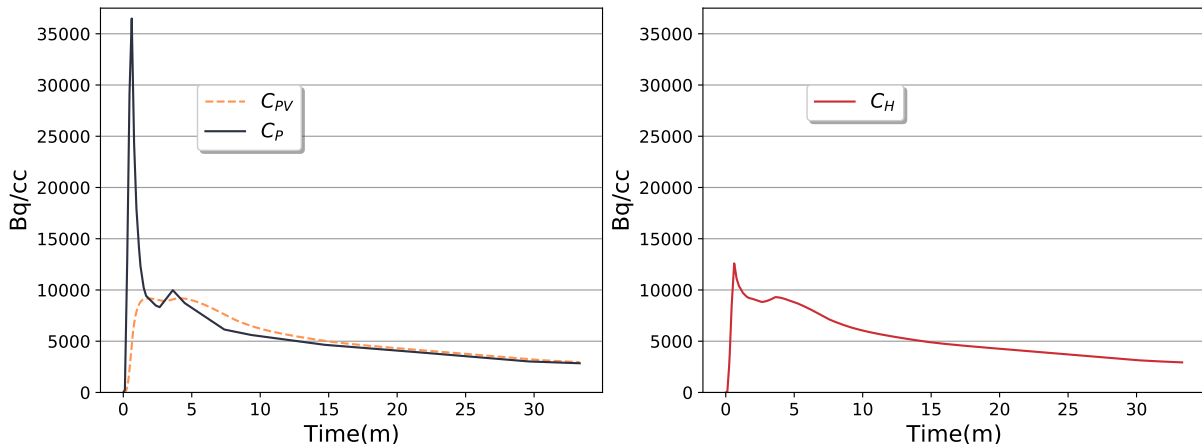


Figure 2.2: Example measured arterial input function $C_P(t)$ and modelled PV input function (using $k_g=0.5 \text{ min}^{-1}$ [77]) (left). Combination of arterial and PV input function to provide $C_H(t)$, assuming a 25/75 ratio (right).

The use of imaging information for non-invasive estimation of the portal vein input function and their effects in pharmacokinetic model estimates over the liver is an active area of research [78–80] with no standardised and widely accepted practices established yet. Further interest and research into DWB imaging is expected to address these issues for accurate WB parametric imaging that accurately accounts for the liner dual input model.

Chapter 3

PET image reconstruction

Image reconstruction is necessary to produce images of activity distribution from the acquired tomographic measurements. Reconstruction algorithms used for this process can be categorised as either analytical or statistical reconstruction methods. Analytical reconstruction methods seek to invert the transformation that links the image to the data domain, using linear analytic approaches. These methods treat the measured LOR data as line integrals over image space and necessitate corrections to be applied on projection data prior to reconstruction, in order to result in valid and quantitatively accurate images. Traditionally the most commonly used analytical reconstruction method is *Filtered Back Projection* which is described very briefly in this chapter. Statistical reconstruction methods are derived from statistical formulations of the detection process and allow for the use of complex system models that include various effects of the acquisition process. These methods result in non-linear formulations of the reconstruction problem which require iterative optimisation methods to reach a solution. The solution sought is a set of image parameters (that describe the activity distribution) that best describes the acquired tomographic data. In this thesis project, we made exclusive use of statistical reconstruction methods due to their ability to incorporate complex system models, including the use of dynamic models which was crucial for the aims of this thesis.

3.1 Projection and back-projection process

Coincidence detection of annihilation photons in PET leads naturally to a line-integral model where the number of coincidence events of an LOR is approximately linearly proportional to the integral of tracer density along the volume joining the two detectors. The projection process can be written as

$$\mathbf{y} = \text{proj}\{\boldsymbol{\lambda}\}, \quad (3.1)$$

where λ is the continuous distribution of radiotracer and y the continuous projection data (or else sinogram data). The 2D projection operation is also known as the Radon transform [81, 82] and translates from the image to the projection data domain. Projections in 3D can be made using the X-ray transform or extension of the Radon transform [37]. The projection's dual operation is back-projection, which translates from the data domain to the image domain.

3.1.1 Image representation

In practice, the spatio-temporal radiotracer distribution is described using a model with a finite number of parameters. The most common choice in common practice is the use of equally sized non-overlapping voxels that cover the useful FOV. Their use can also extend to the temporal domain with a set of voxels describing the FOV for each non overlapping temporal bin. In this case, the sets of voxels per temporal bin are considered temporally independent. If for a moment we consider only the spatial domain and static imaging, we can model the spatial radiotracer distribution λ using voxels with the *rect* function as

$$g(\mathbf{r}; \lambda) = \sum_{j=1}^{n_j} \lambda_j \text{rect}(\mathbf{r} - \mathbf{r}_j), \quad (3.2)$$

for an n_j number of voxels with r_j coordinates and intensity λ_j . For the linear model case, the set of functions describing the distribution are referred to as *spatial basis functions*. From here on we will be using the λ symbol to refer to the n_j dimension vector of λ_j voxel weights that describe the spatial activity distribution as

$$\lambda = \{\lambda_j | j = 1, \dots, n_j\}. \quad (3.3)$$

If we now consider the temporal domain of the activity distribution as well, the *rect* function can be used on the time domain to define a set of n_t independent temporal bins (frames). Later in this chapter, we will show how dynamic models can be used to describe the behaviour of voxel values across the temporal domain, but traditional reconstruction treats frames as independent static datasets. In this case, the activity distribution of each frame t can be written as

$$\lambda_t = \{\lambda_{tj} | j = 1, \dots, n_j\}. \quad (3.4)$$

Equivalently the projection data are binned according to the discretization imposed by the LORs in y_i , where i is the projection bin index and n_i the total number of LORs. Similarly to the image data, the projection data are binned temporally into y_{ti} for each projection bin i at frame t for a total number of number of n_t frames. The data of each frame can then be written as

$$y_t = \{y_{ti} | i = 1, \dots, n_i\}. \quad (3.5)$$

3.1.2 Projection & Analytical reconstruction

Forward projection of image to data space can be treated by summing contributions of voxels across each LOR. As this is a computationally costly process in practice, different methods have been proposed that balance between accuracy and consistency and computing requirements. Some of these methods, which are also implemented in the CASToR reconstruction software, are listed below with a short description.

- **Siddon projector** [83]: Weights the contribution of a voxel to a given LOR by the length of the LOR that intersects the voxel.
- **Distance driven** [84]: An optimised method for calculating weights by mapping pixel boundaries and detector boundaries for each projection to a common axis .
- **Joseph** [85]: Estimates contribution of voxels to LOR based on linear interpolation and their distance from the LOR.
- **Multi-Siddon** [86]: Uses multiple lines from the faces of the detectors in each LOR to approximate the volume intersected between the two detectors and the voxel.

Similarly, back-projectors using the same methods operation assign to voxels in the FOV the contribution from each LOR bin. Analytical reconstruction methods seek to estimate an image by inversion of the forward-projection process, by accounting for contributions from all LORs in image space. This results in analytical algorithms, including the most widely used algorithm of *Filtered Back Projection* (FBP). But while analytical reconstructions are linear processes and computationally fast, accuracy is limited by the simplistic assumptions of the line integral model, ignoring many degrading effects such as positron range, variations in response across LORs etc. In addition, these methods do not account for the statistical properties of the detection process in the data. Finally, the FBP algorithm seeks to solve an ill-posed problem meaning that small changes in the data can result in largely disproportional effects on the reconstructed image. As the projection data include stochastic noise from the detection process, without regularisation the reconstruction suffers from artefacts. In practice, smooth low pass filters like the Hann apodization filter are applied in the reconstruction process to reduce the strength of these artefacts at the cost of degraded spatial resolution. The sub-optimal trade-off between strength of artefacts and spatial resolution can be adjusted by changing the filter's cut-off frequency.

3.2 Formulation of the system model

The analytical reconstruction methods are based on the idealised description of the scanning process using the line integral model. But in fact, there are many effects that should ideally be considered in the scanning system model. For example the statistical nature of the detection process, positron range and detection resolution effects, the detection of scattered and random events as well as the discrete nature of the detection and scanner geometries that do not result in complete sampling. But as the scanning model complexity is increased, analytic expressions that seek to inverse the scanning process are not feasible. For this reason, iterative algorithms are employed, which seek a solution by optimising an objective function that expresses some distance between the measured data and the modelled data from an image estimate.

We can define the system model using an $n_i \times n_j$ system matrix P . Each element P_{ij} of the matrix is the probability of detection by voxel j to data bin i . As discussed, many effects can be included in this matrix elements which will be outlined below. By contrast, scatter effects can be hard to implement in the system matrix and random effects are non-linear effects that cannot be modelled linearly. As such the scatter and random events are considered to be known for each detector bin and included as an additive background b_i for each data bin i in the system model.

The model of the data at bin i from an image λ can be written as a sum over voxels of the probability of detection in this bin

$$\hat{y}_i = \sum_{j=1}^{n_j} P_{ij} \lambda_j + b_i, \quad (3.6)$$

where \hat{y}_i is the modelled data mean.

The system matrix can be decomposed to the individual contributing components as separate sparse matrices and vectors

$$\hat{y}_i = n_i a_i \sum_{j=1}^{n_j} X_{ij} \sum_{k=1}^{n_j} H_{jk} \lambda_k + b_i, \quad (3.7)$$

where

- n_i are the normalisation factors for each LOR bin
- a_i are the attenuation factors for each LOR bin
- X_{ij} is the geometrical projection matrix
- H_{jk} is the resolution modelling matrix, applied as a convolution in image space to account for different effects impacting resolution (positron range, detector size, etc.)
- b_i the background events for each LOR bin.

Resolution modelling can be applied on both data and image space of the system model, but in practice is applied on one of the two domains [87]. In the CASToR reconstruction software that was used in this project, resolution modelling is implemented in image space as written in the above expression.

If Time of Flight (TOF) measurements are available, the additional information regarding the probability of the annihilation event along the LOR can be incorporated in the model. TOF weights are assumed to be independent of the other system matrix elements and thus act as an additional multiplication factor. Depending on the type of TOF information, the weights can either be quantized (for each TOF bin) or expressed as a continuous function. More details on both options and the implementation of TOF reconstruction can be found in the work of Filipović *et al.* [88].

3.3 Formulation of the objective function

We can consider the total number of events in each projection bin to be modelled as a random sample from a Poisson distribution. According to the probability mass function, the conditional probability or likelihood function for \hat{y}_i given the measured data y_i will be

$$p(y_i|\hat{y}_i) = L(\hat{y}_i|y_i) = e^{-\hat{y}_i} \frac{\hat{y}_i^{y_i}}{y_i!}. \quad (3.8)$$

With the assumption that measurements of counts in each bin are independent random processes, the likelihood of the data over all bins will be

$$p(\mathbf{y}|\hat{\mathbf{y}}) = L(\hat{\mathbf{y}}|\mathbf{y}) = \prod_i^{n_i} e^{-\hat{y}_i} \frac{\hat{y}_i^{y_i}}{y_i!}. \quad (3.9)$$

By substituting the system model equation 3.6 in equation 3.9, we can write an expression of likelihood of the image λ given the measured data y

$$L(\lambda|\mathbf{y}) = \prod_i^{n_i} e^{-(\sum_{j=1}^{n_j} P_{ij}\lambda_j + b_i)} \frac{(\sum_{j=1}^{n_j} P_{ij}\lambda_j + b_i)^{y_i}}{y_i!}. \quad (3.10)$$

This expression can be used as the objective function in the optimisation process of seeking the most likely (ML) estimate of λ from a measurement y . It is more convenient to take the expression of the log likelihood and since the log function is monotonic the log likelihood can be used to arrive to the same ML estimate.

The log likelihood expression is

$$\ln L(\boldsymbol{\lambda}|\mathbf{y}) = \sum_{i=1}^{n_i} \left[y_i \ln \left(\sum_{j=1}^{n_j} P_{ij} \lambda_j + b_i \right) - \sum_{j=1}^{n_j} P_{ij} \lambda_j - b_i - \ln(y_i!) \right]. \quad (3.11)$$

This expression of the Poisson log-likelihood will be used to arrive to the maximum likelihood estimate image $\boldsymbol{\lambda}$, which will be noted as $\boldsymbol{\lambda}^{ML}$, that maximises the likelihood of the modelled data given the measured data \mathbf{y}

$$\boldsymbol{\lambda}^{ML} = \arg \max_{\boldsymbol{\lambda}} (\ln L(\boldsymbol{\lambda}|\mathbf{y})). \quad (3.12)$$

3.4 Maximum Likelihood - Expectation Maximisation

The second partial derivative of the log-likelihood to λ can be shown to be negative semidefinite to all allowed images and thus the log-likelihood function is a concave function. This means that a found local maximum through the optimisation process will be the global maximum of the function.

Seeking to solve equation 3.11 to find analytically the maximum likelihood image $\boldsymbol{\lambda}^{ML}$, we can take its first partial derivative to λ_j and set it to be equal to zero.

$$\frac{\partial \ln L(\boldsymbol{\lambda}|\mathbf{y})}{\partial \lambda_j} = \sum_{i=1}^{n_i} \left[y_i \frac{\sum_{j=1}^{n_j} P_{ij}}{\sum_{j=1}^{n_j} P_{ij} \lambda_j + b_i} - \sum_{j=1}^{n_j} P_{ij} \right] = 0, \quad (3.13)$$

but this expression has no closed form solution. The arrival to this expression shows the need for iterative methods to seek the $\boldsymbol{\lambda}^{ML}$ solution.

The most common algorithm used for this problem is the Expectation Maximisation (EM) algorithm that was first applied on statistical PET reconstruction by two key works by Shepp and Vardi [89] and Lange and Carson [90]. In these works the solution is derived through the introduction of the "complete data" concept [91]. Let z be the complete data random dataset of $x_{ij} + g_i$ values which describes the exact number of emissions from voxel j that contribute to the measurement at projection bin i , with the many to one mapping $y_i = \sum_{j=1}^{n_j} x_{ij} + g_i$. The complete dataset is unknown, but the conditional expectation of the complete data can be expressed using an image estimate (a guess) noted as $\boldsymbol{\lambda}^{(k)}$ and the measured data \mathbf{y} as

$$\hat{x}_{ij}(\boldsymbol{\lambda}^{(k)}, y_i) = y_i \frac{P_{ij} \lambda_j^{(k)}}{\sum_{d=1}^{n_j} P_{id} \lambda_d^{(k)} + b_i}, \quad (3.14)$$

$$\hat{g}_i(\boldsymbol{\lambda}^{(k)}, y_i) = y_i \frac{b_i}{\sum_{d=1}^{n_j} P_{id} \lambda_d^{(k)} + b_i}. \quad (3.15)$$

The complete dataset follows a Poisson distribution, with its log-likelihood being

$$\ln L(\boldsymbol{\lambda}|\mathbf{z}) = \sum_{i=1}^{n_i} \left[\sum_{j=1}^{n_j} (x_{ij} \ln(P_{ij}\lambda_j) - P_{ij}\lambda_j) + g_i \ln(b_i) - b_i \right], \quad (3.16)$$

where parameters not related to its optimisation to λ have been dropped. If we replace the expectation of the complete data using equations 3.14 and 3.15 we can then seek to maximise this likelihood function to obtain the ML image estimate of the expected complete data. Using the Kuhn-Tucker conditions we arrive at a closed form solution

$$\lambda_j^{(k+1)} = \frac{\lambda_j^{(k)}}{\sum_{i=1}^{n_i} P_{ij}} \sum_{i=1}^{n_i} P_{ij} \frac{y_i}{\sum_{d=1}^{n_j} P_{id}\lambda_d^{(k)} + b_i}, \quad (3.17)$$

that provides a new estimate $\lambda^{(k+1)}$. This single update equation combines the two steps of the optimisation process. First, given an image estimate $\lambda^{(k)}$ the expectation of the complete data is estimated. Then, the log-likelihood of the expectation of the complete data is maximised. This iterative process results in monotonic increase of the original log-likelihood function. As the original log-likelihood is concave, the process will result in convergence to the global maximum. This process is the Maximum Likelihood Expectation Maximisation (MLEM) algorithm.

The use of the conditional expectation of the data is an example of the general concept of optimisation transfer, where the construction of surrogate functions is made to be used with a simpler optimisation process, that leads to optimisation of the main function as well. One advantage of this algorithm is that an update over all voxels of the image can be made with a single pass over the data. The disadvantage is that it results in very slow convergence speeds. To accelerate convergence the Ordered Subsets Expectation Maximisation (OSEM) algorithm is used in most practices, which makes use of subsets of the data at each update step (each subset) to reduce computing time for each image update.

3.5 Dynamic reconstruction

Soon after the proposition of the EM algorithm for iterative PET reconstruction by Shepp and Vardi [89] and Lange and Carson [90], the former group proposed an extension of the EM algorithm to update parameters of a dynamic model and a version of the update algorithm that iterates through the whole of dynamic PET data in each iteration [92]. Dynamic PET data are traditionally divided among many time bins (frames) resulting in limited counts in each frame. Independent reconstruction of each frame dataset and post-reconstruction kinetic modelling results in noisy and potentially biased parameter estimates. Furthermore, the noise in each frame image estimate is spatially correlated and is hard to be accounted for in the post-reconstruction modelling. The use of a dynamic reconstruction approach that updates over parameters using all the dy-

namic PET raw data offers the advantages of accurate noise modelling of the raw data and accurate system modelling directly in the process of the dynamic model parameter estimation. Unfortunately, one major disadvantage of this approach was very slow convergence properties making it difficult for use in practice and the topic was not researched further at that time [92].

More than 10 years later the approach was revisited by Matthews *et al* [93] where it was combined with linear models. As it will be shown in this chapter the MLEM algorithm can be easily extended to parametric space with the use of linear dynamic models. On their application, the benefits in reducing parametric image noise were seen, at the cost of very slow convergence speeds. For use with linear models, attempts to accelerate convergence were made by use of OSEM [94] and computing acceleration and compression techniques [95]. In the case of dynamic reconstruction with OSEM it was shown that the algorithm exhibits the common OSEM problem of limit-cycles, for which a decreasing subsets scheme was used to eliminate this effect [96].

It was not until the work of two groups in 2010, Wang *et al* [97] and Matthews *et al* [98], that allowed for practical and more widespread use of dynamic reconstruction. Their methods, based on principles of optimisation transfer by Lange [99], decouple the dynamic reconstruction process to an EM update over all data and to a ML problem in image space. The first step iterates through the tomographic data and updates the activity estimate images, while the second step simply updates the dynamic model parameters using the updated activity images. With the second step being much faster, multiple dynamic model updates can be conducted for each update over data which results in acceleration of overall convergence. Results were demonstrated by Wang *et al* [97] for EM and Preconditioned Conjugate Gradient (PCG) based optimisations using linear models. While that work was limited to linear dynamic models, the work by Matthews *et al* [98] generalised on the optimisation of the image space ML problem by the use of an equivalence to a weighted least-square minimisation problem. This formulation allowed for use of existing Least Squares (LS) optimisation algorithms, that are commonly used for post-reconstruction model fitting, to be used in 4D reconstruction for linear and non-linear models. The disadvantage of this approach is that the resulting formulation is not strictly concave and thus does not guarantee monotonic convergence to a global maximum. Nevertheless, convergence behaviour has been observed in practice with different weighting schemes [100, 101].

The use of non-linear models within dynamic reconstruction has shown clear benefits in precision and accuracy [100, 102, 103] but are more sensitive to initialisation and reconstruction parameters and could lead to unpredictable behaviour.

3.5.1 Dynamic models

As described in chapter 2, dynamic data are used to seek parameters of kinetic models for the understanding of underlying molecular processes. Conventionally the data of each frame are reconstructed as individual static datasets and the resulting images are used for post-reconstruction modelling. When the parameters sought are calculated at the voxel level, the result is a set of parameters for each voxel in the FOV, which are referred to as parametric maps.

If we assume an example dynamic model that describes the dynamic behaviour of the radiotracer distribution with n_p number of p parameters, then the set of parameters for each voxel j can be expressed as

$$\boldsymbol{\theta}_j = \{\theta_{pj} | p = 1, \dots, n_p\}. \quad (3.18)$$

These can be used to model the activity behaviour at each time frame t according to

$$\lambda_{tj} = f_{tj}(\boldsymbol{\theta}_j), \quad (3.19)$$

where $f()$ is the function of the dynamic model that estimates radiotracer activity values over n_t time frames given a set of n_p model parameters. Assuming that the dynamic model is the same for all voxels in the image space, we can write for short

$$\boldsymbol{\lambda} = f(\boldsymbol{\theta}), \quad (3.20)$$

with the complete set of parametric maps and spatio-temporal images being respectively

$$\boldsymbol{\theta} = \{\theta_{pj} | p = 1, \dots, n_p; j = 1, \dots, n_j\}, \quad (3.21)$$

$$\boldsymbol{\lambda} = \{\lambda_{tj} | t = 1, \dots, n_t; j = 1, \dots, n_j\}. \quad (3.22)$$

The dynamic model $f()$ can be either linear or non-linear to the set of parameters p .

3.5.2 Dynamic reconstruction - Nested optimisation

Similar to 3.4, the conditional expectation of the complete data can be written using the generic dynamic model $f()$

$$\hat{x}_{tij}(\boldsymbol{\theta}^{(k)}, y_{ti}) = y_{ti} \frac{P_{ij} f_{tj}(\boldsymbol{\theta}^{(k)})}{\sum_{d=1}^{n_j} P_{id} f_{td}(\boldsymbol{\theta}^{(k)}) + b_{ti}}, \quad (3.23)$$

$$\hat{g}_{ti}(\boldsymbol{\theta}^{(k)}, y_{ti}) = y_{ti} \frac{b_{ti}}{\sum_{d=1}^{n_j} P_{id} f_{td}(\boldsymbol{\theta}^{(k)}) + b_{ti}}, \quad (3.24)$$

where now the additive corrections vector b is used for the known corrections on each frame t and data bin i . Here we have assumed that the system matrix P does not depend on time frame t . The complete log-likelihood function can then be formed, using the above expected complete data and maximised to get an update of the $\boldsymbol{\theta}^{(k)}$ estimate. By dropping terms that do not contribute to the optimisation we result in

$$\boldsymbol{\theta}^{(k+1)} = \arg \max_{\boldsymbol{\theta}} (\ln L(\boldsymbol{\theta} | \hat{\mathbf{z}})) = \sum_{t=1}^{n_t} \sum_{b=1}^{n_j} \left[\sum_{i=1}^{n_i} P_{ib} \right] \left[-f_{tb}(\boldsymbol{\theta}_b) + \ln(P_{ib} f_{tb}(\boldsymbol{\theta}_b)) \frac{\sum_{i=1}^{n_i} \hat{x}_{tib}}{\sum_{i=1}^{n_i} P_{ib}} \right]. \quad (3.25)$$

The last part of the expression is equivalent to an EM update over all tomographic data as

$$\frac{\sum_{i=1}^{n_i} \hat{x}_{tib}}{\sum_{i=1}^{n_i} P_{ib}} = \frac{f_{tb}(\boldsymbol{\theta}^{(k)})}{\sum_{i=1}^{n_i} P_{ib}} \sum_{i=1}^{n_i} P_{ib} \frac{y_{ti}}{\sum_{d=1}^{n_j} P_{id} f_{td}(\boldsymbol{\theta}^{(k)}) + b_{ti}}. \quad (3.26)$$

This set of images can be referred to as the EM update image

$$f_{tb}^{(EM)}(\boldsymbol{\theta}^{(k)}) = \frac{f_{tb}(\boldsymbol{\theta}^{(k)})}{\sum_{i=1}^{n_i} P_{ib}} \sum_{i=1}^{n_i} P_{ib} \frac{y_{ti}}{\sum_{d=1}^{n_j} P_{id} f_{td}(\boldsymbol{\theta}^{(k)}) + b_{ti}}. \quad (3.27)$$

By substituting the equation 3.27 in the log-likelihood maximisation we have

$$\boldsymbol{\theta}^{(k+1)} = \arg \max_{\boldsymbol{\theta}} \sum_{t=1}^{n_t} \sum_{b=1}^{n_j} \left[\sum_{i=1}^{n_i} P_{ib} \right] \left[-f_{tb}(\boldsymbol{\theta}) + \ln(f_{tb}(\boldsymbol{\theta})) f_{tb}^{(EM)}(\boldsymbol{\theta}^{(k)}) \right]. \quad (3.28)$$

Equations 3.27 and 3.28 form the two step process of nested optimisation. An update over PET raw data for each voxel and each time frame is performed using 3.27, followed by an image based optimisation of the dynamic model parameters for each voxel using equation 3.28. It is important to note that the model fitting process of equation 3.28 can be performed independently for each voxel.

3.5.3 Linear dynamic models - direct 4D reconstruction

As described in chapter 2, many dynamic models utilised in practice for parametric imaging are linear models. These can be expressed in the form of matrices, which effectively are a set of temporal basis functions of the dynamic model. The modeled activity using a linear model of n_p number of parameters is

$$\lambda_{tj} = \sum_{p=1}^{n_p} B_{tp} \theta_{pj}. \quad (3.29)$$

In this particular case of linear dynamic models it is straightforward to incorporate the model in the MLEM update equation 3.17 as

$$\theta_{pj}^{(k+1)} = \frac{\theta_{pj}^{(k)}}{\sum_{t=1}^{n_t} B_{tp} \sum_{i=1}^{n_i} P_{ij}} \sum_{t=1}^{n_t} B_{tp} \sum_{i=1}^{n_i} P_{ij} \frac{y_{ti}}{\sum_{d=1}^{n_j} P_{id} \sum_{q=1}^{n_p} B_{tq} \theta_{qd}^{(k)} + b_{ti}}. \quad (3.30)$$

Unfortunately, this simple form of the dynamic reconstruction problem using linear models suffers from very slow convergence speeds, as found previously [92, 93]. Strategies to improve the convergence speed are still being investigated [104], as this direct reconstruction approach can be beneficial in applications of list-mode level motion correction and other potential applications.

3.5.4 Linear dynamic models - Nested EM

To accelerate convergence of dynamic reconstruction using linear models the nested optimization framework can be utilised. By substituting the linear model equation 3.29 into equation 3.28 we have

$$\boldsymbol{\theta}^{(k+1)} = \arg \max_{\boldsymbol{\theta}} \sum_{t=1}^{n_t} \sum_{b=1}^{n_j} \left[\sum_{i=1}^{n_i} P_{ib} \right] \left[- \sum_{p=1}^{n_p} B_{tp} \theta_{pb} + \ln \left(\sum_{p=1}^{n_p} B_{tp} \theta_{pb} \right) f_{tb}^{(EM)}(\boldsymbol{\theta}^{(k)}) \right]. \quad (3.31)$$

This expression can be optimised for each voxel independently as

$$\theta_j^{(k+1)} = \arg \max_{\theta_j} \sum_{t=1}^{n_t} \left[\sum_{i=1}^{n_i} P_{ij} \right] \left[- \sum_{p=1}^{n_p} B_{tp} \theta_{pj} + \ln \left(\sum_{p=1}^{n_p} B_{tp} \theta_{pj} \right) f_{tj}^{(EM)}(\boldsymbol{\theta}^{(k)}) \right]. \quad (3.32)$$

As we have assumed that the system matrix P does not depend on time, the sensitivity term $[\sum_{i=1}^{n_i} P_{ij}]$ can be dropped from this optimisation. The right parenthesis of this voxel-wise optimisation expression is similar to the log-likelihood from the static reconstruction problem in equation 3.11, with different parameters and data being optimised. This function can be optimised using a similar MLEM update solution that is now applied over image space for the estimation of the model parameters

$$\theta_{pj}^{(k+1)} = \frac{\theta_{pj}^{(k)}}{\sum_{t=1}^{n_t} B_{tp}} \sum_{t=1}^{n_t} B_{tp} \frac{f_{tj}^{(EM)}(\boldsymbol{\theta}^{(k)})}{\sum_{q=1}^{n_p} B_{tq} \theta_{qj}^{(k)}}. \quad (3.33)$$

This results in a nested optimisation framework for linear models using equation 3.27 for updating over tomographic data and equation 3.33 for the dynamic model update resulting in updated parametric images. In this project, in all applications of dynamic reconstruction, we made use of linear models within the nested optimisation framework.

Chapter 4

CASToR

CASToR stands for Customizable and Advanced Software for Tomographic Reconstruction and is an open source fully quantitative reconstruction platform that has been developed within a collaboration project, partly financed by France Life Imaging (FLI). It is available on the website of the collaboration project (<https://castor-project.org/>). This PhD project relied heavily on the use of CASToR for developing and performing reconstructions, on both simulated and real patient data. The work conducted in this project resulted in the development and evaluation of new functionalities, which are now part of the released public version 3.1.1. These are described in detail in chapter 6.

In this chapter, we provide a short introduction to the functionalities and innovative reconstruction methods provided in CASToR that play an important role in the work performed in this PhD project. The platform is developed using the C and C++ programming languages and supports PET, SPECT and CT imaging. In this short description, the focus is on PET reconstruction for static and dynamic imaging. A more detailed description of all the functionalities of CASToR can be found on the official website and the official publication by Merlin *et al.*[11].

The main philosophy behind the design of the platform is genericity and abstraction. The code architecture is divided into main components which manage global tasks. These are named "managers" and handle tasks such as reading datafiles, handling reconstruction dynamic aspects, managing the scanner geometry, computing a projection, etc. Each "manager" component is utilising abstract classes which include a representation of all the desired functionalities, required by the component, as virtual functions. The final step is to implement these virtual functions using a specific implementation as a specific class. Using this strategy, generic code of basic functionalities is implemented only once while specific classes require coding of only the basic functionalities that are specific to the implementation. This allows for the development of specific

classes with a minimal amount of coding, that can be used as plug-ins to the existing generic architecture. An example of this design is shown in figure 4.1, with the *oProjectorManager* as the main component, the *vProjector* as the virtual class which includes all the generic functionalities of a projector, and finally the projector implementations which include code that calculates a projection using a specific implementation. Template classes are also provided for instructing how new implementations, of projectors in this example, can be made.

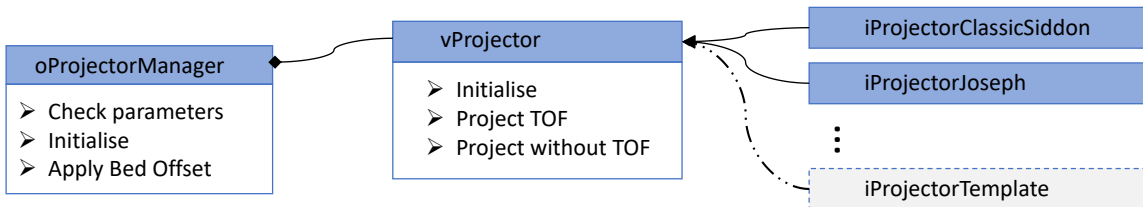


Figure 4.1: Example of CASToR abstraction design for the projection component.

4.1 Datafile

Data are provided in CASToR in the form of a CASToR datafile, which is based on a generic data description that is identical for both list-mode and histogram data. A "CASToR event" is either a list-mode event or a histogram bin. The minimum information required for each CASToR event of the datafile are a time-stamp, pair of detector IDs and number of events. Additional information can also be provided per event such as scatter and random corrections, normalisation factors, TOF, gating information, etc.

List-mode data maintain the exact timing information of each event. This is advantageous in the reconstruction of dynamic datasets, as the choice of the desired frames for reconstruction is made within CASToR, during reconstruction and using the framing selected by the input of reconstruction parameters. This of course is limited in the case of real data by the corrections used in the reconstruction, which are pre-computed using a specific framing definition prior to construction of the CASToR datafile.

Histograms are by definition events that have been histogrammed for a specific time range. All events of a CASToR histogram datafile have the same timestamp which is the timestamp of the first time point of the histogrammed data. Thus dynamic data need to be pre-processed into individual histograms, one histogram per dynamic frame, using a predefined framing definition. Multiple histograms from a dynamic dataset can be concatenated together into a single file before used in CASToR for dynamic reconstruction. In this case, reconstructions can be performed using the concatenated file and solely with the framing definition used to create the histograms. Use of other framing definitions would require re-processing of the data before

providing them into CASToR for reconstruction.

In this project, when possible, the use of list-mode datafiles was preferred due to the offered flexibility. List-mode datafiles were used for reconstructions of real PET datasets, while histograms were used for reconstructions of simulated datasets (from analytical simulations).

4.1.1 Real Data Corrections

Although in simulations it is relatively easy to get an estimate of corrections, these are harder to obtain for real data. Various estimation methods, as outlined in chapter 1, are employed by scanner manufacturers to generate corrections that are necessary for quantitatively accurate reconstruction. CASToR does not provide any functionalities for estimation of corrections. These must be pre-computed and included in the construction process of the castor datafile.

In this project we made use of real data from GE and Siemens PET systems. Both manufacturers provide offline processing tools (*GE-PET toolbox* for GE systems and *E7 tools* for Siemens systems) for reconstruction, which permit the extraction of corrections. These tools were used in this project for generation of all the corrections, when using real data in our evaluations.

4.2 Geometry

A generic description of the geometry of an imaging system in CASToR allows for the definition of any PET system. Individual detector elements are defined by 3D Cartesian coordinates and an orientation vector. These are pre-computed and input as look-up tables, or are computed by CASToR using a system definition similar to that used for GATE simulations [105].

In this project the geometries of the Signa PET/MR and Siemens mMR PET/MR scanners were used, for which lookup tables are provided with the current version of CASToR (Version 3.1).

4.3 Dynamic aspects

The use of generic functions and generic datafile definition allows for the reconstruction to be performed by a single implementation of an iterative algorithm. The main steps performed within this iterative algorithm are shown in algorithm 1.

The platform is designed to handle three temporal levels of binning. It makes temporal binning for dynamic frames and binning in two levels of gating (for example cardiac and respiratory motions).

Algorithm 1: CASToR core iterative loop

```

for  $i \leftarrow 1$  to nb of iterations do
    for  $j \leftarrow 1$  to nb of subsets do
        index start  $\leftarrow$  current subset;
        index step  $\leftarrow$  number of subsets;
        Perform Image-based Convolution (forward step);
        // loop over bed positions
        for  $s \leftarrow 1$  to nb of beds do
            // Parallel loop
            for  $e \leftarrow \text{index start}$  to nb events step index step do
                Get Event corresponding to e;
                if Deformation required for e then
                    | Perform Image-Based Deformation(forward step);
                end
                // apply axial offset for bed
                Apply bed offset;
                // Recover system matrix elements associated with this event
                Compute/load the system matrix elements associated to this Event;
                // Compute the update term associated to the optimization algorithm
                Compute the forward model;
                Compute the update term(s) to be back-projected;
                Back-project update term(s);
            end
        end
        Perform Image-based Convolution (backward step);
        Perform Image-Based Deformation (backward step);
        Update image according to the optimization algorithm;
        // Make use of a dynamic model with nested optimisation
        if Nested use of Dynamic model then
            Estimate/Fit dynamic model ;
            Estimate image from fitted dynamic model ;
        end
    end
end

```

4.3.1 Motion correction and image deformation

Image based deformations can be performed within the iterative loop, over gate bins or sub-frames defined by involuntary motion, that can counteract effects of motion in the data while still using all data (without the need of rejection or individual reconstructions per gate). Unfortunately, with the current version of CASToR the available implemented deformations are limited to rigid deformation. Although this deformation can be adequate for brain imaging, it is not suitable for modelling elastic motion that is commonly found in whole body studies. Owing to this limitation at this time, no motion correction was considered in the reconstructions and evaluations performed in this project.

4.3.2 Dynamic reconstruction

Multi-frame reconstruction of individual frames can be performed within CASToR with a single execution. The framing details can be provided in the reconstruction input. For each event, a dynamic switch function is used to identify to which frame the data belongs. Image update is performed accordingly to each respective frame image.

The dynamic series of images is stored in CASToR using a set of temporal basis functions and images of basis coefficients, similar to the description in equation 3.29. In the case of individual frame reconstructions, the set of basis is an identity matrix and the coefficient images are the frame images. For dynamic reconstructions using a dynamic model, the model derived basis functions can be used directly in CASToR, in which case the image update terms directly update the parametric images. But as discussed previously in section 3.5, dynamic reconstruction can be performed more efficiently when using optimisation transfer principles and nested optimisation for the dynamic model fitting. This functionality was developed in CASToR, as part of the developments made during this PhD project. Details of the implementation are provided in chapter 6.

4.4 Multi-bed reconstruction

With the generic description of the geometry implemented in CASToR, system matrix elements related to each detection event are computed on-the-fly, by projecting a ray through image space, or they are read from a pre-computed system matrix. The on-the-fly computation allows for additional flexibility, which has been used to enable direct multi-bed reconstruction. As described in section 1.5.1, multi-bed Step and Shoot (SS) acquisitions make use of overlapping beds to increase the sensitivity at the edges of each bed's FOV. The raw PET data for a static WB acquisition comprise of a total number of n_s datasets, one for each bed position s . We can represent each bed's raw PET dataset as

$$\mathbf{y}_s = \left\{ y_{si}, i = 1, \dots, n_i \right\}. \quad (4.1)$$

By incorporating the offset of each bed position in the projection operation, equation 3.17 can be re-written for direct reconstruction of the whole acquisition effective FOV, using all acquired raw data, as

$$\lambda_j^{(k+1)} = \frac{\lambda_j^{(k)}}{\sum_{s=1}^{n_s} \sum_{i=1}^{n_i} P_{sij}} \sum_{s=1}^{n_s} \sum_{i=1}^{n_i} P_{sij} \frac{y_{si}}{\sum_{d=1}^{n_j} P_{sid} \lambda_d^{(k)} + b_{si}}, \quad (4.2)$$

where now the image λ has the dimensions of the whole effective FOV, and the additive correction terms

C_{si} is provided for each respective bed position s .

Direct reconstruction of multi-bed data, which combines data from overlapping acquisitions within the iterative reconstruction loop, improves the statistics of the overlapping region that are available for each iteration. It has been shown that this technique can result in improved contrast to noise ratios at the overlapping regions, for specific levels of acquisition statistics [50].

This method has been implemented in CASToR by making use of an additional loop over bed positions and an "Apply bed offset" function, as seen in the CASToR iterative algorithm 1, which applies the bed offset to the projector for the events of each bed [51].

Part II

Contributions

Chapter 5

Multi-bed Dynamic Whole-Body PET: Acquisition Optimization

5.1 Introduction

In PET imaging one of the needs in many clinical and research applications is the acquisition of information over the whole body. Moreover, dynamic information over the whole body can allow for research applications of PET, such as in pharmacokinetics, to expand to the whole body and enable potential future clinical applications. But an important limitation of DWB protocols in scanners with limited A-FOV is the result of temporal gaps in the acquired data of any given bed position. In practice for scanners that have no in-build DWB protocols, such as the Signa PET/MR, a large fraction of the temporal gaps in DWB protocols can be attributed to a greater extend to system processes that are launched automatically between WB sweeps rather than to time taken to move the bed between bed positions. These processes include the transfer of raw data files and reconstructions performed during scanning. Reducing these system delays is therefore of prime importance for reducing temporal gaps in the data.

In this chapter, we review results of acquisition performance for a DWB protocol implemented on the Signa PET/MR scanner as part of the IsotoPK pharmacokinetic study [9]. A short introduction on the design of the protocol using current scanner features is provided, with additional details on the protocol and data processing of this protocol's data provided in Appendix A. We then describe the implementation of an experimental fully-automated protocol for DWB acquisitions on the Signa PET/MR, that was designed with the aim of reducing acquisition delays and allowing for greater flexibility in the selection of bed positions. The development of this protocol was conducted in collaboration with GE Healthcare, as part of this PhD project

(which was also a milestone within HYBRID). Finally, we present results from the use of the experimental acquisition protocol on a Non-Human Primate (NHP) study and compare against the standard DWB protocol used in the IsotoPK study using data from fourteen volunteer scans.

5.2 Methods & Results

5.2.1 Design of IsotoPK DWB protocol on the Signa PET/MR

Prior to commencing this PhD project and in perpetration for the IsotoPK study, a DWB protocol was designed on the GE Signa PET/MR scanner. The desired axial coverage was achieved using 5 bed positions and a reduced overlap, as shown in diagram (C) of figure 1.9. The relatively small overlap (half compared to routine clinical protocols) was selected to reduce the number of beds and subsequently the acquisition temporal gaps. The study design was limited to a total duration of 1 hour from injection and includes an initial dynamic single bed (DSB) phase centred over the liver, where the highest expression of the transporters under study was expected. The DSB position was imaged for 3 minutes from injection, prior to the start of DWB acquisition. Because the system has no in-build protocols for DWB imaging, a custom protocol had to be made using a sequence of static WB acquisitions. Each WB pass had to be individually pre-planned, which resulted in hard-coded bed positions (identical positions for all subjects, relevant to a reference mark). Each volunteer positioning was made using a chest-landmark, with no further adjustments of the protocol being possible for the optimum arrangement of the bed positions, relative to each patient's size.

For the design of the framing used in the IsotoPK DWB protocol, the following empirical metric has been taken under consideration. We define the Delays to Acquisition ratio (DAR) as the ratio of total delays to acquisition time for every WB sweep, using the relationship

$$\text{DAR}(n_s) = \frac{dl_{bed} \cdot (n_s - 1) + dl_{Sweep}^{(n_s)}}{t_{duration} \cdot n_s}, \quad (5.1)$$

where n_s is the number of beds in the acquisition, $t_{duration}$ is the frame duration for a single bed of the WB sweep, dl_{bed} the delays between adjacent beds and $dl_{Sweep}^{(n_s)}$ the delay between WB sweeps (for a DWB protocol of n_s bed positions). This relationship is based on the assumption that all beds in a WB sweep have the same frame duration. First estimations of the delay times for the Signa PET/MR had shown a delay of approximately 6 seconds between adjacent bed positions and 20 seconds between WB sweeps. Using this information, the framing sequence shown in table 5.1 was chosen with the shortest frame duration set to 20 seconds in order to maintain a DAR below 50% at the early phases of the DWB study.

The MR sequences required for attenuation correction (MRACs) were performed prior to injection and dur-

Table 5.1: Framing of IsotoPK DWB protocol.

Phase ID	Description	Frame Duration (s)	Number of frames per bed position	DAR
1	DSB	10	18	N/A
2	DWB	20	9	44%
3	DWB	30	8	29%
4	DWB	40	2	22%

ing the DWB protocol acquisition. The first MRAC sequence at each bed location lasted approximately 35 seconds (conducted prior to injection), with subsequent scans over the same locations lasting approximately 21 seconds per bed. This difference in time requirements between initial and subsequent MRAC sequences is caused by the MR shimming sequences that are performed before MR imaging. At first, shimming is conducted in full to optimise MR homogeneity, while only a faster shimming update is conducted on subsequent scans of the same bed positions. MRAC acquisitions were not repeated for all WB sweeps of the DWB protocol, to allow for staff entry in the room for blood sampling which is required for the derivation of the input function and metabolite analysis.

The acquired DWB data were initially reconstructed at the system console. Then, as part of this PhD project, the raw data were retrospectively exported for offline processing and reconstruction with CASToR, using an automated pipeline which is described in Appendix A.

5.2.2 Results from IsotoPK study

The result beds positions of the DWB protocol can be seen in figures 5.1 and 5.2 for the included fourteen studies from the IsotoPK protocol. Using the timing information of the extracted raw PET data, the average delay times per imaged subject were estimated, shown in the form of box-plots for dl_{bed} in figure 5.3 and for $dl_{Sweep}^{(5)}$ in figure 5.4.

It is noteworthy that with the accumulation of experience in using the PET/MR system for performing the DWB protocol, the delays between sweeps were reduced considerably, which can be seen by comparing the most recent examinations against the first. This can be attributed in part to improved preparation of the PET/MR system before performing the protocol (ex. reboot of the system prior to study, etc.). Before this practice was established, as the system software has not been designed for acquiring multiple whole-body passes many system crashes had been experienced using this custom protocol. These have caused losses of acquisition time (which has not been included in this evaluation) and also resulted in differences in the number of WB passes per subject. Secondly, in part, the reduction in delays can be attributed to improved staff training on the use of the protocol and awareness of common problems. For the 3 more recent subject

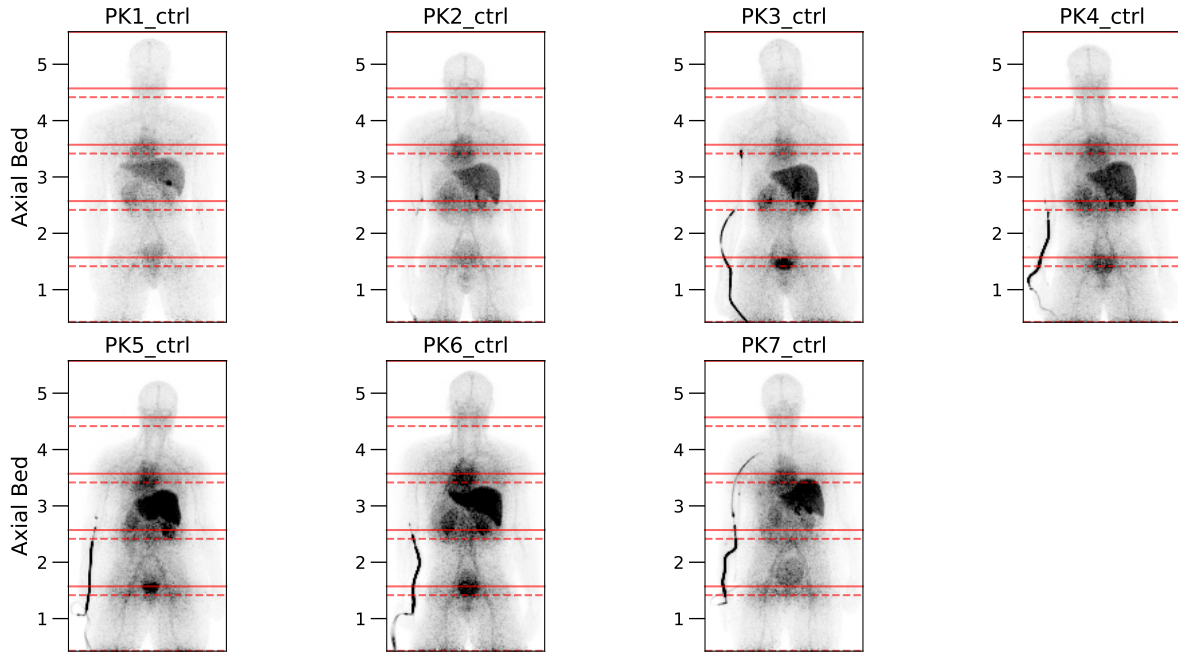


Figure 5.1: Coronal MIP projections of 7 volunteer control DWB scans with overlay of axial bed start (—) and end (----) location.

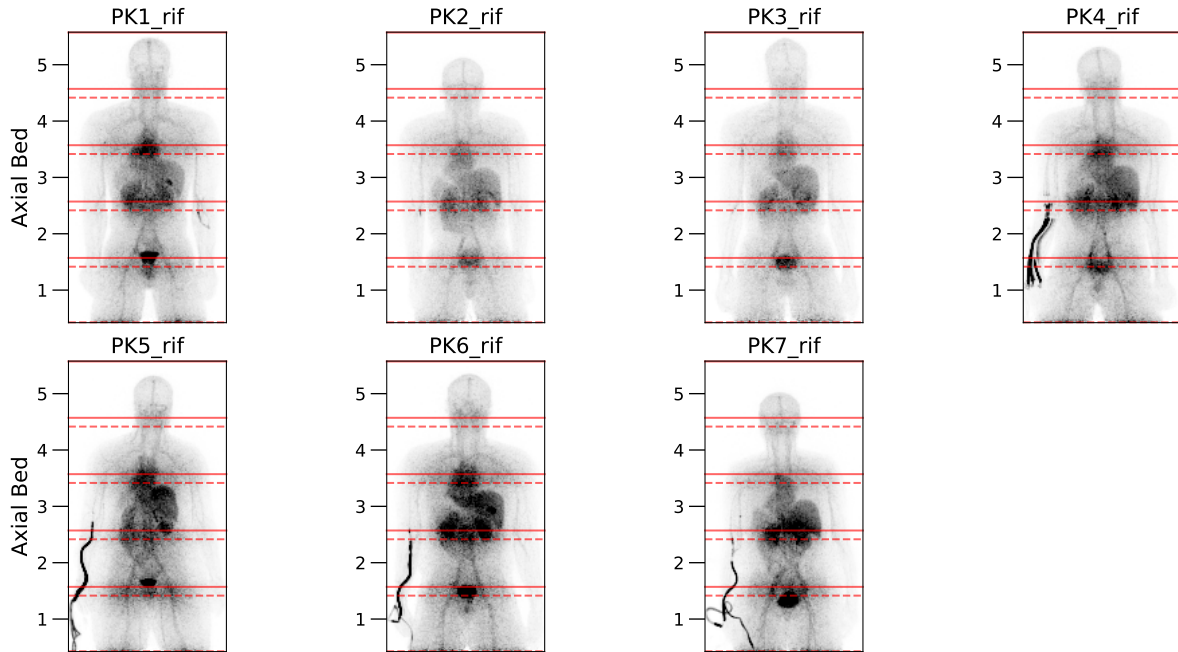


Figure 5.2: Coronal MIP projections of 7 volunteer rif DWB scans with overlay of axial bed start (—) and end (----) location.

examinations the average intra-bed delay time dl_{bed} was 5.69 s (95%CI: 5.63, 5.75) and the average delay time between sweeps $dl_{Sweep}^{(5)}$ was 26.17 s (95%CI: 26.13, 26.22). This measured average $dl_{Sweep}^{(5)}$ value is slightly higher than the value considered in the design of the protocol. With these average measurements, the DAR for the WB sweeps of beds with 20 s frame duration becomes approximately 49%.

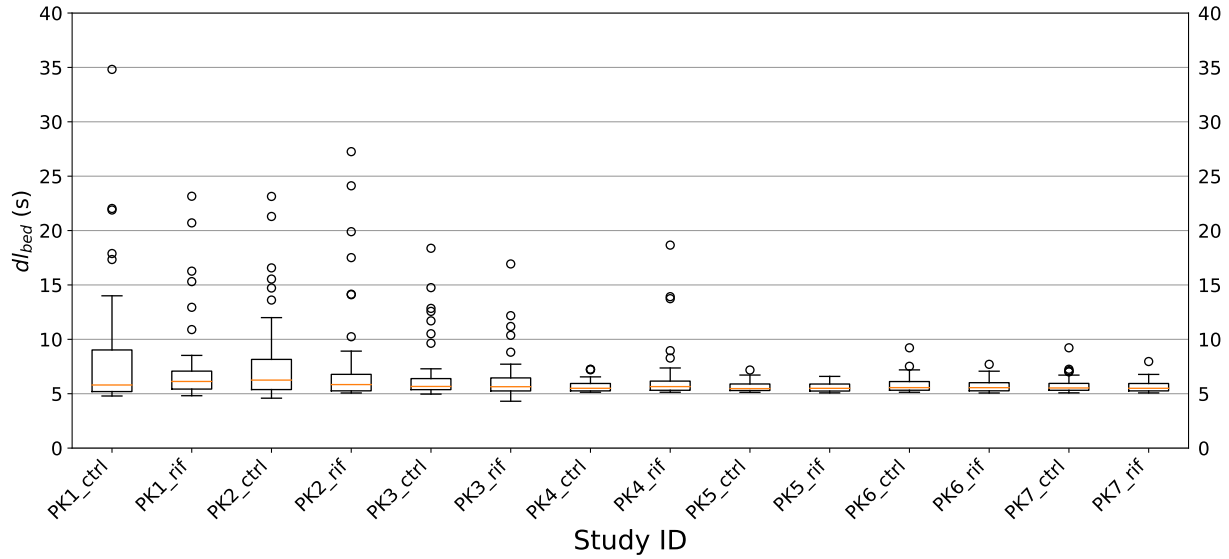


Figure 5.3: Box plots of intra-bed delays dl_{bed} of the IsotoPK DWB protocol used in practice.

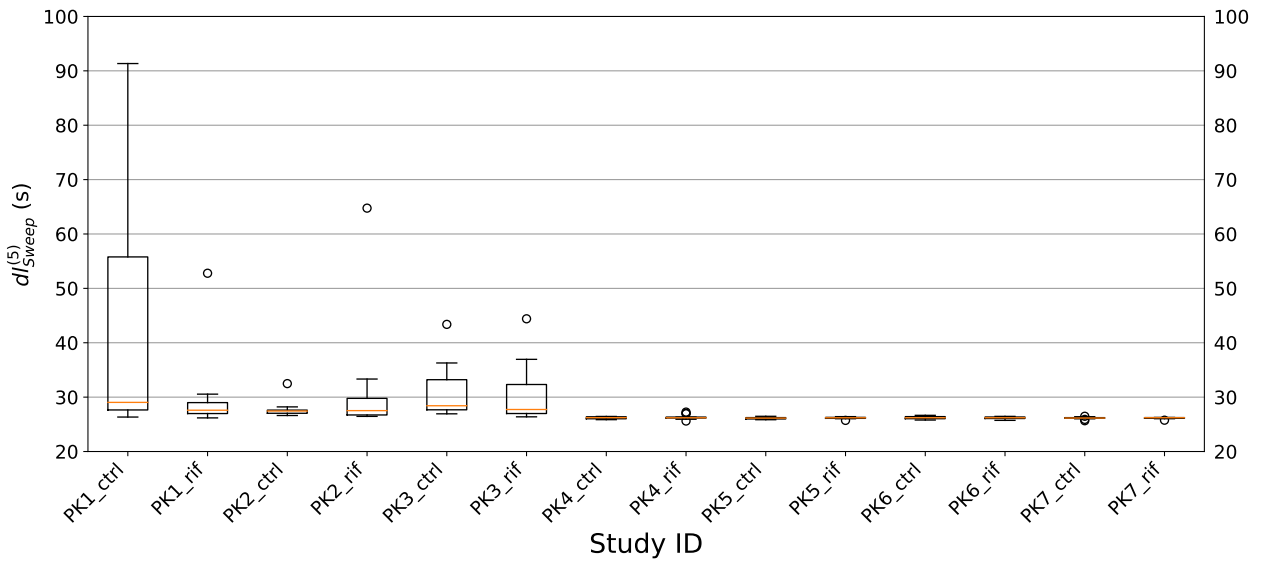


Figure 5.4: Box plots of delay between WB Sweeps dl_{Sweep} of the IsotoPK DWB protocol used in practice.

5.2.3 Design of a fully-automated DWB protocol on the Signa PET/MR

Part of this PhD project was allocated for the development of a fully automated DWB protocol on the Signa PET/MR. The main requirement for the envisioned protocol was to allow for continuous capture of PET data during DWB acquisition, into a single list-mode file for all bed positions and WB sweeps. Then the data would be processed after the acquisition, split into individual data for each bed position and reconstructed with the correct bed positional information. Using such an acquisition strategy, the delays between bed

positions and WB sweeps could be brought down to the time taken by the physical motion of the scanner table alone.

Towards this goal a three week secondment was planned at factory facilities of GE healthcare (Waukesha, Wisconsin, USA). There with help of the PET/MR team it was made possible to exploit in-build factory tools of the Signa PET/MR for the purposes of DWB automation. The two key tools necessary were:

- **Table Emulation**

This tool allows for disassociation of the table position between the MR and PET systems. It is the key tool that allows for the PET system to acquire continuously, while the MR system governs table motion. A disadvantage of this functionality is that once table emulation is enabled MR acquisitions cannot be performed.

- **Table Motion**

This tool commands the MR system to execute movements of the scanner bed. It can be used to drive the bed to a target location at a desired speed.

The automated DWB protocol was implemented as a Python class because the Python programming language is available on the PET/MR system's console and allowed for easy integration of the system tools with our custom made routines, all under a common system clock for accurate timing of bed movements and registration of events. The protocol was named "Auto-IsotoPK", but despite its name is a generic DWB protocol that is not limited to the IsotoPK pharmacokinetic study. It allows for an optional DSB scan to be acquired before starting the DWB acquisition. The protocol also allows for any number of beds to be used for DWB acquisition, with custom positioning of the beds for each examination using an initial MR scout image. Because MR acquisitions cannot be performed after *Table Emulation* is enabled, all bed position MRACs must be acquired before the PET examination and used for all WB sweeps of the study. A short Standard Operating Procedure (SOP) on the operation of the protocol is given in Appendix A.

After the procedure is completed, the whole PET study is stored as a single list-mode file, but without bed positional information. The precise timing information of the acquired bed positions is saved in a separate log file, which is used for post-processing the data and separation of the bed positions before reconstruction.

5.2.4 Results from NHP study

After initial tests using phantoms, the automated DWB protocol was tested on an actual pre-clinical DWB study. A macaque was scanned under full sedation with a novel [¹⁸F]Crizotinib tracer. Crizotinib is an anti-cancer drug used in the therapy of Non-Small-Cell Lung Carcinoma (NSCLC). The DWB study was

conducted to examine the tracer uptake in the brain as well as uptake and excretion from other organs. The macaque was injected with 185 MBq of the novel tracer. Directly after injection an initial DSB scan was conducted, centred over the brain for a duration of 90 s, followed by DWB acquisition of three bed positions. The study was planned for an approximate total duration of one hour. A total of 28 WB sweeps were fitted in the study, with the framing of 3×10 s, 5×20 s, 5×30 s, 5×45 s, 10×60 s for each of the three bed positions.

Acquisition of the required MRACs was performed prior to injection, at the planned bed positions shown in figure 5.5. In this acquisition, only the body coil of the PET-MR system was used, which is optimised for use with the human body size. Their use resulted in sub-optimal quality of MR images and generated attenuation maps. The attenuation maps were edited manually before being used for PET data reconstruction.

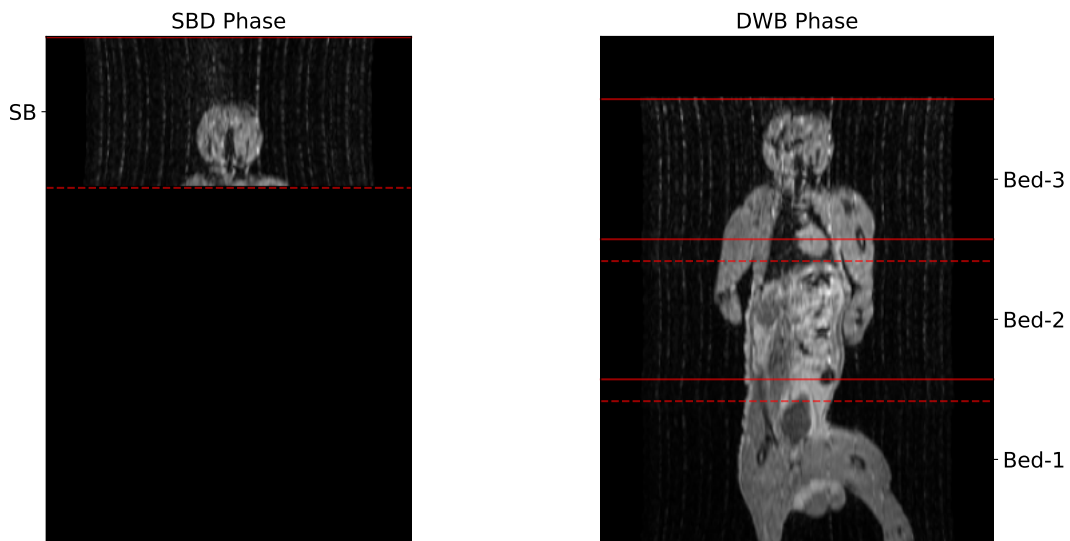


Figure 5.5: MRAC acquisitions of NHP study showing the planned bed positions of the two acquisition phases, with overlay of axial bed start (—) and end (----) location.

The complete study dataset was recorded in a single list-mode file, of which the head curve (curve of prompts rate with time) can be seen in figure 5.6. By overlaying the recorded timing information over this curve, the two phases of the acquisition (DSB and DWB), as well as the three bed position of the DWB acquisition, can be distinguished. The initial 260 seconds of the recorded list-data's head curve with the overlaid phases and bed positions are shown in figure 5.7.

Using the timing information recorded in the acquisition log file, the data were split into four individual bed position datasets (one from DSB and three from DWB) and were processed with the GE-PET toolbox as individual single bed dynamic studies, to generate corrections necessary for reconstructions using CASToR. The list-mode data along with the generated corrections were then converted into the CASToR data-file format for subsequent reconstruction tests. A coronal Maximum Intensity Projection (MIP) view of 3D recon-

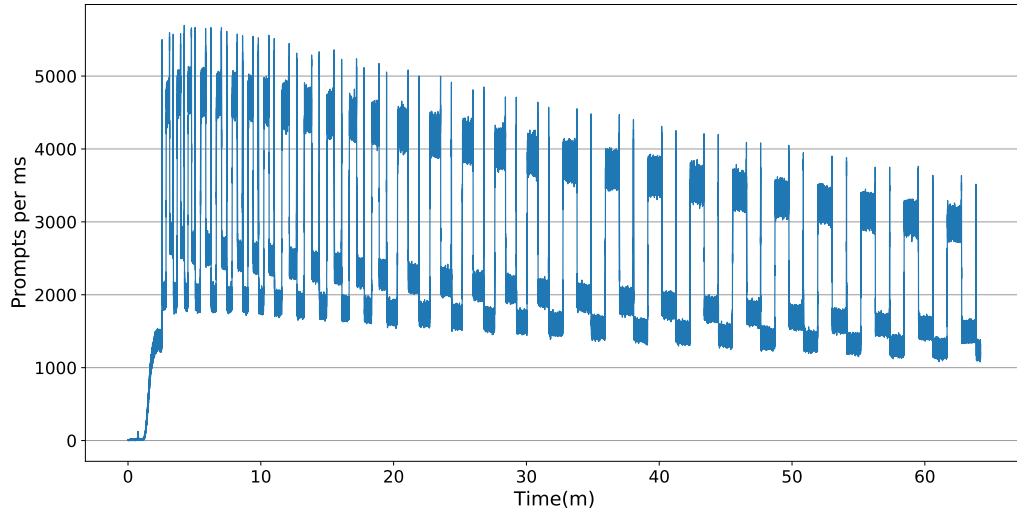


Figure 5.6: Head curve (prompts rate against time) of the acquired NHP study data in a single list-mode file using the fully-automated protocol.

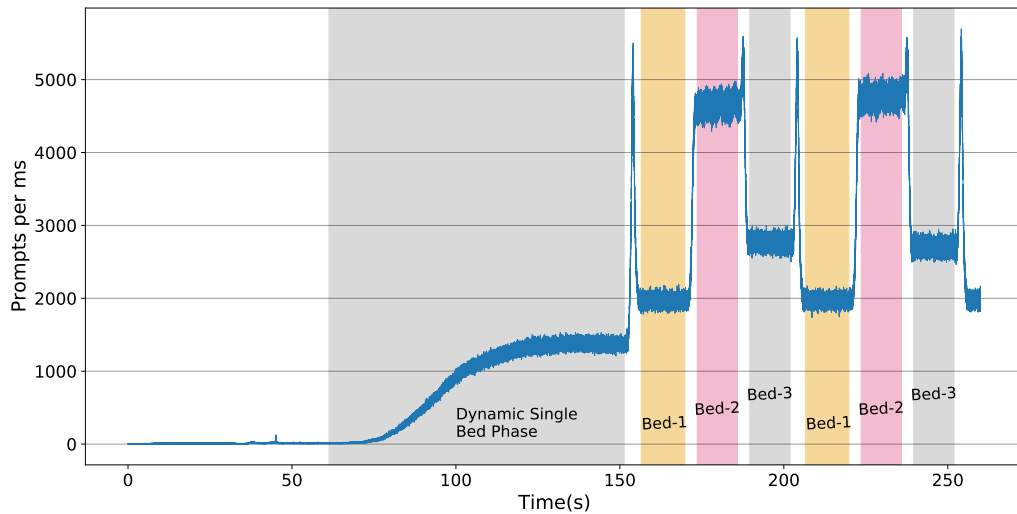


Figure 5.7: Head curve (prompts rate against time) of the acquired NHP study showing the DSB and DWB phases of the acquisition and the three DWB bed positions.

structions (averaged across all dynamic frames) is shown in figure 5.8.

An Image Derived Input Function (IDIF) was estimated from the reconstructed PET data. A right carotid Volume Of Interest (VOI), that was visible on both phases of the acquisition, and a left ventricle VOI on the Bed-3 position were used for the estimation. Both VOIs provided similar blood activity values for the DWB phase and were averaged to produce the final IDIF, shown in figure 5.9. This test showed that extraction of an IDIF, using multiple VOIs on both phases of the acquisition was possible and in good agreement between the used VOIs. Finally, an estimation of the delays (time gaps) for this single NHP study using the automated acquisition protocol was made using log timing information. The results showed an average intra-bed delay time dl_{bed} of 3.77 s (95%CI: 3.62, 3.91) and an average delay time between sweeps $dl_{Sweep}^{(3)}$

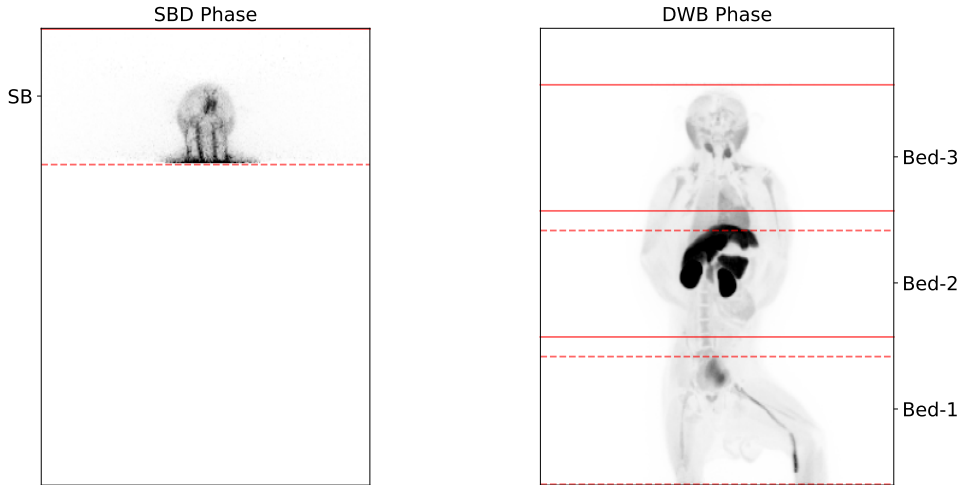


Figure 5.8: Coronal MIP views of the NHP study's reconstructed PET images, for the two phases of the acquisition, with overlay of axial bed start (—) and end (---) location.

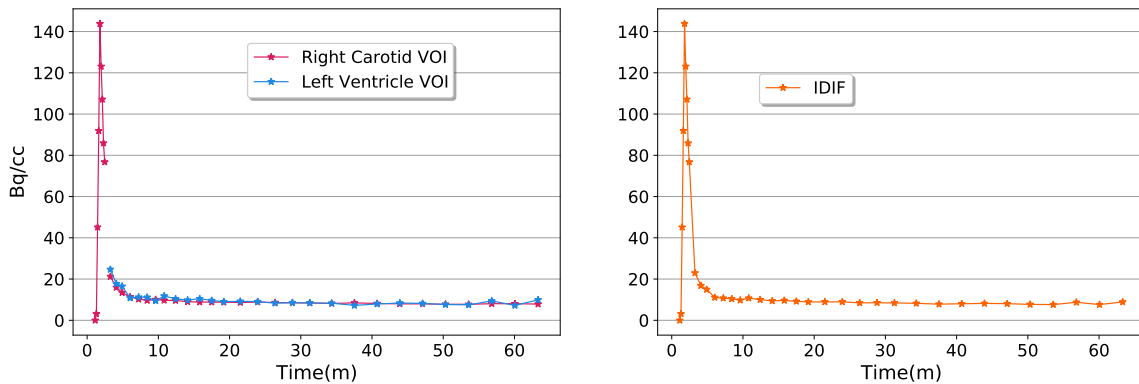


Figure 5.9: NHP study's image derived input function using information from multiple bed positions.

of 4.6 s (95%CI: 4.53, 4.67).

5.3 Comparison of protocols

The design and implementation of the fully-automated DWB protocol was made with the intentions of reducing delay times, compared to the custom implementation of a DWB protocol for the IsotoPK study. Before direct comparison of the protocols, the measured delay times between WB sweeps need to be adjusted to account for the difference in the number of bed positions between the two assessed protocols. Assuming a linear relationship between delays due to bed motion and the number of beds, the following relationship can be expressed

$$dl_{Sweep}^{(5)} = \frac{5}{3} dl_{Sweep}^{(3)}, \quad (5.2)$$

where now $dl_{Sweep}^{(5)}$ is the assumed delay between sweeps that would be achieved by the fully automated protocol for DWB imaging of 5 bed positions. It is expected that this value is an overestimation of the delays that would be achieved by the fully-automated protocol as the delays due to bed motion include an acceleration and deceleration phase that impacts shorter bed movements greater than longer movements. Using the measurements from the NHP study, the estimated $dl_{Sweep}^{(5)}$ that could be achieved is 7.66 s. Using this value we can estimate that the DAR for 20 s frames can be reduced from 49% to approximately 22.7%, by use of the fully automated protocol instead of the current IsotoPK DWB protocol. Furthermore, using the reduced $dl_{Sweep}^{(5)}$ delays a DAR of approximately 45.5% can be achieved for 10 s frames, allowing for more frequent sampling in the early phases of DWB acquisition without significantly compromising the quantity of acquired statistics.

Additionally, besides the reduced acquisition gaps, the fully automated protocol allows for more flexibility in the arrangement of bed positions for DWB imaging. By contrast, the hard-set bed positions of the IsotoPK DWB protocol do not always allow for optimum use of the effective A-FOV in each examination, as seen for example in examination PK2 in figures 5.1 and 5.2. In some cases, a lesser number of bed positions might be adequate and preferable as it would lead to a substantial increase of sampling frequency per bed.

5.4 Discussion

As seen by the reduction of acquisition delay times and reduction of DAR for short frame duration, the implementation of the fully-automated DWB protocol allows for improved DWB imaging with reduced acquisition temporal gaps. This gain can be used towards improving acquisition statistics by reducing the DAR ratio and towards a higher sampling frequency of early frames. A limitation in this assessment is that the comparisons were based on the empirical metric of DAR, without relating directly to the final kinetic analysis performed on the data and produced parametric images. In practice, faster sampling could also be achieved with larger acquisition gaps at the cost of reduced acquisition statistics and vice versa with higher statistics achieved at the cost of reduced sampling frequency. These trade-offs are expected to affect mostly kinetic estimations that are sensitive to fast dynamic information shortly after injection. Ideally, the DWB acquisition protocol should be optimised for the expected kinetics under study and the parameters of interest. Nevertheless, towards this optimisation, the developed fully-automated protocol can allow for greater variability in the available trade-off options of acquisition statistics vs. sampling frequency of early frames. Another aspect where fast sampling can be beneficial is for the derivation of the IDIF from DWB data. Given the fast initial sampling that can be achieved using a fully-automated protocol, it is possible to reduce the initial DSB acquisition duration or potentially remove it completely while still sampling frequently enough for an estima-

tion of the IDIF. In the NHP application presented in this chapter we showed that it is possible to combine IDIFs from multiple VOIs and from both DSB and DWB phases, without need for an identical bed position between the two acquisition phases. This flexibility can also allow flexibility in the DSB position placement over the WB scan, without compromising the derivation of the IDIF.

Additionally, another consideration that needs to be accounted for concerning fast sampling of early frames is the acquisition of MRAC sequences. For the Signa PET/MR the fastest MRAC sequence is performed in approximately 21 seconds (including preparation sequences) and as such shorter PET frames would have to be conducted without MRACs. In the IsotoPK DWB protocol, multiple MRACs are acquired in order to best account for any potential subject motion in the attenuation correction used for each WB pass. Their use can also be potentially expanded to the investigation of motion correction techniques. But if motion can be assumed to be small and negligible, then multiple MRACs would not be required and shorter PET frames can be acquired using MRACs acquired prior to injection.

In this evaluation, a practical limitation that has not been considered is safety limits on table movement that are needed to avoid undesirable effects from electromagnetic induction on patients/volunteers, which are caused by the fast movement of the bed within the MR field. For the tests conducted on the NHP, these limits have not been considered. These limits are expected to reduce the speed that would be permissive for human subjects, in compliance also with patient comfort requirements, and thus reduce to some degree the potential gains from the use of the fully automated DWB protocol.

In our tests we have considered only the use of S&S acquisition in the implementation and optimisation of DWB protocols. In a previous study on DWB protocols utilising CBM acquisition, advantages favouring the use CBM acquisition for DWB protocols were seen [55]. Beyond the aspects of reduced acquisition delays, CBM offers other benefits such as uniform axial sensitivity of acquisition, flexibility in sampling frequency by adjustments in table speed within each WB sweep, improved patient comfort, etc. Overall, use of CBM naturally overcomes many of the limitations posed by the use of multi-bed DWB protocols and S&S acquisition. Additionally, CBM protocols can also allow for bi-directional motion that eliminates delays between WB sweeps. These acquisition modes, their effects on acquisition gaps and result parametric image quality were considered further in the simulation study presented in chapter 6. Using the fully automated protocol and the developed tools we were able to emulate a CBM acquisition for the NHP study, by selecting a relatively slow table speeds and recording PET data continuously. But normalization and quantitative reconstruction of the acquired CBM datasets is a demanding, task as previously described [5], and thus quantitative reconstruction of these data was not considered further in this PhD project.

Overall the implementation of this fully automated protocol serves as proof of concept for flexible bed position placement and selection of frames duration, being limited only by the bed speed of the GE Signa

PET/MR and not by software or other system components. This protocol is a significant improvement from the currently used DWB protocol of the IsotoPK study. As the system has not been designed with DWB capabilities, the current DWB protocol involves manual planning of each WB sweep, multiple delays in data transfers and individual WB sweep reconstructions, etc.

However, the automated method does not allow for bed positional information to be recorded in the raw data and necessitate ad-hoc techniques to record bed positions and bed movements in separate files. These limitations necessitate custom processing steps to be performed after acquisition and prior to reconstruction, to allow for accurate and quantitative reconstruction of the acquired data. Furthermore, the current implementation of the automated protocol does not allow for MRI to be acquired during PET acquisition. Although a mixed acquisition using the automated protocol and the current implemented DWB protocol could allow for MR in the acquisition, it would further increase complexity and risk of system failures.

Due to the discussed limitations of the automated protocol and the considerations for safety, it was not used for subsequent DWB acquisitions within the IsotoPK study and was not considered further in the context of this thesis. It served only as a proof of concept for future developments.

5.5 Conclusion

A fully automated DWB protocol was developed on the GE Signa PET/MR as a proof of concept for fully automated and flexible acquisition of DWB imaging, recorded on a single list-mode file for the whole study. Data using this protocol were successfully acquired, processed and reconstructed in a test NHP study. Use of the protocol allowed for considerable reduction of delay times, enabling faster sampling without loss of PET data statistics. Thanks to the automated protocol, the minimum bed frame duration can be reduced from 20 to 10 s while maintaining the same DAR , compared to the DWB protocol currently in use. A considerable limitation of the implementation of this protocol is the unavailability of the MR system for MRI acquisitions during the DWB acquisition, which is caused by the bespoke utilities on which our experimental protocol was based upon. Finally, further considerations of permissible table speeds for patient safety and comfort need to be applied before using this protocol on human subjects.

Chapter 6

Dynamic Reconstruction

Implementation and Application to a Patlak Simulation Study

As shown previously in multiple applications in the literature, dynamic reconstruction can improve activity and parametric image estimates by making use of dynamic models directly in the reconstruction process, enabling more accurate modelling of the noise in the raw PET data for the parametric estimation process [10].

In this chapter, we briefly describe the implementation of a dynamic reconstruction framework and dynamic reconstruction functionalities in CASToR. A fraction of this PhD project was focused on the development and validation of these functionalities, that were necessary to achieve the project aims. The developments were conducted in collaboration with other CASToR developers, mainly with Dr Thibaut Merlin, Dr Simon Stute and Dr Marina Filipović. In addition, dynamic functionalities were implemented within a generic framework that allows for future expansion and contributions by developers of CASToR, to include more dynamic models and enable more complex and higher dimensional modelling (eg. dynamic and respiratory "5D" modelling , etc.).

In the remaining of this chapter, we present work conducted with simulated and real data, on the use and respective benefits of various dynamic reconstruction strategies for DWB parametric imaging. This study was submitted to the journal of **Physics in Medicine & Biology** for review in May 2021.

6.1 Introduction

Positron Emission Tomography (PET) imaging is well known and established in clinical applications and pathways, with an important role towards the delivery of precision medicine [2]. The established clinical practices rely on static imaging after a certain uptake period and semi-quantitative measures, such as the standardised uptake value (SUV). But these measures are vulnerable to many unknown factors that can vary between PET examinations, such as body composition, retention clearance, inconsistencies in uptake time and imaging practices [106]. On the other hand dynamic PET imaging can be used to fully characterise underlying tracer kinetics and provide fully quantitative measures, that could overcome many limitations of current static imaging practices and enable use of PET for new applications in clinical practice [1, 18, 107]. Current clinical scanners are limited in coverage by their axial field of view (A-FOV), with values ranging from 15 to 26 cm [3]. This is sufficient for single organ dynamic studies but cannot directly provide synchronous whole-body coverage, which is essential for some clinical applications such as tumour staging in oncology. In practice for static imaging whole-body coverage is achieved using multiple bed positions at different axial locations to provide the desired axial coverage [4], or alternatively via continuous axial bed motion (CBM) during the acquisition [5]. Recently scanners with increased A-FOV have been developed [13, 14], even with nearly 2 meters long A-FOV which provides total-body coverage [15]. But these scanners are still not widely adopted in the clinic. Using similar methods as in static whole-body imaging, dynamic whole body (DWB) protocols have been developed using multiple bed positions and repeated whole-body passes [6–8]. These types of acquisition protocols have also been incorporated into clinical products [16], and it has been shown that their use in clinical practice is feasible [56, 57].

The immediate effect of transition from single bed dynamic studies to multi-bed dynamic studies is the introduction of temporal gaps in the acquired data of any given bed position. These are introduced at each bed position by the time spent on imaging other bed positions and by scanner system delays due to the time required to move the bed to the next position and prepare for the next acquisition. These gaps cause a significant reduction in the sensitivity of the acquisition, with fewer total counts collected for each axial location when compared to single bed dynamic acquisitions. Furthermore, estimation of fast temporal changes in tracer uptake are compromised as the early time points of the acquisition are not fully sampled for all beds. Finally the established clinical protocols that make use of image derived input function (IDIF) to ease integration in clinical practice further sacrifice imaging time in the study's early phase, which is spent in acquiring fast frames over a single bed location centred over the heart and the aorta [16].

The generation of parametric images from dynamic data requires fitting of the dynamic model of interest on time activity curves (TAC) for every voxel in the image. Due to the poor statistics and high noise associated with TAC measurements at the voxel level, in particular for DWB acquisitions, parametric image estimates

can be heavily corrupted by noise and potentially biased. The use of direct dynamic reconstruction has been proposed to improve on this task by making use of dynamic models directly in the reconstruction. These techniques allow for more accurate modelling of the noise from the raw PET data in the generation process of parametric images and can improve parametric image noise and reduce bias [10]. For DWB acquisitions specifically, it has been shown using simulated and real data that direct dynamic reconstruction provides reduced noise, bias and improved parametric image contrast when compared to post-reconstruction parametric imaging [55].

In this work, we evaluate the performance of dynamic reconstruction algorithms for DWB fluorodeoxyglucose ($[^{18}\text{F}]\text{FDG}$) PET imaging for various dynamic reconstruction methods and for different DWB acquisition protocols. The evaluation is based on simulations of single bed and multi-bed dynamic studies and results are illustrated in a real dynamic FDG PET study.

In detail we evaluate for WB Patlak K_i parametric imaging (1) the benefits of using direct Patlak dynamic reconstruction in DWB protocols against single bed dynamic protocols and indirect parametric imaging from regular 3D reconstruction, (2) the use of the Spectral analysis dynamic model [70] in dynamic reconstruction for indirect parametric imaging, (3) the use of two different optimization algorithms for dynamic reconstruction and finally (4) the impact of different DWB acquisition strategies.

6.2 Methods

6.2.1 Development of the dynamic reconstruction framework in CASToR

The framework for dynamic reconstruction was developed within the general CASToR framework and following its general principles, to allow for future expansions and in order to make our developments publicly available within the public release of CASToR. To handle the use of dynamic models in reconstruction a new component was implemented in the code (called Dynamic-Model-Manager) that interacts with the reconstruction process within the main CASToR iterative loop (steps *Estimate/Fit dynamic model* and *Estimate image from fitted dynamic model* of algorithm 1). The main tasks of the Dynamic-Model-Manager are to prepare dynamic models for use and to fit these models if needed, given an estimate of a time series of image data, and subsequently estimate the time series image data from the fitted dynamic model. As described in section 3.5, dynamic reconstruction for linear dynamic models can be made using a set of basis functions directly implemented within the system matrix [10, 93, 108]. But as this method results in algorithms with substantially slow overall convergence properties, the nested framework [97, 98] is preferred, which decouples the dynamic model fitting process over image space from the tomographic update process over the raw PET data. We have designed the Dynamic-Model-Manager in order to allow for both options

of dynamic reconstruction, which we will refer to as non-nested and nested dynamic reconstruction respectively. In the examples and evaluations in this project, we made exclusive use of the nested framework, for practical computational requirements, which is also the method that predominates in most applications of dynamic reconstruction. But the availability of the non-nested option can allow for comparisons between the two approaches as well as the use of dynamic reconstruction with optimisation methods that might not necessarily support extension to nested optimization.

A diagram of the implemented framework within the dynamic-model-manager is given in figure 6.1. A generic dynamic model (`vDynamicModel`) was designed as a virtual function, which implements the requirements for model fitting processes, as well as some common optimization algorithms (Least-Squares (LS) and Non-Negative Least-Squares (NNLS) optimization algorithms).

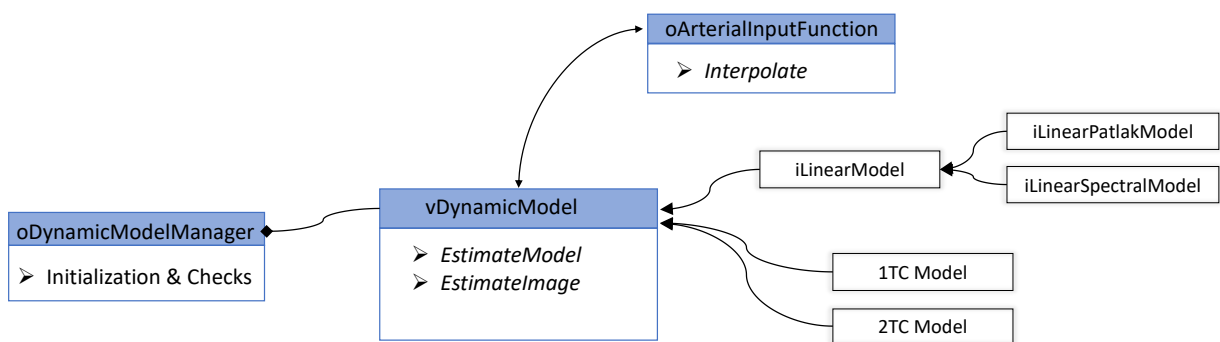


Figure 6.1: CASToR framework for dynamic reconstructions.

Specific dynamic models can be directly implemented by inheriting these functions from the `vDynamicModel` class, such as for example the implemented 1TC and 2TC models. These models are based on micro-parameters estimation of the respective compartmental models and make use of non-linear optimization or linearization techniques that are unique to these specific models. Beyond these specific models, many models used in practice for parametric imaging are linear models and share common optimization methods. For this reason, a generic Linear model (`iLinearModel`) was developed, with EM, LS and NNLS optimization algorithms included for model fitting over voxel TACs. This linear model can be used directly if basis functions are provided as input or alternatively other more specific linear models can inherit its functions and define their own temporal basis functions. In our implementation, we have implemented two specific linear models, the Patlak model [69] and the spectral analysis model [70]. Furthermore, as many dynamic models that relate to physiological kinetic parameters require a blood input function, a specific class was created (`oArterialInputFunction`). This class takes a provided input function and performs linear interpolation of the input data points, before its use by the dynamic model. Finally, an additional castor toolkit (`castor-imageDynamicTools`) was included in the public release to allow the use of the developed models for

post-reconstruction model fitting using the included image space optimization algorithms.

6.2.2 Development of analytical simulator for dynamic data

In a similar fashion to the design of the dynamic reconstruction framework, a dynamic modelling framework was implemented within an existing in-house developed analytical PET simulator [109]. Specifically the 1TC and 2TC models were implemented, using equation 2.4 and equation 2.8, while also accounting for blood fraction using equation 2.2. The simulator was used to validate the implemented dynamic reconstruction framework in CASToR and to conduct the simulations used in this study.

6.2.3 Simulated acquisition protocols

A single bed (SB) dynamic protocol (continuous in time with no temporal gaps) and three DWB acquisition protocols of five bed positions (with temporal gaps) were simulated for this study, using the geometry characteristics of the GE Signa PET/MR scanner [47]. With the provided 25 cm A-FOV per bed and a bed overlap of 3.34 cm, axial coverage of 110.3 cm can be achieved with five bed positions. The relatively small overlap (same as in the IsotoPK protocol and approximately half compared to routine clinical protocols) was selected to reduce the number of beds and subsequently the acquisition temporal gaps. A total study duration of 60 minutes was used in the design of all protocols, including an initial single bed dynamic phase of 3 minutes centred over the aorta to mimic requirements for IDIF estimation.

- The first DWB protocol (DWB-1) considers a step and shoot (S&S) acquisition using the timing characteristics of the Signa PET/MR, with a delay of 6 seconds between adjacent bed positions and 36 seconds between whole-body sweeps, resulting to 8 whole-body sweeps in the duration of the study. The timing characteristics of this protocol are similar to the ones considered in the design of the IsotoPK DWB protocol described in chapter 5.
- The second DWB protocol (DWB-2) differs from DWB-1 by use of system delays that mimic a continuous bed motion (CBM) acquisition of the same length, with no delays between adjacent bed positions and 12 seconds delay between whole-body sweeps to account for bed speed and acquisition overscan (used to obtain reasonable axial sensitivity at the edges of the acquisition [5]). This protocol results in 9 whole-body sweeps. The actual simulation for DWB-2 did not make use of continuous bed motion in the simulation process but made use of the accurate timings that reflect reduction of delays and framing achieved with CBM on the same system geometry. This is conceptually equivalent to CBM sinogram data (sometimes referred as "chunks" [110]) with uniform framing over the FOV instead of slice-dependent timings as in actual CBM sinograms.

- The third DWB protocol (DWB-3) replicates the timing properties of DWB-2 for CBM acquisition but utilises a bi-directional acquisition that reduces delays between sweeps to the time spent for the overscan. This acquisition motion provides more sweeps in the same study duration but results in non-uniform sampling. This protocol results in 10 whole-body sweeps.
- A fourth DWB protocol (DWB-4) was simulated, in addition to the above protocols, for evaluating parameters estimation that depends on early dynamic information. In particular, in this evaluation, we were interested in the estimation of K_1 parametric images. For this protocol, the timing of the DWB-1 protocol was considered, with the addition of an early dynamic single bed acquisition over the same bed location. The single bed acquisition was split into nine frames of 20 seconds each.

Unlike what will be presented in chapter 7 for multi-bed dynamic reconstruction, in this chapter and for this simulation study we consider the dynamic reconstruction of each bed position separately. The results of these reconstructions could still be used for WB parametric imaging, by post-reconstruction merging of each bed's parametric images [55]. This parametric merging approach was effectively used in chapter 8, due to limitations that will be discussed in that chapter by the use of the adaptive reconstruction algorithm.

Due to practical limitations and simulation time needs, the simulation study was focused on a single bed position from the assumed DWB protocols of five bed positions. The second bed position from the top was selected, to emphasise on sampling differences between uni-directional and bi-directional CBM motion. Furthermore, this option practically aided in the consideration for CBM timings in simulation as it avoids having to consider further complexity in CBM protocols (ex. overscan at edge position). This bed position is centred over the upper chest, as seen in figure 6.2. The PET data simulations were conducted solely for this bed position using the timing details of the protocols described above. The exact framing information are available in appendix B.

6.2.4 Digital phantom & analytical simulation

The Zubal brain phantom [12] was chosen for the simulations of PET [^{18}F]FDG data, even though its anatomy doesn't correspond to the anatomy that would be found in the axial location of the simulated bed position. The choice of the phantom was made to incorporate higher complexity structures than those offered from common lung/chest phantoms. Furthermore the use of the brain phantom, centred in the FOV, aided in avoiding analysis of areas falling in the overlapping regions, whose behaviour under DWB acquisition and reconstruction is yet another subject for investigation. The Zubal brain phantom was segmented into 19 unique regions and a non-reversible two tissue compartment model was assigned uniformly to each region to simulate realistic FDG kinetics, with K_1 , k_2 , k_3 and V_b values drawn from the literature and a real

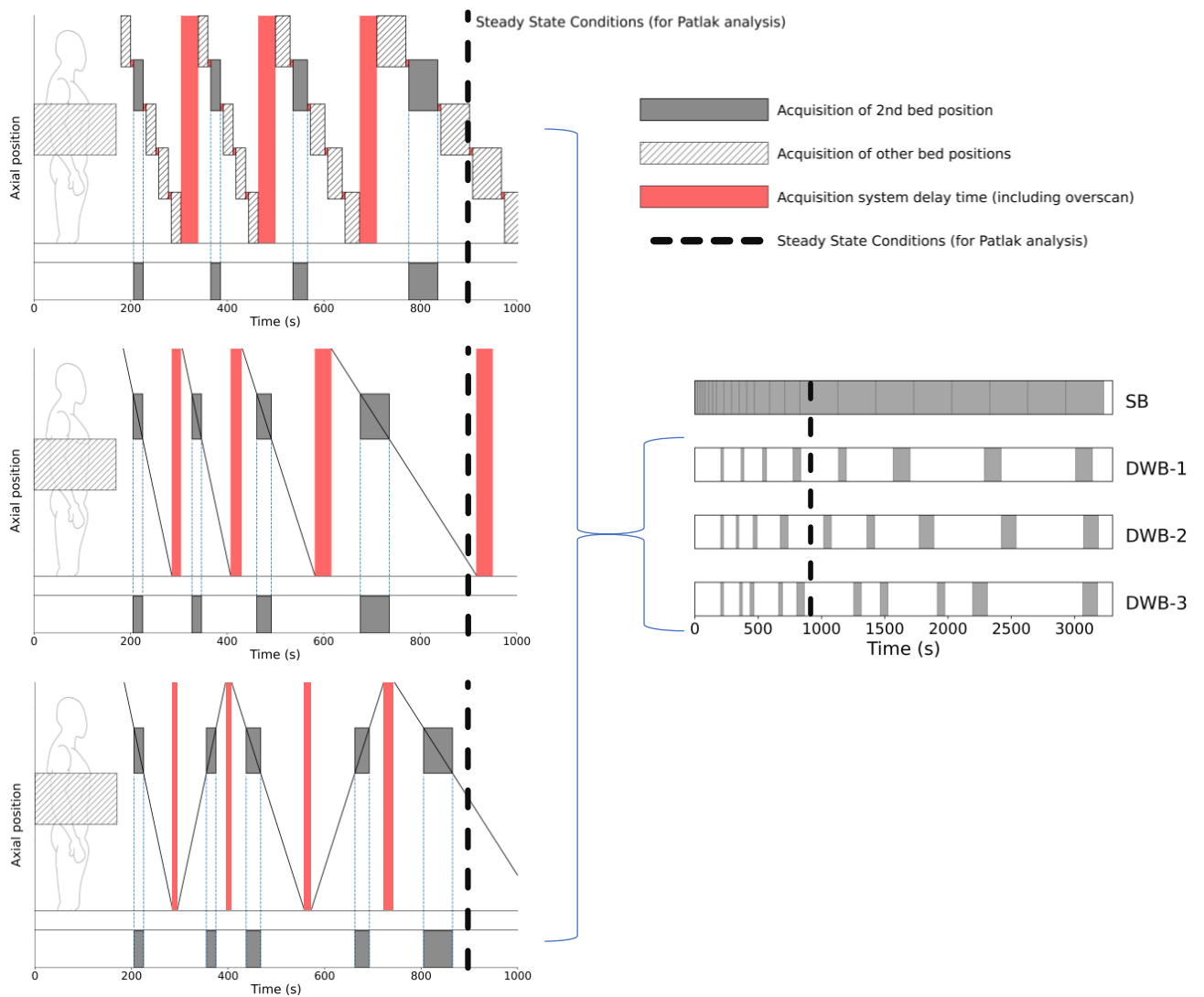


Figure 6.2: Dynamic whole-body acquisition protocols considered for simulation.

measured input function. A selection of the simulated kinetic parameters is provided in appendix B. The developed analytical simulator was used to generate raw PET sinogram data. The simulations included attenuation and detector resolution effects, scattered and random coincidences, while Poisson noise was added to the sinogram data. The simulation did not include time of flight (TOF) information in the data. Fifty different noise realisations were simulated for each DWB protocol. For the SB protocol the number of noise realisation was reduced to twenty as simulation and reconstruction times of the SB datasets were substantially higher.

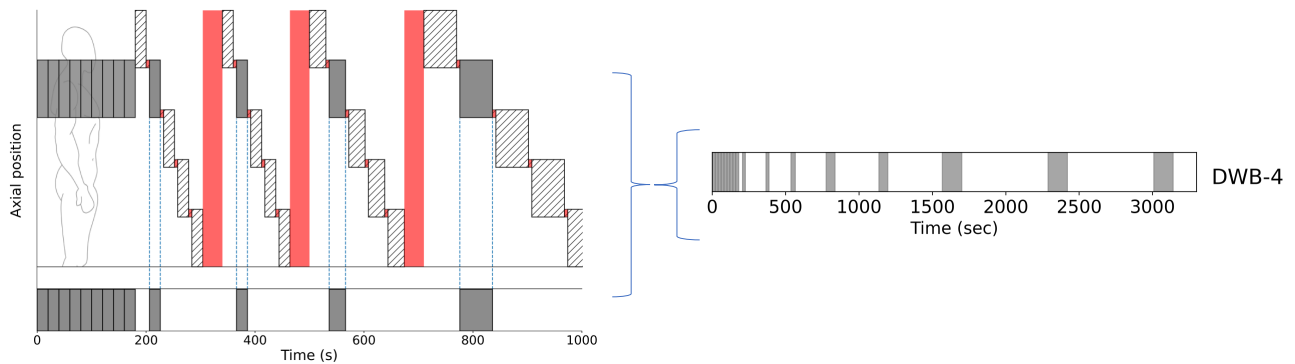


Figure 6.3: Fourth dynamic whole-body acquisition protocol considered for simulation, which includes an initial dynamic single bed phase centred over considered bed position.

6.2.5 Reconstruction and kinetic modelling

Both 3D and dynamic iterative reconstructions were used. All reconstructions were run within an OSEM framework, for 40 iterations and 28 subsets, using the developed dynamic reconstruction framework in CASToR [11]. All reconstructions were performed with a voxel size of $2.2 \text{ mm} \times 2.2 \text{ mm} \times 2.8 \text{ mm}$ and included resolution modelling as well as corrections for attenuation and for random and scattered coincidences (generated from the simulation). Dynamic reconstructions are made by combining dynamic models that describe the tracer kinetics with the tomographic reconstruction process. When the dynamic model of interest is used this technique results in direct reconstruction of parametric images of interest and allows for accurate modelling of the raw data noise in the estimation process [92, 93, 108, 111]. Use of generic dynamic models can also be made for dynamic reconstruction, where dynamic models impose temporal regularisation in the frame activity estimation process. Post-reconstruction (indirect) estimation of parametric images can then be made and indirectly benefit from the use of dynamic reconstruction [10, 112]. Linear dynamic models can be directly implemented within the system matrix [10, 93, 108] but result in algorithms with substantially slower overall convergence properties. Instead a nested optimization framework [97, 98] can be used, which decouples the dynamic model fitting process on image space data from the tomographic update process over the raw PET data. This allows for multiple nested sub-iterations of dynamic model fitting to be run within each tomographic iteration of the reconstruction process, resulting in convergence acceleration and reasonable computing time requirements. The separation of the two processes allows for various optimization algorithms to be implemented in the nested dynamic model fitting process [98]. One particular method of interest is the Non-Negative Least Squares (NNLS) algorithm [113], that enforces non-negativity and is commonly used in post-reconstruction kinetic modelling. The NNLS algorithm is self-terminating and for dynamic reconstruction it has been shown that a single execution of nested NNLS results in parametric images with similar Root Mean Square Error (RMSE) to that of 15 iterations of nested MLEM [98]. Therefore

use of nested NNLS optimization has the potential for reduced overall reconstruction times. In this work we made use of both nested MLEM and NNLS optimizations to compare their performance and reconstruction time requirements for their implementation within CASToR. The nested MLEM optimization was used with 20 sub-iterations of the dynamic model fitting process after each subset of the OSEM tomographic update process, which has been found to be the optimal number of sub-iterations in a previous similar study [55]. Hereafter we will refer to nested dynamic reconstruction simply as *4D reconstruction*.

In this work we evaluated two different linear dynamic models for 4D reconstructions, the Patlak model and the Spectral analysis model.

4D Patlak

The Patlak model describes the activity in tissue $C_T(t)$ as

$$C_T(t) = K_i \int_0^t C_P(\tau) d\tau + V_\alpha C_P(t), \quad t > t_{ss}, \quad (6.1)$$

where C_P is the activity concentration in arterial blood plasma at time point t , K_i is the steady state trapping rate and V_α the apparent volume of distribution. The Patlak model is valid once steady state conditions have been reached (denoted as t_{ss}). For a PET measurement the observed activity is

$$C_{PET}(t) = (1 - V_B)C_T(t) + V_B C_B(t), \quad (6.2)$$

where conventionally it is assumed that the blood fraction V_B is small (≤ 0.05) in most tissues. If we assume for FDG that the total blood activity concentration C_B is proportional to C_P with $C_B = rC_P$, define the Patlak slope $\theta_1 = (1 - V_B)K_i$ and the Patlak intercept $\theta_2 = V_\alpha + rV_B$, then the observed activity of acquisition frame f between time points t_{start} and t_{end} is modelled according to the Patlak model as

$$\int_{t_{start}}^{t_{end}} C_{PET}(\tau) d\tau = \theta_1 \int_{t_{start}}^{t_{end}} \int_0^\tau C_P(\tau_1) d\tau_1 d\tau + \theta_2 \int_{t_{start}}^{t_{end}} C_P(\tau) d\tau, \quad (6.3)$$

where $C_{PET}(t)$ is the observed activity map. Using this representation a linear model of two basis functions can be constructed, which when fitted to TAC data provides parametric images $\theta = [\theta_1, \theta_2]$. 4D dynamic reconstruction with the Patlak model directly results in parametric images of θ_1 and θ_2 . In our study 4D Patlak reconstruction was applied using frame data after the first 15 minutes, from where we assumed steady state conditions ($t_{ss} = 15$ min).

It is important to note that a limitation of the Patlak model is that the estimated K_i from the Patlak slope θ_1 is susceptible to systematic errors in its estimation and can deviate from the true underlying $K_i (= \frac{K_1 k_3}{k_2 + k_3})$.

In addition, V_B is not necessarily known a priori and Patlak analysis can not distinguish between K_i and $(1 - V_B)$. In this study we use the Patlak slope θ_1 as the K_i value of interest for parametric imaging, as well as the ground truth target, generated from Patlak fits on noiseless simulated TAC data.

4D Spectral

4D reconstruction using the spectral analysis model is inspired from the 1993 homonym method [70] that is used to describe the generic behaviour of any compartmental system as a sum of decaying exponential functions with decay rates β which describe the exchange between compartments, convolved with an input function [71]. For a measurement within an acquisition frame f between time points t_{start} and t_{end} , the observed PET activity can be described according to the Spectral analysis model with $M+1$ number of parameters ϕ as

$$\int_{t_{start}}^{t_{end}} C_{PET}(\tau) d\tau = \sum_{b=0}^{M-1} \phi_b \int_{t_{start}}^{t_{end}} e^{-\beta_b \tau} * C_P(\tau) d\tau + \phi_M \int_{t_{start}}^{t_{end}} C_P(\tau) d\tau . \quad (6.4)$$

Assuming C_B is proportional to C_P then the parametric map ϕ_M is proportional to the blood fraction V_B , while for irreversible kinetics the decay rate $\beta_0 \rightarrow 0$ and the parametric map ϕ_0 describes tracer trapping. Parametric maps $\phi_1 \dots \phi_{M-1}$ describe the exchange between compartments, with decay rates $\beta_1 \dots \beta_{M-1}$ chosen to be logarithmic spaced within a range of values that covers the expected underlying kinetics. In our tests we used 3 different sets of numbers of basis functions ($M+1=17, 9$ and 6), with $\beta_1 \dots \beta_{M-1}$ logarithmically spaced within the range of 3 to 0.001 min^{-1} .

Unlike the Patlak model, the spectral analysis model is valid from the start of the acquisition and by default was applied to all time frames. The parameters ϕ_b of the spectral model have physiological meaning and in combination can be used to derive macro-parameters maps such as K_1 and either K_i or V_D , depending on the irreversible or reversible kinetic behaviour [71]. However, this derivation is sensitive to the acquisition's early kinetics after the injection, which are not necessarily sampled for DWB protocols except for the bed position that matches the initial dynamic phase, commonly used for IDIF estimation. For this reason, the DWB-4 protocol was designed to evaluate the estimation of K_1 parametric images, for bed positions of DWB protocols that are covered by the single bed dynamic phase. Accurate K_1 estimation requires correction for the blood fraction ratio, as shown in equation 2.20. We intentionally ignored this term in the estimation of parametric images to avoid the introduction of noise by the voxel-to-voxel division with the blood fraction image. We will refer to this approximate value as K_1^* . In this project K_1^* parametric images were estimated

using

$$\mathbf{K}_1^* = \sum_{b=0}^{M-1} \phi_b. \quad (6.5)$$

The ability to derive and compare K_1 and K_i parametric images is clinically relevant, as it can reflect differences in the behaviour of early and late kinetics. For example, the use of images of this type for lung tumours has been shown to provide complementary information [17].

In the rest of the study, the main focus is parametric imaging of Patlak K_i , for which the spectral analysis model is used to enforce temporal regularisation without any strong assumptions on an underlying model [114]. The activity estimates of the 4D Spectral reconstruction are fitted post-reconstruction with the Patlak model to estimate the parametric images of Patlak K_i . In this sense the use of 4D Spectral reconstruction for parametric K_i imaging can be regarded as indirect dynamic reconstruction.

One could argue that since the parametric image ϕ_0 of the fitted spectral model describes tracer trapping, it could be used directly as an estimation of K_i . But it has been shown, in regular post-reconstruction spectral analysis, that separation of the irreversible trapping component between ϕ_0 and other spectral components is not complete due to noise and the correlation between the components. Empirical iterative filtering methods have been proposed to improve on such parameters estimations [115–117], but their use falls out of scope for utilisation of the spectral analysis model in 4D reconstruction. In 4D reconstruction, the spectral analysis model is used to enforce temporal regularisation without any strong assumptions on an underlying model. As such the number of spectral functions used is much smaller than the numbers suggested for spectral analysis, which makes the process of successful components separation even more unlikely.

Reconstructions details

As highlighted above the spectral analysis model makes use of all frame data, while the Patlak model uses data after t_{ss} . In order to make a closer comparison between the two models for 4D reconstruction, an additional comparison was made using only data after t_{ss} (reconstructions labelled with $t > t_{ss}$).

With the exception of 4D Patlak reconstructions that directly output parametric images of K_i , all other 4D and 3D reconstruction activity maps were fitted post-reconstruction with the Patlak model at the voxel level, using the Ordinary Least Squares (OLS) optimization algorithm, to generate parametric K_i images. For all 4D reconstructions and post-reconstruction fitting processes the true input function was used.

The reconstruction's namings and parameters are summarised in table 6.1 and table 6.2.

Table 6.1: Evaluated reconstruction parameters.

Name	Dynamic model	Nested Optimization	Algorithm
3D	none	n/a	OSEM(40it28s)
4D Patlak	Patlak	MLEM (20sub-it)	OSEM(40it28s)
4D Spectral(6bf)	Spectral	MLEM (20sub-it)	OSEM(40it28s)
4D Spectral(9bf)	Spectral	MLEM (20sub-it)	OSEM(40it28s)
4D Spectral(17bf)	Spectral	MLEM (20sub-it)	OSEM(40it28s)
4D Spectral(6bf)-NNLS	Spectral	NNLS	OSEM(40it28s)
4D Spectral(9bf)-NNLS	Spectral	NNLS	OSEM(40it28s)
4D Spectral(17bf)-NNLS	Spectral	NNLS	OSEM(40it28s)

Table 6.2: Additional reconstructions characteristics.

Additional Reconstructions	Characteristics
4D Spectral(6bf) $t > t_{ss}$	Provided only with data after t_{ss}
4D Spectral(9bf) $t > t_{ss}$	Provided only with data after t_{ss}

6.2.6 Evaluation metrics

The reconstructed and generated parametric K_i images were evaluated across noise realisations for voxel based and Volumes of Interest (VOI) based metrics. We define $\theta_{j,n}$ as the image K_i value for voxel j in noise realisation n , $\theta_{VOI,n}$ the VOI K_i mean value and θ_{VOI}^{GT} the ground truth value (as measured from Patlak analysis on the noiseless simulated TACs). The following voxel-based metrics were calculated, where (6.8) is the Root Mean Square (RMS) spatial average of (6.6) and (6.7) within a VOI.

$$Bias_j = \bar{\theta}_j - \theta_{VOI}^{GT} \quad , \text{ where } \bar{\theta}_j = \frac{1}{N_{noise}} \sum_{n=1}^{N_{noise}} \theta_{j,n} \quad (6.6)$$

$$CoV_j = \frac{1}{\theta_{VOI}^{GT}} \sqrt{\frac{1}{N_{noise}} \sum_{n=1}^{N_{noise}} (\theta_{j,n} - \bar{\theta}_j)^2} \quad (6.7)$$

$$\text{Metrics for } j \in VOI \left\{ \begin{array}{l} \% RMS Bias : \frac{100}{\theta_{VOI}^{GT}} \sqrt{\frac{1}{N_{VOI}} \sum_{j \in VOI} Bias_j^2} \\ \% RMS CoV : \sqrt{\frac{1}{N_{VOI}} \sum_{j \in VOI} CoV_j^2} \times 100 \end{array} \right. \quad (6.8)$$

The following metrics were used for VOI-based analysis, with the average VOI value being the parameter of interest (as opposed to the pixel value).

$$\text{Metrics for } VOI \left\{ \begin{array}{l} \%Bias_{\theta_{VOI}} = \frac{100}{\theta_{VOI}^{GT} N_{noise}} \sum_{n=1}^{N_{noise}} (\theta_{VOI,n} - \theta_{VOI}^{GT}) \\ \%CoV_{\theta_{VOI}} = \frac{100}{\theta_{VOI}^{GT}} \sqrt{\frac{1}{N_{noise}} \sum_{n=1}^{N_{noise}} (\theta_{VOI,n} - \bar{\theta}_{VOI})^2} \end{array} \right. \quad (6.9)$$

Because Patlak analysis provides different fits on the simulated TACs depending on the DWB protocol framing, the θ_{VOI}^{GT} differ slightly per protocol. The ground truth values used in the evaluations are given in table 6.3. The cortex and an eroded thalamus VOI were evaluated in the analysis. The thalamus VOI was eroded by 2 voxels in order to be less susceptible to partial volume effects. By contrast the cortex VOI is subject to partial volume effects. The same metrics were applied to the parametric K_1^* images, for which θ_j represents the parametric image K_1^* value for voxel j and θ_{VOI}^{GT} the ground truth K_1 values.

Table 6.3: θ_{VOI}^{GT} and true K_i values for the simulated acquisition protocols (min^{-1}).

VOI Name	SB	DWB-1	DWB-2	DWB-3	K_i
Thalamus	0.0305	0.0309	0.0311	0.0303	0.0307
Cortex	0.0390	0.0391	0.0392	0.0388	0.0410

6.2.7 Real Data

A single-bed dynamic examination centred over the lungs region was used to test performance of the evaluated algorithms and to compare results against the simulation findings. Approval for the retrospective use of the real patient data was obtained for this study. The data had been collected with approval from an local ethics committee. The original dataset was acquired on a Signa PET/MR, starting at the injection of 177 MBq of FDG tracer to the patient, for a duration of 1 hour. The imaged patient had been diagnosed with a non small cell lung cancer (NSCLC) at the left lung. The raw list-mode dataset was retrospectively reprocessed (replayed) to create two new datasets. One dataset using the framing of the simulated single bed (SB) study and one dataset using the framing of the simulated DWB-1 study (DWB) including temporal gaps. Both datasets included TOF information provided by the Signa PET-MR. The datasets were reconstructed with and without the use of TOF information in reconstruction. An IDIF from the ascending aorta was measured on activity image data from 3D reconstruction and used for 4D reconstruction and post-reconstruction analysis. The two datasets were reconstructed using the same 3D and 4D dynamic reconstruction algorithms that were used in the simulation study using identical parameters. No respiratory motion correction or gating was applied on the data. Similar to the simulation study, post reconstruction Patlak analysis at the voxel

level was performed with OLS to generate parametric images of K_i . VOIs were drawn over the tumour, the tumour's background (left lung) and the liver, as shown in figure 6.4, to compare between reconstructions and against the findings of the simulation study. Using these the contrast to noise ratio (CNR) was estimated according to

$$CNR = \frac{\theta_{tumour} - \theta_{bkg}}{\theta_{bkg} SD_{liver}}, \quad (6.10)$$

where SD_{VOI} is the spatial standard deviation of a VOI.

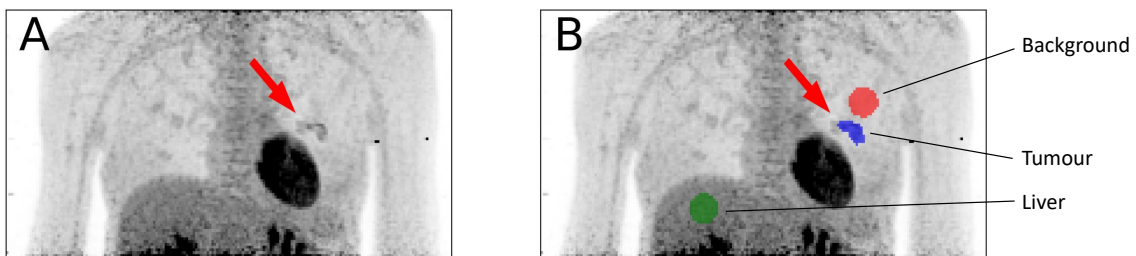


Figure 6.4: Real data MIP SUV image (A) and the drawn VOI (B).

Similarly, CNR was calculated in a single noise realisation of the simulation study to enable direct comparison with the real data. In this case the eroded thalamus VOI was used as the target region and the white matter as the background for both contrast and noise estimation.

6.3 Results

6.3.1 Comparison between SB and DWB protocol data

The VOI and voxel based metrics comparing 3D and 4D Patlak reconstructions for the SB and DWB-1 protocols are shown in figure 6.5. For both metrics and VOIs the 3D reconstruction followed by post-reconstruction Patlak fitting using DWB data resulted in higher CoV values, compared to 3D reconstruction of SB data at matched bias. For the first few iterations the 3D reconstructions of both datasets resulted to similar bias values, while further iterations resulted to a wider range of bias values for the DWB data compared to SB data within 40 iterations.

The use of 4D Patlak reconstruction on DWB data produced results with lower CoV on both evaluated metrics and VOIs, compared to the 3D reconstruction of the same data at matched bias, and a shorter range of bias values within 40 iterations. For the VOI metrics, CoV values of the 4D Patlak reconstruction on both evaluated regions approach those of 3D reconstruction of SB data. Furthermore, the 4D Patlak reconstruction of DWB data resulted in eroded thalamus bias values that evolved towards a steady value of positive

bias, at approximately iteration 12, after which further iterations resulted in small step changes towards lower bias. For the voxel metrics, similar behaviour is seen on early iterations of 4D Patlak reconstruction on DWB data for the CoV, with values approaching those of 3D reconstruction of SB data. But at further iterations the CoV for the 4D Patlak reconstruction in both VOIs surpasses values from 3D reconstruction on DWB data. On the eroded thalamus this was the case beyond iteration 24, while for the cortex from iteration 22 and beyond. These results show that there is a risk of increasing parametric image noise, greater than that of 3D reconstructions, when the 4D reconstruction is run at high iterations to achieve more favourable and stable mean VOI behaviour.

The use of 4D Patlak reconstruction with SB data showed similar effects on behaviour for CoV and bias on both metrics, compared to 3D reconstruction of SB data, and resulted in the lowest CoV values for these comparisons.

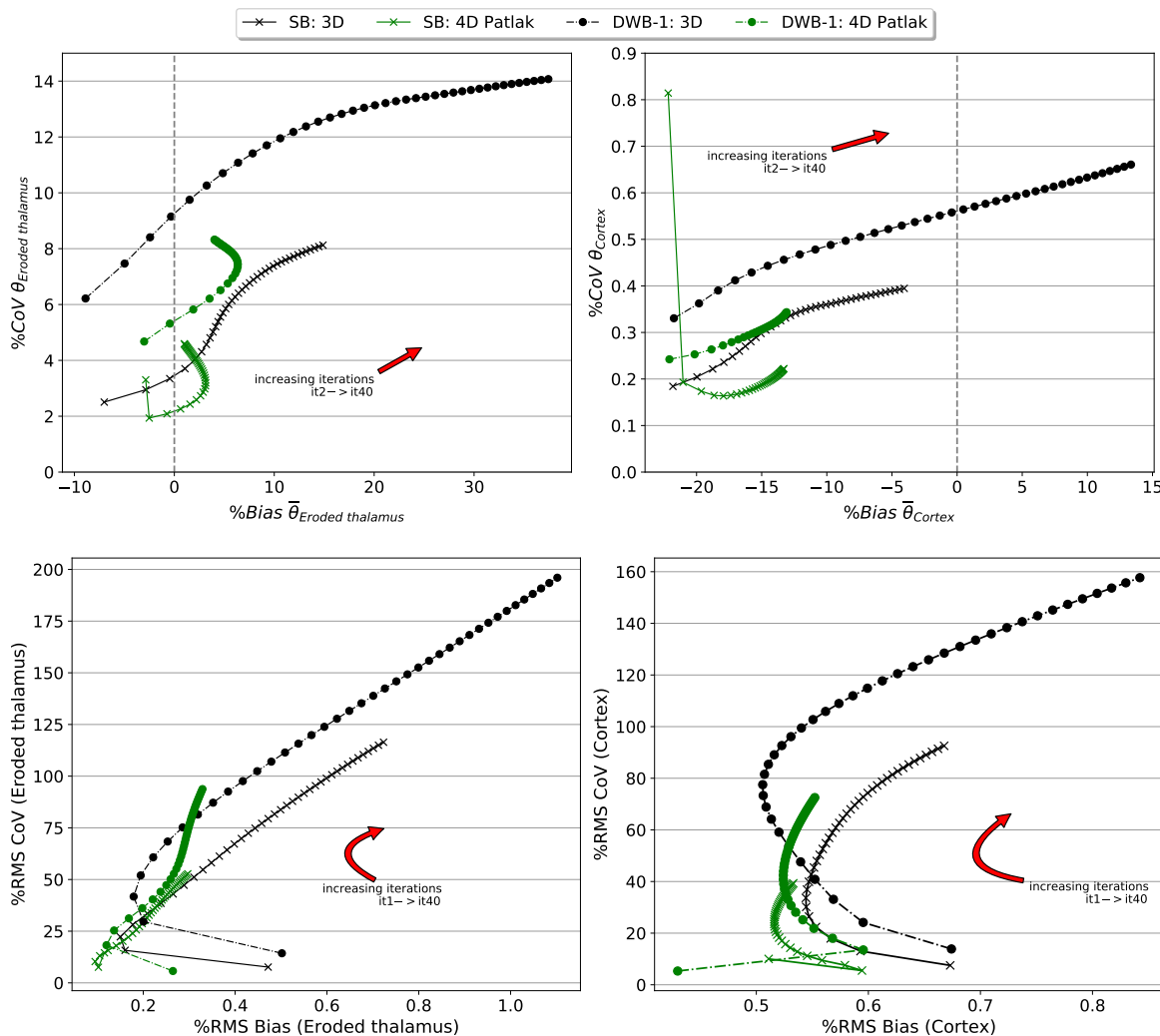


Figure 6.5: Simulation: Eroded thalamus (left) and Cortex (right) noise versus bias trade-off curves for 3D and 4D Patlak reconstructions. VOI based metrics (top row) and voxel-based metrics (bottom row).

6.3.2 Comparison between 4D Dynamic Reconstructions on DWB protocol data

The VOI and voxel based metrics are shown in figure 6.6 for comparison of 4D Patlak and 4D Spectral reconstructions of DWB data. On both metrics and for both regions the use of Spectral reconstruction with 6 basis functions provided the lowest CoV values at matched bias compared to other 4D reconstructions of DWB data and 3D reconstruction of SB data. However 4D Spectral reconstruction with 6 basis also provided the highest bias values in the eroded thalamus. On the cortex the difference on bias metrics was relatively small between all 4D reconstructions.

The 4D Spectral reconstruction with 9 and 17 basis functions resulted to similar bias and CoV values at both regions. Their use resulted in lower CoV compared to 4D Patlak reconstruction and 3D reconstruction of SB data, but higher compared to 4D Spectral using 6 basis. Nonetheless, at the eroded thalamus use of 9 and 17 basis provided improved bias values at matched CoV when compared to the use of 6 basis, closer to bias values from 4D Patlak reconstruction.

When the 4D Spectral reconstructions were provided with the same data as the 4D Patlak reconstructions (4 frames with $t > t_{ss}$) instead of all data (8 frames for DWB-1), it resulted in a noticeable increase of the CoV values, with very close noise versus bias trade-offs between 6 and 9 basis. Their trade-off curves got closer to the one of the 4D Patlak reconstruction, with lower bias values on both metrics but higher RMS CoV compared to the 4D Patlak reconstruction.

6.3.3 Comparing between nested optimizations in 4D reconstruction

Results of 4D Spectral and 4D Patlak reconstructions using MLEM and NNLS nested optimization are shown in figure 6.7. A clear difference in behaviour is seen going from MLEM to NNLS from early iterations, with 4D reconstructions using nested NNLS optimization resulting in higher CoV values at matched bias compared to the respective 4D reconstruction using nested MLEM (with 20 nested sub-iterations). At the same time, NNLS nested optimization often resulted to a slight reduction in bias at matched CoV values. No difference was seen in convergence properties such as convergence speed between the two nested optimization options. Nevertheless the use of a single run of NNLS optimization in each nested loop, instead of 20 nested MLEM iterations, resulted in notable reduction of overall reconstruction times. The average reconstruction times using the two methods on a computer using a 16-core 2.20GHz processor and 96GB of RAM memory are shown in table 6.4.

6.3.4 Comparison between DWB protocols

Comparison of 4D Patlak and 4D Spectral reconstructions between the three simulated DWB protocols is made in figure 6.8. For both VOI regions and 4D reconstructions, data from all three DWB protocols resulted

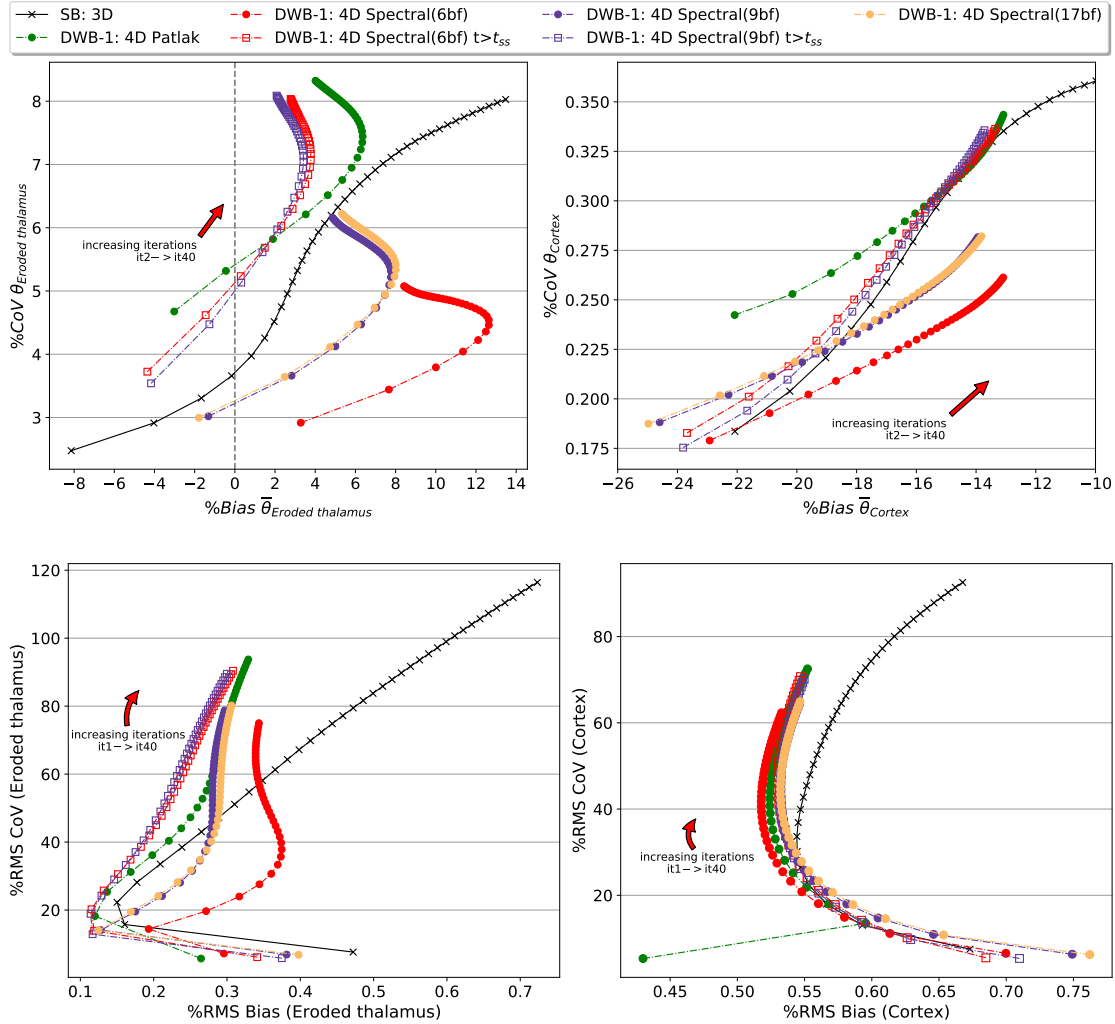


Figure 6.6: Simulation: Eroded thalamus (left) and Cortex (right) noise versus bias trade-off curves for 4D reconstructions of DWB-1 protocol data. VOI based metrics (top row) and voxel-based metrics (bottom row).

Table 6.4: Average reconstruction times for 1 full iteration (28 subsets) over DWB-1 data using CASToR.

Reconstruction	nested MLEM (min)	nested NNLS (min)
4D Patlak	9.6	6.7
4D Spectral(6bf)	14.0	8.2
4D Spectral(9bf)	15.8	8.3
4D Spectral(17bf)	26.6	11.2

in close bias values at matched iteration number, with a slight deviation in RMS bias towards late iterations. Differences in CoV at matched bias values are more profound in VOI metrics of the cortex region, where data from protocol DWB-2 resulted in the lowest CoV values and DWB-1 and DWB-3 data resulted to closer CoV values. This level of reduction in CoV was not seen on the eroded thalamus, neither on VOI or voxel based metrics. In the eroded thalamus the differences of DWB protocols on CoV at matched bias were smaller and their ordering was mixed between the two 4D reconstructions.

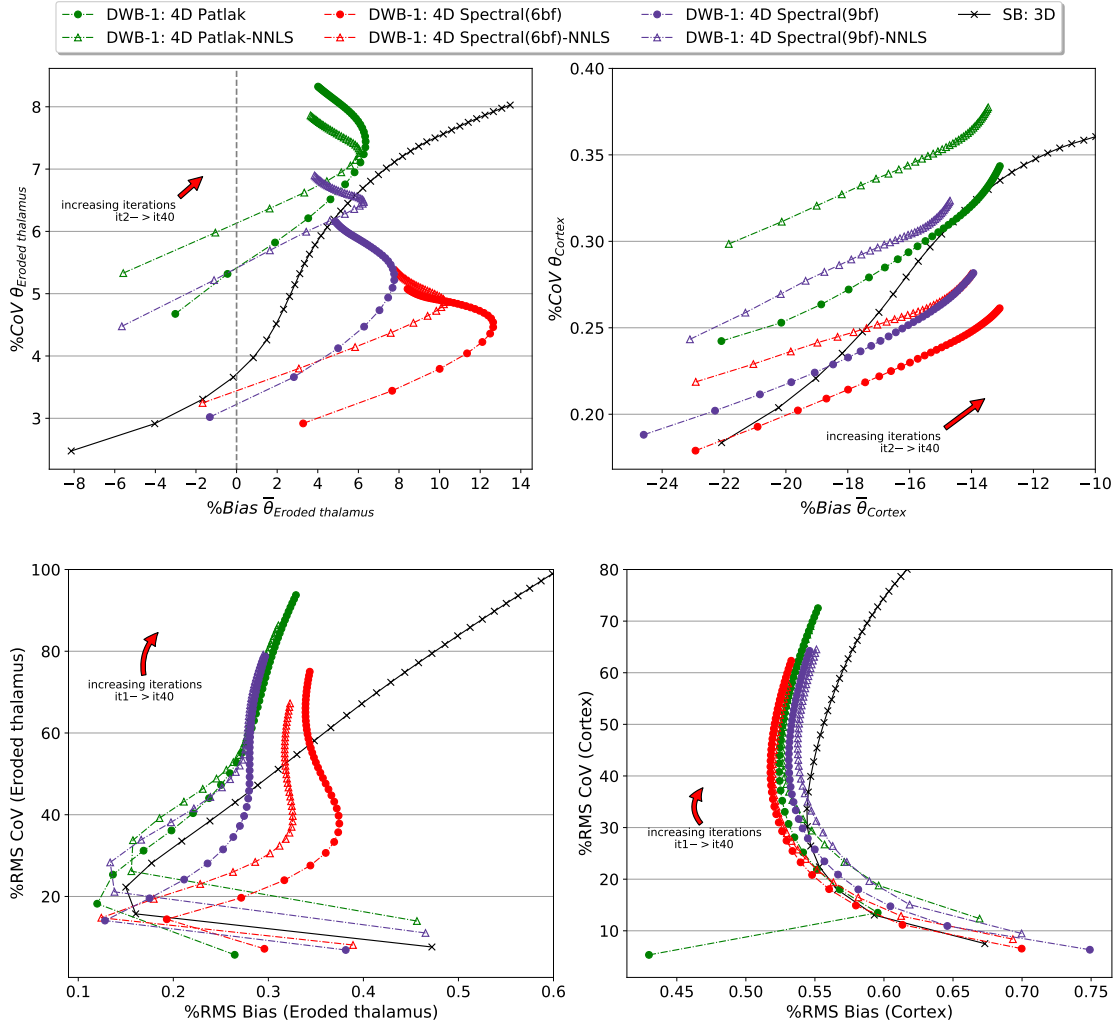


Figure 6.7: Simulation: Eroded thalamus (left) and Cortex (right) noise versus bias trade-off curves for 4D reconstructions, with MLEM and NNLS nested optimization. VOI based metrics (top row) and voxel-based metrics (bottom row).

6.3.5 Comparison with real data

The comparison of reconstructions using a real FDG dataset, reprocessed and reconstructed with the SB and DWB-1 protocol framings, is made in figure 6.9 for non-TOF reconstructions and in figure 6.10 for reconstructions using TOF.

A clear difference in convergence behaviour can be seen by comparing the evolution of CNR curves between the real data non-TOF and TOF reconstructions. For non-TOF reconstructions, a maximum CNR is attained after two to three full iterations, while for TOF reconstructions maximum CNR is seen from the very first iteration (indicating that maximum is attained within the first 28 subsets of the OSEM algorithm). Results in both cases showed similar evolution of CNR with increasing iterations for 4D and 3D reconstructions, in non-TOF and TOF reconstructions respectively. The 4D Spectral reconstruction using 6 basis functions

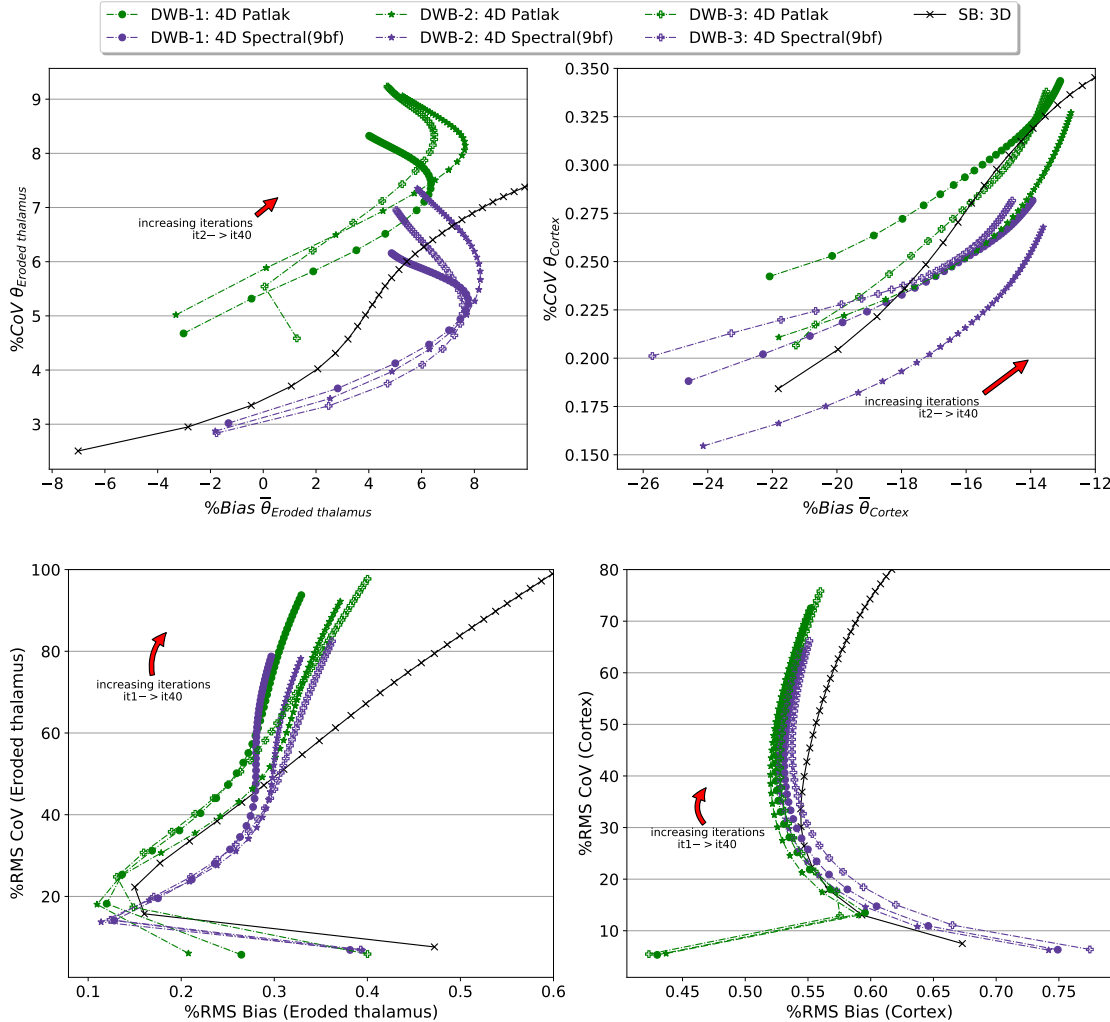


Figure 6.8: Simulation: Eroded thalamus (left) and Cortex (right) noise versus bias trade-off curves for 4D reconstructions of the simulated DWB protocol data. VOI based metrics (top row) and voxel-based metrics (bottom row).

provided the highest CNR values throughout all iterations, followed by the 4D Spectral reconstruction using 9 basis functions and 4D Patlak. Overall, CNR of all 4D reconstructions of DWB data was higher than that of 3D reconstruction of SB data and 3D reconstruction of DWB data.

The liver SD vs tumour mean trade-off curves showed close behaviour between 4D reconstructions using TOF, resulting to SD values in the first 15 to 17 iterations of 4D reconstructions which were lower compared to 3D reconstruction of DWB data at matched tumour mean values. Compared to 3D reconstruction of SB data, all 4D reconstructions of DWB data resulted in higher SD values (for matched tumour mean values where comparison is possible). For 4D reconstructions of DWB data without TOF information, SD values were lower to 3D reconstruction of DWB data for the first 16 to 25 iterations, while higher than 3D reconstructions of SB data at matched mean tumour values. Furthermore, the liver SD vs tumour mean trade-off curves of

4D reconstructions using TOF information showed very small differences in their evolution with increasing iterations. By contrast, the non-TOF 4D reconstructions showed a degree of separation of the 4D Patlak reconstruction from Spectral reconstructions.

Mean tumour K_i values were lower in reconstructions without TOF compared to all reconstructions using TOF at respective 3D and 4D reconstructions. The difference was also seen in VOI TAC measurements of the tumour between non-TOF and TOF 3D reconstructions and could potentially be attributed to differences in contrast recovery within the reconstruction by use of TOF information and its effects in reduction of motion induced blurring.

Parametric K_i images from 3D and 4D reconstructions with TOF at iterations with matched liver SD values of approximately $4 \cdot 10^{-3} \text{ min}^{-1}$ are shown in figure 6.11.

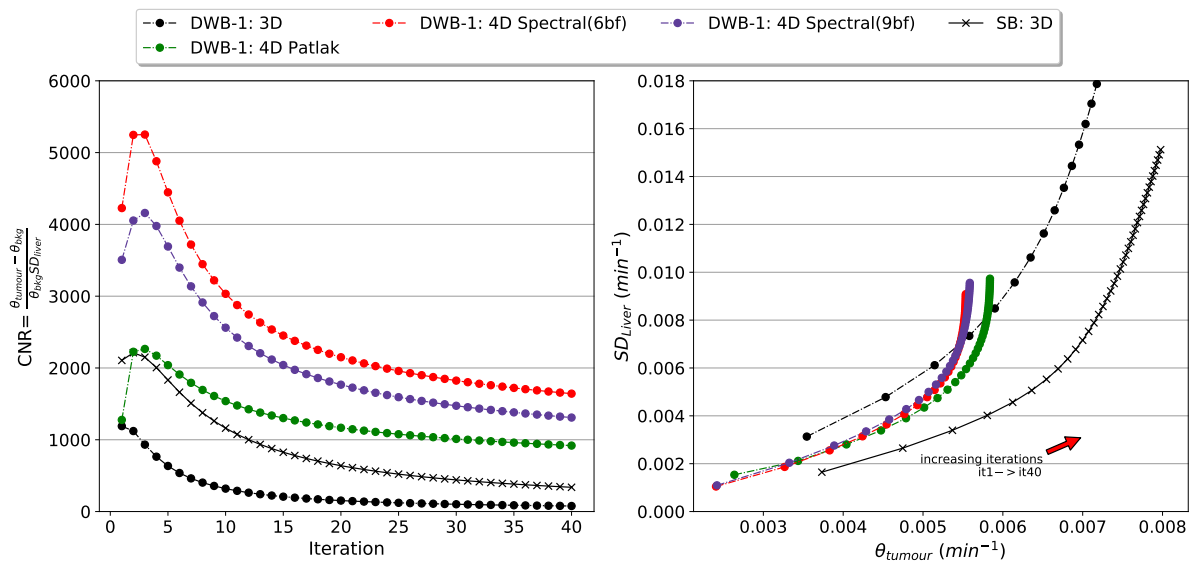


Figure 6.9: Real Data: Contrast to Noise ratio (left) and liver SD vs. VOI mean of the tumour (right) for 3D and 4D reconstructions without TOF information.

For comparison against the simulation study, metrics of CNR and SD vs VOI average trade-off curves from a randomly chosen noise replicate of simulation DWB-1 are shown in figure 6.12. Similarly to the real data, with or without TOF information, values of CNR are highest for 4D Spectral reconstruction using 6 basis functions followed by 4D Spectral reconstruction using 9 basis functions. For the simulation data and real data without TOF, 4D Patlak reconstruction provided lower CNR values compared to 4D Spectral reconstruction using 9 basis functions and closer to the values of 3D reconstruction from SB data at initial iterations. By contrast, real data using TOF resulted in similar CNR values between all 4D reconstructions. The evolution of CNR with increasing iterations was similar between non-TOF real data and simulated data. Finally, the simulation data SD vs VOI average trade-off curves of the eroded thalamus showed greater separation of 4D reconstructions, with 4D Spectral reconstructions providing lower SD values compared to

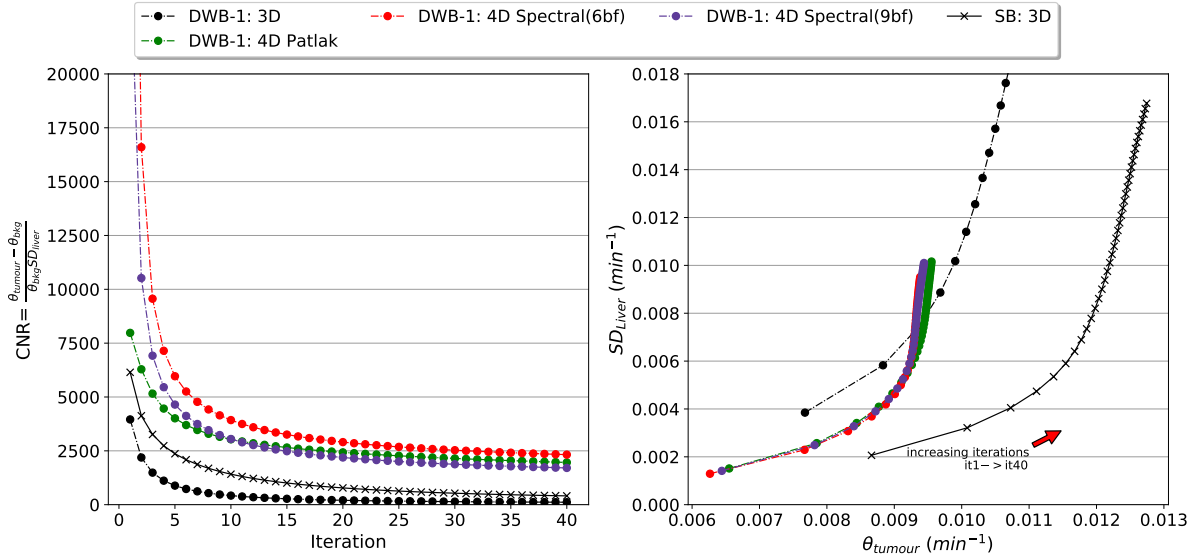


Figure 6.10: Real Data: Contrast to Noise ratio (left) and liver SD vs. VOI mean of the tumour (right) for 3D and 4D reconstructions using TOF information.

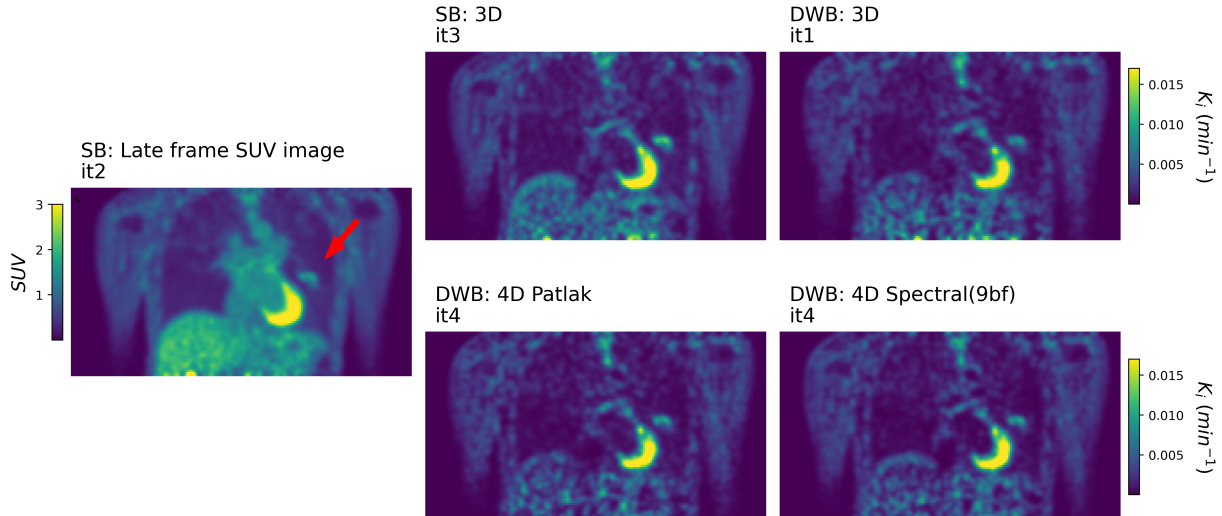


Figure 6.11: Real Data: Parametric K_i images (with 5mm Gaussian Filtering) from SB and DWB replay datasets from 3D and 4D reconstructions, using TOF information, at matched SD values over the liver.

3D and 4D Patlak reconstruction of DWB data, but at higher bias values as shown previously in the analysis of simulation results. Parametric K_i images of 3D and 4D reconstructions at matched RMS CoV values, of approximately 32% as measured at the eroded thalamus VOI, are shown in figure 6.13 for a single noise replicate along with images of mean bias over noise replicates. The single replicate images show that structures of the thalamus seen in 3D reconstruction of SB data are better resolved in DWB when using the 4D Spectral reconstruction. The images of bias show similar behaviour in the thalamus over reconstructions and illustrate the partial volume effects at the cortex region.

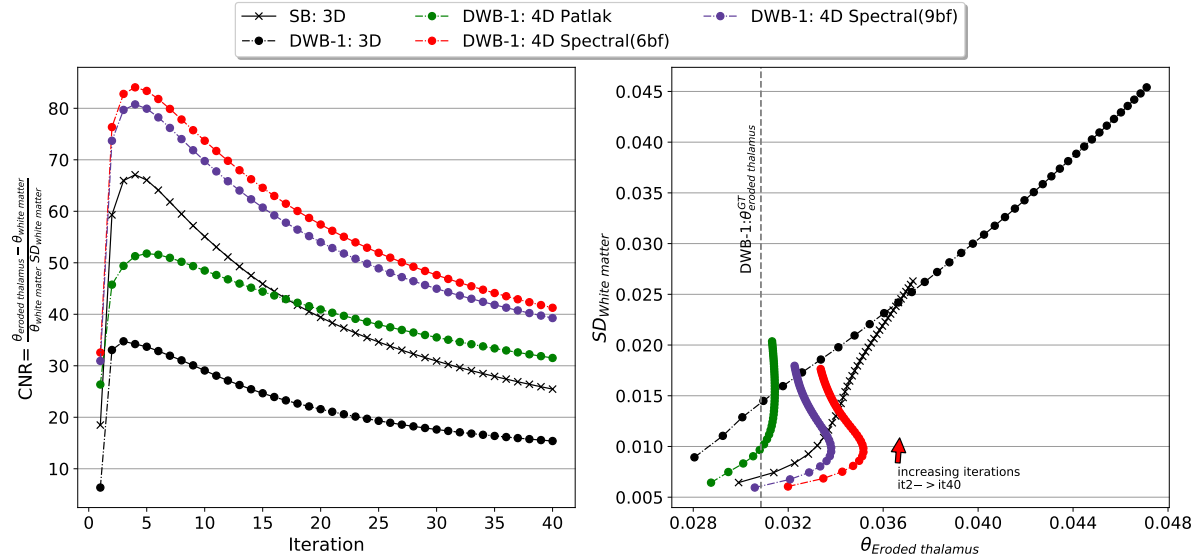


Figure 6.12: Simulation single noise realisation of DWB-1 data: Contrast to Noise ratio (left) and white matter SD vs. eroded thalamus K_i mean for 3D and 4D reconstructions.

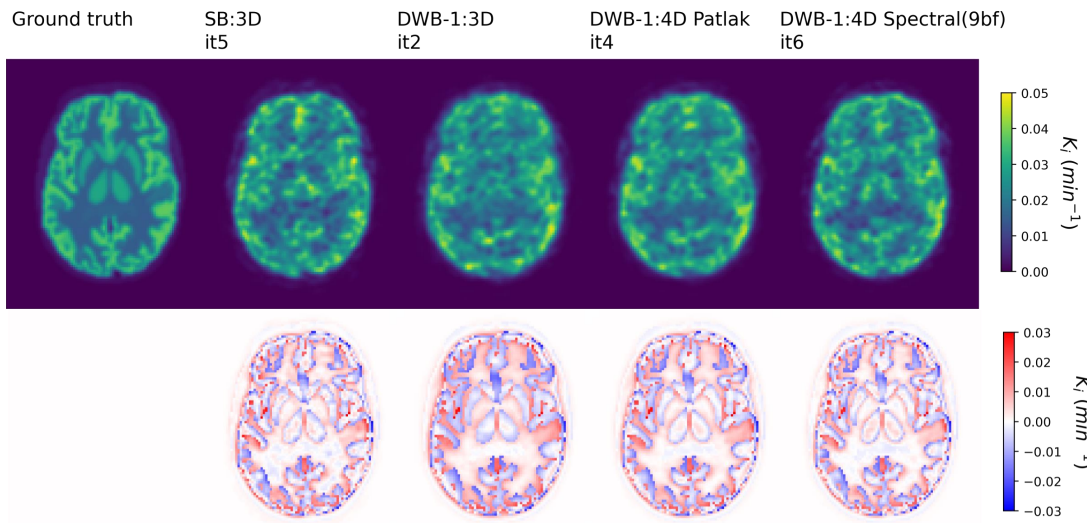


Figure 6.13: Single slice through parametric K_i images of one noise replicate (with 3mm Gaussian Filtering) (top) and their corresponding Bias images (over noise replicates) (bottom) from SB and DWB data 3D and 4D reconstructions at matched RMS CoV in the eroded thalamus.

6.3.6 Parametric K_1^* imaging from 4D Spectral reconstruction

The VOI and voxel based metrics for parametric K_1^* images from the SB, DWB-1 and DWB-4 protocols are shown in figure 6.14 and figure 6.15. For the results from DWB-1 the missing fast dynamic data in the early minutes of the acquisition results in extremely higher bias and noise than the other protocols, on both VOI and voxel based metrics. By contrast, the results from the DWB-4 protocol, which makes use of the early dynamic single bed acquisition along with the DWB acquisition, resulted in VOI and RMS mean similar to that of the SB protocol. For both protocols, results show overestimation of mean VOI measurements

in the eroded thalamus VOI and underestimation in the cortex VOI. It is important to note here that the ignored blood fraction correction in parametric K_1^* images contributes towards an approximate 3% negative bias in quantification if we consider the simulated blood fraction of 0.03 in the thalamus and cortex regions. Measurements of RMS CoV show that data from the DWB-4 protocol result in higher noise compared to SB protocol. Parametric K_1^* images of the evaluated acquisition protocols at matched RMS CoV values, of approximately 40% as measured at the eroded thalamus VOI, are shown in figure 6.16 for a single noise replicate along with images of mean bias over noise replicates. The images from the single replicates of SB and DWB-4 protocol data show similar structures and contrast of these structures, in comparison to the contrast of the ground truth values. The DWB-1 data show the erroneous overestimation of the values and loss of contrast between structures. This is also seen in the bias images for the DWB-1 data, while the bias structures in DWB-4 and SB data are very similar and closer to zero bias. The images of bias illustrate the effect of partial volume effects, similar to the effects shown for K_i imaging.

6.4 Discussion

Our simulation study shows that the dynamic reconstruction of DWB FDG data resulted in substantial reduction of Patlak K_i image noise and more favourable convergence behaviour, compared to 3D reconstruction based parametric imaging. These results, limited to a single level of noise, are in agreement with the findings of Karakatsanis *et al.* [55]. Moreover, we directly compared against a SB dynamic protocol, processed with 3D reconstruction, and showed that comparable values of parametric image noise and bias can be achieved with DWB protocols by the use of a dynamic reconstruction. The choice of the iteration number to terminate a 4D reconstruction algorithm is not evident. For a VOI-based analysis, the convergence of the mean K_i value in the cortex or in the eroded thalamus was not seen in the range of the 40 evaluated OSEM iterations, in particular for a 3D reconstruction. This behaviour was also observed for a 4D reconstruction algorithm, but to a lesser extend. A high number of iterations of 4D reconstruction algorithms provided more stable VOI mean values, but at risk of resulting to higher parametric image noise than that of a 3D reconstructions on the same DWB data. The results obtained with the real data-set showed similar behaviour with mean VOI values continuing to slightly increase even after 40 OSEM iterations and with 4D reconstruction parametric image noise surpassing that of 3D reconstruction at late iterations. This example illustrates that the relative aspects of 4D to 3D comparisons with simulated data for the tested DWB and SB protocols have the capacity to translate to studies with different levels of noise. Overall, the risks of excessive parametric image noise and under-converged K_i values will be lesser for 4D based reconstruction methods than for a 3D reconstruction, which demonstrated considerably more instability with increasing iterations. To ensure convergence of the K_i values while suppressing the increase of parametric image noise, further regularisa-

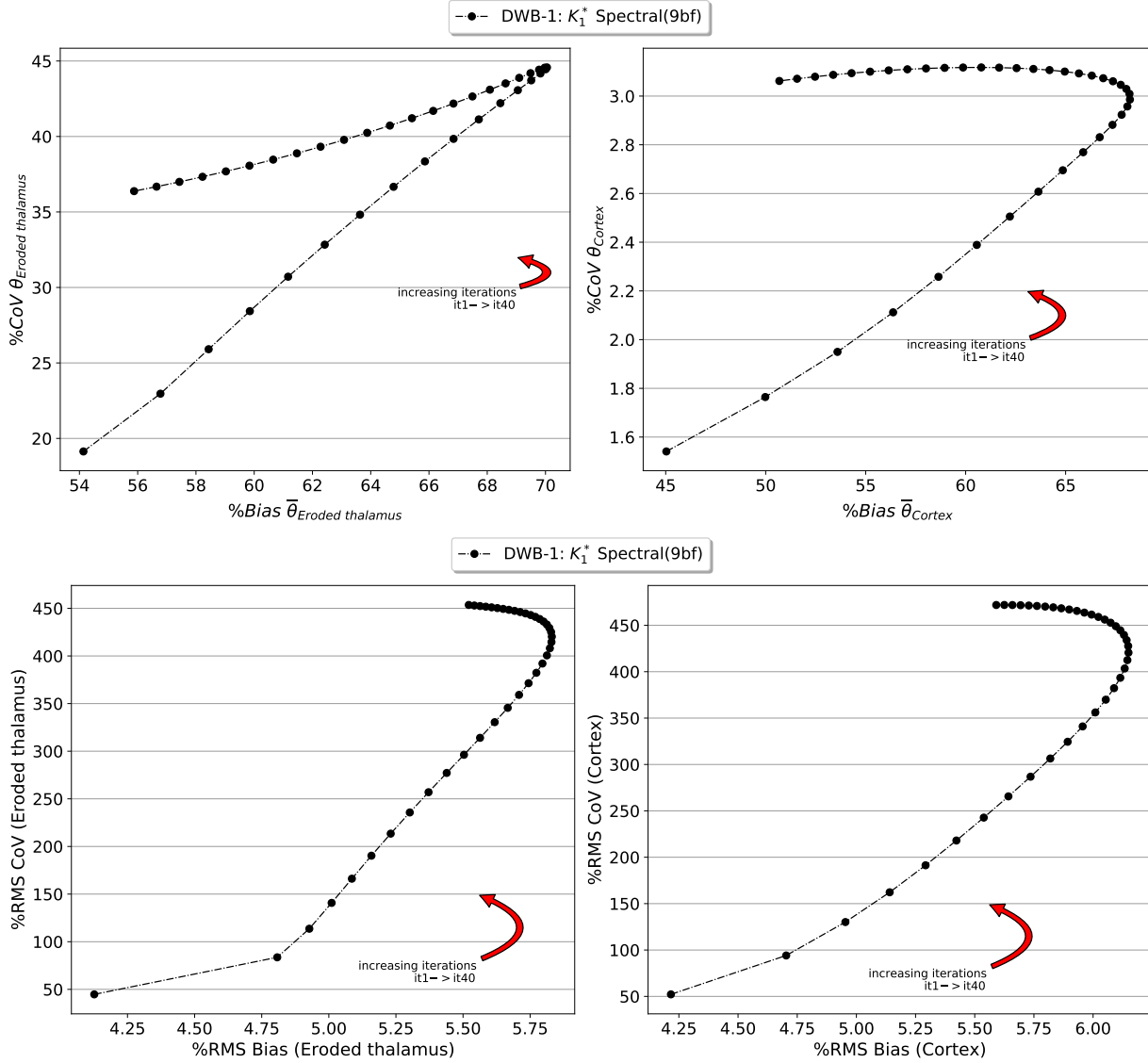


Figure 6.14: Simulation: Eroded thalamus (left) and Cortex (right) noise versus bias trade-off curves for K_1 parametric imaging from 4D spectral reconstructions of the simulated DWB-1 protocol data. VOI based metrics (top row) and voxel-based metrics (bottom row).

tion techniques can be used with methods such as 4D MAP reconstruction [10, 108] or kernel 4D dynamic reconstruction [112, 118].

Our nested optimization tests using NNLS instead of multiple MLEM sub-iterations did not provide any differences in the acceleration of the convergence and showed comparable behaviour to a previous study on the use of NNLS with the spectral model [98]. NNLS did provide computing acceleration by a factor of around two for our data sets, but resulted in an increase of the parametric image noise compared to MLEM sub-iterations for similar bias characteristics. Equivalent or higher acceleration could be potentially achieved if the nested MLEM optimization was conducted in graphical processing units (GPU) instead of the CPUs.

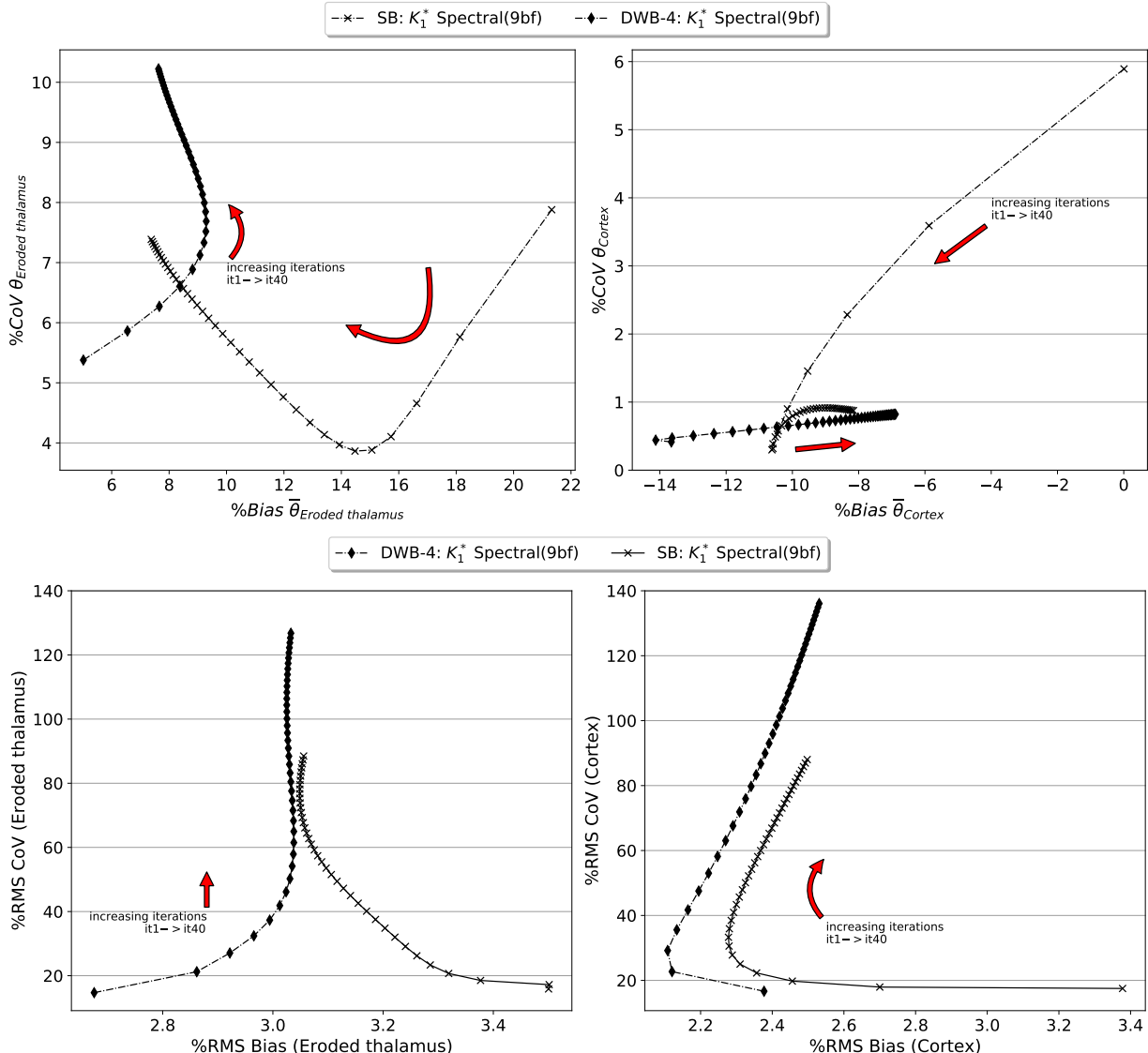


Figure 6.15: Simulation: Eroded thalamus (left) and Cortex (right) noise versus bias trade-off curves for K_1 parametric imaging from 4D spectral reconstructions of the simulated SB and DWB-4 protocol data. VOI based metrics (top row) and voxel-based metrics (bottom row).

In this work, we evaluated the use of an indirect dynamic reconstruction method based on a generic 4D Spectral reconstruction algorithm followed by a post-reconstruction Patlak model fitting. The genericity of the spectral model allows for flexibility in modelling dynamic processes that do not necessarily fall under the idealised behaviour of the kinetic model of interest. In this simulation study, we were limited to irreversible FDG kinetics that can be sufficiently described by the Patlak model. In this case, 4D Spectral reconstruction making use of the full dynamic data outperformed the direct Patlak reconstruction in terms of parametric image noise, while maintaining similar bias behaviour. The benefit of the 4D spectral reconstruction was less obvious when fewer frames were used in reconstructions using $t > t_{ss}$, indicating that its favourable behaviour was mostly due to the use of more temporal frames than the Patlak reconstruction. In real FDG

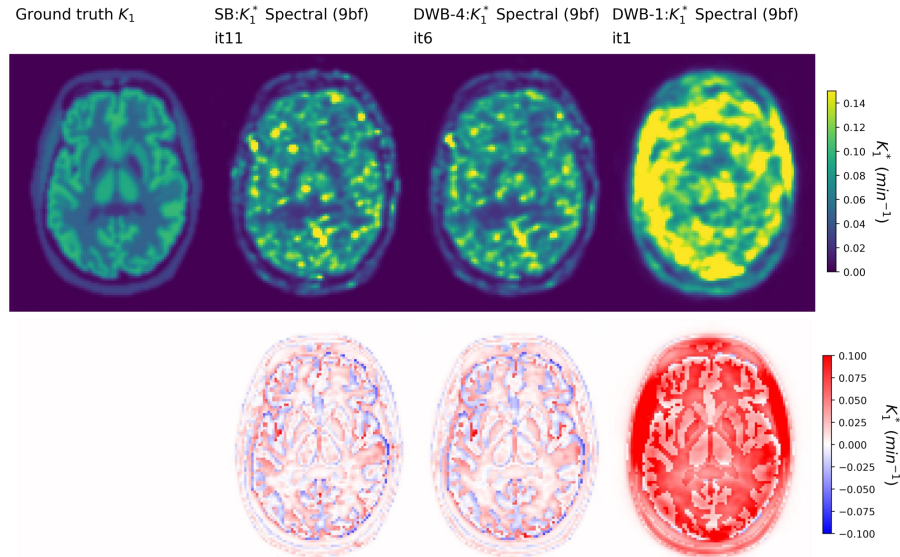


Figure 6.16: Single slice through parametric K_1^* images of one noise replicate (with 3mm Gaussian Filtering) (top) and their corresponding Bias images (over noise replicates) (bottom) from SB and DWB data, for 4D Spectral reconstructions at matched RMS CoV in the eroded thalamus.

studies, it can be desirable to account for reversible FDG kinetics and reduce the bias of the estimated macro-parameters arising from poorly modelled kinetics. The spectral model can allow for more complex compartmental modelling with no strong prior knowledge or enforcement of a specific model. As such it can account for more complex kinetic behaviours, including reversibility of tracer, in the reconstruction process and allow for post-reconstruction exploratory modelling to identify the best model to describe and present the data. Moreover for DWB studies where not all body regions and organs will necessarily be adequately described by a single dynamic model of interest, the proposed indirect method can allow for the assignment of different kinetic models in different regions of the body to ensure appropriate representation of the dynamic tracer behaviour. Depending on the availability of early frame data, the fitted spectral model can be used to directly estimate K_1 [98, 119], while post-reconstruction micro-parameter estimation could be performed for potential uses in clinical applications [112, 120] and indirectly take advantage of the 4D reconstruction temporal regularisation. An important parameter to configure for the spectral model is the number of basis function. Contrary to post-reconstruction spectral analysis where hundreds of basis functions are used to finely sample the space of kinetic exchange rates, a smaller number of basis is desirable in reconstruction to favour reduced image noise. In some cases of our findings the lowest number of basis functions used (6 basis) resulted in higher bias values which indicates less than adequate modelling of the underlying kinetics, compared to reconstructions with more basis functions and to 4D Patlak reconstruction. However this was not the case when fewer frames were used in reconstructions using $t > t_{ss}$ data. These findings indicate that the selection of number of basis functions is important not only for controlling the produced image noise

but also for controlling bias by adequately modelling the kinetics behaviour in reconstruction. For the higher numbers of basis functions, with 9 and 17, almost identical behaviour was seen on the DWB-1 dataset (of 8 frames). Overall on the choice of number of basis functions, results indicate a greater risk in image bias when using a too small number of basis functions, and a lesser risk in image noise when using more basis functions than strictly needed to properly model the underlying kinetics. In any case the number of basis needs to be tuned for every DWB protocol, depending on the number of frames within the dataset and the range of underlying kinetics as well as the level of noise in the PET data.

In this study, the investigation between S&S and CBM DWB protocols was limited to aspects of sampling frequency and uniformity within the total examination time. Our results showed small differences in parametric image bias but noticeable reduction in parametric image noise when utilising CBM acquisition with uniform sampling. Overall differences were inline with previous findings of comparison S&S and CBM on a real data study using different metrics [121]. A limitation in our study is that we have considered a single axial location and hence we cannot generalise the results of the simulation study for the performance of the assumed DWB protocols over their effective FOV. Furthermore beyond the aspects of reduced acquisition delays and higher sampling frequency, CBM acquisition has other desirable properties for DWB acquisitions as outlined previously [121]. The most important aspect is the result uniform axial sensitivity profile at any choice of acquisition speed. That can be of importance in DWB parametric imaging where multiple regions of interest are expected in the effective FOV. In our study we have not considered this aspect for the CBM protocols and we did not examine regions in the overlap range of the S&S protocol. But the observed improvements related to reduced delays in acquisition coupled with uniformity of axial sensitivity favour the choice of CBM over S&S protocols. We investigated further potential reductions in system delays by allowing for non-uniform axial sampling using bi-directional CBM. In that case we did not see the same effects as in the transition from S&S to CBM. But our results on bi-directional CBM are limited to the specific framing of the evaluated protocol design which offered more total frames but resulted in less total counts compared to the other protocols. Additional tests are required on the exploitation of the flexibility offered by bi-directional CBM to assess other potential benefits against uni-directional CBM.

Finally an additional evaluation was made for parametric K_1 imaging, by use of the spectral model and the spectral coefficient images, to explore additional potential benefits from the use of 4D Spectral reconstruction in parametric imaging. The tests showed, as expected from previous single bed dynamic studies [119], that the first few minutes of the acquisition are crucial for the estimation of K_1 . Estimates of K_1 were extremely biased and noisy for estimates that did not make use of dynamic data from the first 3 minutes, as shown with K_1 imaging from DWB-1 protocol data. The DWB-4 protocol that made use of the first 3 minute acquisition provided results that were very similar to those of the single bed protocol data with no gaps. These results

are promising for the estimation of K_1 parametric images from DWB protocols that include an initial dynamic single bed phase. These estimations will be limited thought to the areas covered by this initial acquisition. A considerable limitation in our tests for K_1 parametric imaging using 4D Spectral reconstructions is that quantification accuracy was compromised by not considering the blood volume fraction in K_1^* estimation. Similarly to other works in the literature [66], this was done to avoid excessive parametric image noise by the division operation that is required by equation 2.20 to correct K_1^* for blood volume fraction. Alternatively to completely neglecting the blood volume fraction correction, a constant value could be assumed for certain regions of the image or smoothing and other denoising operations could be performed on the 4D spectral reconstruction estimated blood fraction image ϕ_M before being applied to the K_1^* image via division.

Finally, an open question remaining unanswered is whether a DWB protocol (limited by the scanner's hardware imposed acquisition delays) could be optimised in a way that it could provide sufficient dynamic information on early kinetics for the reliable estimation of K_1 maps over the whole-body. As already mentioned, K_1 information can be complementary to K_i and thus of interest to be estimated over the whole body. Furthermore, in pharmacological applications, such as the one presented in chapter 7, estimation of K_1 over the whole body could be of great interest.

6.5 Conclusion

Dynamic reconstruction capabilities were successfully developed and validated in CASToR, for multiple dynamic models and optimization algorithms. Along with dynamic developments for a PET analytical simulator, those tools have enabled an extensive evaluation of dynamic reconstruction methods for application in DWB imaging. The developed tools were used for the application of dynamic reconstruction on real data and were further evaluated and expanded for use with real DWB data, in the work that is described in the following chapter.

The study presented here focused on a single bed location, even though the simulation considered multi-bed acquisition protocols. In the following chapter, the use of the developed reconstructions will be extended to multi-bed dynamic reconstruction using a direct dynamic approach for all bed positions, which will be applied on real DWB data. The assumed approach in the study presented here was the reconstruction of each bed individually, which necessitate the DSB phase of the acquisition to be aligned with one of the bed locations of the DWB phase, in order to take advantage of the fast kinetic information within the dynamic reconstruction. As we will present in the following chapter, the developments on multi-bed dynamic reconstruction on CASToR lift this limitation.

In this study we have shown that 4D dynamic reconstruction is necessary in DWB parametric imaging to

achieve accurate and stable quantification. For FDG Patlak K_i parametric imaging we have shown results of direct Patlak dynamic reconstruction with noise and bias values that were comparable to 3D reconstruction based parametric imaging from single bed dynamic studies. In this work we proposed the use of an indirect method for DWB parametric imaging, based on the spectral analysis model. This more flexible approach allows for complex kinetic modelling to be used during reconstruction for temporal regularisation, with minimal assumptions on the underlying kinetics. In Patlak K_i parametric imaging this method outperformed the direct Patlak approach, by making use of all the acquired data for temporal regularisation from which post-reconstruction parametric imaging benefitted by further reduction of noise compared to the Patlak approach. Furthermore, the spectral model approach can be used for more complex post-reconstruction modelling, for example in parametric imaging of FDG micro-parameters. In our evaluation we showed that in addition to post-reconstruction fitting, dynamic reconstruction with the spectral model can be used for estimation of K_1 parametric images when early dynamic information are available.

Finally, we investigated the impact of various acquisition modes (for CBM and S&S) resulting in different temporal sampling of the data. Benefits of reduced delays and increased acquisition statistics were partially seen in reduced parametric image noise for the CBM protocol with uni-directional axial sampling. By contrast CBM using bi-directional motion resulted to parametric image noise levels that were similar to the S&S protocol. Further investigation is required to assess the potential benefits from bi-directional CBM against uni-directional CBM and effects of non-uniform sampling over the entire FOV of the DWB protocols.

Overall, use of 4D dynamic reconstruction for DWB parametric imaging offers desirable properties that enables the transition from single bed dynamic studies and common 3D reconstruction parametric imaging practices without loss of image quality and with additional benefits for accuracy of parametric images. Potential applications of DWB parametric imaging are expected to rely on quantification of images and so there should be no compromise between parametric image accuracy and image noise. Our results showed that 4D reconstruction need to be sufficiently iterated to ensure accurate quantification, with potential for improvement in maintaining low parametric image noise by use of additional regularisation methods.

Chapter 7

Extension of Dynamic Reconstruction to Multi-Bed Reconstruction and Applications in a Whole-Body Pharmacological Study

7.1 Introduction

Acquisition of DWB datasets in S&S mode with overlapping bed positions result in complex datasets of PET raw data, in relation to timing and positional information. Moreover, the addition of an initial DSB acquisition, conducted for IDIF derivation purposes or for the sampling of fast kinetics to allow for more complex kinetic modelling [120], increases the complexity of the PET raw dataset.

Suggested practices [7] and state of the art implementations [16] of DWB protocols regard the two datasets (DSB and DWB) as independent and suggest performing independent reconstructions on each dataset. Post-reconstruction kinetic model fitting is then used to combine the TAC information over both datasets. Furthermore, the DWB dataset contains locations at the overlapping bed regions which are sampled twice as much as central bed regions, as a result of the overlap sampling necessary to increase sensitivity at the bed position edges. The overlap timing information combines the timing of the adjacent bed positions. In post-reconstruction kinetic modelling, which is applied independently on each voxel TAC, suggested practices make use of modified timing information (average of two bed position timings) for voxels that fall at

overlapping regions [7] which result in a degree of degradation of the timing information. Another suggestion is to make use of independent dynamic reconstruction of each bed position from the DWB dataset, as it was conducted in the previous chapter, and apply post-reconstruction overlapping of parametric images [55]. In this case if the DSB data are to be included in the dynamic reconstruction, the placement of the DSB bed position needs to be identical to one of the bed positions of the multi-bed dynamic study.

It is important to note that DWB acquired in CBM mode, although free of the need of overlapping bed positions still require similar considerations to be taken into account for each axial location of the DWB acquisition [16, 121].

The flexibility offered by the CASToR reconstruction platform that allows for direct reconstruction of multi-bed data [50] can be expanded to direct multi-bed dynamic reconstruction of DWB data, using the exact timing information of the dataset and all bed positions within the same iterative loop. Furthermore, the offered flexibility can allow for the use of both DSB and DWB datasets within one unique reconstruction loop, with no constraints in the positioning of the DSB acquisition. In this chapter, we describe how this novel DWB protocol reconstruction concept was implemented in CASToR and present results from a dynamic reconstruction of real DWB data from the IsotoPK study, which were also presented in the EANM2020 conference [122].

7.2 Methods

7.2.1 Dynamic Whole Body Datasets

A diagram of axial position against time for an example three bed position DWB protocol is shown in figure 7.1, to demonstrate the differences in temporal sampling between central locations and locations at the bed overlapping regions. The bed locations in this example are identical to the setup used for the NHP study on the Signa PET/MR described in chapter 5. As it can be seen in the left diagram of figure 7.1 axial positions that fall outside of the overlap region result in framing that is equal to the framing of their respective bed positions. Positions over the overlap regions, seen at the right diagram of figure 7.1, result in framing equal to that of both adjacent bed positions, which gives twice the number of frames compared to locations outside the overlap. Locations at the overlap regions are not sampled continuously from both contributing bed positions due to the interruption by the movement of the bed and system delays. Finally, complexity is increased when the DSB data are included, as shown in figure 7.2, with that information contributing to different locations of the DWB acquisition that might fall in overlap regions or not depending on the protocol setup.

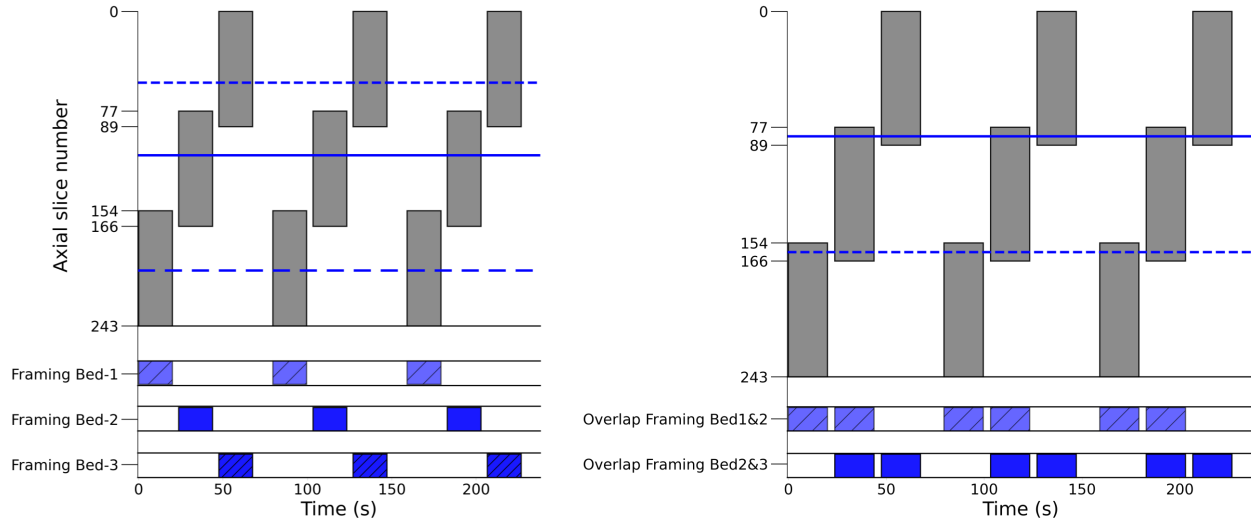


Figure 7.1: Axial slice number vs time for an example three bed positions DWB acquisition. Central axial slices (left) and slices at the overlapping regions (right) considered for the result framing.

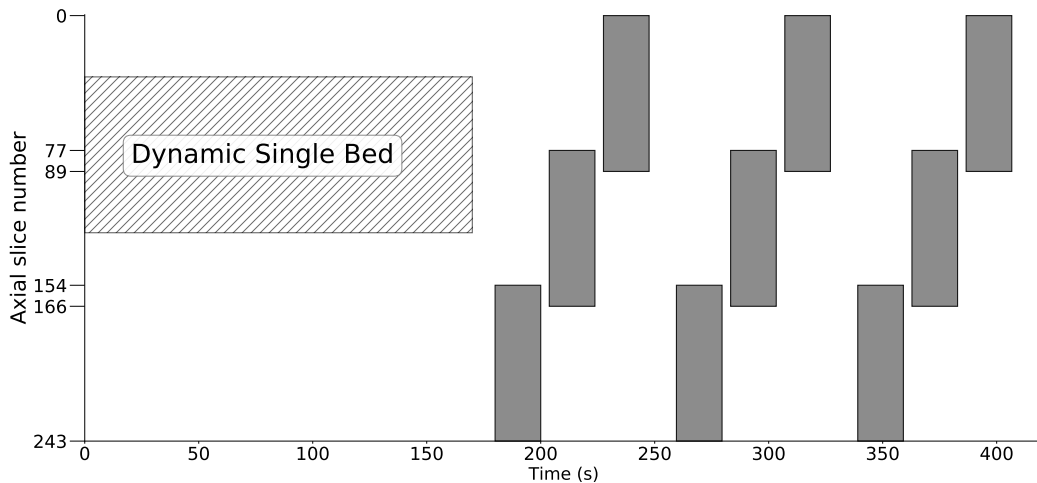


Figure 7.2: Axial slice number vs time for an example three bed positions DWB acquisition, including an initial DSB phase of 180 s.

If considering only the DWB dataset, and each individual S&S acquisition as an independent frame, the total number of frames in the DWB dataset will be defined by all the individual S&S steps. But not all frames need to be considered for all regions of the effective FOV. The choice of the appropriate framing for each location, whether within or outside the overlap, can be made using a mask image that indicates which locations are sampled on each frame. This type of mask could be used for example with post-reconstruction parametric imaging, applied at each voxel to mark which frames need to be considered.

With CASToR the use of multi-bed data can be made directly within a single iterative loop, using the methodology described in section 4.4. The same framework can be extended to direct multi-bed dynamic reconstruction of DWB datasets, using the same iterative loop. For linear dynamic models, dynamic reconstruction

(without the use of nested optimization) can be applied directly next to the system matrix, as shown in equation 3.30, within a single iterative loop over all dynamic data y_{ti} .

For DWB data, incorporation of the bed offset information in the projection operation can naturally lead to direct multi-bed dynamic reconstruction, where the selection of the sampled time points for the location of a voxel j is conducted by the projection operation. In this case, the projection operation and consequently the system matrix elements will depend on the frame index number t . This can also be expressed as an extension of the direct multi-bed reconstruction, described by equation 4.2, to dynamic reconstruction where the axial offset of each bed position is incorporated in the time-dependent information of the system matrix. This provides

$$\theta_{pj}^{(k+1)} = \frac{\theta_{pj}^{(k)}}{\sum_{t=1}^{n_t} B_{tp} \sum_{i=1}^{n_i} P_{tij}} \sum_{t=1}^{n_t} B_{tp} \sum_{i=1}^{n_i} P_{tij} \frac{y_{ti}}{\sum_{d=1}^{n_j} P_{tid} \sum_{q=1}^{n_p} B_{tq} \theta_{qd}^{(k)} + b_{ti}}, \quad (7.1)$$

where the set of basis functions B is precomputed for all time frames of the DWB acquisition, but is effectively applied in each voxel j for the time frames t that result to non-zero contribution by the back-projection operation ($\sum_{i=1}^{n_i} P_{tij} \neq 0$). It is important to note that with this unique iterative loop there is no need for additional considerations after reconstruction of the overlapping operation and regions. The result parametric images θ have dimensions of the effective FOV, having accounted for the overlap spatial sensitivity and timing information within the reconstruction.

Use of the same framework to perform individual frame reconstructions of DWB data is also possible, by setting the matrix B to be the identity matrix of size equal to the number of total frames. An example from the use of this framework for frame reconstructions is shown in figure 7.3 for a group of three consecutive frames from the NHP study of chapter 5. The sensitivity images for the same frames, as estimated by the back-projection operation $\sum_{i=1}^{n_i} P_{tij}$, are shown in figure 7.4. The sensitivity images clearly show the sampled locations per frame and the overlapping locations for adjacent frames. Individual frame reconstruction of DWB data results directly to images that account for the bed offset in image space, which can subsequently be directly used for post-reconstruction kinetic model fitting without the need for positional considerations. Additionally, for post-reconstruction kinetic model fitting, the result sensitivity frame images can be used as a mask for the application of the dynamic model on each frame and voxel combination.

In addition to DWB data alone, the described methodology for direct multi-bed dynamic reconstruction allows for any sequence of the acquired bed/frames to be used within the iterative reconstruction loop. Furthermore, the use of the DSB dataset can also be included in the iterative loop, regardless of its axial position, while also being sub-divided into multiple short frames.

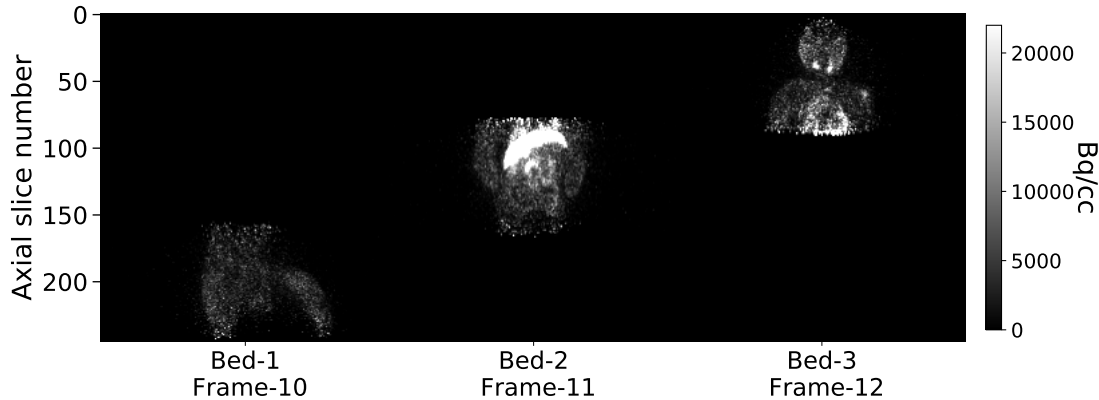


Figure 7.3: Example three frame images from a three bed DWB acquisition (NHP study of chapter 5)

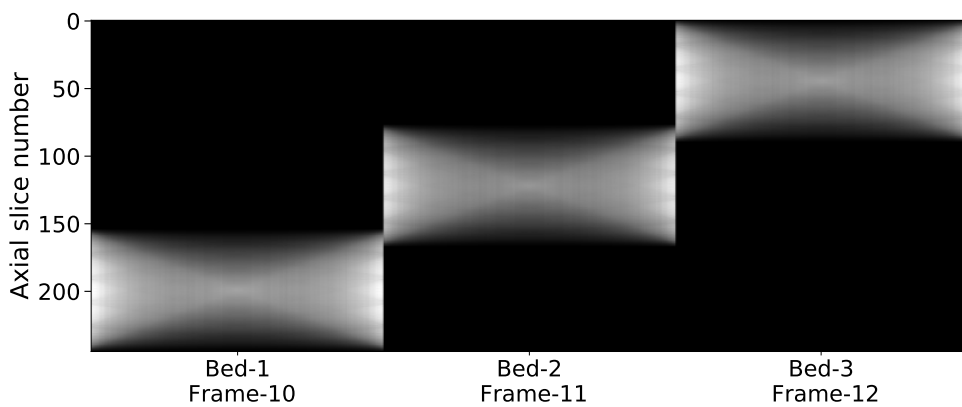


Figure 7.4: Example three frame sensitivity images from a three bed positions DWB acquisition.

7.2.2 Dynamic reconstruction: nested optimization for DWB datasets

As described previously, dynamic reconstruction is often performed using the nested optimization framework, to accelerate convergence [97, 98]. Some additional considerations need to be made before the use of this multi-bed dynamic reconstruction framework with nested optimization.

The nested optimization framework decouples the tomographic update process over the PET data from the dynamic model fitting process on image space. The two steps are conducted respectively with an MLEM update over the PET raw data using equation 3.27 to get an individual EM update image for each frame, followed by kinetic model fitting which optimises the likelihood function of equation 3.28.

For single bed dynamic data the sensitivity term of the likelihood function, $[\sum_{i=1}^{n_i} P_{ib}]$ of equation 3.28, can be ignored assuming that it is constant over time for each voxel b , and the likelihood function can be optimised using an image based EM update over image space with equation 3.33 [10, 97]. It is important to note that if dead-time corrections, necessary for accurate quantitative reconstruction, are included in the system matrix then the sensitivity term needs to be kept and accounted for in the nested optimisation.

But in most applications of nested optimisation on single-bed dynamic data in the literature this term is ignored.

In the case of DWB data and overlapping bed positions, the sensitivity term $[\sum_{i=1}^{n_i} P_{tij}]$ has to be maintained, as its value will change with different frames for voxels j in the overlapping regions. Thus the two step process, for direct multi-bed dynamic reconstruction with nested optimization, can be written as

$$\begin{cases} f_{tj}^{(\text{EM})}(\boldsymbol{\theta}^{(k)}) = \frac{f_{tj}(\boldsymbol{\theta}^{(k)})}{\sum_{i=1}^{n_i} P_{tij}} \sum_{i=1}^{n_i} P_{tij} \frac{y_{ti}}{\sum_{d=1}^{n_j} P_{tid} f_{td}(\boldsymbol{\theta}^{(k)}) + b_{ti}} \\ \boldsymbol{\theta}^{(k+1)} = \arg \max_{\boldsymbol{\theta}} \sum_{t=1}^{n_t} \sum_{j=1}^{n_j} [\sum_{i=1}^{n_i} P_{tij}] \left[-f_{tj}(\boldsymbol{\theta}) + \ln(f_{tj}(\boldsymbol{\theta})) f_{tj}^{(\text{EM})}(\boldsymbol{\theta}^{(k)}) \right]. \end{cases} \quad (7.2)$$

The tomographic update of this two-step optimization process is effectively an update over the DWB data for independent frame reconstruction, followed by an image space optimization process that now needs to consider the sensitivity $[\sum_{i=1}^{n_i} P_{tij}]$ of each time point t in the TAC of each voxel j . For linear models, where before an image based MLEM algorithm was used for this image space optimization process, a weighted MLEM update can be used with the sensitivity of each time point t as the weight. Alternatively, for linear and non-linear models, WLS based optimization algorithms can be used with the sensitivity value used as the weight. Both of these options were implemented in CASToR, with results shown in this chapter were produced by the use of the nested EM approach.

7.2.3 Real Data

Two DWB scans from the IsotoPK study were used for assessing the described direct multi-bed dynamic reconstruction method. Both scans were conducted on a single volunteer in a single day, without and with the use of the inhibitor (rifampicin) respectively. The two scans will be referred to as *CTRL* and *RIF* scans, standing for control and rifampicin. The two dynamic scans were conducted with the injection of 141.53 MBq and 90.77 MBq of $[^{11}\text{C}]$ Glyburide respectively. The first scan was conducted with 14 WB passes, with 9×20 , 5×30 s frames per bed position. The second scan included 15 WB passes, with 9×20 , 6×30 s frames per bed position. Both scans begin with a 180 s DSB acquisition centred over the liver, starting at the time of injection, before the DWB acquisition. By splitting the DSB into 18×10 s frames and considering each Step and Shoot acquisition as an individual frame, the two scans resulted in a total of 88 and 93 frames respectively. The planned bed positions are shown in figure 7.5 for the DSB and DWB phase of the *CTRL* scan.

The complete *CTRL* and *RIF* datasets, including the DSB and DWB data, were reconstructed within the

developed direct multi-bed dynamic reconstruction platform, using an OSEM algorithm with 28 subsets and EM nested optimization of 20 sub-iterations. Both datasets made use of TOF information within the reconstruction. As the IsotoPK study is an exploratory pharmacokinetic study, dynamic reconstructions were performed with the spectral model for temporal regularisation of frame activity estimates as well as for the direct estimation of K_1 parametric images, without imposing strong assumptions about the underlying kinetics. Additional dynamic reconstructions were performed for DWB data, without the use of the initial DSB data, to test extrapolation of the spectral model on early (non-sampled) frames. A total number of 17 spectral basis functions ($M = 16$) were used, with $\beta_1 \dots \beta_{M-1}$ logarithmically spaced within the range of 3 to 0.001 min^{-1} , while including β_0 and β_M to account for trapping and the blood fraction in the data. Similarly to the simulation study, the assumption of the total blood activity concentration C_B being proportional to the arterial blood plasma C_P was used in the estimation of the basis functions. Manual arterial blood samples were taken during both scans, to derive the input function and for blood analysis (to measure the metabolites fraction and for plasma binding of the tracer). The measured input functions were linearly interpolated and then used in the estimation of the spectral basis functions. Initial results on the study have shown very little metabolic activity of Glyburide, which did not require modelling, allowing for the assumption of constant ratio of arterial to total blood to be made.

Using the fitted spectral model, the approximate K_1^* parametric images were estimated similar to the methodology used in the simulation study of chapter 6. In addition to the dynamic reconstructions, individual frames (3D) reconstruction was performed using the same framework and OSEM algorithm with 28 subsets.

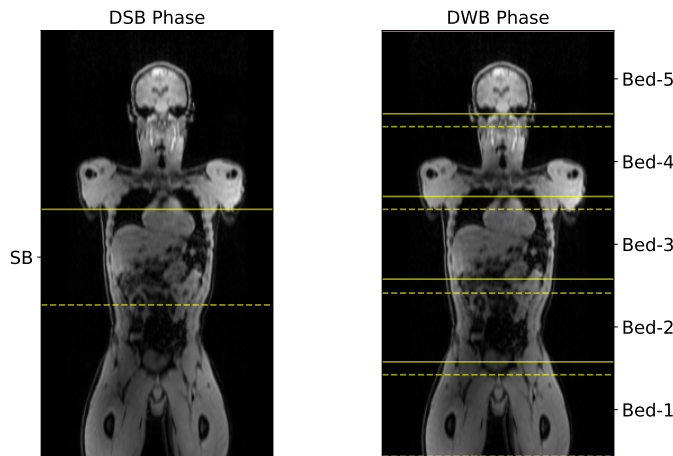


Figure 7.5: Planned DSB and DWB bed positions shown on coronal MRAC image, with bed start (—) and end (----) positions.

The VOIs listed in table 7.1 were drawn manually and used to validate and compare the reconstruction methods.

Table 7.1: VOIs used for evaluation of DWB scans.

VOI Name	Availability in Data
Brain	DWB
Myocardium	DSB & DWB
Left Ventricle (LV)	DSB & DWB
Left Kidney (Kidney _L)	DSB & DWB
Right Kidney (Kidney _R)	DSB & DWB
Spleen	DSB & DWB
Liver	DSB & DWB
Aorta	DSB & DWB
Bladder	DWB
Leg Muscle	DWB

Liver dual-input function simulation

For the liver which is one of the main organs of interest in the IsotoPK study, as discussed in section 2.6.1, the dual input function model is necessary for accurate modelling of tracer behaviour. When this is not accounted for, parametric estimates derived from single input function models are expected to be biased. A toy simulation was conducted to study how quantification of K_1^* is affected by the use of the spectral model with a single input function and to study whether relative differences of true underlying K_1 , such as those expected from the comparison of the *CTRL* to the *R/F* scan, can still be accurately deduced using the spectral model's estimated K_1^* . This short simulation study is presented in appendix C.

7.3 Results

7.3.1 Comparison between 3D and 4D spectral reconstruction on DWB data

Coronal MIP images of 3D reconstructions from the *CTRL* scan are shown in figure 7.6 and figure 7.7, for a late frame of the DSB acquisition and early frames of the DWB acquisition respectively. Similarly, MIP images of 4D spectral reconstruction of the *CTRL* scan are shown in figure 7.8 and figure 7.9 for the same respective frames. As the spectral model is applied to the image space of the entire effective FOV, the 4D reconstruction results in frame images that are estimated from the fitted model on the entire FOV. As such, activity estimates of locations that are not sampled for a given frame within the DWB scan are interpolated from the frame data of the entire DWB scan. For the frames of the DSB scan, locations that are not sampled by the single bed acquisition have activity estimates that are extrapolated from the fitted spectral model of later frames.

Plots of mean VOI activity against iteration, for early and late frames over the liver and the leg muscle VOI were used to evaluate at which iteration the mean values begin to converge. These plots are shown in fig-

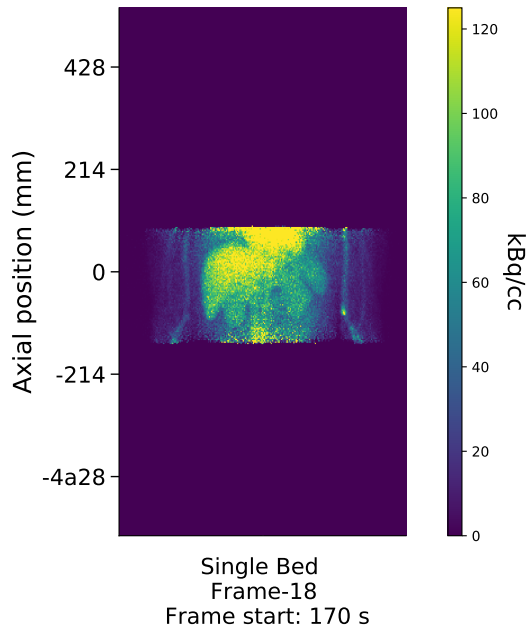


Figure 7.6: Coronal MIP image of 3D reconstruction (4it28sub) of a single frame from the DSB acquisition on the *CTRL* scan

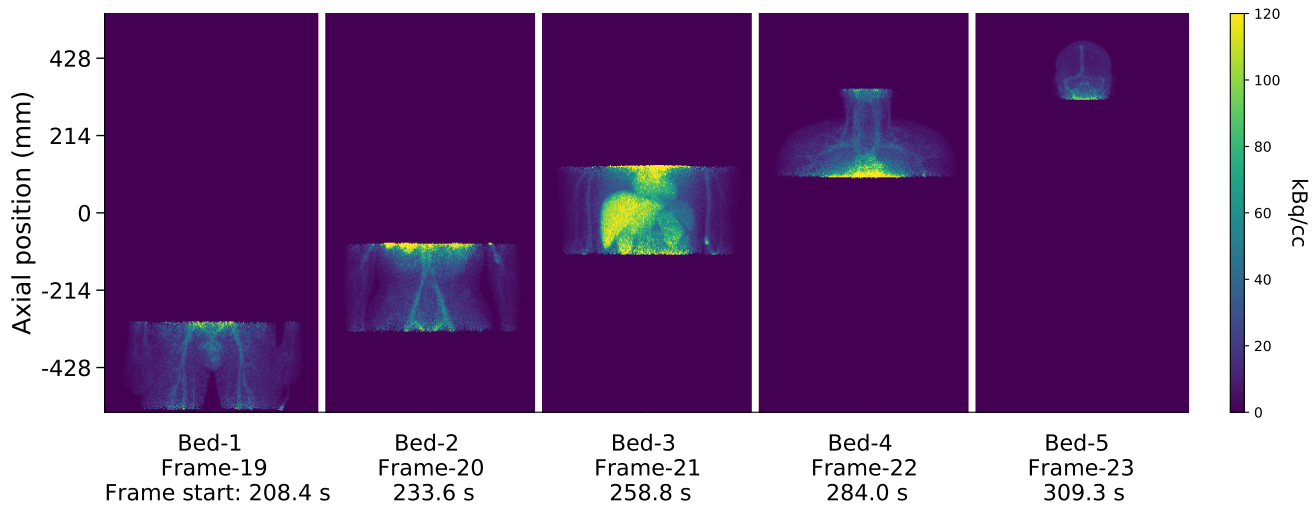


Figure 7.7: Coronal MIP images of 3D reconstructions (4it28sub) of a single frame per bed position from the first whole-body pass of the DWB acquisition on the *CTRL* scan.

ure ?? and figure ?? of the appendix C. For 4D spectral reconstruction, the evaluated mean values showed relatively stable behaviour from the 15th iteration onwards, which was chosen for subsequent comparisons of reconstructions. For 3D reconstruction mean values did not show stable behaviour in both regions within the first 8 iterations and the 4th iteration was chosen in subsequent comparisons as a comprise between the reliability of mean values convergence and image noise.

TACs of the evaluated VOIs are plotted in figure 7.10 and 7.11, for VOIs sampled in both DSB and DWB acquisitions and for VOIs sampled only during the DWB acquisition respectively. In figure 7.11 the time point

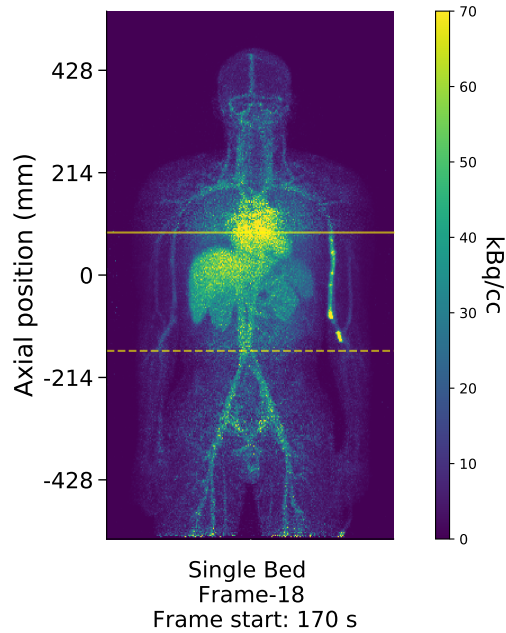


Figure 7.8: MIP image of a single frame from 4D reconstruction (15it28sub) of the CTRL scan

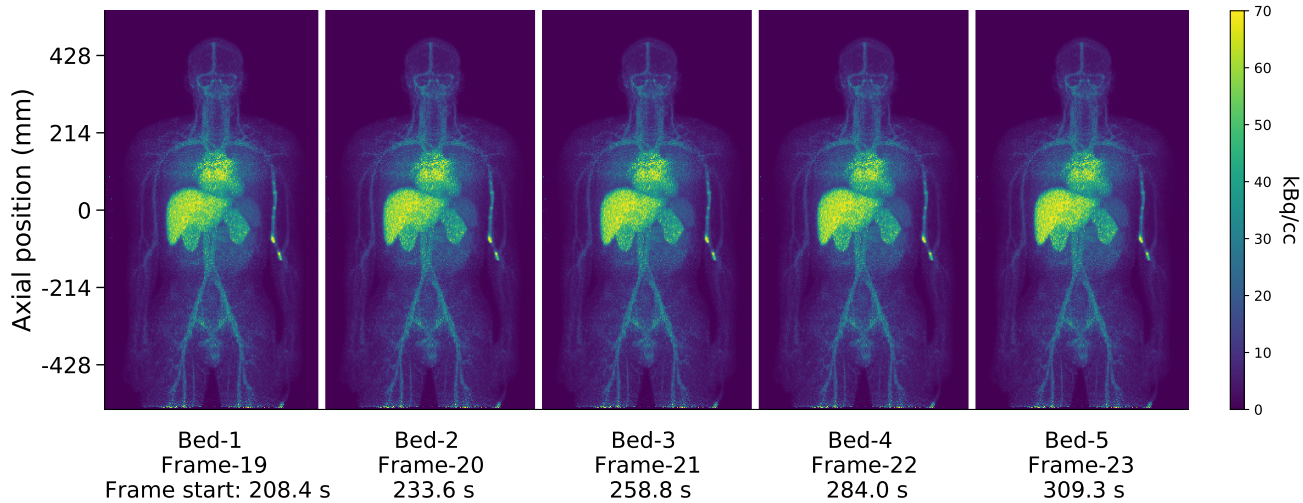


Figure 7.9: MIP image of the first whole-body pass frames from 4D reconstruction (15it28sub) of the CTRL scan.

of the start of the DWB acquisition is indicated by the red dotted line. As already mentioned, the 4D spectral reconstruction results in an activity estimate of every location of the image for every frame of the study, while 3D reconstruction results in activity estimates for the sampled frames only at each location. This is why the TACs from the 4D reconstruction of the *CTRL* data show a total of 88 frame points for all VOIs, while for 3D reconstruction a total of 32 frame points (18 from DSB plus 14 from DWB) is seen for regions included in the DSB acquisition and 14 frame points for regions seen solely by the DWB acquisition.

For the VOIs seen by both DSB and DWB acquisitions, the TACs between 3D and 4D spectral reconstruction

are in good agreement for all evaluated VOIs, as seen in 7.10. For the brain and muscle VOIs seen by the DWB acquisition alone, there is a relatively good agreement, with slight overestimation in early frames of the brain region and underestimation on later frames as seen in 7.11. By contrast, at the bladder VOI there is a strong mismatch of the 3D and 4D spectral reconstruction, with the 3D reconstruction showing clearly the bladder filling process and the 4D spectral reconstruction showing an increasing behaviour produced by the exponential functions. The VOI means of the spectral parametric images are given in the appendix material, where it is seen that the component of full trapping ϕ_0 is strongly used in the bladder region, in an attempt to fit the underlying process. But the use of the input function and the decaying exponentials is not enough to fit this process. Further considerations to this issue are addressed in the section 7.3.4.

7.3.2 Comparison of 4D Spectral reconstruction on DWB data, with and without the use of DSB data

A comparison between 4D spectral reconstructions, with and without the use of the initial DSB data, is made in figure 7.12, for VOIs covered by both DSB and DWB acquisitions. These show a good agreement of the two spectral reconstructions, with a consistent slight error in the early DWB frame estimations of the reconstruction without the use of DSB data. This error is relatively small compared to the mean activity of each VOI (maximum of 12.7% error seen in Spleen VOI). A very good agreement is seen on the liver between the two reconstructions.

The extrapolation of the fitted spectral model from DWB data alone can be made for the early non sampled frames. These show a sharp drop of the fitted TACs, indicating the inadequacy of the used data for extrapolation of the fast early frame behaviour and the cause for the systematic mismatch at early frames of the DWB acquisition. In particular, the extrapolated model is unable to reproduce the early peak, as seen clearly in the ventricle, the myocardium and the spleen, which indicates that separation between the exchange components and the blood fraction component of the spectral model is compromised when the early dynamic data are not available.

7.3.3 Direct WB parametric image estimation from 4D Spectral reconstructions

Using the set of equations 2.20 and specifically the equation for the derivation of K_1 , the parametric maps of K_1^* were produced by summation of basis $(\phi_0 - \phi_{M-1})$. Similar to the simulation study before, the blood fraction correction was neglected in favour of avoiding excessive noise propagation into voxel parameter estimates. The result parametric maps for both *CTRL* and *RIF* scans are shown in figure 7.13 and figure 7.14, as a MIP in the coronal plane and as a single coronal slice showing the liver, the kidneys and the spleen.

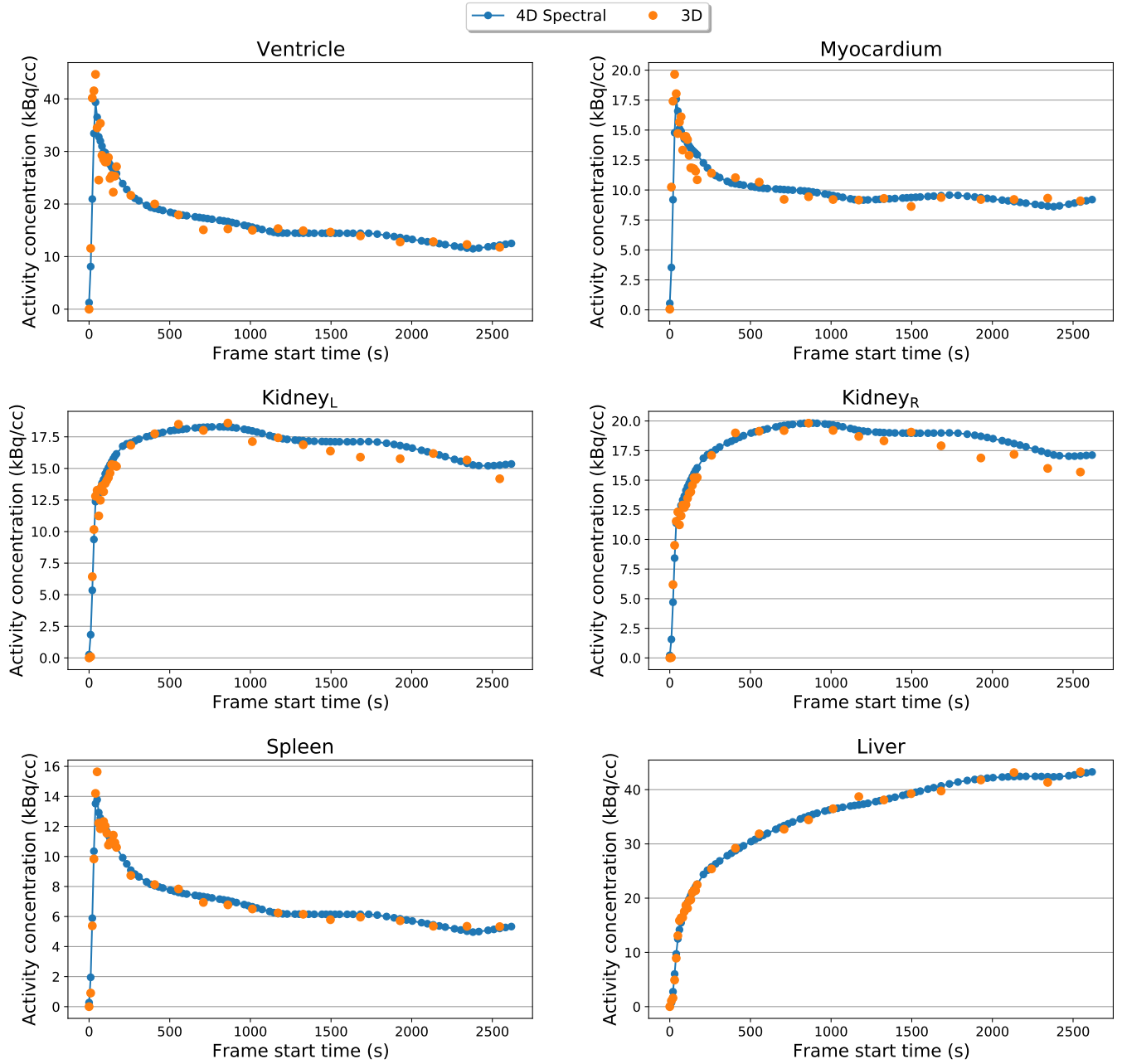


Figure 7.10: VOI mean time activity curves for 3D and 4D spectral reconstruction. VOI regions shown which are included in both DSB and DWB acquisition.

Mean VOI K_1^* values, shown in figure 7.15, show a considerable reduction from the *CTRL* to the *R/F* scan by the administration of the inhibitor. This drop reflects the difference between specific and non-specific uptake of the novel Glyburide tracer in the various imaged organs, with the strongest apparent difference seen in the liver.

The results of a short dual input simulation study, given in appendix C, indicate that accurate quantification of K_1 (or K_1^*) in the liver using only the arterial input function as an input is not achievable as expected. But the

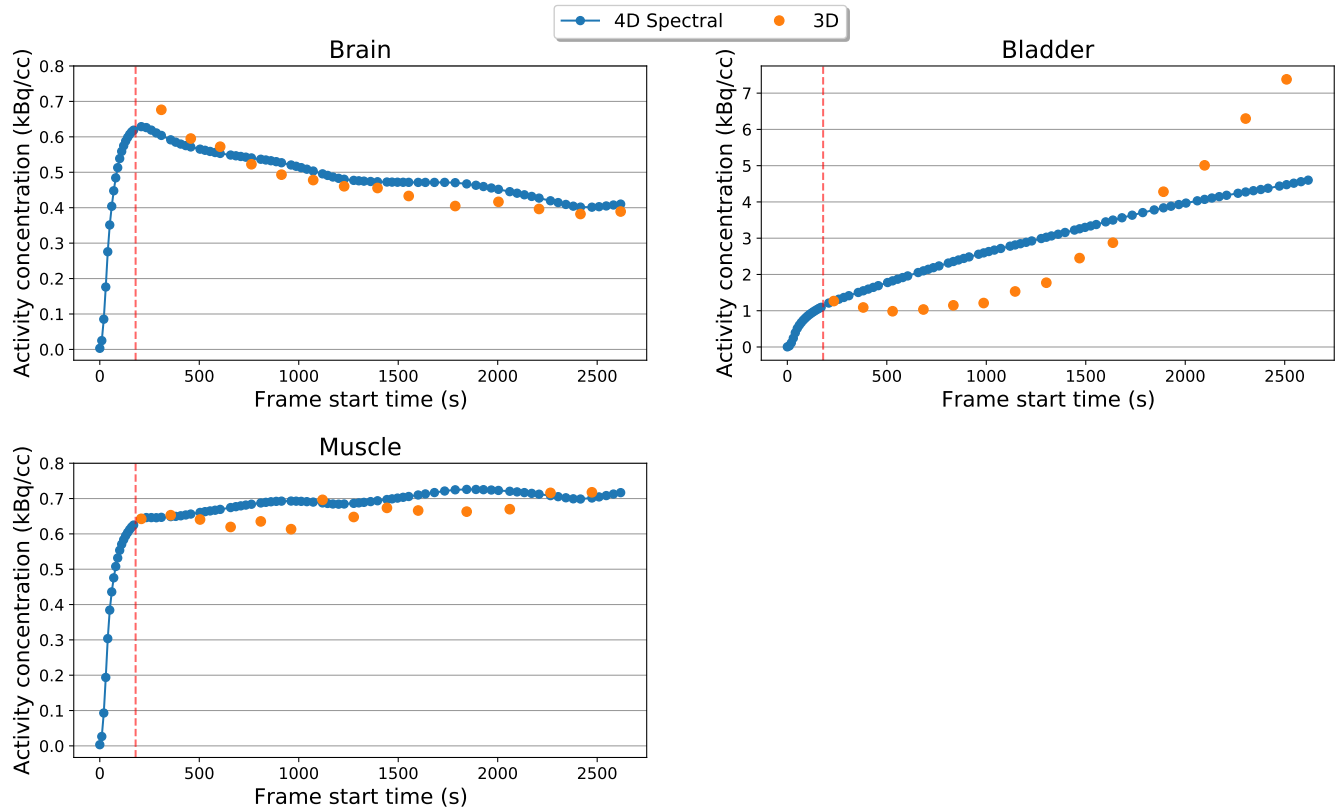


Figure 7.11: VOI mean time activity curves for 3D and 4D spectral reconstruction. VOI regions shown which are covered only by the DWB acquisition, whose start time is designated with a vertical dotted line.

simulation showed that a relative comparison of spectral model K_1^* estimates reflects approximately linearly the differences of the true underlying K_1 , without the explicit need for modelling the dual input function. These simulations are however based on a simple one parameter model for the portal vein, and do not include delay in the input functions (which can be expected, especially for the portal vein input function). Further investigations are needed in the use of the spectral model within the liver, starting from simple mathematical formulations of the problem before testing further using PET simulated data or the real data. In any case, knowledge or valid assumptions on the rate of dispersion and the ratio of portal to arterial blood in the liver can be advantageous as they would reduce the number of unknown parameters. Furthermore, joint estimation approaches in the estimation of parameters in the liver could be assessed for uses in WB dynamic studies.

7.3.4 Fit errors and error propagation

As seen in figure 7.11, the mismatch between the 3D and 4D spectral reconstructions at the bladder TAC is the strongest from all the evaluated VOIs. The source of this error is the inability of the spectral model to fit the bladder filling process, by any combination of the decaying exponentials convolved with the arterial input

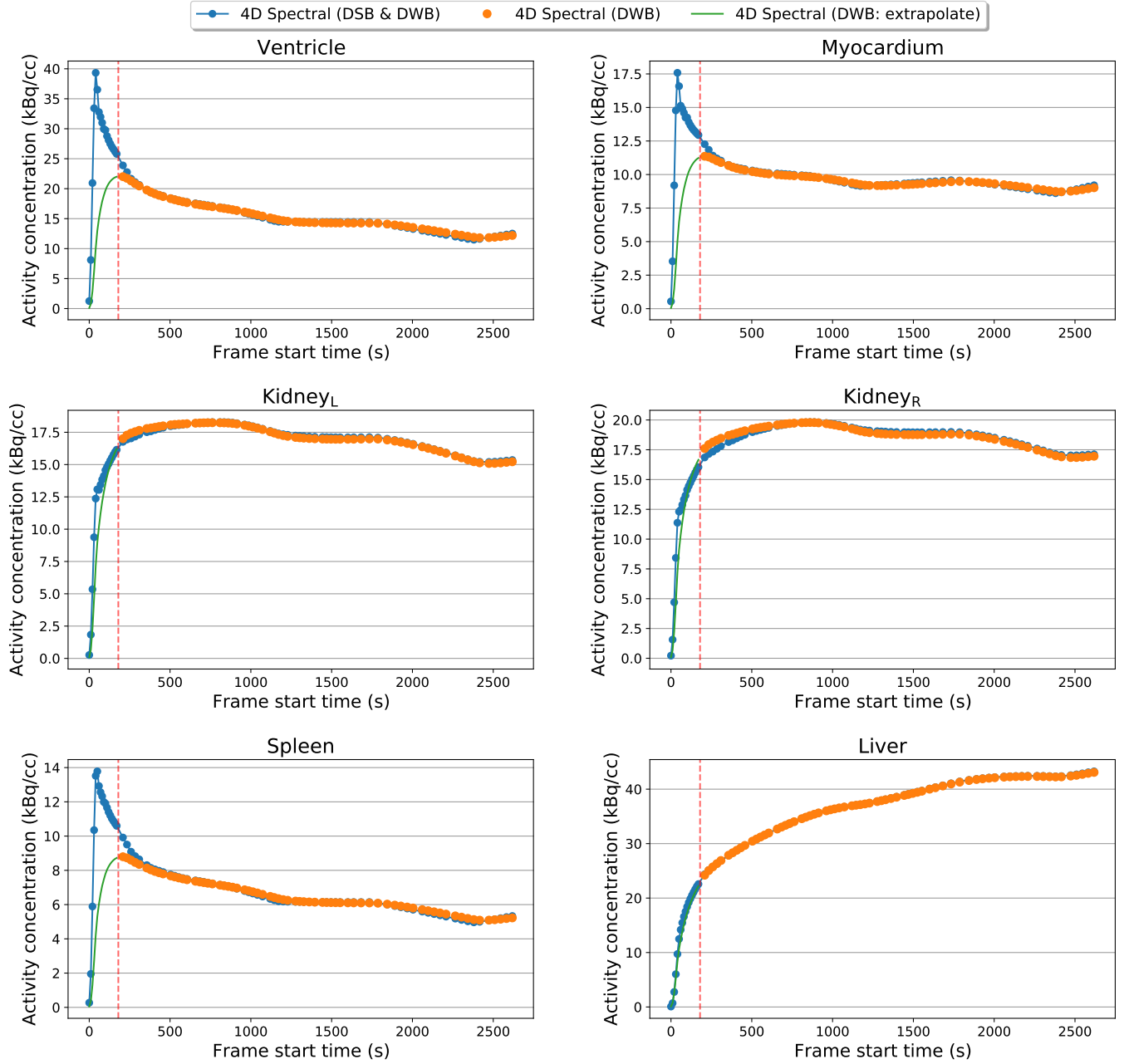


Figure 7.12: VOI mean time activity curves for 4D spectral reconstructions, with and without the use of DSB data. VOI regions shown are included in both DSB and DWB acquisitions.

function. This mismatch is of particular concern for dynamic reconstruction as it can be the source of errors that propagate spatially during the dynamic reconstruction process over the entire field of view [123, 124]. This issue is addressed further in the work presented in chapter 8 by use of adaptive residual modelling for dynamic reconstruction.

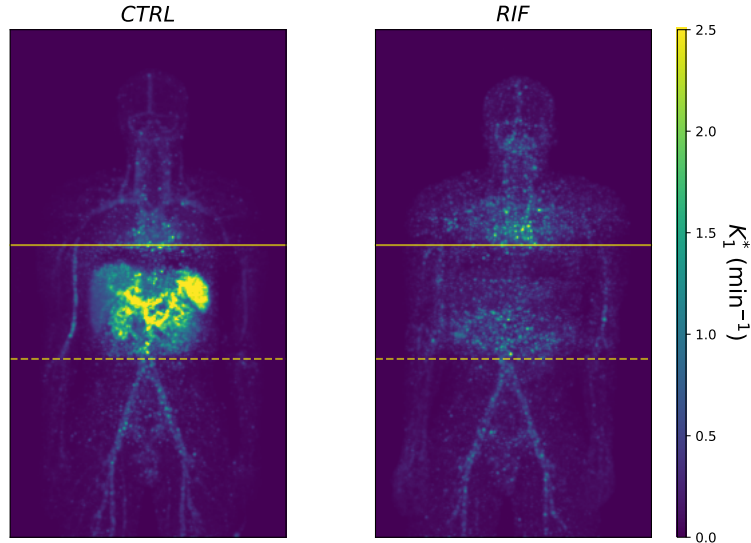


Figure 7.13: K_1^* MIP images from the 4D spectral reconstruction using both DSB and DWB acquisitions, shown for the *CTRL* and *RIF* scan.

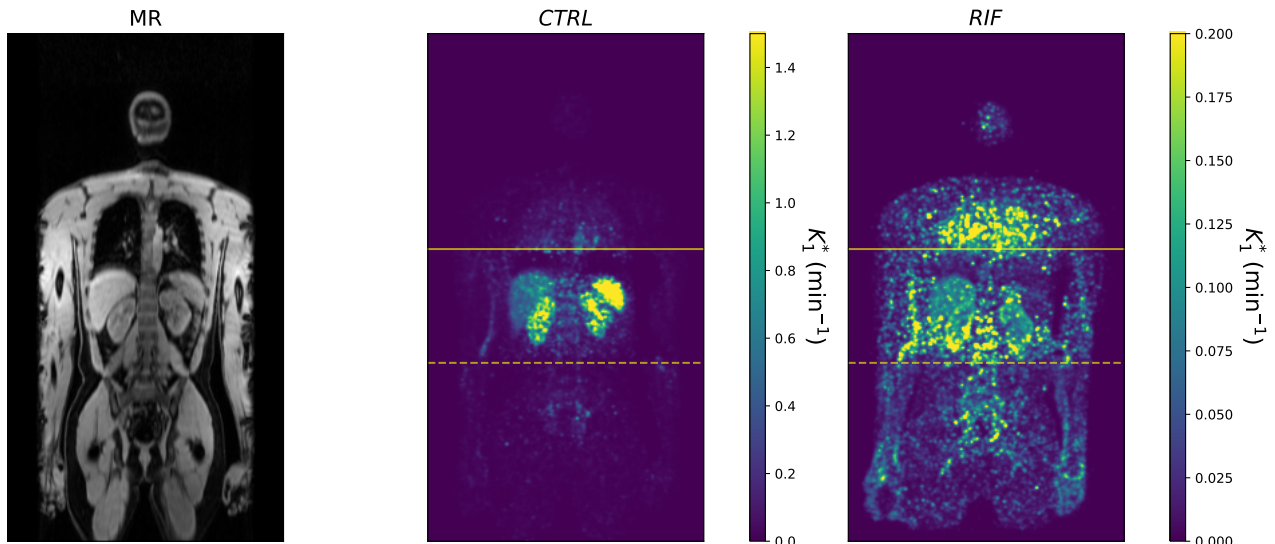


Figure 7.14: K_1^* values as estimated from the 4D spectral reconstruction for VOI regions included in both DSB and DWB acquisitions , shown for the *CTRL* and *RIF* scan

7.4 Discussion

We have developed and presented a framework for direct multi-bed dynamic reconstruction of DWB data, that allows for synchronous use of both DSB and DWB PET raw data, typically acquired in dynamic studies over the whole body [7]. This framework can be used for dynamic reconstruction by making use of the accurate positional and timing information of all the individual bed raw PET data within a single iterative loop, performed either directly within a single system matrix or using the nested optimization approach. In this study, we have tested this framework with real DWB data, from a first in man pharmacological study, where

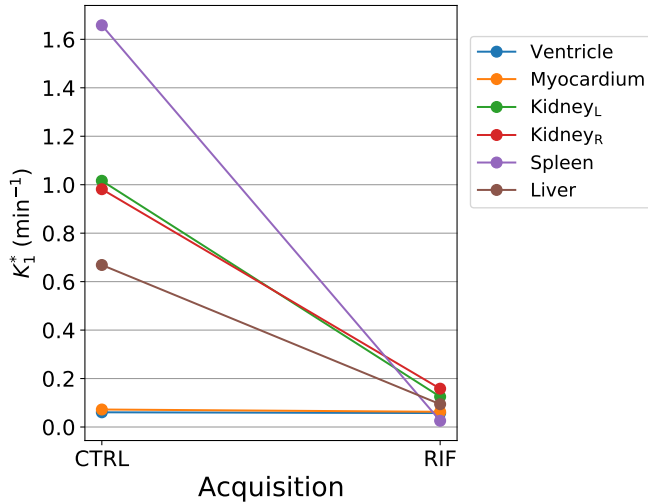


Figure 7.15: K_1^* values as estimated from the 4D spectral reconstruction for VOI regions included in both DSB and DWB acquisitions , shown for the *CTRL* and *RIF* scan

the spectral model was used within the reconstruction to avoid having to assume and enforce a specific compartmental model. The result (temporally regularised) activity images show estimates with a smooth transition in the axial direction across the effective FOV, in terms of image activity values and image noise. Although we hypothesised that use of the data within a single iterative loop results in improved estimates at the overlap region, compared to the state of the art methods that perform parametric image overlapping after reconstruction [16, 55], we do not directly compare with these methods. To address this comparison, we performed an evaluation study for these methods using the NHP dataset of chapter 5, but results were inconclusive and showed the need for a detailed simulation study to assess differences in terms of bias and noise properties of the overlapping regions against known ground truth simulated values.

The IsotoPK real DWB data used in this study included a 180 s DSB acquisition centred over the liver prior to the DWB acquisition. This has enabled the estimation of K_1^* parametric images over the region covered by both DSB and DWB acquisitions. As shown before in chapter 6, that initial information is crucial for the estimation of K_1 . Thus, although the use of the DSB initial phase allows for adequate sampling of fast kinetics and estimation of fast kinetics sensitive parameters in DWB studies, it still limits the estimation for parametric images to an axial coverage of a single bed position. All other regions outside this bed coverage were sampled with a 180 s delay, which as shown in chapter 6 produces erroneous estimates of K_1^* . In this study this relates to K_1^* estimates in regions outside the coverage of the DSB acquisition in figure 7.13 and figure 7.14. Further investigation in the setup of the acquisition protocol is required to quantify the minimum amount of fast kinetics sampling required for reliable deduction of parametric K_1 images and other parametric images sensitive to early fast kinetics. An analogous study conducted for the estimation of 2TC micro-parameters in FDG imaging resulted in evaluation of the sensitivity of micro-parameters against a

sampling of specific time points [125]. A similar study for the spectral model analysis method can evaluate the need of the DSB phase for estimation of K_1 and other parameters and if possible adapt the acquisition for reliable estimation of those parameters over the whole effective FOV. Another disadvantage of the need for a DSB acquisition is the uneven sampling over different locations of the effective FOV that results in different noise properties across the axial direction. Equal sampling of all regions is preferred to provide comparable noise properties in the axial direction of the FOV.

There are many challenges and limitations in dynamic reconstruction and parametric imaging, which are of particular concern for DWB imaging where the dynamic model is applied over the whole body [20]. Firstly, a single input function has been used for the estimation of the basis functions of the spectral model which is then applied over the entire effective FOV. The use of a single input function does not account for dispersion and delay effects that are varying for different locations in the body. As kinetic models and in particular the spectral model rely heavily on the input function, any errors or inaccuracies can lead to considerable estimation errors. Ideally, the delay and dispersion properties of the input function need to be estimated for each region, which would then be used for calculating a set of spatially variant spectral basis functions. Furthermore, the input function was derived from manual samples whose sampling frequency compromises the measurements of the peak of the input function. This information over the peak is of significant importance for the estimation of micro-parameters. Methods for joint-estimation of dispersion and delays or joint estimation of the input function itself within the reconstruction process have been previously proposed [10, 101], but so far have only been applied in DSB studies [10] and studies using total-body data [65] where sensitivity and sampling-frequency are much higher compared to multi-bed DWB imaging. Many considerations are needed to evaluate the translation of these methods in multi-bed DWB, where the poorer data statistics and sampling frequency might not allow for reliable estimation of all the involved parameters of these joint estimations. Image derived input functions can also be used as an alternative to manual samples, but they also suffer from limitations regarding sampling frequency over the input function peak and are normally measured from a few locations without accounting for delay or dispersion.

Moreover, regarding the application of the input function over the effective FOV, certain organs might not follow well the single input function models. In this study, a major organ of interest is the liver, which is supplied with blood via two different routes. We showed using a simple simulation that although the spectral model is able to fit the liver TAC relatively well, the result K_1^* parameters were strongly biased. Accurate quantification requires estimation of both input functions. Recently joint estimation approaches [78] and image derivation approaches [80] have been shown to produce good results in DSB studies. Their translation to DWB and generalisation for use with other tracers requires further research. Nevertheless, this example of the liver shows again that in the quantification of parameters there is a need for spatially variant modelling.

Still, the use of a generic model such as the spectral model has the ability to adequately fit the underlying tracer behaviour and provide temporally regularised activity estimates.

Another considerable limitation, that has not been addressed in this study, is subject voluntary and involuntary motion. Inevitably these types of motion will be present in dynamic studies, especially when imaging the whole body with DWB that involve frequent bed movements. In dynamic reconstruction these effects need to be accounted for within the reconstruction process, to avoid image artefacts and modelling errors. But when considering the whole-body, there are many types of complex motion taking place during the duration of a dynamic study. These include respiratory motion, cardiac motion, head movements, bowel motion and other internal organ movements, etc [20]. Estimation of all these types of motion is a complex task. Many data driven [126–128] and joint estimation approaches [129, 130] have been proposed for motion estimation and correction, but their use for complex elastic motion is still actively researched. Recently machine learning approaches have been proposed to improve on elastic motion estimation from low statistic gated images [131, 132]. For complex motion detection over the whole-body, the use of histo-images (COD images), which is constantly improving with TOF hardware advancements, is actively being researched for use in motion detection/estimation [133]. Nevertheless, the task of motion detection from dynamic PET data is more complex when considering a dynamically changing tracer distribution rather than a static tracer distribution, which is assumed in most approaches discussed above. Specifically for PET/MR imaging, the use of specialised MR sequences has been previously suggested and successfully used for complex elastic motion estimation [134, 135], but these motion detection MR sequences can be time consuming. In DWB imaging where delays between individual bed position acquisitions have a strong impact on the estimation of kinetic parameters, there can be a great impact on PET parametric image quality by the sacrifice of sampling frequency due to additional MR sequences on each bed position.

7.5 Conclusion

A direct multi-bed dynamic reconstruction method was presented and tested using real data from a DWB pharmacokinetic study. Evaluation tests for dynamic spectral reconstruction against regular frame by frame reconstruction of the data showed relatively good agreement of VOI TAC data in all regions except the bladder, where the filling process was badly modelled. Finally, there is a need for accurate motion estimation and correction within the dynamic reconstruction process that is imperative for artefact free and error free parametric image estimations over the whole body. Estimation of all types of complex motion over the whole body, using ideally data driven approaches, needs to be addressed further for DWB acquisitions.

Chapter 8

Dynamic Reconstruction Using the Spectral Model and Adaptive Residual Modelling

In this chapter, we discuss the complications arising from kinetic model fitting errors in dynamic reconstruction, for DWB imaging and WB parametric maps. We present our work towards the reduction of these errors using adaptive residual modelling for dynamic reconstruction, applied on the IsotoPK CTRL dataset presented in the previous chapter. The focus of this application was the model fitting mismatch over the bladder region and any potential propagating errors. To our knowledge, this is the first time a method of this type has been applied to real DWB data.

The results of this work were presented in the **IEEE/MIC** 2020 conference. This chapter is adapted from the conference record of this submission.

8.1 Introduction

Dynamic PET has been traditionally utilised in single organ studies, but recently there has been increased interest in dynamic whole body imaging, for research and for potential future clinical applications [8, 18, 56, 136]. Synchronous dynamic PET of the whole body requires scanner geometries that can encompass the entire length of the human body. Although systems capable of whole body axial coverage have been recently developed [59], their availability is not yet widespread. Current clinical scanners achieve whole body coverage using multiple axial bed positions or acquisition protocols with continuous axial bed motion. Based on these acquisition modes, dynamic whole body protocols have been developed that make use of repeated whole body passes [7]. Conventional analysis of dynamic data is performed with independent 3D reconstructions of frame data, followed by kinetic model fitting. Whole-body dynamic protocols make the task of reconstruction and subsequent kinetic modelling more challenging due to the introduction of large temporal gaps in the data which can lead to biased estimates and increased noise, especially for parametric maps. To improve image quality and account for the noise in the raw data, 4D reconstruction algorithms can be used to directly incorporate the dynamic model of interest in the reconstruction [10]. Depending on the choice of the dynamic model, these reconstructions can directly provide the parameters of interest or temporal regularisation on the reconstruction process of frame data. The spectral analysis model, inspired by the homonym method [70], fits on any underlying kinetic behaviour that can be described by compartmental modelling. When used in 4D reconstruction it provides temporal regularisation as well as direct estimation of some kinetic parameters. Use of this model has shown to reduce noise and bias of kinetic parameter estimates when applied on data from dynamic whole body protocols [137].

When considering the effective field of view of dynamic whole body studies, certain regions might not fulfil the generic assumptions of the spectral analysis model. For example processes such as delay of tracer delivery and non-arterial tracer delivery (ex. bladder filling). In 4D reconstruction, the tomographic update process is entangled with the dynamic model and errors from the temporal model fit have the potential to spatially propagate to other regions. Due to the fact that raw data from multi-bed dynamic whole body studies are acquired and reconstructed as separate beds, the potential for errors propagation is limited in the bed position where they originate from. It has also been shown that use of time of flight (TOF) information in the reconstruction aids in reducing spatial propagation of errors [124]. Nevertheless, model fit errors have the potential to propagate and when possible should be corrected or accounted for. For this reason, when 4D reconstruction is used and especially when applied on whole body datasets extra consideration has to be given on improving the model fit for all regions.

The application of an adaptive residual model as a second dynamic model has been previously suggested

for reducing model fit errors [138]. Its application in 4D reconstruction has been shown to reduce bias at the cost of increased noise for direct estimation of kinetic micro-parameters [123]. The objective of this work was to implement and evaluate adaptive residual modelling in 4D reconstruction, using real dynamic whole body PET data, with no prior knowledge of the underlying kinetics and the distribution of residuals. For this purpose, the spectral analysis model was used in conjunction with a residual model in 4D reconstruction to maintain genericity in the reconstruction with minimum assumptions on the underlying kinetics. The end objective was to assess if adaptive residual modelling can be permanently applied in 4D reconstruction, with no prior knowledge of kinetics and model fit errors, by relying on the selectivity of the algorithm for correction of underlying model fit errors, when and where those arise.

8.2 Methods

8.2.1 Data acquisition

Dynamic whole body (DWB) data using a novel ^{11}C -Glyburide tracer were acquired from a healthy volunteer on the GE Signa PET/MR, using a dedicated DWB protocol of 5 bed positions to provide sufficient coverage of the body. The data were acquired as part of the exploratory pharmacological study IsotoPK which is conducted in our centre for studying the distribution of OATP transporters in the body and their role in the delivery of drugs to tissues [9]. In this work a control scan was used (*CTRL* scan from chapter 7). In detail the dynamic acquisition consisted of a single bed acquisition centred over the liver, imaged for 3 minutes from tracer injection, followed by 14 whole body passes of 9x20s and 5x30s frames for each bed position. Arterial blood samples were collected manually during the whole study, to derive the input function.

8.2.2 Reconstruction

The spectral analysis model was used in all 4D reconstructions, using 6 spectral basis functions ($M = 5$) with $\beta_1 \dots \beta_{M-1}$ logarithmically spaced within the range of 3 to 0.001 min^{-1} , while including β_0 and β_M to account for trapping and the blood fraction in the data. The 4D reconstruction algorithm with adaptive residual modelling was developed using the spectral model as primary model and an adaptive secondary model, similar to the proposed method by Matthews et al. [138].

The steps of the adaptive residual modelling 4D reconstruction algorithm are:

1. Start with image estimate $\lambda_{tj}^{(k)}$, for voxel j and frame t at iteration k .
2. Perform tomographic update using MLEM to get the EM update images $f_{tj}^{(EM)}$.
3. Perform primary model fit using the NNLS algorithm on $f_{tj}^{(EM)}$ and estimate model parameters $\theta_j^{(k+1)}$.

4. Calculate residuals as $r_{tj} = f_{tj}^{(EM)} - f_{tj}^{(spectral)}(\theta_j^{(k+1)})$.
5. Perform PCA analysis on residuals to estimate a set of residual basis functions (RBF) which form the secondary (adaptive) model.
6. Estimate modelled residuals g_{tj} from the LS fit of the secondary model on the r_{tj} data.
7. Estimate optimal fraction K_j for residuals re-introduction, using generalised cross validation.
8. Add fraction of modelled residuals in image estimate $\lambda_{tj}^{(k+1)} = f_{tj}^{(spectral)}(\theta_j^{(k+1)}) + K_j g_{tj}$ and repeat from step 2,

where NNLS stands for Non-Negative Least Squares and $f_{tj}^{(spectral)}(\theta_j)$ is the spectral model which provides activity estimates for voxel j at frame t given model parameters θ_j .

In step (5) of our adaptive modelling implementation, the residual data were spatially smoothed with an isotropic Gaussian kernel of 32mm FWHM, to enhance the PCA analysis results. Smoothing of the residuals was not however applied in the fitting process of the secondary model in step (6). A fixed number of the most significant PCA components was used as basis functions of the adaptive residual model. The components were updated on each iteration of the 4D algorithm.

For the estimation of the optimal fraction K_j , the following equation from Matthews *et al.* [138] was used, which is derived from generalised cross-validation,

$$K_j = \frac{1 - \frac{r_{df}}{r_{RSS}}}{1 - r_{df}}, \quad (8.1)$$

where $r_{df} = \frac{n_s}{n_f - n_p}$, with n_p and n_s being the number of parameters of the primary and secondary model respectively, and r_{RSS} being the fraction of modelled to measured residuals sum of squares.

The dynamic data from each bed of the study were reconstructed as individual frames using 3D MLEM (150it), using 4D reconstruction (300it) and with the developed adaptive algorithm 4D-ResidMod (300it). No subsets were used for the reconstructions performed in this work. The adaptive reconstruction algorithm was evaluated using the 2 and 3 most significant PCA components as RBFs, referred to as 4D-ResidMod-2RBF and 4D-ResidMod-3RBF respectively. We also implemented a version of the adaptive algorithm with the addition of temporal Gaussian smoothing of 62s FWHM applied on the residual data used for PCA analysis in step (5) of the algorithm, referred as reconstruction 4D-ResidMod-3RBF-Tempfilt.

All reconstructions were performed with the open source reconstruction platform CASToR [11], using resolution modelling and TOF information. Correction for motion has not been included in the reconstructions. PCA analysis was performed using the Eigen library [139].

8.3 Results

As seen in Fig. 8.1 (top row) by the difference in activity estimates from 3D and 4D reconstruction in a late frame, the 4D algorithm with the spectral model alone resulted in lower activity estimates over the bladder region and higher activity estimates in some large blood vessels at the shoulders and pelvic regions. No noticeable differences were seen in other areas, apart from random variations in activity due to differences in noise levels of the compared reconstructions.

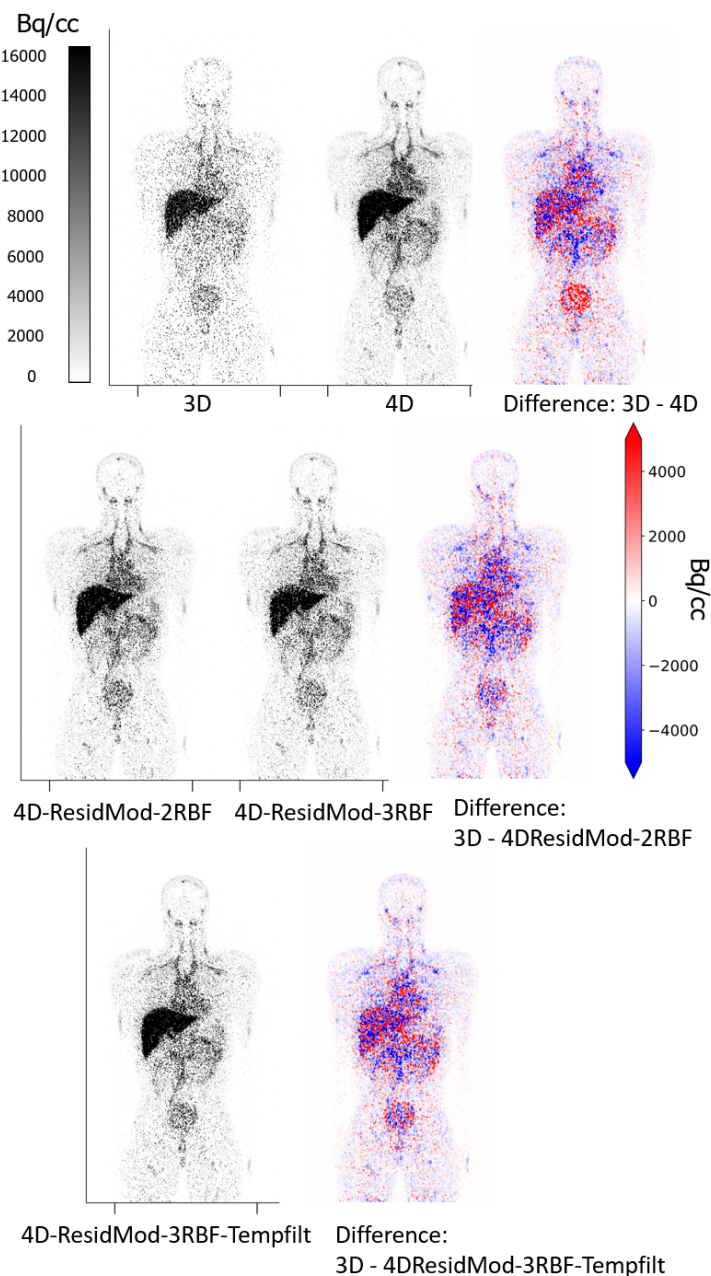


Figure 8.1: Coronal view of activity distribution from the evaluated reconstructions (frames of 41.2 to 44.1 minutes post injection). Difference images are also shown for selected cases against the 3D reconstruction.

As expected, the filling process of the bladder seen in the bladder time activity curve from 3D reconstruction in Fig. 8.2 (bottom row) cannot be modelled by the spectral model because the filling process is not directly relatable to arterial tracer delivery at the local (voxel) level. Differences in some large blood vessels could potentially be attributed to delay of the input function, which is not accounted for in the spectral model where a single input function is assumed to apply for all regions.

Reconstruction of the data with adaptive residual modelling resulted in improved estimation of the bladder filling process, for both options of residual modelling using 2 and 3 residual basis, as it can be seen in the difference images of Fig. 8.1 (middle row) and the bladder TAC in Fig. 8.2. No improvements were seen for the differences at the blood vessels of the shoulders and pelvic regions.

At the liver, where most of the tracer uptake is concentrated, 4D and 3D reconstruction TACs show a subtle mismatch between 1100 and 1500 seconds (Fig. 8.2, top row). Analysis on the liver dome VOI (Fig. 8.3, top row) clearly shows this difference, which originates from underlying respiratory motion that has been captured in the PET dynamic data. 4D reconstruction alone was unable to model these fluctuations, as expected, but the adaptive algorithm using 3 residual basis has achieved to model for this behaviour as seen in Fig. 8.3. Since physiological kinetic processes, whether sufficiently modelled or not, are not expected to result in sudden changes of activity between adjacent frames, we implemented a version of the algorithm with temporal smoothing prior to PCA analysis to prevent from modelling changes due to fast processes such as respiratory motion. On this case this algorithm (4D-ResidMod-3RBF-Tempfilt) has managed to maintain the selective adaptive modelling behaviour over the bladder while avoiding fitting the motion related effects over the liver dome as seen in Fig. 8.3.

In all regions of the effective FOV the addition of adaptive modelling has resulted in the increase of image noise, compared to 4D reconstruction, with the higher number of residual basis resulting in higher noise. The introduction of temporal filtering in the adaptive model estimation process has aided in reducing the induction of noise for the majority of the evaluated regions in our study. A comparison of the effect on image noise across regions within this whole body study can be made by the VOIs standard deviation shown in Fig. 8.5 for all evaluated algorithms. An example map of the fraction K_j and the modelled residuals g_{jf} is given in Fig. 8.4. These maps demonstrate the desired selectivity of the algorithm, concentrated over the bladder in this case, but also the spill of noise from the residual space in these maps which is subsequently added in the reconstruction process.

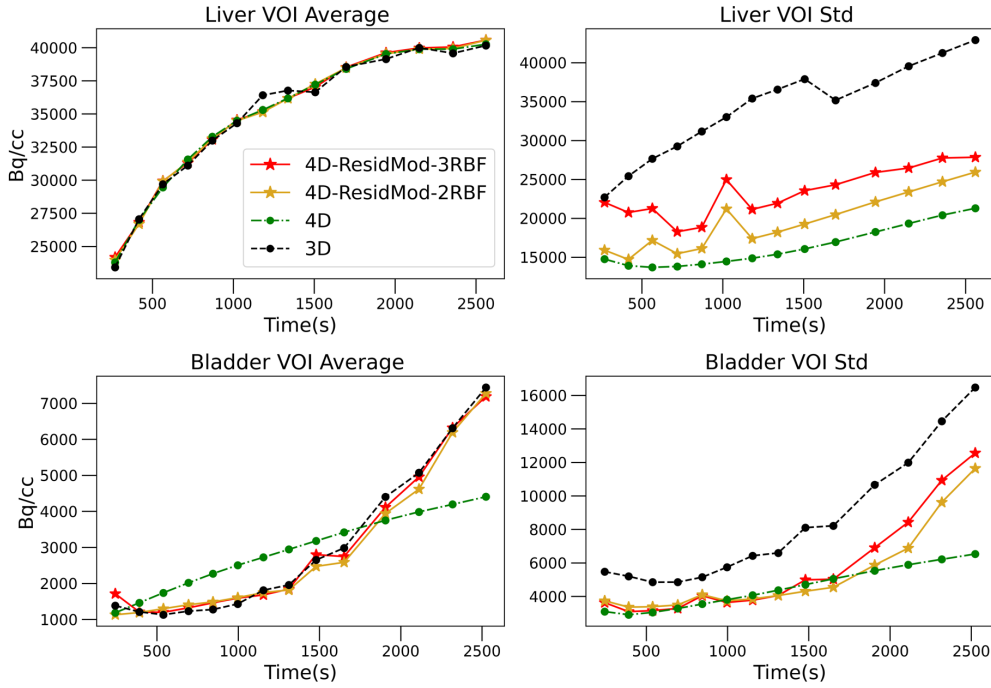


Figure 8.2: Average and standard deviation time curves of the liver and bladder VOIs, for the comparison of 3D to 4D reconstruction results as well as 4D reconstruction with residual modelling using different number of residual basis functions.

8.4 Discussion

In this work, we presented the application of a previously suggested method for adaptive residual modelling in dynamic reconstruction to reduce errors that arise from poorly modelled regions. General dynamic models, such as the spectral analysis model, can be useful in 4D reconstruction of DWB data using new tracers, as they do not impose strong assumptions about the underlying kinetics. But over the effective field of view of DWB imaging, certain regions and their physiological processes might not fulfil the general assumptions of the model. In these cases, the adaptive residual modelling strategy can be utilised to improve parameter estimates for these regions and help in minimising the risk of spatial propagation of errors to other well-modelled regions. In our application, 4D reconstruction with the spectral analysis model and adaptive residual modelling was applied on real DWB data from a first in man study of a new tracer. The algorithm identified and selectively corrected the image activity estimates over the poorly modelled bladder region, by modelling the residuals of that region. This resulted in a 4D reconstruction that did not suffer from the model fit errors over the bladder and potential errors propagated to other regions originating from the bladder region. But the use of the adaptive model as a secondary model increased the complexity of the modelling in the reconstruction process and resulted in an increase in image noise. The higher the number of residual basis functions used resulted in higher induction of image noise, as expected and inline with previous observations in a simulation study [123]. Overall, we saw that noise from the residual space propagates to

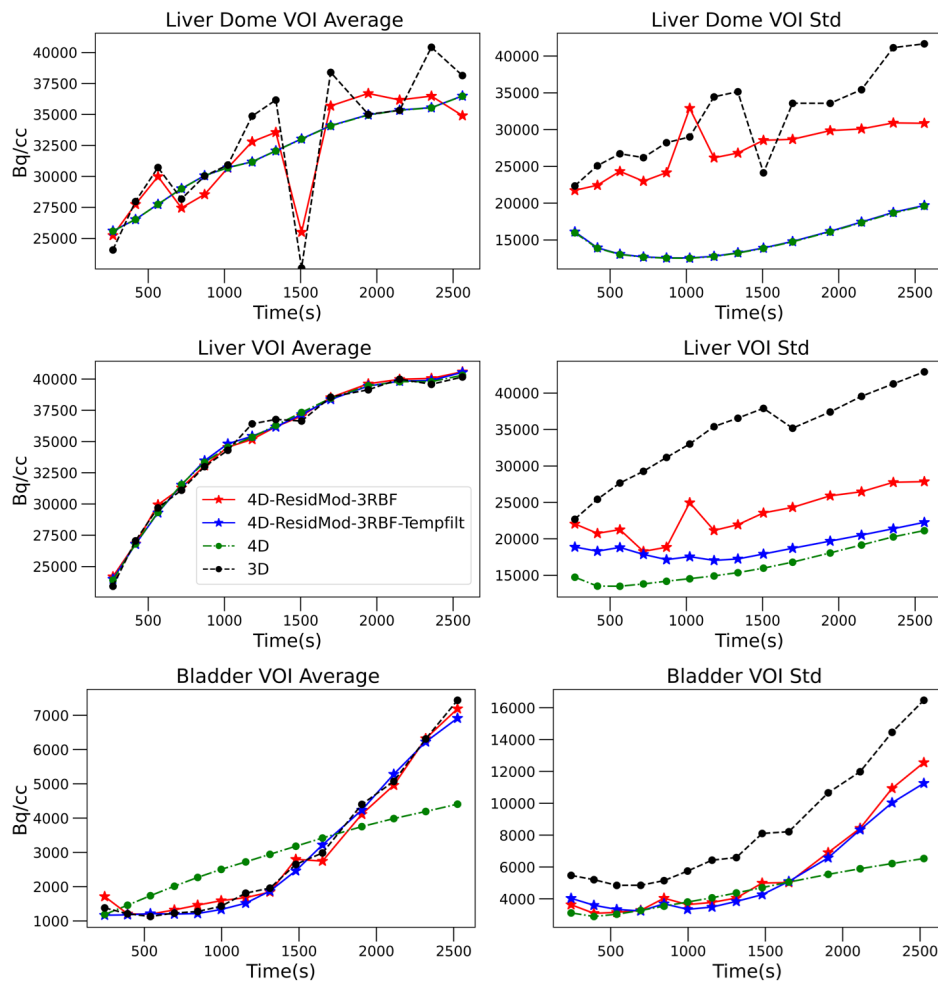


Figure 8.3: Average and standard deviation time curves of the dome of the liver the whole liver and bladder VOIs, for the comparison of 4D reconstruction with residual modelling with and without temporal filtering of residuals.

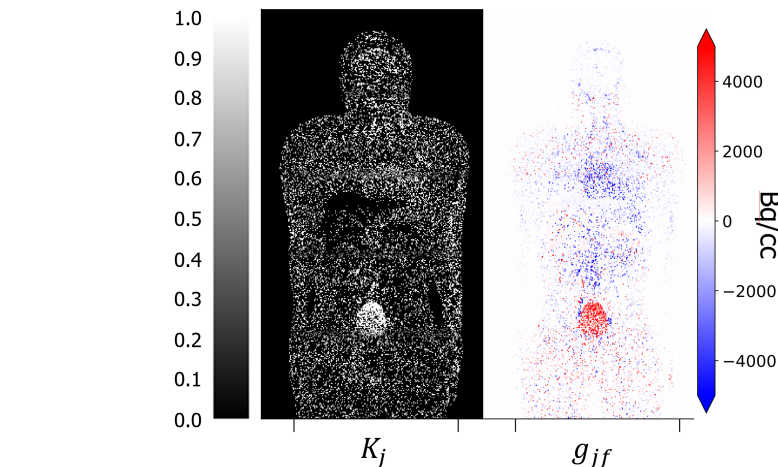


Figure 8.4: Fraction map of K_j and modelled residuals g_{jf} of the residual model 4D-ResidMod-3RBF-Tempfilt at iteration 75.

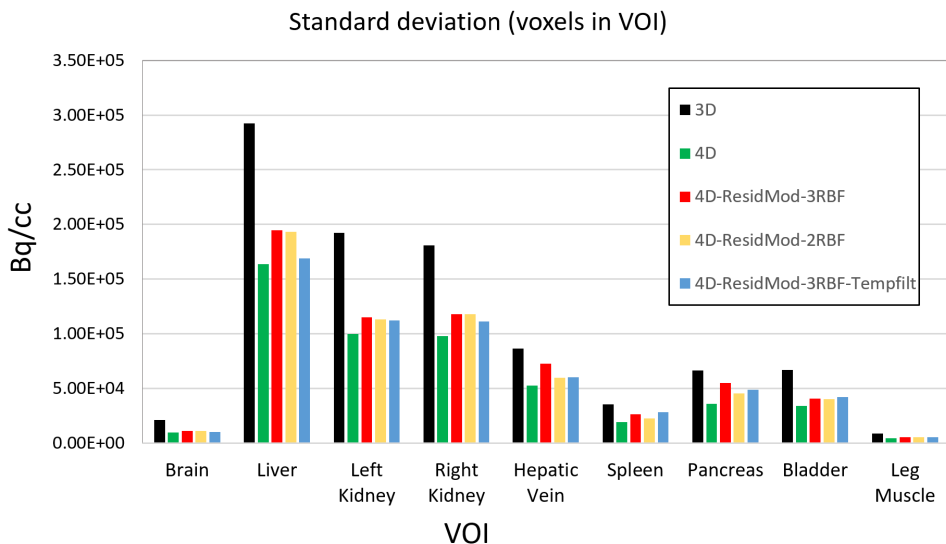


Figure 8.5: Standard deviation of VOIs for regions in the whole-body, for all evaluated reconstructions.

the modelled residuals and the optimum fraction values of the secondary model, as seen in Fig. 8.4, from where it is subsequently re-introduced in the reconstruction process.

Motion will unavoidably always be present in the raw data of dynamic studies. When it is not accounted for in the 4D reconstruction process it will give rise to model fit errors. In our evaluation we saw that the adaptive algorithm attempted to model residuals caused by respiratory motion, when the level of complexity of the secondary model permitted that, even though this was not the intended use for applying residual modelling. As any tracer's kinetic processes are expected to be slower than variations due to respiratory motion, pre-treatment of residuals with temporal filtering in the residual model estimation step aided in averting the adaptive model from fitting these motion induced differences. This temporal filtering approach did not compromise the methods ability to model kinetic processes. In addition, temporal filtering also aided in reducing the increase in noise from the use of the secondary model. But although spatial and temporal filtering in pre-treatment of residual data successfully avoided the fitting of motion induced residuals, these types of residuals should ideally not be considered as model errors since they involve TACs of multiple locations that are affected by motion. Motion correction can be easily integrated in the dynamic reconstruction with adaptive modelling, and should be performed when reliable motion estimations are available. Nevertheless, temporal filtering did reduce the induction of noise by the residual modelling process and thus can still be considered for general use even with motion corrected data.

A limitation in our approach is that we made use of full MLEM iterations (without the use of subsets) which resulted in slow convergence and necessitated to be run at high iterations. The implemented framework in CASToR could support the use of OSEM, with nested optimisation performed after each subset update,

followed by residual modelling in each subset. But initial tests had shown that the buildup of residuals on each sub-set update was not strong enough to be identified and re-introduced by the adaptive modelling approach, using the generalised cross validation derived optimum fraction. Further work is required in taking into account the differences in convergence and buildup of residuals by use of subsets in the optimum fraction K_j , without also resulting in excessive induction of noise from the residuals space.

Another limitation in adaptive modelling within multi-bed dynamic reconstruction is that each bed position is sampled at different time points. In our implementation PCA analysis was performed in a bed-by-bed basis, which enforced the use of individual bed dynamic reconstruction. Subsequently, for the application presented here, the reconstructed images of each bed were combined after reconstruction using weighted averaging. Further considerations are required for extracting residual information over different regions of the DWB scan, with attention to structures that fall in the overlap regions, to enable the use of this approach with direct multi-bed reconstruction. Segmentation approaches on residual space, previously proposed for residual modelling [140], could be employed for the extension of residual modelling in direct multi-bed dynamic reconstruction.

8.5 Conclusion

In this work we conclude that the use of the secondary adaptive model based on PCA analysis can be a practical solution to spectral analysis model fit errors, when added to a generic 4D reconstruction algorithm used with dynamic whole body data from new tracers. The combination of spatial and temporal filtering in the treatment of residual data prior to PCA analysis provided the optimal results in our tests, in terms of algorithm selectivity and levels of added noise. Further work is required to enable the use of data-driven adaptive modelling approaches for direct multi-bed dynamic reconstruction on the DWB setup.

Conclusions and prospects

The objective of this thesis was to explore and assess methods for improving whole-body parametric imaging, for clinical and research pharmacological applications, using multi-bed dynamic whole body PET/MRI data. As hybrid PET/MR scanners and the majority of other PET systems provide only a limited axial field-of-view (FOV), dynamic whole-body (DWB) protocols are used to extend the effective FOV over the required axial length. But these acquisitions come at the cost of limitations in acquisition counts and sampling frequency that degrade parametric image quality and accuracy. Several aspects were investigated, throughout the process of DWB data acquisition to data processing and reconstruction. We largely focused on the use of dynamic reconstruction algorithms for improving the use of the PET acquired data in the estimation of activity and parametric images.

Specifically, in this project we have

1. Developed an optimised protocol for S&S multi-bed DWB acquisitions on the Signa PET/MR.
2. Evaluated and compared advanced dynamic reconstruction algorithms for whole-body parametric imaging, with focus in oncological imaging.
3. Explored the use of a direct multi-bed dynamic reconstruction framework on a real WB pharmacological study.
4. Evaluated the use of adaptive residual modelling applied in DWB data and a generic dynamic reconstruction algorithm.

Firstly, we have worked closely with the manufacturer of the GE Signa PET/MR in methods for reducing the loss of counts and sampling frequency in DWB imaging by means of reducing delays in the acquisition process. This resulted in a custom fully-automated protocol that has shown to considerably reduce delays when applied on a real DWB study on a NHP subject. However, approval for use of this protocol with human studies requires a more thorough review of safety measures and closer collaboration with the manufacturer. Ideally, CBM acquisition techniques should also be considered for implementation as they can contribute

further towards improvements and flexibility in acquisition.

Secondly, we made use of dynamic reconstruction for DWB parametric imaging, with focus on oncology applications of dynamic FDG PET and Patlak parametric imaging, using simulated and real data. We proposed the use of an indirect method for DWB parametric imaging based on the spectral analysis model and dynamic reconstruction which allows for generic compartmental modelling to be used during reconstruction for temporal regularisation. While the Patlak model is limited to data after steady state conditions have been reached, this novel spectral reconstruction approach enables the use of all dynamic data in the reconstruction and offers greater modelling flexibility. Post-reconstruction Patlak parametric imaging using the regularised data of the spectral reconstruction outperformed direct Patlak dynamic reconstruction. But even this method did result in high parametric image noise when reconstruction was iterated sufficiently to ensure accurate quantification. Potentials for improvement should be examined further using additional regularisation methods to deliver acceptable parametric image noise for clinical applications and ensure accurate quantification. Finally, we have expanded our application of dynamic reconstruction to real data from an exploratory, first in man, WB pharmacological study. We extended the use of the dynamic reconstruction to direct multi-bed reconstruction, which enabled the use of the complete DWB dataset within a single iterative loop for dynamic reconstruction. This approach inherently handles the individual bed position data's sensitivity and timing information, notably for the bed overlapping positions where previously suggested practices made use of compromising solutions, while also allowing for the use of the DSB phase data independently of its axial position. In this type of applications, the use of spectral reconstruction is favoured as it does not impose strong assumptions on the unknown underlying kinetics. Preliminary results using VOI based analysis showed good agreement with results from 3D regular reconstruction. These applications also enabled the generation of surrogate parametric K_1 maps, for relative comparison between scans. Further comparisons with post-reconstruction parametric imaging need to be conducted to explore the reliability and additional benefits of this reconstruction approach towards accurate parametric imaging, but these were not conducted at this preliminary stage of the study.

In this application, we identified a limitation in the modelling process over the bladder, that had the potential to be the source of spatially propagating errors within the dynamic reconstruction process. To minimise this risk we have included an adaptive residual modelling approach within the reconstruction. This method identified and selectively corrected the model activity estimates over the poorly modelled bladder region, which provided a significant reduction of model fit errors at the cost of added noise over the entire FOV. Some optimisation advancements were made using pre-treatment of residual data, but further developments are needed for reducing the induction of noise by this approach.

A major limitation in the application of dynamic reconstruction on WB data is motion and motion induced

artefacts that affect image quality and quantification. In the setting of DWB imaging, complex motion exists in the PET data that ideally needs to be accounted for and corrected for within the reconstruction process. Many approaches for including motion correction in the reconstruction have been proposed and successfully used. But estimation of the underlying elastic motion vectors over time and over the WB is a challenging task. Moreover, the limited sampling of MR and PET in DWB acquisitions may reduce the sensitivity of many data-driven approaches for motion estimation. In our evaluations, using PET raw data and MR data from attenuation correction sequences, we were unable to use common motion estimation tools for the successful estimation of elastic motion vectors. Recently numerous Machine Learning (ML) applications for motion estimation and correction have been proposed in medical imaging. This increasing use of ML approaches for motion estimation could lead to further developments that could be useful in the DWB motion estimation problem.

During the course of this project, the introduction of the first Total-Body PET scanner in 2018 has ignited the research interest in DWB imaging. The considerable increase in sensitivity and sampling frequency by synchronous dynamic total-body scans resulted in research projects that span from clinical applications of parametric imaging to joint estimation of complex parameters over the whole-body. These also include innovative methods using the PET TOF information for motion detection and correction. But the availability of these systems is limited, due to the very high cost and no exclusive total-body clinical applications at this time.

More recently, extended FOV scanners became available by commercial providers with an axial FOV of approximately one meter. These offer considerably more coverage than current systems of 15-26 cm axial FOV. At this time there are two systems installed in clinics, with more underway. The greater availability of extended FOV (ex-FOV) systems will lead to more research projects of DWB imaging for clinical applications [19]. As in clinics the systems with limited FOV will still be used in the near future, there can be many opportunities for interesting comparison studies on WB parametric imaging to identify the limits of multi-bed DWB imaging with respect to synchronous DWB imaging by ex-FOV scanners. For example, it could be envisaged that for dynamic imaging of slow processes, such as in the case of Patlak FDG, the DWB protocols on regular scanners could provide sufficient parametric image quality for clinical applications and exclusive use of ex-FOV scanners is not necessary. On the other hand, for kinetics sensitive to early fast dynamics synchronous DWB imaging from ex-FOV scanners is expected to provide strong and clear benefits.

There is a considerable research focus on the subject, from whole-body modelling, whole-body corrections and reconstruction approaches, to ML applied in whole-body image analysis. The technological advancements are going to further fuel this growth of interest, but what is left to be seen is which applications of these techniques and technologies will be predominant in future clinical and pharmacokinetic applications.

Bibliography

- [1] Steven R. Meikle, Vesna Sossi, Emilie Roncali, Simon R. Cherry, Richard Banati, David Mankoff, Terry Jones, Michelle James, Julie Sutcliffe, Jinsong Ouyang, Yoann Petibon, Chao Ma, Georges El Fakhri, Suleman Surti, Joel S. Karp, Ramsey D. Badawi, Taiga Yamaya, Go Akamatsu, Georg Schramm, Ahmadreza Rezaei, Johan Nuyts, Roger Fulton, André Kyme, Cristina Lois, Hasan Sari, Julie Price, Ronald Boellaard, Robert Jeraj, Dale L. Bailey, Enid Eslick, Kathy P. Willowson, and Joyita Dutta. Quantitative PET in the 2020s: A roadmap. *Physics in Medicine and Biology*, 66(6), mar 2021. doi: 10.1088/1361-6560/abd4f7.
- [2] Rathan M Subramaniam. Precision Medicine & PET/CT: Challenges and Implementation Rathan. *PET Clinics*, 12(1):1–5, 2017. doi: 10.1016/j.cpet.2016.08.010.Precision.
- [3] Stefaan Vandenberghe, Paweł Moskal, and Joel S. Karp. State of the art in total body PET. *EJNMMI Physics*, 7(1), 2020. doi: 10.1186/s40658-020-00290-2.
- [4] Scott F. Schubert, Sinisa Pajevic, and Richard E. Carson. Whole body PET using overlapped 3D acquisition and weighted image summation. *IEEE Nuclear Science Symposium & Medical Imaging Conference*, 2:1285–1289, 1996. doi: 10.1109/nssmic.1996.591681.
- [5] V. Y. Panin, A. M. Smith, J. Hu, F. Kehren, and M. E. Casey. Continuous bed motion on clinical scanner: Design, data correction, and reconstruction. *Physics in Medicine and Biology*, 59(20):6153–6174, 2014. doi: 10.1088/0031-9155/59/20/6153.
- [6] Nicolas A. Karakatsanis, Martin A. Lodge, Yun Zhou, Joyce Mhlanga, Muhammad A. Chaudhry, Abdel K. Tahari, William P. Segars, Richard L. Wahl, and Arman Rahmim. Dynamic multi-bed FDG PET imaging: Feasibility and optimization. In *2011 IEEE Nuclear Science Symposium Conference Record*, pages 3863–3870, 2011. doi: 10.1109/NSSMIC.2011.6153735.
- [7] Nicolas A. Karakatsanis, Martin A. Lodge, Abdel K. Tahari, Y. Zhou, Richard L. Wahl, and Arman Rahmim. Dynamic whole-body PET parametric imaging: I. Concept, acquisition protocol optimization and clinical application. *Physics in Medicine and Biology*, 2013. doi: 10.1088/0031-9155/58/20/7391.

- [8] Arman Rahmim, Martin A. Lodge, Nicolas A. Karakatsanis, Vladimir Y. Panin, Yun Zhou, Alan McMilian, Steve Cho, Habib Zaidi, Michael E. Casey, and Richard L. Wahl. Dynamic whole-body PET imaging: principles, potentials and applications. *European Journal of Nuclear Medicine and Molecular Imaging*, 46(2):501–518, 2019. doi: 10.1007/s00259-018-4153-6.
- [9] Solène Marie, Claude Comtat, Fabien Caillé, Laurent Becquemont, Michel Bottlaender, and Nicolas Tournier. 11 C-glyburide PET imaging unveils the negligible brain penetration of glyburide in humans. *Neurology*, 92(17):813–814, apr 2019. doi: 10.1212/WNL.0000000000007378.
- [10] Andrew J. Reader and Jeroen Verhaeghe. 4D image reconstruction for emission tomography. *Physics in Medicine and Biology*, 59(22):R371–R418, 2014. doi: 10.1088/0031-9155/59/22/R371.
- [11] Thibaut Merlin, Simon Stute, Didier Benoit, Julien Bert, Thomas Carlier, Claude Comtat, Marina Filipovic, Frédéric Lamare, and Dimitris Visvikis. CASToR: a generic data organization and processing code framework for multi-modal and multi-dimensional tomographic reconstruction. *Physics in Medicine & Biology*, 63(18):185005, sep 2018. doi: 10.1088/1361-6560/aadac1.
- [12] I. George Zubal, Charles R. Harrell, Eileen O. Smith, Zachary Rattner, Gene Gindi, and Paul B. Hoffer. Computerized three-dimensional segmented human anatomy. *Medical Physics*, 21(2):299–302, feb 1994. doi: 10.1118/1.597290.
- [13] Joel S. Karp, Varsha Viswanath, Michael J. Geagan, Gerd Muehllehner, Austin R. Pantel, Michael J. Parma, Amy E. Perkins, Jeffrey P. Schmall, Matthew E. Werner, and Margaret E. Daube-Witherspoon. PennPET explorer: Design and preliminary performance of a whole-body imager. *Journal of Nuclear Medicine*, 61(1):136–143, 2020. doi: 10.2967/jnumed.119.229997.
- [14] SB Siegel, A Mehmet, H Bal, B Bendriem, D Bharkhada, J Cabello, L Eriksson, V Panin, H Rothfuss, and M Conti. Preliminary Performance of a Prototype, One Meter Long PET Tomograph. In *2020 IEEE Nuclear Science Symposium and Medical Imaging Conference (NSS/MIC)*, pages 1–2, 2020.
- [15] Simon R Cherry, Terry Jones, Joel S Karp, Jinyi Qi, William W Moses, and Ramsey D Badawi. Total-Body PET: Maximizing Sensitivity to Create New Opportunities for Clinical Research and Patient Care. *Journal of Nuclear Medicine*, 59(1):3–12, jan 2018. doi: 10.2967/jnumed.116.184028.
- [16] Jicun Hu, Vladimir Panin, Anne M. Smith, Bruce Spottiswoode, Vijay Shah, Carl CA von Gall, Matthew Baker, William Howe, Frank Kehren, Michael Casey, and Bernard Bendriem. Design and Implementation of Automated Clinical Whole Body Parametric PET With Continuous Bed Motion. *IEEE Transactions on Radiation and Plasma Medical Sciences*, 4(6):696–707, nov 2020. doi: 10.1109/TRPMS.2020.2994316.

- [17] Florent L. Besson, Brice Fernandez, Sylvain Faure, Olaf Mercier, Andrei Seferian, Xavier Mignard, Sacha Mussot, Cecile le Pechoux, Caroline Caramella, Angela Botticella, Antonin Levy, Florence Parent, Sophie Bulifon, David Montani, Delphine Mitilian, Elie Fadel, David Planchard, Benjamin Besse, Maria Rosa Ghigna-Bellinzoni, Claude Comtat, Vincent Lebon, and Emmanuel Durand. 18F-FDG PET and DCE kinetic modeling and their correlations in primary NSCLC: first voxel-wise correlative analysis of human simultaneous [18F]FDG PET-MRI data. *EJNMMI Research*, 10(1), 2020. doi: 10.1186/s13550-020-00671-9.
- [18] Adriaan A. Lammertsma. Forward to the past: The case for quantitative PET imaging. *Journal of Nuclear Medicine*, 58(7):1019–1024, 2017. doi: 10.2967/jnumed.116.188029.
- [19] Riemer H. J. A. Slart, Charalampos Tsoumpas, Andor W. J. M. Glaudemans, Walter Noordzij, Antoon T. M. Willemse, Ronald J. H. Borra, Rudi A. J. O. Dierckx, and Adriaan A. Lammertsma. Long axial field of view PET scanners: a road map to implementation and new possibilities. *European Journal of Nuclear Medicine and Molecular Imaging*, June 2021. doi: 10.1007/s00259-021-05461-6.
- [20] Jean-Dominique Gallezot, Yihuan Lu, Mika Naganawa, and Richard E. Carson. Parametric Imaging With PET and SPECT. *IEEE Transactions on Radiation and Plasma Medical Sciences*, 4(1):1–23, 2019. doi: 10.1109/trpms.2019.2908633.
- [21] M M Ter-Pogossian, M E Phelps, E J Hoffman, and N a Mullani. A positron-emission transaxial tomograph for nuclear imaging (PETT). *Radiology*, 114(5):89–98, 1975. doi: 10.1148/114.1.89.
- [22] M. E. Phelps, E. J. Hoffman, N. A. Mullani, and M. M. Ter Pogossian. Application of annihilation coincidence detection to transaxial reconstruction tomography. *Journal of Nuclear Medicine*, 16(3): 210–224, 1975.
- [23] Ronald Nutt. 1999 ICP Distinguished Scientist Award. The history of positron emission tomography. *Molecular imaging and biology*, 4(1):11–26, 2002. doi: 10.1016/s1095-0397(00)00051-0.
- [24] M. Dahlbom, E. J. Hoffman, C. K. Hoh, C. Schiepers, G. Rosenqvist, R. A. Hawkins, and M. E. Phelps. Whole-body positron emission tomography: Part I. Methods and performance characteristics. *Journal of Nuclear Medicine*, 33(6):1191–1199, 1992.
- [25] J. B. Bomanji, D. C. Costa, and P. J. Ell. Clinical role of positron emission tomography in oncology. *Lancet Oncology*, 2(3):157–164, 2001. doi: 10.1016/S1470-2045(00)00257-6.
- [26] Terry Jones and David Townsend. History and future technical innovation in positron emission tomography. *Journal of Medical Imaging*, 4(1):011013, 2017. doi: 10.1117/1.jmi.4.1.011013.
- [27] Kengo Shibuya, E. Yoshida, F. Nishikido, T. Suzuki, T. Tsuda, N. Inadama, T. Yamaya, and H. Mu-

- rayama. Limit of Spatial Resolution in FDG-PET due to Annihilation Photon Non-Collinearity. In *World Congress on Medical Physics and Biomedical Engineering 2006*, volume 14, pages 1667–1671. Springer Berlin Heidelberg, Berlin, Heidelberg, 2007. ISBN 9783540368397. doi: 10.1007/978-3-540-36841-0_411.
- [28] Maurizio Conti and Lars Eriksson. Physics of pure and non-pure positron emitters for PET: A review and a discussion. *EJNMMI Physics*, 3(1), 2016. doi: 10.1186/s40658-016-0144-5.
- [29] J Anthony Seibert and John M Boone. Part 2: X-ray interactions and image formation. *J Nucl Med Technol*, 33(1):3–18, 2005.
- [30] P. E. Kinahan, D. W. Townsend, T. Beyer, and D. Sashin. Attenuation correction for a combined 3D PET/CT scanner. *Medical Physics*, 25(10):2046–2063, oct 1998. doi: 10.1118/1.598392.
- [31] C. C. Watson, D. Newport, and M. E. Casey. A single scatter simulation technique for scatter correction in 3d PET. In *Computational Imaging and Vision*, pages 255–268. Springer Netherlands, 1996. doi: 10.1007/978-94-015-8749-5_18.
- [32] Irene Polycarpou, Kris Thielemans, Ravindra Manjeshwar, Pablo Aguiar, Paul K. Marsden, and Charalampos Tsoumpas. Comparative evaluation of scatter correction in 3D PET using different scatter-level approximations. *Annals of Nuclear Medicine*, 25(9):643–649, 2011. doi: 10.1007/s12149-011-0514-y.
- [33] Dale L Bailey, David W Townsend, Peter E Valk, and Michael N Maisey. *Positron Emission Tomography*. Springer-Verlag, London, 2005. ISBN 1-85233-798-2. doi: 10.1007/b136169.
- [34] Frederic H Fahey. Data Acquisition in PET Imaging. *J Nucl Med Technol*, 30:39–49, 2002.
- [35] Simon R Cherry and Magnus Dahlbom. Pet: Physics, instrumentation, and scanners. In *PET*, pages 1–124. Springer, 2004.
- [36] Martin A. Belzunce and Andrew J. Reader. Assessment of the impact of modeling axial compression on PET image reconstruction. *Medical Physics*, 44(10):5172–5186, 2017. doi: 10.1002/mp.12454.
- [37] F. Natterer. *The Mathematics of Computerized Tomography*. Society for Industrial and Applied Mathematics, January 2001. doi: 10.1137/1.9780898719284.
- [38] David W. Townsend. Combined Positron Emission Tomography-Computed Tomography: The Historical Perspective. *Seminars in Ultrasound, CT and MRI*, 29(4):232–235, 2008. doi: 10.1053/j.sult.2008.05.006.
- [39] Thomas Beyer, David W. Townsend, Tony Brun, Paul E. Kinahan, Martin Charron, Raymond Roddy,

- Jeff Jerin, John Young, Larry Byars, and Ronald Nutt. A Combined PET/CT Scanner for Clinical Oncology. *Journal of Nuclear Medicine*, 41(8), 2000.
- [40] Armin Kolb, Hans F. Wehrli, Matthias Hofmann, Martin S. Judenhofer, Lars Eriksson, Ralf Ladebeck, Matthias P. Lichy, Larry Byars, Christian Michel, Heinz Peter Schlemmer, Matthias Schmand, Claus D. Claussen, Vesna Sossi, and Bernd J. Pichler. Technical performance evaluation of a human brain PET/MRI system. *European Radiology*, 22(8):1776–1788, aug 2012. doi: 10.1007/s00330-012-2415-4.
- [41] Jonathan A. Disselhorst, Ilja Bezrukov, Armin Kolb, Christoph Parl, and Bernd J. Pichler. Principles of PET/MR imaging, jun 2014.
- [42] H. Zaidi, N. Ojha, M. Morich, J. Griesmer, Z. Hu, P. Maniawski, O. Ratib, D. Izquierdo-Garcia, Z. A. Fayad, and L. Shao. Design and performance evaluation of a whole-body Ingenuity TF PET-MRI system. *Physics in Medicine and Biology*, 56(10):3091–3106, 2011. doi: 10.1088/0031-9155/56/10/013.
- [43] Patrick Veit-Haibach, Felix Pierre Kuhn, Florian Wiesinger, Gaspar Delso, and Gustav Von Schulthess. PET-MR imaging using a tri-modality PET/CT-MR system with a dedicated shuttle in clinical routine. *Magnetic Resonance Materials in Physics, Biology and Medicine*, 26(1):25–35, 2013. doi: 10.1007/s10334-012-0344-5.
- [44] Yiping Shao, Simon R. Cherry, Keyvan Farahani, Ken Meadors, Stefan Siegel, Robert W. Silverman, and Paul K. Marsden. Simultaneous PET and MR imaging. *Physics in Medicine and Biology*, 42(10):1965–1970, oct 1997. doi: 10.1088/0031-9155/42/10/010.
- [45] Jane E. Mackewn, Philip Halsted, Charles Edwards Geoffrey, Richard Page, John J. Totman, Kavitha Sunassee, Daniel Strul, William A. Hallett, Jauregui Osoro Maite, Peter Liepins, Steven C.R. Williams, Tobias Schaeffter, Stephen F. Keevil, and Paul K. Marsden. Performance evaluation of an MRI-compatible pre-clinical PET system using long optical fibers. *IEEE Transactions on Nuclear Science*, 57(3 PART 1):1052–1062, jun 2010. doi: 10.1109/TNS.2010.2044891.
- [46] Gaspar Delso, Sebastian Fürst, Björn Jakoby, Ralf Ladebeck, Carl Ganter, Stephan G. Nekolla, Markus Schwaiger, and Sibylle I. Ziegler. Performance measurements of the siemens mMR integrated whole-body PET/MR scanner. *Journal of Nuclear Medicine*, 52(12):1914–1922, dec 2011. doi: 10.2967/jnumed.111.092726.
- [47] Alexander M. Grant, Timothy W. Deller, Mohammad Mehdi Khalighi, Sri Harsha Maramraju, Gaspar Delso, and Craig S. Levin. NEMA NU 2-2012 performance studies for the SiPM-based ToF-PET

- component of the GE SIGNA PET/MR system. *Medical Physics*, 43(5):2334–2343, apr 2016. doi: 10.1118/1.4945416.
- [48] Craig S. Levin, Sri Harsha Maramraju, Mohammad Mehdi Khalighi, Timothy W. Deller, Gaspar Delso, and Floris Jansen. Design Features and Mutual Compatibility Studies of the Time-of-Flight PET Capable GE SIGNA PET/MR System. *IEEE Transactions on Medical Imaging*, 35(8):1907–1914, aug 2016. doi: 10.1109/TMI.2016.2537811.
- [49] Tinsu Pan, Samuel A. Einstein, Srinivas Cheenu Kappadath, Kira S. Grogg, Cristina Lois Gomez, Adam M. Alessio, William C. Hunter, Georges El Fakhri, Paul E. Kinahan, and Osama R. Mawlawi. Performance evaluation of the 5-ring GE discovery MI PET/CT system using the national electrical manufacturers association NU 2-2012 standard. *Medical Physics*, 46(7):3025–3033, May 2019. doi: 10.1002/mp.13576.
- [50] S. Ross, C. Stearns, R. Manjeshwar, and M. Iatrou. A method of overlap correction for fully 3D OSEM reconstruction of PET data. *IEEE Nuclear Science Symposium Conference Record*, 6(3):3497–3500, 2004. doi: 10.1109/nssmic.2004.1466640.
- [51] S. Stute and C. Comtat. Could Simultaneous Reconstruction of Multiple Bed Positions Have Benefits in Whole-Body PET ? In *2014 IEEE Nuclear Science Symposium and Medical Imaging Conference (NSS/MIC)*, 2014.
- [52] Magnus Dahlbom, Johnny Reed, and John Young. Implementation of true continuous bed motion in 2-D and 3-D whole-body PET scanning. *IEEE Transactions on Nuclear Science*, 48(4 II):1465–1469, 2001. doi: 10.1109/23.958381.
- [53] D. Brasse, D. Newport, J. P. Carney, J. T. Yap, C. Reynolds, J. Reed, J. Bao, P. Luk, C. Michel, and D. W. Townsend. Continuous bed motion acquisition on a whole body combined PET/CT system. *IEEE Nuclear Science Symposium and Medical Imaging Conference*, 2:951–955, 2002. doi: 10.1109/nssmic.2002.1239481.
- [54] Imke Schatka, Desiree Weiberg, Stephanie Reichelt, Nicole Owsianski-Hille, Thorsten Derlin, Georg Berding, and Frank M. Bengel. A randomized, double-blind, crossover comparison of novel continuous bed motion versus traditional bed position whole-body PET/CT imaging. *European Journal of Nuclear Medicine and Molecular Imaging*, 43(4):711–717, 2016. doi: 10.1007/s00259-015-3226-z.
- [55] Nicolas A. Karakatsanis, Michael E. Casey, Martin A. Lodge, Arman Rahmim, and Habib Zaidi. Whole-body direct 4D parametric PET imaging employing nested generalized Patlak expectation-

- maximization reconstruction. *Physics in Medicine and Biology*, 61(15):5456–5485, 2016. doi: 10.1088/0031-9155/61/15/5456.
- [56] Guillaume Fahrni, Nicolas A. Karakatsanis, Giulia Di Domenicantonio, Valentina Garibotto, and Habib Zaidi. Does whole-body Patlak 18F-FDG PET imaging improve lesion detectability in clinical oncology? *European Radiology*, 2019. doi: 10.1007/s00330-018-5966-1.
- [57] André Dias, Mette Pedersen, Helle Danielsen, Ole Munk, and Lars Gormsen. Improved lesion detection in whole-body parametric 18f-fdg pet/ct vs. static 18f-fdg pet/ct. *Journal of Nuclear Medicine*, 61 (supplement 1):97–97, 2020.
- [58] Suleman Surti, Austin R. Pantel, and Joel S. Karp. Total Body PET: Why, How, What for? *IEEE Transactions on Radiation and Plasma Medical Sciences*, 4(3):283–292, 2020. doi: 10.1109/trpms.2020.2985403.
- [59] Simon R. Cherry, Terry Jones, Joel S. Karp, Jinyi Qi, William Moses, and Ramsey Badawi. Total-Body Pet: Maximizing Sensitivity To Create New Opportunities for Clinical Research and Patient Care. *Journal of Nuclear Medicine*, page jnumed.116.184028, 2017. doi: 10.2967/jnumed.116.184028.
- [60] Ramsey D. Badawi, Hongcheng Shi, Pengcheng Hu, Shuguang Chen, Tianyi Xu, Patricia M. Price, Yu Ding, Benjamin A. Spencer, Lorenzo Nardo, Weiping Liu, Jun Bao, Terry Jones, Hongdi Li, and Simon R. Cherry. First human imaging studies with the explorer total-body PET scanner. *Journal of Nuclear Medicine*, 60(3):299–303, 2019. doi: 10.2967/jnumed.119.226498.
- [61] Austin R. Pantel, Varsha Viswanath, Margaret E. Daube-Witherspoon, Jacob G. Dubroff, Gerd Muehllehner, Michael J. Parma, Daniel A. Pryma, Erin K. Schubert, David A. Mankoff, and Joel S. Karp. PennPET explorer: Human imaging on a whole-body imager. *Journal of Nuclear Medicine*, 61 (1):144–151, 2020. doi: 10.2967/jnumed.119.231845.
- [62] Xuezhu Zhang, Zhaocheng Xie, Eric Berg, Martin S. Judenhofer, Weiping Liu, Tianyi Xu, Yu Ding, Yang Lv, Yun Dong, Zilin Deng, Songsong Tang, Hongcheng Shi, Pengcheng Hu, Shuguang Chen, Jun Bao, Hongdi Li, Jian Zhou, Guobao Wang, Simon R. Cherry, Ramsey D. Badawi, and Jinyi Qi. Total-body dynamic reconstruction and parametric imaging on the uexplorer. *Journal of Nuclear Medicine*, 61(2): 285–291, 2020. doi: 10.2967/jnumed.119.230565.
- [63] Xuezhu Zhang, Simon R. Cherry, Zhaocheng Xie, Hongcheng Shi, Ramsey D. Badawi, and Jinyi Qi. Subsecond total-body imaging using ultrasensitive positron emission tomography. *Proceedings of the National Academy of Sciences of the United States of America*, 117(5):2265–2267, 2020. doi: 10.1073/pnas.1917379117.

- [64] Guobao Wang, Mamta Parikh, Lorenzo Nardo, Yang Zuo, Yasser Abdelhafez, Jinyi Qi, Terry Jones, Patricia Price, Simon Cherry, Chong-Xian Pan, and Ramsey Badawi. Total-body dynamic pet of metastatic cancer: First patient results. *Journal of Nuclear Medicine*, 61(supplement 1):208–208, 2020.
- [65] Tao Feng, Yizhang Zhao, Hongcheng Shi, Hongdi Li, Xuezhu Zhang, Guobao Wang, Ramsey D. Badawi, Patricia M. Price, Terry Jones, and Simon R. Cherry. The Effects of Delay on the Input Function for Early Dynamics in Total Body Parametric Imaging. *2019 IEEE Nuclear Science Symposium and Medical Imaging Conference, NSS/MIC 2019*, 2019. doi: 10.1109/NSS/MIC42101.2019.9059886.
- [66] Tao Feng, Yizhang Zhao, Hongcheng Shi, Hongdi Li, Xuezhu Zhang, Guobao Wang, Patricia M. Price, Ramsey D. Badawi, Simon R. Cherry, and Terry Jones. Total-Body Quantitative Parametric Imaging of Early Kinetics of ¹⁸ F-FDG . *Journal of Nuclear Medicine*, 62(5):738–744, 2021. doi: 10.2967/jnumed.119.238113.
- [67] Guobing Liu, Pengcheng Hu, Haojun Yu, Hui Tan, Yiqiu Zhang, Hongyan Yin, Yan Hu, Jianying Gu, and Hongcheng Shi. Ultra-low-activity total-body dynamic PET imaging allows equal performance to full-activity PET imaging for investigating kinetic metrics of ¹⁸F-FDG in healthy volunteers. *European Journal of Nuclear Medicine and Molecular Imaging*, January 2021. doi: 10.1007/s00259-020-05173-3.
- [68] Albert Gjedde. Calculation of cerebral glucose phosphorylation from brain uptake of glucose analogs in vivo: A re-examination. *Brain Research Reviews*, 4(2):237–274, jun 1982. doi: 10.1016/0165-0173(82)90018-2.
- [69] Clifford S Patlak and Ronald G Blasberg. Graphical Evaluation of Blood-to-Brain Transfer Constants from Multiple-Time Uptake Data. Generalizations. *Journal of Cerebral Blood Flow & Metabolism*, 5(4):584–590, dec 1985. doi: 10.1038/jcbfm.1985.87.
- [70] Vincent J. Cunningham and Terry Jones. Spectral Analysis of Dynamic PET Studies. *Journal of Cerebral Blood Flow & Metabolism*, 13(1):15–23, jan 1993. doi: 10.1038/jcbfm.1993.5.
- [71] Roger N. Gunn, Steve R. Gunn, Federico E. Turkheimer, John A. D. Aston, and Vincent J. Cunningham. Positron Emission Tomography Compartmental Models: A Basis Pursuit Strategy for Kinetic Modeling. *Journal of Cerebral Blood Flow & Metabolism*, 22(12):1425–1439, dec 2002. doi: 10.1097/01.wcb.0000045042.03034.42.
- [72] Mattia Veronese, Gaia Rizzo, Alessandra Bertoldo, and Federico E. Turkheimer. Spectral Analysis of Dynamic PET Studies: A Review of 20 Years of Method Developments and Applications. *Computational and Mathematical Methods in Medicine*, 2016, 2016. doi: 10.1155/2016/7187541.

- [73] Solène Marie, Salvatore Cisternino, Irène Buvat, Xavier Declèves, and Nicolas Tournier. Imaging Probes and Modalities for the Study of Solute Carrier O (SLCO)-Transport Function In Vivo. *Journal of Pharmaceutical Sciences*, 106(9):2335–2344, 2017. doi: 10.1016/j.xphs.2017.04.031.
- [74] Nicolas Tournier, Wadad Saba, Salvatore Cisternino, Marie Anne Peyronneau, Annelaure Damont, Sébastien Goutal, Albertine Dubois, Frédéric Dollé, Jean Michel Scherrmann, Héric Valette, Bertrand Kuhnast, and Michel Bottlaender. Effects of selected OATP and/or ABC transporter inhibitors on the brain and whole-body distribution of glyburide. *AAPS Journal*, 15(4):1082–1090, 2013. doi: 10.1208/s12248-013-9514-2.
- [75] Fabien Caillé, Philippe Gervais, Sylvain Auvity, Christine Coulon, Solène Marie, Nicolas Tournier, and Bertrand Kuhnast. Automated two-step manufacturing of [¹¹C]glyburide radiopharmaceutical for PET imaging in humans. *Nuclear Medicine and Biology*, 84-85:20–27, may 2020. doi: 10.1016/j.nucmedbio.2019.12.008.
- [76] Michael Winterdahl, Susanne Keiding, Michael Sørensen, Frank Viborg Mortensen, Aage Kristian Olsen Alstrup, and Ole Lajord Munk. Tracer input for kinetic modelling of liver physiology determined without sampling portal venous blood in pigs. *European Journal of Nuclear Medicine and Molecular Imaging*, 38(2):263–270, 2011. doi: 10.1007/s00259-010-1620-0.
- [77] N. Kudomi, L. Slimani, M. J. Järvisalo, J. Kiss, R. Lautamäki, G. A. Naum, T. Savunen, J. Knuuti, H. Iida, P. Nuutila, and P. Iozzo. Non-invasive estimation of hepatic blood perfusion from H₂15O PET images using tissue-derived arterial and portal input functions. *European Journal of Nuclear Medicine and Molecular Imaging*, 35(10):1899–1911, 2008. doi: 10.1007/s00259-008-0796-z.
- [78] Guobao Wang, Michael T. Corwin, Kristin A. Olson, Ramsey D. Badawi, and Souvik Sarkar. Dynamic PET of human liver inflammation: Impact of kinetic modeling with optimization-derived dual-blood input function. *Physics in Medicine and Biology*, 63(15), 2018. doi: 10.1088/1361-6560/aac8cb.
- [79] Irene Hernández Lozano, Rudolf Karch, Martin Bauer, Matthias Blaickner, Akihiro Matsuda, Beatrix Wulkersdorfer, Marcus Hacker, Markus Zeitlinger, and Oliver Langer. Towards Improved Pharmacokinetic Models for the Analysis of Transporter-Mediated Hepatic Disposition of Drug Molecules with Positron Emission Tomography. *AAPS Journal*, 21(4):1–14, 2019. doi: 10.1208/s12248-019-0323-0.
- [80] Jingnan Wang, Yunwen Shao, Bowei Liu, Xuezhu Wang, Barbara Katharina Geist, Xiang Li, Fang Li, Haitao Zhao, Marcus Hacker, Haiyan Ding, Hui Zhang, and Li Huo. Dynamic 18F-FDG PET imaging of liver lesions: evaluation of a two-tissue compartment model with dual blood input function. *BMC Medical Imaging*, 21(1):1–13, 2021. doi: 10.1186/s12880-021-00623-2.

- [81] Johann Radon. Über die bestimmung von funktionen durch ihre integralwerte längs gewisser manigfaltigkeiten. *Ber. Verh. Saechs. Akad. Wiss. Leipzig Math. Phys. Kl.*, 69:262, 1917.
- [82] Johann Radon. On the determination of functions from their integral values along certain manifolds (Translation of 1917 original). *IEEE Transactions on Medical Imaging*, 5(4):170–176, dec 1986. doi: 10.1109/TMI.1986.4307775.
- [83] Robert L. Siddon. Fast calculation of the exact radiological path for a three dimensional CT array, 1985.
- [84] Bruno De Man and Samit Basu. Distance-driven projection and backprojection in three dimensions. *Physics in Medicine and Biology*, 49(11):2463–2475, 2004. doi: 10.1088/0031-9155/49/11/024.
- [85] Peter M. Joseph. An Improved Algorithm for Reprojecting Rays Through Pixel Images. *IEEE Transactions on Medical Imaging*, 1(3):192–196, 1982. doi: 10.1109/TMI.1982.4307572.
- [86] Sascha Moehrs, Michel Defrise, Nicola Belcari, Alberto Del Guerra, Antonietta Bartoli, Serena Fabbri, and Gianluigi Zanetti. Multi-ray-based system matrix generation for 3D PET reconstruction. *Physics in Medicine and Biology*, 53(23):6925–6945, 2008. doi: 10.1088/0031-9155/53/23/018.
- [87] Simon Stute and Claude Comtat. Practical considerations for image-based PSF and blobs reconstruction in PET. *Physics in Medicine and Biology*, 58(11):3849–3870, jun 2013. doi: 10.1088/0031-9155/58/11/3849.
- [88] Marina Filipović, Claude Comtat, and Simon Stute. Time-of-flight (TOF) implementation for PET reconstruction in practice. *Physics in Medicine & Biology*, 64(23):23NT01, nov 2019. doi: 10.1088/1361-6560/ab4f0b.
- [89] Y. Vardi, L. A. Shepp, and L. Kaufman. A statistical model for positron emission tomography. *Journal of the American Statistical Association*, 80(389):8–20, 1985. doi: 10.1080/01621459.1985.10477119.
- [90] K. Lange and R. Carson. EM reconstruction algorithms for emission and transmission tomography. *Journal of Computer Assisted Tomography*, 8(2):306–316, 1984.
- [91] A P Dempster, N M Laird, and D B Rubin. Maximum Likelihood from Incomplete Data via the EM Algorithm. *Journal of the Royal Statistical Society. Series B (Methodological)*, 39(1):1–38, 1977.
- [92] Richard E. Carson and Kenneth Lange. Comment: The EM parametric image reconstruction algorithm. *Journal of the American Statistical Association*, 80(389):20–22, 1985. doi: 10.1080/01621459.1985.10477120.
- [93] Julian Matthews, John Ashburner, Dale Bailey, Robert Harte, Pat Price, and Terry Jones. Direct

- calculation of parametric images from raw pet data using maximum likelihood iterative reconstruction. *IEEE Nuclear Science Symposium & Medical Imaging Conference*, 2:1311–1315, 1995. doi: 10.1109/nssmic.1995.510499.
- [94] Charalampos Tsoumpas, Federico E. Turkheimer, and Kris Thielemans. Study of direct and indirect parametric estimation methods of linear models in dynamic positron emission tomography. *Medical Physics*, 35(4):1299–1309, 2008. doi: 10.1118/1.2885369.
- [95] Inki Hong and Andrew J. Reader. Ultra fast 4D PET image reconstruction with user-definable temporal basis functions. *IEEE Nuclear Science Symposium Conference Record*, pages 5475–5478, 2008. doi: 10.1109/NSSMIC.2008.4774492.
- [96] Georgios I. Angelis, Kris Thielemans, Andri C. Tziortzi, Federico E. Turkheimer, and Charalampos Tsoumpas. Convergence optimization of parametric MLEM reconstruction for estimation of Patlak plot parameters. *Computerized Medical Imaging and Graphics*, 35(5):407–416, 2011. doi: 10.1016/j.compmedimag.2011.01.002.
- [97] Guobao Wang and Jinyi Qi. Acceleration of the direct reconstruction of linear parametric images using nested algorithms. *Physics in Medicine and Biology*, 55(5):1505–1517, 2010. doi: 10.1088/0031-9155/55/5/016.
- [98] J C Matthews, G I Angelis, F A Kotasidis, P J Markiewicz, and A J Reader. Direct reconstruction of parametric images using any spatiotemporal 4D image based model and maximum likelihood expectation maximisation. In *IEEE Nuclear Science Symposium & Medical Imaging Conference*. IEEE, October 2010. doi: 10.1109/nssmic.2010.5874225.
- [99] Kenneth Lange, Avid R. Hunter, and Ilsoon Yang. Optimization Transfer Using Surrogate Objective Functions. *Journal of Computational and Graphical Statistics*, 9(1):1–20, 2000. doi: 10.1080/10618600.2000.10474858.
- [100] Paul Gravel and Andrew J. Reader. Direct 4D PET MLEM reconstruction of parametric images using the simplified reference tissue model with the basis function method for [11C]raclopride. *Physics in Medicine and Biology*, 60(11):4533–4549, 2015. doi: 10.1088/0031-9155/60/11/4533.
- [101] Guobao Wang and Jinyi Qi. Direct estimation of kinetic parametric images for dynamic PET. *Theranostics*, 3(10):802–815, 2013. doi: 10.7150/thno.5130.
- [102] Georgios I. Angelis, Julian C. Matthews, Fotis A. Kotasidis, Pawel J. Markiewicz, William R. Lionheart, and Andrew J. Reader. Evaluation of a direct 4D reconstruction method using generalised linear least

- squares for estimating nonlinear micro-parametric maps. *Annals of Nuclear Medicine*, 28(9):860–873, 2014. doi: 10.1007/s12149-014-0881-2.
- [103] Fotis A. Kotasidis, Julian C. Matthews, Andrew J. Reader, Georgios I. Angelis, Patricia M. Price, and Habib Zaidi. Direct parametric reconstruction for dynamic [18F]-FDG PET/CT imaging in the body. *IEEE Nuclear Science Symposium Conference Record*, pages 3383–3386, 2012. doi: 10.1109/NSSMIC.2012.6551770.
- [104] Jean-Dominique Gallezot, Yihuan Lu, Kathryn Fontaine, Chi Liu, and Richard E Carson. Strategies to improve direct EM patlak reconstructions. In *2017 IEEE Nuclear Science Symposium and Medical Imaging Conference (NSS/MIC)*. IEEE, October 2017. doi: 10.1109/nssmic.2017.8532674.
- [105] S Jan, D Benoit, E Becheva, T Carlier, F Cassol, P Descourt, T Frisson, L Grevillot, L Guigues, L Maigne, C Morel, Y Perrot, N Rehfeld, D Sarrut, D R Schaart, S Stute, U Pietrzyk, D Visvikis, N Zahra, and I Buvat. GATE V6: a major enhancement of the GATE simulation platform enabling modelling of CT and radiotherapy. *Physics in Medicine and Biology*, 56(4):881–901, feb 2011. doi: 10.1088/0031-9155/56/4/001.
- [106] Ronald Boellaard. Need for standardization of 18F-FDG PET/CT for treatment response assessments. *Journal of Nuclear Medicine*, 52(Suppl. 2):93–100, 2011. doi: 10.2967/jnumed.110.085662.
- [107] Antonia Dimitrakopoulou-Strauss, Leyun Pan, and Christos Sachpekidis. Kinetic modeling and parametric imaging with dynamic PET for oncological applications: general considerations, current clinical applications, and future perspectives. *European Journal of Nuclear Medicine and Molecular Imaging*, 48(1):21–39, 2021. doi: 10.1007/s00259-020-04843-6.
- [108] Guobao Wang, Lin Fu, and Jinyi Qi. Maximum a posteriori reconstruction of the Patlak parametric image from sinograms in dynamic PET. *Physics in Medicine and Biology*, 53(3):593–604, 2008. doi: 10.1088/0031-9155/53/3/006.
- [109] S Stute, C Tauber, C Leroy, M Bottlaender, V Bralon, and C Comtat. Analytical simulations of dynamic PET scans with realistic count rates properties. In *2015 IEEE Nuclear Science Symposium and Medical Imaging Conference (NSS/MIC)*, pages 1–3, 2015. doi: 10.1109/NSSMIC.2015.7582064.
- [110] Jicun Hu, Vladimir Panin, Frank Kehren, and Michel Casey. Gated reconstruction for PET scan with continuous bed motion. In *2014 IEEE Nuclear Science Symposium and Medical Imaging Conference (NSS/MIC)*, pages 1–3. IEEE, nov 2014. ISBN 978-1-4799-6097-2. doi: 10.1109/NSSMIC.2014.7430793.
- [111] M.E. Kamasak, C.A. Bouman, E.D. Morris, and K Sauer. Direct reconstruction of kinetic parameter

- images from dynamic PET data. *IEEE Transactions on Medical Imaging*, 24(5):636–650, may 2005. doi: 10.1109/TMI.2005.845317.
- [112] Philip Novosad and Andrew J. Reader. MR-guided dynamic PET reconstruction with the kernel method and spectral temporal basis functions. *Physics in Medicine and Biology*, 61(12):4624–4645, 2016. doi: 10.1088/0031-9155/61/12/4624.
- [113] Charles L. Lawson and Richard J. Hanson. *Solving Least Squares Problems*. Society for Industrial and Applied Mathematics, jan 1995. doi: 10.1137/1.9781611971217.
- [114] Andrew J. Reader, Julian C. Matthews, Florent C. Sureau, Claude Comtat, Régine Trébossen, and Irène Buvat. Fully 4D image reconstruction by estimation of an input function and spectral coefficients. *IEEE Nuclear Science Symposium Conference Record*, 5(1):3260–3267, 2007. doi: 10.1109/NSSMIC.2007.4436834.
- [115] F Turkheimer, R. M. Moresco, G. Lucignani, L Sokoloff, F Fazio, and K Schmidt. The use of spectral analysis to determine regional cerebral glucose utilization with positron emission tomography and [¹⁸F]fluorodeoxyglucose: Theory, implementation, and optimization procedures. *Journal of Cerebral Blood Flow and Metabolism*, 14(3):406–422, 1994. doi: 10.1038/jcbfm.1994.52.
- [116] Mattia Veronese, Alessandra Bertoldo, Shrinivas Bishu, Aaron Unterman, Giampaolo Tomasi, Carolyn Beebe Smith, and Kathleen C. Schmidt. A spectral analysis approach for determination of regional rates of cerebral protein synthesis with the L-1-11 Cleucine PET method. *Journal of Cerebral Blood Flow and Metabolism*, 30(8):1460–1476, 2010. doi: 10.1038/jcbfm.2010.26.
- [117] Mattia Veronese, Kathleen C. Schmidt, Carolyn Beebe Smith, and Alessandra Bertoldo. Use of spectral analysis with iterative filter for voxelwise determination of regional rates of cerebral protein synthesis with L-[1-¹¹C]leucine PET. *Journal of Cerebral Blood Flow and Metabolism*, 32(6):1073–1085, 2012. doi: 10.1038/jcbfm.2012.27.
- [118] Kuang Gong, Jinxiu Cheng-Liao, Guobao Wang, Kevin T. Chen, Ciprian Catana, and Jinyi Qi. Direct Patlak Reconstruction from Dynamic PET Data Using the Kernel Method with MRI Information Based on Structural Similarity. *IEEE Transactions on Medical Imaging*, 37(4):955–965, 2018. doi: 10.1109/TMI.2017.2776324.
- [119] Steven R. Meikle, Julian C. Matthews, Vincent J. Cunningham, Dale L. Bailey, Lefteris Livieratos, Terry Jones, and Pat Price. Parametric image reconstruction using spectral analysis of PET projection data. *Physics in Medicine and Biology*, 43(3):651–666, 1998. doi: 10.1088/0031-9155/43/3/016.
- [120] Neda Zaker, Fotis Kotasidis, Valentina Garibotto, and Habib Zaidi. Assessment of Lesion Detectability

- in Dynamic Whole-Body PET Imaging Using Compartmental and Patlak Parametric Mapping. *Clinical Nuclear Medicine*, 45(5):E221–E231, 2020. doi: 10.1097/RNU.00000000000002954.
- [121] Nicolas A. Karakatsanis, Valentina Garibotto, Olivier Rager, and Habib Zaidi. Continuous bed motion Vs. step-and-shoot acquisition on clinical whole-body dynamic and parametric PET imaging. In *2015 IEEE Nuclear Science Symposium and Medical Imaging Conference, NSS/MIC 2015*. Institute of Electrical and Electronics Engineers Inc., oct 2016. ISBN 9781467398626. doi: 10.1109/NSSMIC.2015.7582184.
- [122] Z Chalampalakis, S Stute, M Filipovic, S Marie, M Bottlaender, N Tournier, and C Comtat. Application of a generic dynamic reconstruction algorithm on PET whole-body pharmacokinetic studies. In *European Journal of Nuclear Medicine and Molecular Imaging*, volume 47, pages S416–S416, 2020.
- [123] F. A. Kotasidis, J. C. Matthews, A. J. Reader, G. I. Angelis, and H. Zaidi. Application of adaptive kinetic modelling for bias propagation reduction in direct 4D image reconstruction. *Physics in Medicine and Biology*, 59(20):6061–6084, 2014. doi: 10.1088/0031-9155/59/20/6061.
- [124] F. A. Kotasidis, A. Mehranian, and H. Zaidi. Impact of time-of-flight on indirect 3D and direct 4D parametric image reconstruction in the presence of inconsistent dynamic PET data. *Physics in Medicine and Biology*, 61(9):3443–3471, 2016. doi: 10.1088/0031-9155/61/9/3443.
- [125] Yang Zuo, Souvik Sarkar, Michael T Corwin, Kristin Olson, Ramsey D Badawi, and Guobao Wang. Structural and practical identifiability of dual-input kinetic modeling in dynamic PET of liver inflammation. *Physics in Medicine & Biology*, 64(17):175023, sep 2019. doi: 10.1088/1361-6560/ab1f29.
- [126] P. J. Schleyer, J. T. Dunn, S. Reeves, S. Brownings, P. K. Marsden, and K. Thielemans. Detecting and estimating head motion in brain PET acquisitions using raw time-of-flight PET data. *Physics in Medicine and Biology*, 60(16):6441–6458, 2015. doi: 10.1088/0031-9155/60/16/6441.
- [127] Adam Kesner, C Ross Schmidlein, and Claudia Kuntner. Real-time data-driven motion correction in PET. *EJNMMI Physics*, 6(1):3, dec 2019. doi: 10.1186/s40658-018-0240-9.
- [128] Yihuan Lu, Mika Naganawa, Takuya Toyonaga, Jean Dominique Gallezot, Kathryn Fontaine, Silin Ren, Enette Mae Revilla, Tim Mulnix, and Richard E. Carson. Data-Driven Motion Detection and Event-by-Event Correction for Brain PET: Comparison with Vicra. *Journal of nuclear medicine : official publication, Society of Nuclear Medicine*, 61(9):1397–1403, 2020. doi: 10.2967/jnumed.119.235515.
- [129] Alexandre Bousse, Richard Manber, Beverley F. Holman, David Atkinson, Simon Arridge, Sébastien Ourselin, Brian F. Hutton, and Kris Thielemans. Evaluation of a direct motion estimation/correction

- method in respiratory-gated PET/MRI with motion-adjusted attenuation. *Medical Physics*, 44(6):2379–2390, 2017. doi: 10.1002/mp.12253.
- [130] Jieqing Jiao, Alexandre Bousse, Kris Thielemans, Ninon Burgos, Philip S. J. Weston, Jonathan M. Schott, David Atkinson, Simon R. Arridge, Brian F. Hutton, Paweł Markiewicz, and Sébastien Ourselin. Direct Parametric Reconstruction With Joint Motion Estimation/Correction for Dynamic Brain PET Data. *IEEE Transactions on Medical Imaging*, 36(1):203–213, jan 2017. doi: 10.1109/TMI.2016.2594150.
- [131] Bo Zhou, Yu-Jung Tsai, and Chi Liu. Simultaneous denoising and motion estimation for low-dose gated PET using a siamese adversarial network with gate-to-gate consistency learning. In *Medical Image Computing and Computer Assisted Intervention – MICCAI 2020*, pages 743–752. Springer International Publishing, 2020. doi: 10.1007/978-3-030-59728-3_72.
- [132] Bo Zhou, Yu Jung Tsai, Xiongchao Chen, James S. Duncan, and Chi Liu. MDPET: A Unified Motion Correction and Denoising Adversarial Network for Low-dose Gated PET. *IEEE Transactions on Medical Imaging*, XX(Xx):1–12, 2021. doi: 10.1109/TMI.2021.3076191.
- [133] Vladimir Panin, Eva Panin, Deepak Bharkhada, and William Whiteley. Respiratory motion correction in long axial fov scanners. *Journal of Nuclear Medicine*, 62(supplement 1):1551–1551, 2021.
- [134] Charalampos Tsoumpas, Jane E. MacKewn, Philip Halsted, Andrew P. King, Christian Buerger, John J. Totman, Tobias Schaeffter, and Paul K. Marsden. Simultaneous PET-MR acquisition and MR-derived motion fields for correction of non-rigid motion in PET. *Annals of Nuclear Medicine*, 24(10):745–750, 2010. doi: 10.1007/s12149-010-0418-2.
- [135] Ciprian Catana. Motion Correction Options in PET/MRI. *Seminars in Nuclear Medicine*, 45(3):212–223, may 2015. doi: 10.1053/j.semnuclmed.2015.01.001.
- [136] Richard Leahy, Ronald Boellaard, and Habib Zaidi. Whole-body parametric PET imaging will replace conventional image-derived PET metrics in clinical oncology. *Medical Physics*, 45(12):5355–5358, 2018. doi: 10.1002/mp.13266.
- [137] Zacharias Chalampalakis, Simon Stute, Marina Filipovic, Thibaut Merlin, and Claude Comtat. Whole-body dynamic PET: Effect of temporal gaps on FDG Ki quantification from 3D and 4D reconstruction algorithms. In *2019 IEEE Nuclear Science Symposium and Medical Imaging Conference (NSS/MIC)*. IEEE, October 2019. doi: 10.1109/nss/mic42101.2019.9059840.
- [138] Julian C. Matthews, Andrew J. Reader, Georgios I. Angelis, Pat M. Price, Paweł J. Markiewicz, and Fotis A. Kotasidis. Adaptive parametric kinetic modelling for improved full field of view fitting of PET

- data. *IEEE Nuclear Science Symposium Conference Record*, pages 3925–3929, 2012. doi: 10.1109/NSSMIC.2012.6551900.
- [139] Gaël Guennebaud, Benoît Jacob, et al. Eigen v3. <http://eigen.tuxfamily.org>, 2010.
- [140] Mary Germino, Albert J. Sinusas, Chi Liu, and Richard E. Carson. Assessment of kinetic modeling quality of fit by cluster analysis of residuals: Application to direct reconstruction of cardiac PET data. *2015 IEEE Nuclear Science Symposium and Medical Imaging Conference, NSS/MIC 2015*, pages 6–9, 2016. doi: 10.1109/NSSMIC.2015.7582243.
- [141] Lalith Kumar Shiyam Sundar, David Iommi, Otto Muzik, Zacharias Chalampalakis, Eva-Maria Klebermass, Marius Hienert, Lucas Rischka, Rupert Lanzenberger, Andreas Hahn, Ekaterina Pataria, Tatjana Traub-Weidinger, Johann Hummel, and Thomas Beyer. Conditional generative adversarial networks aided motion correction of dynamic 18f-FDG PET brain studies. *Journal of Nuclear Medicine*, 62(6):871–880, November 2020. doi: 10.2967/jnumed.120.248856.

Appendices

Appendix A

Multi-bed Dynamic Whole Body PET: Data exportation and processing

Dynamic Whole Body Protocol implementation for IsotoPK study

The implementation of the DWB protocol used for human subjects of the IsotoPK study on the Signa PET/MR was made using a series of multiple static WB sweeps from a typical WB static protocol. Details of the WB passes are given in table A.1.

Export and offline reconstruction of IsotoPK DWB data

Reconstruction of DWB on the Signa PET-MR console is made with certain limitations and does not allow for full and accurate use of the acquired data, with the correct timing information per bed acquisition which is especially important in estimation of parametric maps.

To make better use of these datasets, an export and offline processing pipeline was developed as part of this PhD project. The pipeline is based on custom-made python scripts and matlab scripts, that integrate with the GE-PET toolbox. This is a toolbox provided by GE for certain offline reconstruction operations. In this pipeline the Toolbox is used for generation of image corrections. These include normalisation factors, attenuation factors from MRACs, random and scatter corrections as well as dead-time corrections.

Table A.1: Details of Whole Body Sweeps of IsotoPK DWB protocol.

Whole Body Sweep ID	PET Bed Frame Duration (s)	MRAC (Acquired or copied)
CE00 blanc	N/A	Yes
Liver	10x18	Yes
CE01	20	From CE00
CE02	20	From CE00
CE03	20	Yes
CE04	20	From CE03
CE05	20	Yes
CE06	20	From CE05
CE07	20	Yes
CE08	20	From CE07
CE09	20	Yes
CE10	30	Yes
CE11	30	From CE10
CE12	30	Yes
CE13	30	Yes
CE14	30	From CE13
CE15	30	Yes
CE16	30	Yes
CE17	30	From CE16
CE18	40	Yes
CE19	40	Yes

A.0.1 Export from Console

DWB studies are exported from the PET-MR console using a custom export tool provided by GE.

Those are then processed using the custom-made pipeline as follows:

- **Step1: Verify Injection Time**

Before organising the DWB data, it is important to verify the injection time point, to which all the DWB will be decay corrected to. In this pipeline we verify the injection time by inspecting the total prompt to time curve from the list-mode dataset of the single-bed dynamic phase, as shown in figure.

- **Step2: DWB data sorting**

The data are re-sorted to single directories per WB sweep, where each directory includes the list-mode data of sweep's five bed positions and their corresponding MRACs if acquired. Subsequently, for sweeps with no acquired MRAC, the MRACs of previous sweeps are copied in these directories. At this step all the timing information from the headers of the PET list and MRAC files are extracted and saved in a database.

- **Step3: GE-PET Toolbox processing**

The data in each sweep's directory are unlisted and reconstructed with the GE-PET Toolbox as individual static acquisitions. This process generates the required corrections for reconstruction. Similar

processing is applied for the single-bed dynamic phase, which is reconstructed by the toolbox as a dynamic study.

- **Step4: Conversion to CASToR datafiles**

The list-mode raw data and the generated corrections are used to make CASToR list-mode datafiles as well as normalization files for each bed position of the acquisition and for all dynamic frames of the single-bed dynamic phase. The time-tags of each list-mode file are modified accordingly, to the injection time point reference, using the database information build earlier.

Standard Operating Procedure: fully automated DWB protocol

A short SOP for the developed fully automated DWB protocol, that was tested on the NHP study, is given in the following steps:

1. Load "IsotoPK_Commander" python class and create new object on a terminal in the PET-MR console.
2. Perform scout of subject, plan the desired bed positions for PET acquisition and perform MRAC acquisition.
3. Capture the position of the planned PET bed positions.
4. Load the "Timing Table" with the frame duration per bed positions and sweep number.
5. If a dynamic phase is required, plan the acquisition and acquire an MRAC for this position.
6. Enable table emulation.
7. Initiate a one hour long PET acquisition and once acquisition is ongoing perform injection of the subject.
8. After adequate time has passed for the single-bed dynamic phase start the automated DWB procedure.
9. Once the acquisition has been completed, disable table emulation.

,"

,,,

Appendix B

Simulation Study Supplementary material

The framing of the simulated PET protocols are given in table ???. The TACs used in simulations were made using using equation B.1. A selection of the simulated kinetic parameters is given in table ?? and the corresponding TACs are shown in figure ??.

$$C_{PET}(t) = (1 - V_B) \left(\frac{K_1 k_2}{k_2 + k_3} e^{-(k_2 + k_3)t} + \frac{K_1 k_3}{k_2 + k_3} \right) C_P(t) + V_B C_P(t) \quad (\text{B.1})$$

5555555

Appendix C

Direct multi-bed dynamic reconstruction: Supplementary material

Supplementary graphs, used in the analysis of the evaluated IsotoPK studies of chapter 7, are provided here. Additionally, an brief simulation study for the behaviour of the spectral analysis model in the liver and the effects from the dual-input function is included.

Supplementary graphs

.....

.....

Liver dual-input function simulation study

This short simulation was conducted using noiseless TACs to test the effects of the use of a dual input function model against spectral analysis that only accounts for one single input function. The following equations were used for the simulation. The portal vein input function was simulated using equation C.1 and a dispersion value $k_g = 0.5\text{min}^{-1}$ from the literature [77]. The dual input function was then simulated with a 25/75 ratio using equation C.2 and provided to the equation C.3 of the 2TC model for simulating liver TACs. Finally the blood fraction was included using equation C.4. The simulated K_1 values varied between 0.3 and 2.4 min^{-1} . The simulated k_2 , k_3 and V_B values were 0.15 min^{-1} , 0.05 min^{-1} and 0.03 respectively. These values, using a $K_1 = 0.7 \text{ min}^{-1}$, approach the TAC of the IsotoPK CTRL scan from chapter 7. Spectral analysis was performed using the single input function of $C_P(t)$.

$$C_{PV}(t) = k_g e^{-k_g t} * C_P(t). \quad (\text{C.1})$$

$$C_H(t) = 0.75 \cdot C_{PV}(t) + 0.25 \cdot C_P(t). \quad (\text{C.2})$$

$$C_T(t) = K_1(e^{-(k_2+k_3)t} + \frac{k_3}{k_2+k_3}(1 - e^{-(k_2+k_3)t})) * C_H(t) \quad (\text{C.3})$$

$$C_{PET}(t) = (1 - V_B)C_T(t) + V_B C_H(t), \quad (\text{C.4})$$

The simulated TACs are shown in figure ??, while the result K_1^* values of the spectral analysis against simulated K_1 values are shown in ???. The results show an closely linear relationship between simulated K_1 and estimate K_1^* values, with a deviation from a slope of 1. A part of this deviation is attributed to not correcting the K_1^* values for blood fraction, but mostly it is due to unaccounted behaviour of the dual input function.

,,,

.....

Secondary Contributions

PET FDG Improved Tumour Definition using Deep Learning

Within the HYBRID secondments schedule, a 1-month secondment for Laura Dal Toso (LDT) from King's College London (KCL) was planned to take place at our lab. This secondment aimed in performing simulations for creation of large datasets that could be used for the training of Deep Learning (DL) methods.

For applications of PET imaging in oncology, quantification and shape of tumours are regularly used by medical professionals for the characterisation and classification of disease. For the case of NSCLC imaging, and not only limited to that, these image characteristics are often degraded by image noise and partial volume effects. In this work, a method for improving tumour shape definition and quantification was proposed, by use of Deep Learning (DL). As DL methods require a large number of training datasets, simulations were used to train the proposed DL method.

The aim was to ultimately use the DL method for real NSCLC image data from an mMR PET/MR scanner (installed at KCL). Thus the implementation of the mMR geometry in the PET analytical simulator was needed, which was performed by me (ZC) with guidance from Dr Simon Stute. After the successful integration of the geometry for simulations and validation of reconstructions using CASToR, a large dataset of ground truth tumours (placed within the XCAT phantom) was created by LDT and provided for PET simulation. A total of 2210 cases were simulated and reconstructed, using a custom made pipeline by ZC on two computer clusters of our lab. Details on the methodology used and results are provided in the attached draft paper, which will be submitted for publication.

Data Driven Motion Correction for Brain PET Dynamic Imaging

A 2-week secondment was planned for me at the MUW in Vienna, with the aim of making use of dynamic reconstruction techniques developed during this PhD project to a cohort of epilepsy dynamic PET data. But this secondment was performed mostly from distance due to the pandemic and the time was spent towards the implementation and evaluation of novel motion estimation method for dynamic PET brain studies.

Towards this goal, a method was developed using ultra-short frame reconstruction and a Cycle Generative Adversarial Network (cGAN). The cGAN was designed to improve image quality of the short frame reconstructions for better motion estimation. In the training of the cGAN, data from the cohort of epilepsy patients was used. The datasets had been acquired on an mMR PET/MR scanner.

During this project, a converter was adapted to support conversion of dynamic mMR PET data, including all corrections generated by the e7 tools, to the CASToR datafile format. Using the converted data, dynamic reconstructions were performed in CASToR using the involuntary motion correction option. These reconstructions were used to assess the effect of intra-frame motion correction in result activity and parametric images. The development work and application of the cGAN has resulted in the attached publication by Shiyam Sundar *et al.* [141]. The work performed using CASToR has not been included in this publication, but it is considered for use in a future project on the topic of motion correction.

RESEARCH

Improved 3D Tumour Definition and Quantification of Radiotracer Uptake Using Deep Learning

Laura Dal Toso^{1*}, Zacharias Chalampalakis², Irène Buvat³, Claude Comtat², Gary Cook¹, Vicky Goh¹, Julia A. Schnabel¹ and Paul K. Marsden²

*Correspondence:

laura.dal_toso@kcl.ac.uk

¹School of Biomedical Engineering and Imaging Sciences, King's College London, London, UK
Full list of author information is available at the end of the article

Abstract

Background: In clinical positron emission tomography (PET) imaging, quantification of radiotracer uptake in tumours is often performed using semi-quantitative measurements such as the standardised uptake value (SUV). For small objects, the accuracy of SUV estimates is limited by the noise properties of PET images and the partial volume effect. There is need for methods that provide more accurate and reproducible quantification of radiotracer uptake.

Methods: In this work, we present a deep learning approach with the aim of improving quantification of tumour radiotracer uptake and tumour shape definition. A set of simulated tumours, assigned with "ground truth" radiotracer distributions, are used to generate realistic PET raw data which are then reconstructed into PET images. In this work, the ground truth images are generated by placing simulated tumours characterised by different sizes and activity distributions in the left lung of an anthropomorphic phantom. These images are then used as input to an analytical simulator to simulate realistic raw PET data. The PET images reconstructed from the simulated raw data and the corresponding ground truth images are used to train a 3D convolutional neural network.

Results: When tested on an unseen set of reconstructed PET phantom images, the network yields improved estimates of the corresponding ground truth. The same network is then applied to reconstructed PET data generated with different point spread functions. Overall the network is able to recover better defined tumour shapes and improved estimates of tumour maximum and median activities.

Conclusion: Our results suggest that the proposed approach, trained on data simulated with one scanner geometry, has the potential to restore PET data acquired with different scanners.

Keywords: CNN; PET imaging; Analytical simulator

Introduction

Positron emission tomography (PET) is an imaging modality which is extensively used in oncology to detect and stage tumours, and to monitor response to treatment. In clinical routine, image interpretation is usually performed by visual inspection of PET images, which leads to inter- and intra-observer variability. Although in many cases visual assessment may be sufficient, more challenging tasks such as the evaluation of the response to therapy of solid tumours require some form of

quantification [1]. In PET, uptake quantification is usually performed using semi-quantitative measurements of tumour radiotracer uptake, such as the standardised uptake value (SUV). The SUV is defined as the ratio of the radioactivity concentration in a region of interest (ROI) to the average radioactivity concentration in the whole body and can be calculated as follows:

$$SUV = \frac{\text{Activity Concentration}_{ROI} (\text{kBq/ml})}{\text{Injected Activity (MBq)} / \text{Body Weight (kg)}} \quad (1)$$

Usually a normalization by a mass density of 1 (g/ml) is assumed, and SUV is presented as a dimensionless metric. Different SUV metrics, such as SUV_{max} , SUV_{mean} and SUV_{peak} can be defined. These semi-quantitative metrics are affected by the noise properties of PET images as well as partial volume effects (PVE), which compromise the accuracy and reproducibility of the measurements [1] [2]. The PVE, which results from the poor spatial resolution of PET scanners and from image sampling, degrades the quantitative accuracy of PET images and it can result in large biases on measures of tracer uptake in small tumours [3] [4]. Most commonly SUV_{max} , which is calculated using the most intense tumour voxel within the ROI, is reported. SUV_{max} is widely used as it is user-independent, but it is also affected by noise. A metric that is less dependent on noise is SUV_{mean} , but its disadvantage is that it depends on the delineation of the volume of interest (VOI) in which the measurement is performed. SUV_{peak} measures the average activity concentration within a VOI. Various definitions of SUV_{peak} using different VOI shapes, sizes and locations [5] can be found in literature. In this paper, the maximum SUV_{peak} value measured in a 1 cm^3 spherical VOI within the tumour is reported. SUV_{peak} is less affected by image noise than SUV_{max} , but it presents some issues when applied to small tumours, especially if they are smaller than the VOI in which the peak is measured. There is need for reproducible methods that allow for more accurate quantification of tumour radiotracer uptake. Improved uptake quantification would lead to a more accurate assessment of response to treatment, especially at the early stages.

The use of artificial intelligence in the field of medical imaging has increased dramatically over the last decade. In PET imaging, machine learning and deep learning methods have been successfully applied to tumour segmentation, classification, automatic detection and image reconstruction [6, 7, 8, 9]. In recent years, deep learning methods have been used to denoise static PET images, and they have demonstrated better performance than traditional denoising approaches for various tracers and tasks. The two main deep learning architectures that have been used for denoising are convolutional neural networks (CNNs) [10] and generative adversarial networks (GANs) [11]. In previous work we developed a deep learning algorithm, using a 3D CNN, with the aim to improve quantification of tumour radiotracer uptake in simulated PET images [12]. The network was trained on simulated “ground truth” images that presented 3D shapes with typical tumour activity distributions found in clinical FDG images and a corresponding set of simulated PET images. The network was able to robustly estimate the original activity, yielding improved images in terms of shape, activity distribution and quantification of activity. The

main limitation of our previous work was that the PET images were simulated in a simplistic way, which did not take into account many of the effects that degrade the image quality in PET images.

Supervised deep learning methods require large amounts of labelled data, which are hard to obtain in PET imaging. Usually PET studies only comprise a relatively small number of patients. Furthermore, the true radionuclide distribution, which would correspond to the “label” of the PET images, is very difficult to obtain and rarely known. This limitation affects not only deep learning-based methods, but all the PET data processing methods (i.e. image reconstruction) which can never be fully evaluated *in vivo*. The use of phantoms and realistic PET simulators partially overcomes the lack of large labelled datasets. Monte Carlo simulation is the most commonly used technique to generate realistic PET data, but it has the disadvantage of being computationally very demanding. A number of analytical simulators have been developed to generate simulated PET images in a shorter time [13, 14]. While analytical simulators are not as accurate as Monte Carlo based simulators, they enable fast generation of PET data with realistic noise properties, which makes them particularly useful for creating large numbers of datasets. The simulation of realistic tumours also has some limitations. Real tumours are often characterised by inter- and intra-tumour heterogeneity, and by complex spatial structures. The mathematical and computational models of cancer that have been implemented so far mainly focus on describing a few specific aspects of the disease [15]. These models are not able to capture all the characteristics of tumour biology. In clinical practice, biopsies are performed to obtain ground truth information on tumour composition, but this method only provides limited information as the samples are extracted from a small region, and they cannot provide a description of the whole tumour. In this work, we generated a dataset of tumours assigned with three different activity patterns. The simulated dataset offers a wide variety of tumour activity values and tumour shapes, located at different positions within the left lung of an anthropomorphic phantom. This dataset is then used to train and test a 3D convolutional neural network (CNN) that can recover the real activity distribution from the signal seen on the PET image. We build on our previous deep learning approach described in [12] by significantly enhancing the simulation of PET images, using an analytical simulator developed by Stute et al. [16] and by testing the proposed approach on two different simulated datasets.

Material and methods

An overview of the proposed deep learning approach is presented in Fig. 1. Tumours with different sizes, shapes and activity distributions were simulated and subsequently placed in the left lung of an anthropomorphic phantom [17]. Different activities were assigned to each organ to create the “ground truth” images. Additionally, the corresponding attenuation maps were created. These two were used as input to an analytical PET simulator to generate PET raw data, which were subsequently reconstructed to provide the simulated PET images, as is detailed in section . The ground truth images and simulated PET images were used to train a 3D CNN, which is described in section .

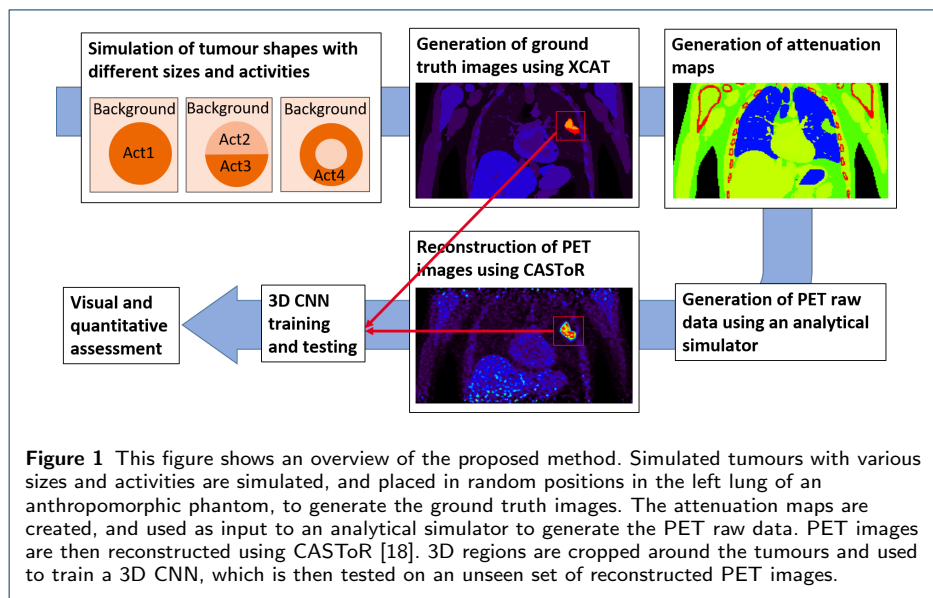


Figure 1 This figure shows an overview of the proposed method. Simulated tumours with various sizes and activities are simulated, and placed in random positions in the left lung of an anthropomorphic phantom, to generate the ground truth images. The attenuation maps are created, and used as input to an analytical simulator to generate the PET raw data. PET images are then reconstructed using CASToR [18]. 3D regions are cropped around the tumours and used to train a 3D CNN, which is then tested on an unseen set of reconstructed PET images.

Simulation of ground truth images

At first, tumour-like 3D shapes with different volumes, spanning 0.01 to 200 ml, were simulated. This set of tumours was composed of three groups, each corresponding to a different activity pattern: tumours filled with uniform activity, tumours split into halves (each assigned with a different activity), and hollow tumours with background activity in the inner part, to mimic necrotic regions. The thickness of the external layer of hollow tumours was set to half the radius of the tumour, and the inner core of the tumour was assigned with background activity. The background activity was set to 1/10th of the maximum tumour activity. The choice of this specific set of activity patterns was based on the work of E. Pfaehler et al. [19], in which realistic phantom inserts were designed according to Non-Small Cell Lung Cancer (NSCLC) tumours extracted from patient studies. The simulated tumours were subsequently placed in random positions into the left lung region of the XCAT phantom [17]. In order to shorten the simulation times, the XCAT phantom was reduced to $344 \times 344 \times 127$ voxels including only the torso. The voxel size of the cropped image was $[2.09, 2.09, 2.03] \text{ mm}^3$. Realistic activity values drawn from a range of radioactivity concentrations measured from real patients PET images were assigned to each simulated tumour. Attenuation maps were generated for each XCAT image using the XCAT phantom attenuation values.

PET data simulation and reconstruction

To generate realistic PET raw data we used an analytical PET simulator developed by Stute et al. [16]. The geometry, detector resolution, and sensitivity of a positron emission tomography/magnetic resonance (PET/MR) system, more specifically the Siemens mMR scanner (Siemens Biograph mMR, Erlangen, Germany), were used in the simulation. In this work only the PET component of the simulator was modelled and we did not use any anatomical information from the MR. PET raw data were generated from the ground truth images each with 100 million total prompt counts, including scatter and random events. This corresponds to 12.4 million Noise

Equivalent Counts (NEC). Subsequently, image reconstruction was performed using the open source fully quantitative reconstruction platform CASToR [18], with an iterative ordered subset expectation maximization (OSEM) algorithm run to 6 iterations with 21 subsets. The reconstructed voxel size was [2.09, 2.09, 2.03] mm³, as in the XCAT phantom images. Image reconstructions were performed with image-based PSF modelling. Two different datasets were generated using the analytical simulator. The first one, called dataset 1, was composed of 800 uniform tumours, 721 tumours split in half and 589 hollow tumours. In this case the analytical simulator generated the PET data with an anisotropic, spatially invariant PSF with FWHM (4.5, 4.5, 4.0) mm, which was also used in the reconstruction of the simulated PET images. A total of 2110 simulated PET raw datasets and images were generated.

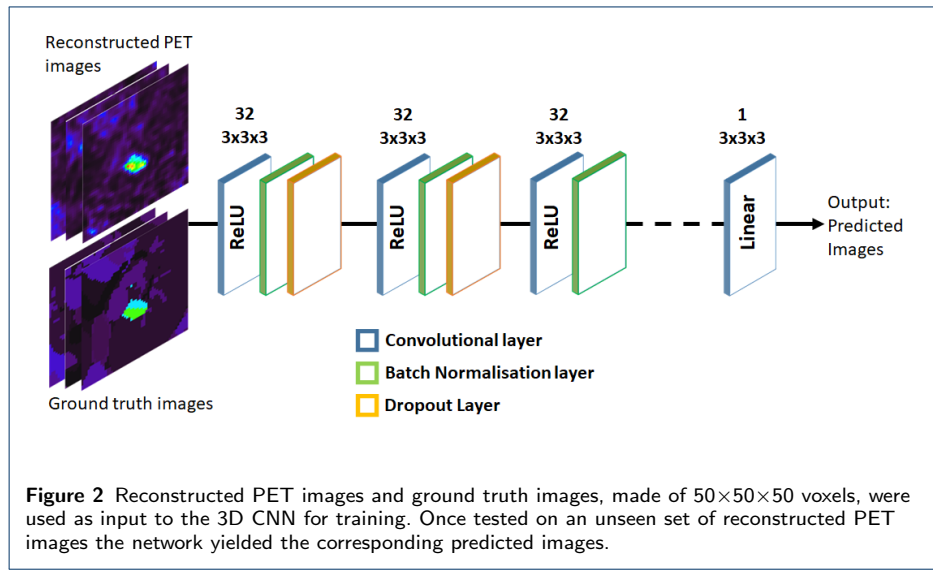
One of the aims of this work was to test if the proposed algorithm trained on a given dataset could generalise well to data acquired with different scanners. One way to simulate the diversity between different scanners is to generate and reconstruct PET images using a range of PSFs. As a result, a new dataset (called dataset 2) composed of 100 images, with 33 uniform tumours, 34 tumours in halves and 33 hollow tumours was generated using a range of anisotropic spatially-invariant PSFs. A value randomly drawn from a Gaussian distribution (mean $\mu = 4.5$ mm and sigma $\sigma = 0.2$ mm) was assigned to the transaxial components of the PSF, both in the simulation and in the reconstruction, with a perfect match. The axial component was calculated by dividing this value by 1.125 and a constant ratio between transaxial and axial PSF components was maintained.

Network architecture

Convolutional neural networks (CNNs) are among the most commonly used algorithms for medical imaging applications [20]. These networks are composed of a series of convolutional layers, which can extract features from the input images, at multiple levels of abstraction. In this work 3D CNNs with different depths were tested, and a visual and quantitative assessment suggested that a 3D CNN with 7 convolutional layers yielded the best results on our dataset. The proposed 3D CNN, presented in Fig. 2, is composed of 7 convolutional layers each followed by a batch normalisation layer except for the final layer. The convolutional layers are characterised by 32 filters with dimensions 3×3×3, and by ReLU activation functions except for the final one which has linear activation function. Two dropout layers, with dropout rate 0.3, were added after the first and second batch normalisation layers. Mean squared error was used as loss function during training and the optimizer was Adam [21]. The learning rate was set to the default value 0.001. The training was performed using a NVIDIA Tesla K40 GPU and the network architecture was implemented in the Keras Framework with Tensorflow [22].

Experiments

All the simulated PET images were cropped around the tumours to a final dimension of 50×50×50 voxels, before being processed by the convolutional neural network. The network inputs were normalised using the MinMaxScaler, which is a function provided in the scikit-learn Python package [23]. Using this function, the



training, testing and validation datasets were scaled in the range [0,1]. The normalisation factors were stored and subsequently applied to the network's predictions to rescale the resulting images, before performing any quantitative analysis. In all experiments, a visual assessment of the predicted images was at first performed using a free software tool for multimodality medical image analysis (AMIDE) [24]. Subsequently, the images were quantitatively assessed. In order to provide a baseline comparison we used multiple metrics for the quantitative assessment of the results. The maximum, median and peak values were estimated for each tumour in order to quantitatively compare the reconstructed PET images to the images predicted by the CNN. Tumour masks defined on the ground truth images were subsequently applied to the reconstructed PET images and to the CNN's predicted images to measure the median and peak values. Following the PERCIST guidelines [25], in this paper the peak value was measured within a 1 cm^3 -volume spheric VOI, centred around the hottest voxel in the tumour mask. To present the results in a more compact way, the recovery coefficients defined as the ratio between the observed activity and the ground truth activity, were calculated using the maximum, median and peak values as shown in Eq. 2, Eq. 3 and Eq. 4 respectively.

$$RC_{max} = \frac{\text{Max activity}_{prediction}}{\text{Max activity}_{ground truth}} \quad (2)$$

$$RC_{median} = \frac{\text{Median activity}_{prediction}}{\text{Median activity}_{ground truth}} \quad (3)$$

$$RC_{peak} = \frac{\text{Peak activity}_{prediction}}{\text{Peak activity}_{ground truth}} \quad (4)$$

When testing the network on simulated data, the structural similarity index measure (SSIM) was also calculated. The structural similarity allows the comparison of two images by taking into account their luminance l , contrast c and structure s . The SSIM is defined as:

$$SSIM(x, y) = [l(x, y)]^\alpha \cdot [c(x, y)]^\beta \cdot [s(x, y)]^\gamma \quad (5)$$

where x and y are two non-negative image signals, which could be for example two image patches. α , β and γ are used to adjust the relative importance of the three components. In this paper, α , β and γ are equal to 1. The luminance comparison function l between two image signals depends on the mean intensities of the two signals μ_x and μ_y . After estimating the luminance, the mean intensity is removed from the initial image signal. At this point, contrast comparison between the two signals is performed by measuring their standard deviations σ_x and σ_y . Finally, each signal is normalised by its standard deviation and the structure comparison is made on the normalised signals. In practice, when two images (X, Y) are compared, the overall image quality can be estimated using the MSSIM, which it is expressed as:

$$MSSIM(X, Y) = \frac{1}{M} \sum_{j=1}^M (SSIM(x_j, y_j)) \quad (6)$$

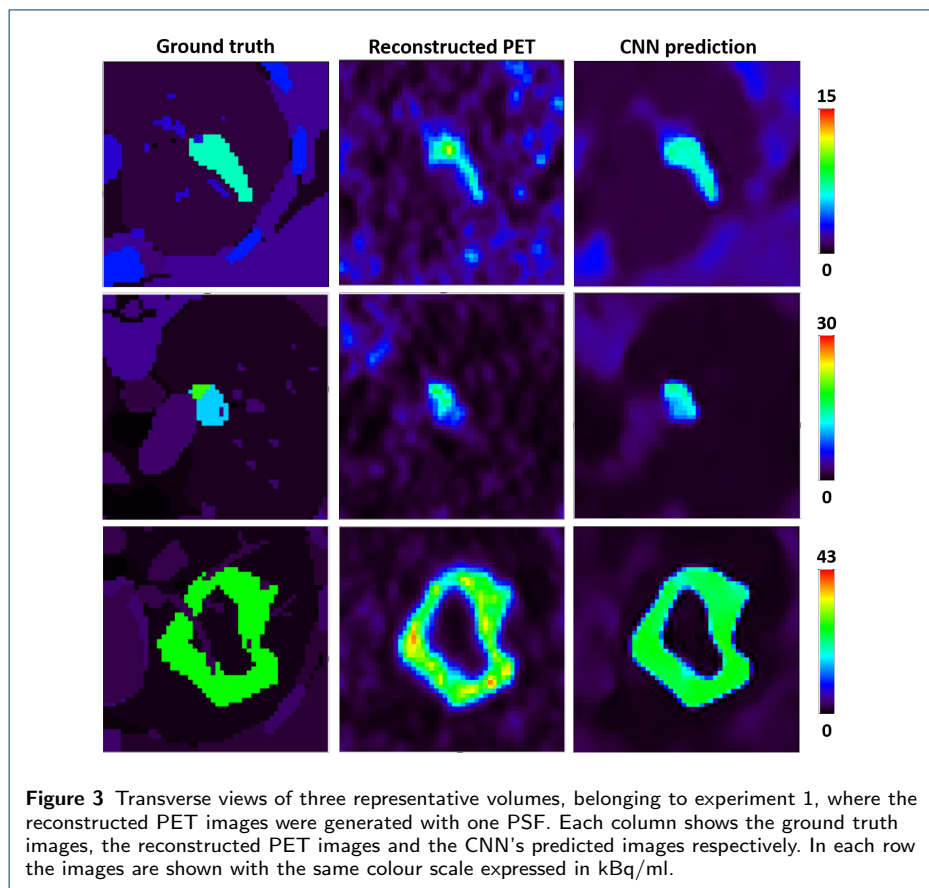
where x_j and y_j are the image contents at the j -th local window and M is the number of local windows in the image. In this work, the MSSIM was used to compare the reconstructed PET images and the predicted images to the ground truth images.

CNN training and testing using PET data generated with a single PSF

This experiment was performed to optimise the network's architecture and test its performance on the simulated data. Dataset 1 was used to train and test the network. In this dataset, the PET images were generated and reconstructed using a spatially invariant PSF with FWHM (4.5 mm, 4.5 mm, 4.0 mm). The simulated images were split into training and testing datasets, with ratio 80/20. 20 % of the training data were used for validation. The training dataset was augmented by scaling some of the bigger tumours with scaling factors ranging from 0.5 to 0.8, with the aim to increase the number of small tumours. As a result, the training dataset was composed of 645 uniform tumours, 645 tumours split in halves (of which 70 were augmented) and 645 hollow tumours (of which 177 were augmented). In this experiment, the network was trained for 500 epochs with batch size 50. The test dataset was made of 422 non-augmented images.

Application to PET data generated with different PSFs

The second aim of this work was to test if the proposed 3D CNN could generalise well to PET data generated with different PSFs and restore these images accurately. In this experiment the 3D CNN was trained on dataset 1, generated with one PSF as described in section , and subsequently applied to dataset 2, generated with a range of PSFs which were not learned during training.

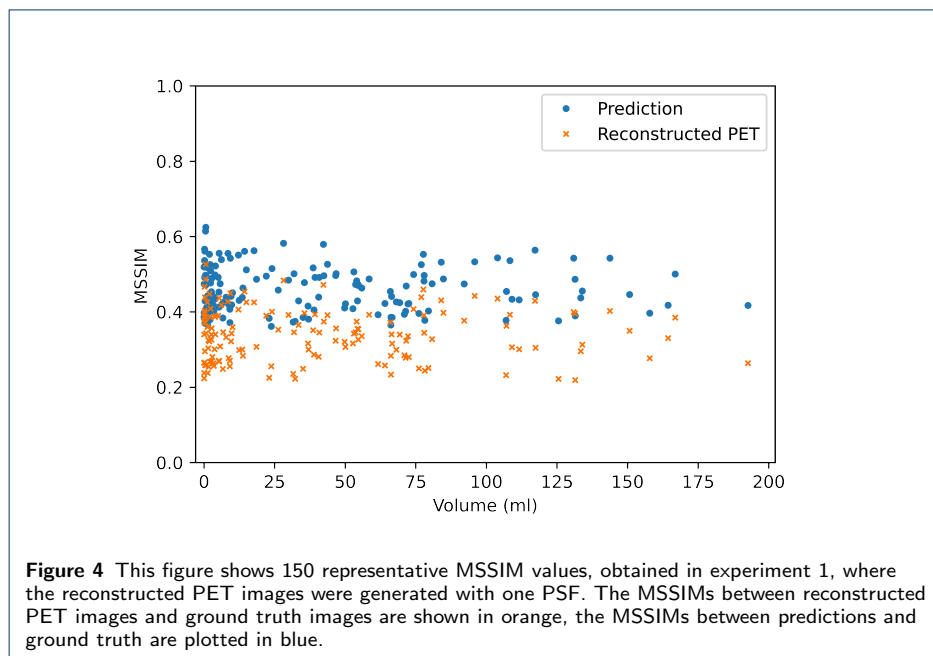


Results

In this section, the results obtained training and testing the 3D CNN on data generated with a single PSF are presented. Subsequently, the same network is applied to PET data generated with a range of PSFs and the results are qualitatively and quantitatively compared to those obtained in the first experiment.

CNN training and testing using PET data generated with a single PSF

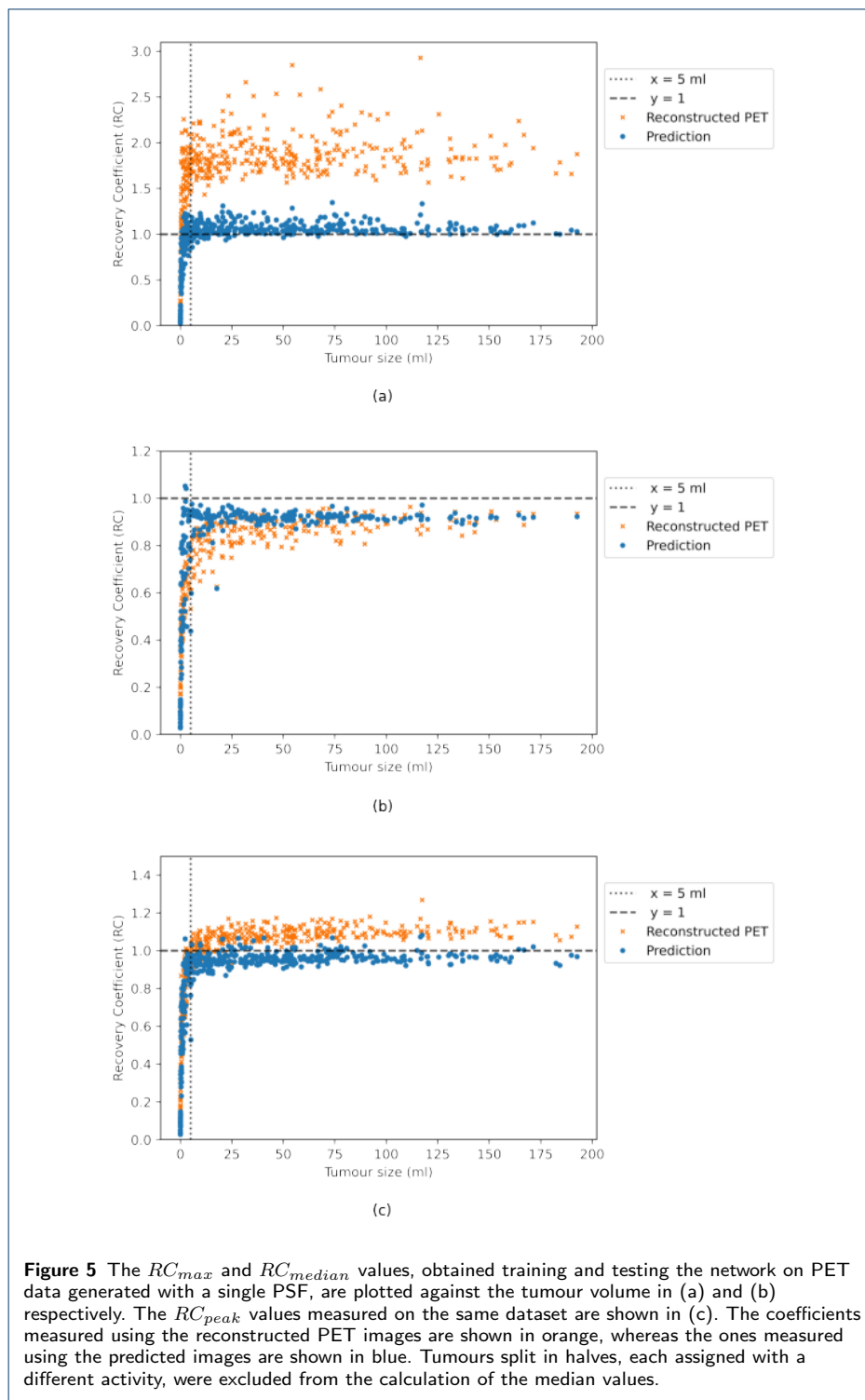
The first experiment was performed using the simulated training and test datasets generated with a single PSF, as described in section . Three representative volumes, each characterised by a different activity pattern, are presented in Fig. 3. The ground truth images are shown in the first column, the corresponding reconstructed PET images are in the second column, and the CNN's predictions are shown in the last column. In this case, the CNN yielded better defined tumour shapes and denoised images. This visual assessment was followed by a quantitative analysis. In Fig. 4, 150 randomly selected MSSIM values are shown. The predicted images are overall characterised by a higher MSSIM to the ground truth images and the absolute MSSIM values are below 0.65 in both datasets. The average MSSIM value measured using the ground truth image and the reconstructed PET images is 0.33 ± 0.06 . An improved MSSIM value equal to 0.47 ± 0.06 is measured using the CNN predictions and the ground truth images.



To further assess the performance of the network, the peak tumour uptake was measured for each image and the recovery coefficients were calculated. We further analysed the results by measuring the maximum and median tumour uptake. The median value was only estimated for the tumours with uniform uptake and for the hollow tumours, which also had uniform uptake. In Fig. 5 the RC are plotted. The maximum, median and peak RC are not well recovered for tumours that have a volume smaller than around 5 ml, so a detailed investigation of the small tumours was performed. Out of all the test images, the network did not recover any tumour uptake for 5 volumes, which had a volume smaller than 0.18 ml (20 voxels). In these predicted images no tumour could be detected. The tumour activities were not accurately recovered for tumours with volumes between 0.18 and 1.33 ml that were located close to other structures (ribs, heart) and that were characterised by a low ground truth activity. The average RC_{max} , RC_{median} and RC_{peak} values measured on the reconstructed PET images and on the CNN predictions are summarised in table 1. The values shown in this table are measurements averaged over the tumours with volume larger than 5 ml. All the recovery coefficients measured for the predicted images are approaching 1, meaning that the CNN yields improved estimates of the maximum and median activity within the tumours.

Table 1 Average RC_{max} , RC_{median} and RC_{peak} values relative to experiment 1, where the reconstructed PET images were generated with one PSF. These values are measured only for tumours larger than 5 ml.

volume \geq 5 ml	RC_{max}	RC_{median}	RC_{peak}
Reconstructed PET	1.87 ± 0.22	0.86 ± 0.07	1.08 ± 0.05
CNN's predictions	1.06 ± 0.07	0.91 ± 0.05	0.96 ± 0.04



Application to PET data generated with different PSFs

The network previously trained in experiment 1, where the reconstructed PET images were generated with one PSF, was then applied to PET data generated

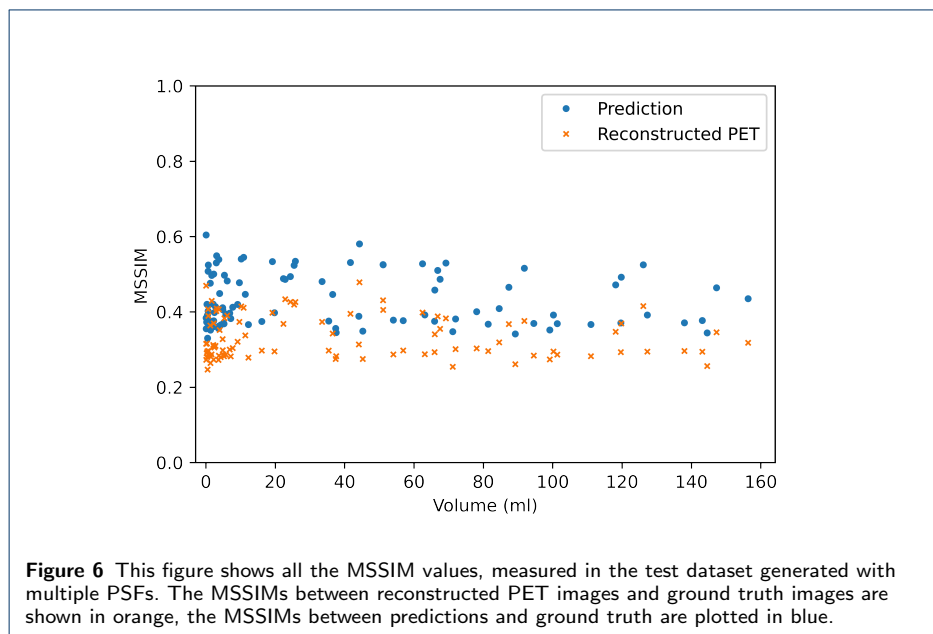
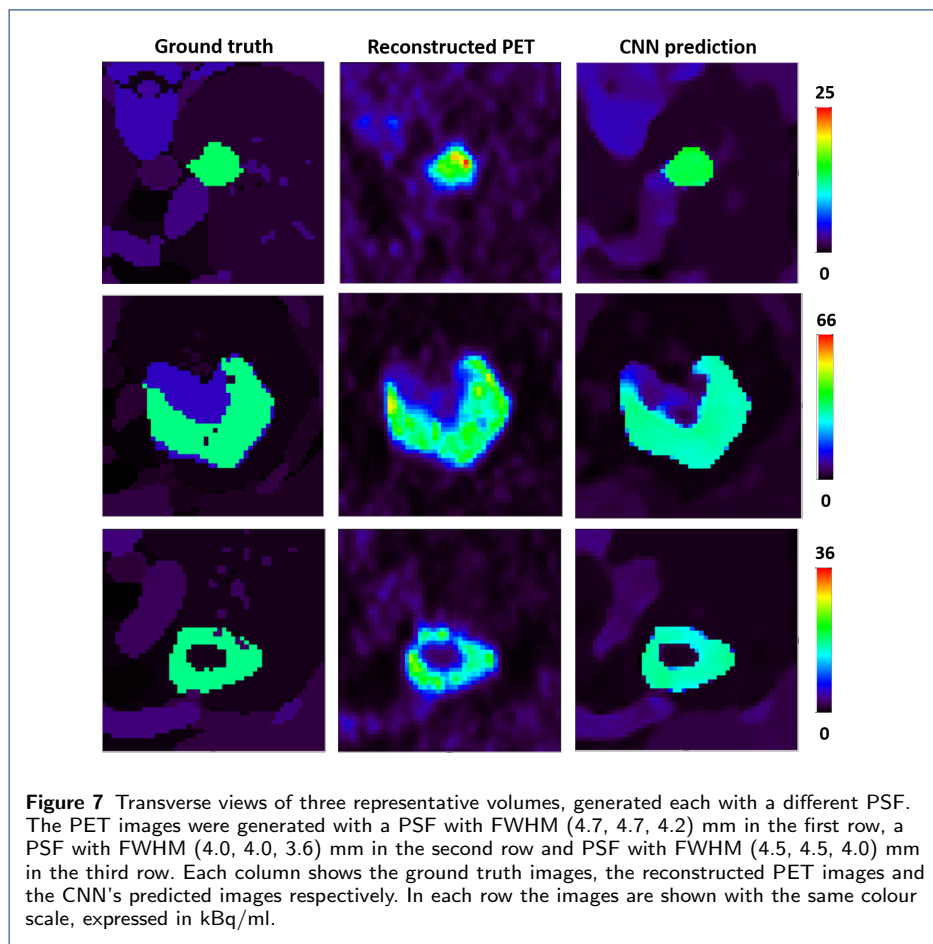


Table 2 Average RC_{max} , RC_{median} and RC_{peak} values relative to PET data generated with different PSFs. These values are averaged over tumours with volume larger than 5 ml.

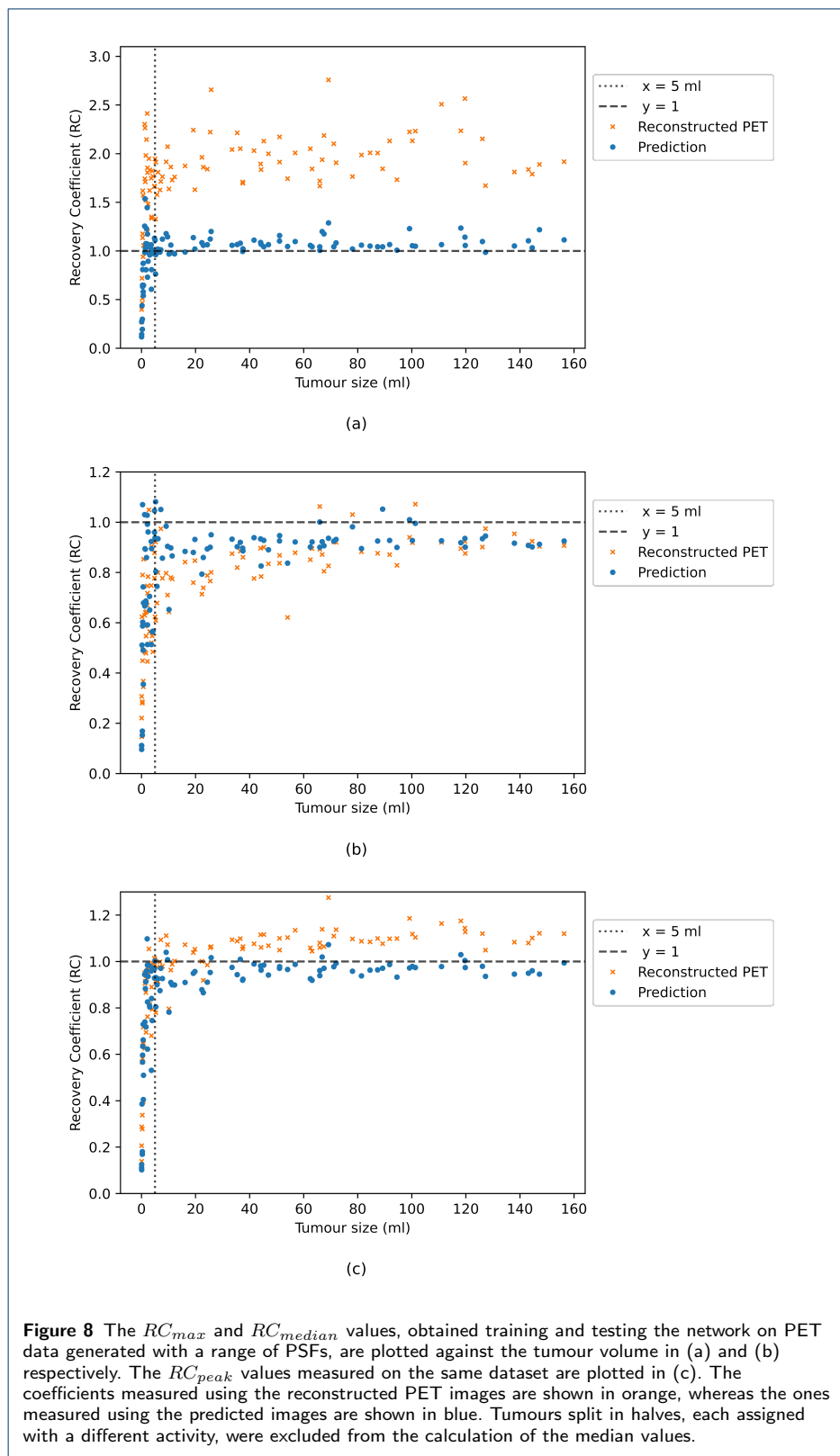
volume \geq 5 ml	volume \geq 5 ml	RC_{median}	RC_{peak}
Reconstructed PET	1.94 ± 0.26	0.84 ± 0.08	1.07 ± 0.08
CNN's predictions	1.07 ± 0.08	0.90 ± 0.05	0.95 ± 0.05

with different PSFs. The MSSIM values measured using the reconstructed PET images and the images predicted by the CNN are shown in Fig. 6. The average MSSIM measure between the ground truth images and the ground truth images is 0.34 ± 0.07 whereas the average MSSIM between the CNN predictions and the ground truth images is 0.43 ± 0.07 . This value is comparable to the MSSIM obtained in the previous experiment. In Fig. 7, three volumes belonging to the test dataset are presented. The PSFs used to simulate the PET raw data and to reconstruct the PET images had FWHM (4.7, 4.7, 4.2) mm for the images in the first row, FWHM (4.0, 4.0, 3.6) mm for the images in the second row and FWHM (4.5, 4.5, 4.0) mm in the third row. Even though the PSFs used in the first and second row did not match the PSF used to generate and reconstruct the PET images used for training, the network was still able to predict improved tumour shapes and activities. In Fig. 8 the RC_{max} , RC_{median} and RC_{peak} are plotted against the tumour volume expressed in ml. The recovery curves show similar behaviours as in the previous experiment and improved values are obtained when estimating the recovery coefficients on the images predicted by the CNNs. The average RC_{max} and RC_{median} measurements are presented in table 2. The CNN yields improved Recovery coefficients. The RC estimated shown in this table are comparable to the ones obtained in the previous experiment, proving that the network can successfully recover the maximum, median and peak activity in the tumours even when tested on images generated with different PSF values.



Discussion and Conclusion

In this paper we propose a deep learning approach to improve quantification of radiotracer uptake and tumour shape definition in PET images. A 3D CNN was successfully trained and tested on simulated data generated with a single PSF and applied to reconstructed PET images generated with a range of PSFs. The results indicate that the network is able to improve the definition of the tumour shapes and to denoise reconstructed PET images. A quantitative analysis of the results obtained using simulated data has shown that the images predicted by the 3D CNN yield improved estimates of the maximum tumour activities. We observed that the peak, maximum and median activities were not accurately recovered for tumours with volumes smaller than 5 ml, so a more detailed analysis was performed on small tumours. Only tumour volumes smaller than 0.18 ml presented critical issues. Bigger volumes located close to other background structures and characterised by a low ground truth activity were generally associated with an inaccurate prediction of the peak, maximum and median activity. In future work, we plan to further augment the training dataset, thus adding more small volumes to the training dataset. We think that this might improve the performance of the network for this class of tumours, as the network would be able to learn from more small tumours during training. A secondary effect that we noticed in our experiments was an improvement



in the recovery of background structures. This effect will be further investigated in future work. Our approach proved successful when the network was applied to a set of reconstructed PET images generated with a range of PSFs that did not match the PSF used to generate the training dataset. Preliminary results suggest that the proposed approach would be able to restore PET images acquired with different scanners and spatially varying PSF. This work has the potential to be extended to larger areas of the body, in order to improve the estimation of the total tumour burden. The proposed approach has been tested on images generated with a single noise level, the robustness of this method to data generated with other noise levels remains to be evaluated. In this work the same spatially invariant PSF was used for the simulation of the PET raw data and for the reconstruction of PET images. On the contrary, in a clinical setting PET images would be characterised by spatially invariant and non stationary PSFs and there may be a mismatch between the system's PSF and the one modelled in the reconstruction algorithm. These aspects will be investigated in future work. Further experimentation is also needed to assess the robustness of the proposed deep learning approach to data generated using PSFs characterised by a different anisotropy and to more complex tumour shapes associated with heterogeneous activities.

Funding

This project has received funding from the European Union's Horizon 2020 research and innovation programme under the Marie Skłodowska-Curie grant agreement No. 764458. This research was supported by the Wellcome/EPSRC Centre for Medical Engineering [WT 203148/Z/16/Z], and by the National Institute for Health Research (NIHR) Biomedical Research Centre based at Guy's and St Thomas' NHS Foundation Trust and King's College London. The views expressed are those of the author(s) and not necessarily those of the NHS, the NIHR or the Department of Health. Cancer Research UK National Cancer Imaging Translational Accelerator Award (C4278/A27066).

Author details

¹School of Biomedical Engineering and Imaging Sciences, King's College London, London, UK. ²Laboratoire d'Imagerie Biomédicale Multimodale (BioMaps), Université Paris-Saclay, CEA, CNRS, Inserm, Service Hospitalier Frédéric Joliot, Orsay, France. ³Laboratoire d'Imagerie Translationnelle en Oncologie, Inserm, Institut Curie, Orsay, France.

References

1. Boellaard, R., Krak, N.C., Hoekstra, O.S., Lammertsma, A.A.: Effects of noise, image resolution, and ROI definition on the accuracy of standard uptake values: A simulation study. *Journal of Nuclear Medicine* **45**(9), 1519–1527 (2004)
2. Zaidi, H., Karakatsanis, N.: Nuclear medicine: physics special feature review article towards enhanced PET quantification in clinical oncology. Technical report
3. Soret, M., Bacharach, S., Buvat, I.: Partial-volume effect in PET tumor imaging. *Journal of Nuclear Medicine* **48**(6), 932–945 (2007). doi:10.2967/jnumed.106.035774
4. Cysouw, M., Kramer, G., Schoonmade, L., Boellaard, R., De Vet, H., Hoekstra, O.: Impact of partial-volume correction in oncological PET studies: a systematic review and meta-analysis. *European Journal of Nuclear Medicine and Molecular Imaging* **44**, 2105–2116 (2017). doi:10.1007/s00259-017-3775-4
5. Vanderhoek, M., Perlman, S.B., Jeraj, R.: Impact of the definition of peak standardized uptake value on quantification of treatment response. *Journal of Nuclear Medicine* **53**(1), 4–11 (2012). doi:10.2967/jnumed.111.093443
6. Gong, K., Berg, E., Cherry, S.R., Qi, J.: Machine learning in PET: From photon detection to quantitative image reconstruction. *Proceedings of the IEEE* **108**(1), 51–68 (2020). doi:10.1109/JPROC.2019.2936809
7. Kim, K., Wu, D., Gong, K., Dutta, J., Kim, J.H., Son, Y.D., Kim, H.K., El Fakhri, G., Li, Q.: Penalized PET reconstruction using deep learning prior and local linear fitting. *IEEE Transactions on Medical Imaging* **37**(6), 1478–1487 (2018). doi:10.1109/TMI.2018.2832613
8. Litjens, G., Kooi, T., Bejnordi, B.E., Setio, A.A.A., Ciompi, F., Ghafoorian, M., van der Laak, J.A.W.M., van Ginneken, B., Sánchez, C.I.: A survey on deep learning in medical image analysis. *Medical Image Analysis* **42**, 60–88 (2017). doi:10.1016/j.media.2017.07.005
9. Shiyam Sundar, L.K., Muzik, O., Buvat, I., Bidaut, L., Beyer, T.: Potentials and caveats of ai in hybrid imaging. *Methods* **188**, 4–19 (2021). doi:10.1016/j.ymeth.2020.10.004. Artificial Intelligence Approaches for Imaging Biomarkers
10. Gong, K., Guan, J., Liu, C.-C., Qi, J.: PET image denoising using a deep neural network through fine tuning. *IEEE Transactions on Radiation and Plasma Medical Sciences* **3**(2), 153–161 (2019). doi:10.1109/TRPMS.2018.2877644

11. Wang, Y., Yu, B., Wang, L., Zu, C., Lalush, D., Lin, W., Wu, X., Zhou, J., Shen, D., Zhou, L.: 3D conditional generative adversarial networks for high-quality PET image estimation at low dose. *NeuroImage* **174**, 550–562 (2018). doi:10.1016/j.neuroimage.2018.03.045
12. Dal Toso, L., Pfaehler, E., Boellaard, R., Schnabel, J.A., Marsden, P.K.: Deep learning based approach to quantification of PET tracer uptake in small tumors. In: Knoll, F., Maier, A., Rueckert, D., Ye, J.C. (eds.) *Machine Learning for Medical Image Reconstruction*, pp. 181–192. Springer, Cham (2019)
13. Berthon, B., Häggström, I., Apte, A., Beattie, B.J., Kirov, A.S., Humm, J.L., Marshall, C., Spezi, E., Larsson, A., Schmidlein, C.R.: PETSTEP: Generation of synthetic PET lesions for fast evaluation of segmentation methods. *Physica Medica* **31**(8), 969–980 (2015). doi:10.1016/j.ejmp.2015.07.139
14. Pfaehler, E., Jong, J., Dierckx, R., van Velden, F., Boellaard, R.: SMART (SiMulAtion and ReconsTruction) PET: an efficient PET simulation-reconstruction tool. *EJNMMI Physics* **5** (2018). doi:10.1186/s40658-018-0215-x
15. Bekisz, S., Geris, L.: Cancer modeling: From mechanistic to data-driven approaches, and from fundamental insights to clinical applications. *Journal of Computational Science*, 101198 (2020). doi:10.1016/j.jocs.2020.101198
16. Stute, S., Tauber, C., Leroy, C., Bottlaender, M., Brulon, V., Comtat, C.: Analytical simulations of dynamic pet scans with realistic count rates properties, pp. 1–3 (2015). doi:10.1109/NSSMIC.2015.7582064
17. Segars, W., Sturgeon, G., Mendonca, S., Grimes, J., Tsui, B.: 4D XCAT phantom for multimodality imaging research. *Medical physics* **37**, 4902–15 (2010). doi:10.1118/1.3480985
18. Merlin, T., Stute, S., Benoit, D., Bert, J., Carlier, T., Comtat, C., Filipovic, M., Lamare, F., Visvikis, D.: CASToR: A generic data organization and processing code framework for multi-modal and multi-dimensional tomographic reconstruction. *Physics in Medicine and Biology* **63** (2018). doi:10.1088/1361-6560/aadac1
19. Pfaehler, E., Beukinga, R., Jong, J., Slart, R., Slump, C., Dierckx, R., Boellaard, R.: Repeatability of 18 F-FDG PET radiomic features: a phantom study to explore sensitivity to image reconstruction settings, noise, and delineation method. *Medical Physics* **46**, 665–678 (2018). doi:10.1002/mp.13322
20. Yamashita, R., Nishio, M., Do, R., Togashi, K.: Convolutional neural networks: an overview and application in radiology. *Insights into Imaging* **9** (2018). doi:10.1007/s13244-018-0639-9
21. Kingma, D., Ba, J.: Adam: A method for stochastic optimization. *International Conference on Learning Representations* (2014)
22. Abadi, M., Agarwal, A., Barham, P., Brevdo, E., Chen, Z., Citro, C., Corrado, G.s., Davis, A., Dean, J., Devin, M., Ghemawat, S., Goodfellow, I., Harp, A., Irving, G., Isard, M., Jia, Y., Kaiser, L., Kudlur, M., Levenberg, J., Zheng, X.: TensorFlow : large-scale machine learning on heterogeneous distributed systems (2015)
23. Pedregosa, F., Varoquaux, G., Gramfort, A., Michel, V., Thirion, B., Grisel, O., Blondel, M., Prettenhofer, P., Weiss, R., Dubourg, V., Vanderplas, J., Passos, A., Cournapeau, D., Brucher, M., Perrot, M., Duchesnay, E.: Scikit-learn: machine learning in Python. *Journal of Machine Learning Research* **12**, 2825–2830 (2011)
24. Loening, A., Sam Gambhir, S.: AMIDE: a free software tool for multimodality medical image analysis. *Molecular Imaging* **2**, 131–137 (2003). doi:10.1162/153535003322556877
25. Wahl, R.L., Jacene, H., Kasamon, Y., Lodge, M.A.: From RECIST to PERCIST: Evolving considerations for PET response criteria in solid tumors. *Journal of Nuclear Medicine* **50**(Suppl 1), 1–50 (2009). doi:10.2967/jnumed.108.057307.From

Conditional Generative Adversarial Networks Aided Motion Correction of Dynamic ^{18}F -FDG PET Brain Studies

Lalith Kumar Shiyam Sundar^{*1}, David Iommi^{*1}, Otto Muzik², Zacharias Chalampalakis³, Eva-Maria Klebermass⁴, Marius Hienert⁵, Lucas Rischka⁵, Rupert Lanzenberger⁵, Andreas Hahn⁵, Ekaterina Pataria⁶, Tatjana Traub-Weidinger⁴, Johann Hummel¹, Thomas Beyer¹

¹QIMP Team, Center for Medical Physics and Biomedical Engineering, Medical University of Vienna, Vienna, Austria; ²Department of Pediatrics, Children's Hospital of Michigan, The Detroit Medical Center, Wayne State University School of Medicine, Detroit, Michigan; ³Service Hospitalier Frédéric Joliot, CEA, Inserm, CNRS, Univ. Paris Sud, Université Paris Saclay, Orsay, France;

⁴Division of Nuclear Medicine, Department of Biomedical Imaging and Image-guided Therapy, Medical University of Vienna, Vienna, Austria; ⁵Department of Psychiatry and Psychotherapy, Medical University of Vienna, Vienna, Austria; and ⁶Department of Neurology, Medical University of Vienna, Austria

This work set out to develop a motion-correction approach aided by conditional generative adversarial network (cGAN) methodology that allows reliable, data-driven determination of involuntary subject motion during dynamic ^{18}F -FDG brain studies. **Methods:** Ten healthy volunteers (5 men/5 women; mean age \pm SD, 27 ± 7 y; weight, 70 ± 10 kg) underwent a test-retest ^{18}F -FDG PET/MRI examination of the brain ($n = 20$). The imaging protocol consisted of a 60-min PET list-mode acquisition contemporaneously acquired with MRI, including MR navigators and a 3-dimensional time-of-flight MR angiography sequence. Arterial blood samples were collected as a reference standard representing the arterial input function (AIF). Training of the cGAN was performed using 70% of the total datasets ($n = 16$, randomly chosen), which was corrected for motion using MR navigators. The resulting cGAN mappings (between individual frames and the reference frame [55–60 min after injection]) were then applied to the test dataset (remaining 30%, $n = 6$), producing artificially generated low-noise images from early high-noise PET frames. These low-noise images were then coregistered to the reference frame, yielding 3-dimensional motion vectors. Performance of cGAN-aided motion correction was assessed by comparing the image-derived input function (IDIF) extracted from a cGAN-aided motion-corrected dynamic sequence with the AIF based on the areas under the curves (AUCs). Moreover, clinical relevance was assessed through direct comparison of the average cerebral metabolic rates of glucose (CMRGlc) values in gray matter calculated using the AIF and the IDIF. **Results:** The absolute percentage difference between AUCs derived using the motion-corrected IDIF and the AIF was $1.2\% \pm 0.9\%$. The gray matter CMRGlc values determined using these 2 input functions differed by less than 5% ($2.4\% \pm 1.7\%$). **Conclusion:** A fully automated data-driven motion-compensation approach was established and tested for ^{18}F -FDG PET brain imaging. cGAN-aided motion correction enables the translation of noninvasive clinical absolute quantification from PET/MR to PET/CT by allowing the accurate determination of motion vectors from the PET data itself.

Key Words: ^{18}F -FDG brain; deep learning; head-motion correction; absolute quantification; Patlak analysis

J Nucl Med 2021; 62:871–879

DOI: 10.2967/jnumed.120.248856

T

he capability of obtaining fully quantitative physiologic measurements from the human body is a fundamental strength of PET methodology (1,2). However, due to the requirement of an arterial input function (AIF), the adoption of absolute quantification into clinical work has been severely limited, and only semiquantitative assessments of tracer uptake using standardized uptake expressed as SUV are commonly performed.

In recent years, several methodologies have been proposed to extract an image-derived input function (IDIF) directly from brain PET data to avoid arterial cannulation for determination of an AIF (3–10). It was demonstrated that a brain IDIF can be calculated either using a combined protocol that integrates PET/CT with MR data (3,7,8) or using a fully integrated PET/MR protocol (4,6,9,10). The calculation of an IDIF typically entails, in addition to the definition of a suitable blood-pool region and accounting for partial-volume effects, an accurate correction for involuntary subject motion. A fully integrated PET/MR system is ideally suited to perform all these tasks due to its capability of providing detailed anatomic information, which also includes MR navigators that track motion. However, due to its high cost, the proliferation of PET/MRI into the clinical realm has been severely limited. In contrast, PET/CT is widespread and cost-effective, thus motivating the transfer of IDIF methodology from PET/MR to PET/CT. The definition of a suitable blood-pool region, as well as the geometric correction for partial-volume effects, can be easily accomplished using coregistered PET/CT and MR data. Nonetheless, the accurate correction for subject motion remains a serious challenge in PET/CT imaging.

Assessment of currently available motion-compensation techniques points toward 3 general approaches: data-driven approaches (11–17), frame-based image registration (18,19), and real-time hardware motion tracking (20). Real-time hardware-based motion tracking detects subject motion with excellent temporal resolution

Received May 02, 2020; revision accepted Oct. 07, 2020.
For correspondence or reprints contact: Otto Muzik (otto@pet.wayne.edu).

*Contributed equally to this work.

Published online Nov. 27, 2020.

Immediate Open Access: Creative Commons Attribution 4.0 International License (CC BY) allows users to share and adapt with attribution, excluding materials credited to previous publications. License: <https://creativecommons.org/licenses/by/4.0/>. Details: <http://jnm.snmjournals.org/site/misc/permission.xhtml>.

COPYRIGHT © 2021 by the Society of Nuclear Medicine and Molecular Imaging.

(20) but is typically not used in clinical routine due to its complexity and the necessity to integrate external data (motion tracking) with the imaging system (applying the motion vector to images). In contrast, data-driven approaches do not require any external information (such as fiducials or laser positioning system), and they are also less computationally demanding. However, the clinical adoption of frame-based motion-correction schemes has been slow due to poor performance when coregistration is applied to frames that display a dissimilar tracer uptake pattern or noise characteristics as well as the difficulty to correct for intraframe motion in long-duration PET frames (>5 min).

Here, we explored the utility of conditional generative adversarial networks (cGAN) (21) as a data-driven approach to facilitate motion correction for involuntary subject motion in dynamic ^{18}F -FDG PET studies of the brain. Thereby, we build on recent studies that have shown the potential of cGAN methodology in converting low-count PET images to high-count images (22). In general, the objective of cGAN processing is the mapping of a low-count tracer distribution pattern to a high-count pattern based on a priori training data, where generic image features—such as overall brain shape and contours—are likely to be correctly reproduced. Put differently, the creation of high-count images enhances image features that are important for the detection of motion artifacts and as a result might improve the performance of subsequently applied conventional rigid body coregistration routines. It is important to note, however, that the so obtained images are devoid of unique characteristics that are specific for a particular subject and cannot be considered as representing the true (subject-specific) high-count uptake pattern beyond the enhancement of generic image features.

In light of the above, our ultimate objective was to determine the accuracy with which involuntary subject motion occurring during the first part of a dynamic ^{18}F -FDG PET/CT study can be detected using conventional motion-correction routines when images are first preprocessed using cGAN methodology, given that early frames are subject to both low-count statistics and dynamically changing tracer uptake patterns. The cGAN preprocessed frames can be thought of as PET navigators whose activity distribution are now temporally invariant, similar to that of the MR navigators. Although our focus was geared toward the derivation of an IDIF, the developed methodology appears to be broader in scope, potentially aiding in improved ability to detect both inter- and intra-frame motion. Consequently, our study was guided by the overarching hypothesis that cGAN preprocessing of images can be used to address low-count limitations of short time frame motion-correction strategies and support an accurate data-driven arterial IDIF calculation.

MATERIALS AND METHODS

Ten healthy volunteers (5 men/5F women; mean age \pm SD, 27 ± 7 y) were included in this study (10,11). The study was approved by the Ethics Committee of the Medical University of Vienna and was performed in accordance with the revised Declaration of Helsinki (1964). All volunteers were deemed to be healthy based on their medical history, physical examinations, and vital signs. Written informed consent was obtained from all subjects before the examinations.

Study Design

We studied 10 subjects, each of whom underwent 2 PET/MR scans (mean time difference = 17 ± 44 d) in a fully integrated PET/MRI system (Biograph mMR; Siemens Healthineers). To correct the PET study for involuntary subject motion, cGAN image preprocessing was

performed before image coregistration, enabling the accurate determination of motion parameters in 3-dimensional (3D) space. These motion parameters were then used to extract the IDIF from the motion-corrected dynamic PET sequence (Fig. 1). To assess the accuracy of the IDIF, arterial blood samples were obtained from a radial artery. Finally, immediately after the PET/MRI examination, a low-dose CT scan of the brain (120 kVp, 50 mAs) was acquired once using a PET/CT system (Biograph TruePoint TrueView 64; Siemens Healthineers, USA) for the purpose of CT-based attenuation correction.

Imaging Protocol

All examinations were conducted in the afternoon; subjects were asked to keep their eyes open without performing any task. Before each scan, the glucose concentration (mmol/L) in blood was measured, and a venous line was established for the injection of the ^{18}F -FDG tracer. In addition, an arterial line was established in the contralateral arm for manual arterial blood sampling. To ensure a high signal-to-noise ratio in the MR images, a head and neck coil was used.

After positioning the brain in the center of the field of view, a 60-min PET list-mode acquisition was initiated with the bolus injection of ^{18}F -FDG (352 ± 66 MBq). Contemporaneously with the PET data

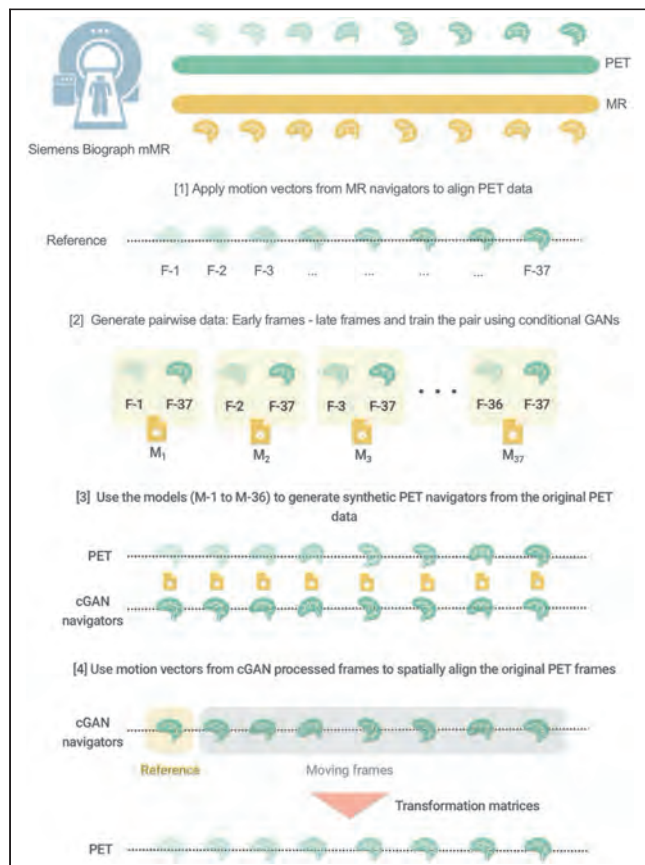


FIGURE 1. Schematic representation of cGAN methodology for motion correction of dynamic PET frames. [1] Motion vectors from the MR navigators are applied to align the PET data. [2] All training data ($n = 14$) are used to calculate mappings ($M_i, i = 1, 36$) between each individual frame (F-1 to F-36) and the reference frame (F-37). [3] These mappings are subsequently used to derive a motion vector based on coregistration of cGAN-produced artificially generated images and the reference image (test data). [4] Application of the motion vector to either rebin frames so that they all correspond spatially or apply the motion vector to the location of region from where a time–activity curve is extracted.

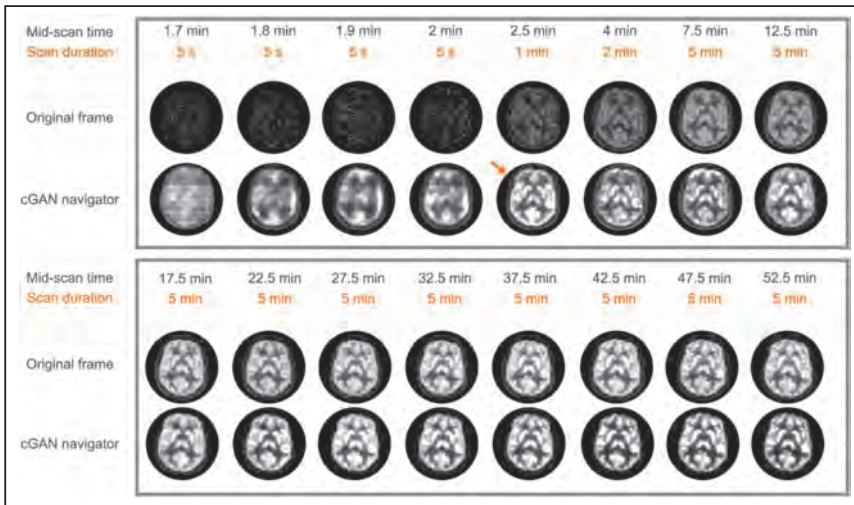


FIGURE 2. Results of cGAN processing for a representative subject. (Top and bottom panels, first rows) Original PET frames at different mid-scan times (1.7 to 52.5 min) with various frame durations (5 s, 1 min, 2 min, and 5 min). (Top and bottom panels, second rows) Corresponding, artificially generated, high-count PET images. cGAN processing is able to produce a tracer distribution pattern that is similar to the reference frame as early as 2.5 min after injection (arrow, top row).

acquisition, multiple MR sequences were acquired: a 3D time-of-flight MR angiography (TOF-MRA) sequence ($0.5 \times 0.5 \times 1$ mm voxel size, echo time = 3.6 ms, repetition time = 21 ms, 25° flip angle, 228×384 matrix, 220 slices) for the definition of the carotid vasculature and a T1-weighted MRI sequence ($1 \times 1 \times 1$ mm voxel size, 256×256 matrix, 192 slices) for anatomic localization. Sparsely sampled MR navigators (2D-EPI, $3.0 \times 3.0 \times 3.0$ mm voxels, 64×64 matrix, 36 slices, echo time = 30 ms, repetition time = 3,000 ms) were interleaved at specific time intervals (0, 2.5, 5, 7.5, 10, 14, 17, 21, 26, 33, 38, 42, 44, and 50.5 min after injection), yielding for each time point a 3D image volume (23) that allowed the determination of subject motion with 6° of freedom (translation in x, y, z direction and rotation with respect to the 3 Euler angles). These 6 motion parameters defined a motion vector, which was used to ensure spatial correspondence between early frames and late frames for cGAN training.

PET list-mode data were rebinned into a dynamic frame sequence (24×5 s, 1×60 s, 1×120 s, 11×300 s) and were reconstructed (e7 tools; Siemens) into a $344 \times 344 \times 127$ matrix (voxel size, $2.08 \times 2.08 \times 2.03$ mm) using the ordinary Poisson ordered-subset expectation maximization 3D algorithm (3 iterations, 28 subsets, 2 mm gaussian filter). Attenuation and scatter correction were performed using CT-based attenuation-corrected maps corrected for motion in each PET frame.

Blood Sampling

Arterial blood samples were collected manually at different time points (24×5 s, 1×60 s, 1×120 s, 1×300 s, 1×600 s, $2 \times 1,200$ s after injection) from the radial artery. Whole-blood radioactivity concentrations were measured using a γ -counter (2480 Wizard2 automatic γ -counter; PerkinElmer). To obtain the arterial input function (AIF), whole-blood samples were centrifuged to separate the plasma component, followed by the measurement of radioactivity in the plasma. The measured whole-blood and plasma tracer concentrations were used to calculate the time-dependent plasma-to-whole-blood ratios for each subject.

3D-cGAN

Generative Adversarial Networks (GANs) are generative algorithms, which belong to the field of unsupervised learning (24). The architecture of a GAN consists of 2 convolutional neural networks that together

constitute an opponent-component system: a neural network (termed the Generator G) that generates artificial data based on a training dataset, and a neural network (termed the Discriminator D) that classifies the artificially created data as being either real (i.e., belonging to the training dataset) or being artificially generated.

Conditional GANs (cGANs) are a supervised extension of the GAN framework (25). Although GANs typically perform a mapping operation from a random noise vector (z) to an output vector (y) expressed as ($G: z \rightarrow y$), cGANs perform a mapping operation from an observed image (x) and a random noise vector (z) to an output image (y), expressed as ($G: \{x, z\} \rightarrow y$). Here, the mapping operation is the process of linking 2 image patterns together and is “learned” from a training set that defines the true correspondence between pairs of input and output images ($x-y$). In short, the training dataset provides a general mapping of 2 images with different noise characteristics (e.g., a low-count to a high-count image). It

is a generic mapping operation that accounts for broad features in the 2 images but does not account for subject-specific attributes. Accordingly, such mapping is representative for the transformation of any ^{18}F -FDG uptake image obtained at a particular time (e.g., 2–3 min after injection) to any ^{18}F -FDG uptake image at a later time (e.g., 55–60 min after injection).

In this 3D-cGAN implementation, corresponding pairs of low-count (early) and high-count (late) PET frame images were used to define the mapping operation (G) by minimizing a loss function expressed as:

$$\mathcal{L}_{cGAN}(G, D) = E_{x,y}[\log D(x, y)] + E_x[\log(1 - D(x, G(x)))] \quad \text{Eq. 1}$$

where G attempts to minimize the loss function (\mathcal{L}_{cGAN}), whereas D strives to maximize it (i.e., $G^* = \arg \min_G \max_D \mathcal{L}_{cGAN}(G, D)$). To create artificially generated high-count images from low-count (early) PET frames, we added an estimation error loss to the Discriminator feedback for the effective training of the Generator (G) (23). The final loss function, G^* , is then expressed as:

$$G^* = \arg \min_G \max_D \mathcal{L}_{cGAN}(G, D) + \lambda \mathcal{L}_{L1}(G), \quad \text{Eq. 2}$$

where $\mathcal{L}_{L1}(G)$ is an additional L1-norm based loss function for the generator, and λ is a tunable parameter, which is greater than zero (in our case $\lambda=1$ (24)). The U-netlike architecture (26) with skip connections was used as the Generator network (Supplemental Fig. 1; supplemental materials are available at <http://jnm.snmjournals.org>), taking 3D subvolumes of the original early frame PET image as input. The skip connections facilitate the preservation of the local image information that is lost during the initial down-sampling process and transfer this information to the later occurring up-sampling phase of the network. We used a PatchGAN (Supplemental Fig. 2) as a Discriminator (22), which classifies each given patch as either true or artificial. In addition, we added 2 more convolutional layers to the Discriminator architecture. The advantage of this architecture is that the network preserves the high-frequency structures of the high-count (late) PET frames using fewer parameters than would be required using the full-size images. Training of the convolutional neural networks was performed using the standard method from Goodfellow et al. (24).

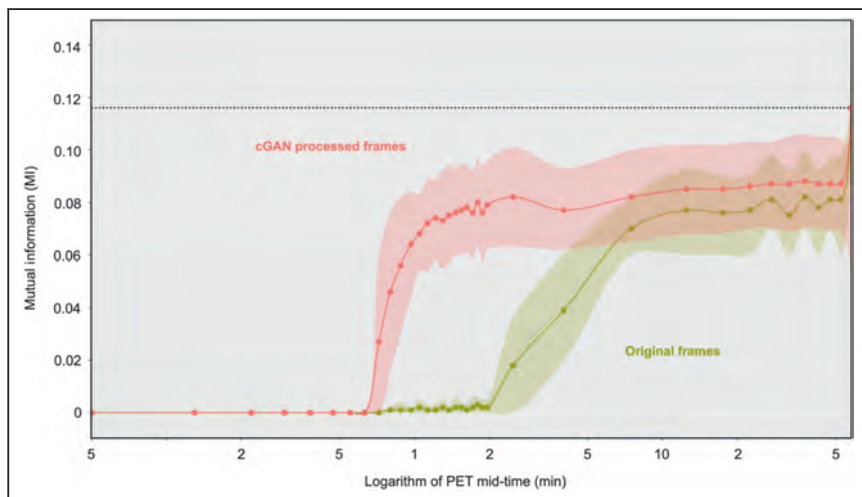


FIGURE 3. Comparison of MI index between the original (green) and cGAN processed (red) dynamic frames with the reference frame as a (log) function of scan time. Note that neither dynamic sequence is motion corrected. Values represent the average and the SD (shown as shaded area) of the test dataset ($n = 6$). cGAN processing increases MI of ^{18}F -FDG brain images with respect to the reference frame close to the MI of late frames (dotted line).

cGAN-Aided Motion Correction

A random 70%-to-30% data split of the full data was used for cGAN training (14 scans) and testing (6 scans). Initially, all studies in the training set (14 measurements with 37 frames each) were corrected for motion using motion vectors obtained from the contemporaneously acquired MR navigators (23) (Fig. 1). Real-time data augmentation (rotation, translation, shearing, additive gaussian noise, brightness, contrast) was performed on the training datasets, resulting in 21,000 synthetic datasets. Subsequently, cGAN mapping was performed between the last high-count PET frame (reference frame 37, representing tracer accumulation at 55–60 min after injection) and all other PET frames, resulting in 36 mappings ($x \rightarrow y$) with variable quality (Fig. 2).

The obtained mappings were then applied to the test datasets to obtain artificially generated high-count images (using cGAN) that imitate the distribution of the reference frame from the original low-count images. After the generation of the cGAN-based high-count images for the test datasets, motion correction was performed by considering the 55–60 min postinjection PET frame as reference frame (F_{ref}), and all other frames were subsequently registered to the F_{ref} using a standard multiscale mutual information (MI) routine (Greedy module ITK 1.2.4, Insight Segmentation and Registration Toolkit). For each frame of the dynamic sequence, this approach resulted in a 6-parameter motion vector.

Standard PET Frame-Based Motion Correction

To evaluate the added value of cGAN-aided motion correction, this methodology was compared with a standard PET frame-based motion correction. PET image frames were aligned using the same multiscale MI-based coregistration routine as described above (Greedy module ITK 1.2.4). This routine performs alignment between images starting at a coarse scale, which is then used to initialize registration at the next finer scale, a process repeated until it reaches the finest possible scale. As for the early images (<3 min after injection), the applied multiscale MI coregistration approach failed due to insufficient count statistics, thus we summed the first 3 min of the dynamic sequence to create a reference frame with sufficient statistics. Subsequently, all later frames (>3 min after injection) were rigidly aligned to this summed frame. It is important to point out that this approach (summing of early frames) is frequently implemented in dynamic studies when low-count

images that do not contain sufficient data that would allow extraction of an accurate motion vector are analyzed. Because robustness of this coregistration procedure can be improved by low-level smoothing (The ITK Software Guide; Kitware Inc.), our standard registration approach therefore consisted of applying a heuristically chosen 4-mm gaussian filter to the images before registration. However, to assess the performance of cGAN methodology when processing the original (low-count) images, this smoothing step was omitted when testing cGAN-processed images.

PET Emission Data and Attenuation Map Alignment

To account for misalignment between the PET emission data and the attenuation map, we used a dual-reconstruction approach. Specifically, PET attenuation correction was performed on the basis of an attenuation map derived from a CT image acquired immediately after the PET/MRI protocol. This CT attenuation map was coregistered to the

first MR sequence of the study protocol (TOF-MRA sequence), and this static map was then used to perform attenuation correction for the whole PET dynamic sequence. However, this approach does not take into account PET interframe motion. Therefore, non-motion-corrected PET frames were initially used to derive a motion vector (using either MR navigators for the training data or cGAN-processed images for the test data), and once the motion vector was determined this information was used to align the CT attenuation map to each PET dynamic frame. The motion-corrected CT attenuation maps were subsequently used to re-reconstruct the whole dynamic PET sequence.

Characterization of cGAN Performance

To assess the degree to which cGAN image processing is able to enhance generic features of brain tracer distribution (such as overall brain shape and contours), cGAN performance of individual frames was assessed on the basis of 2 measures: first, by the improvement in MI between the reference image and the cGAN-generated high-count images relative to the original images, and second, by the comparison of the absolute percentage difference with respect to the histogram area-under-the-curve (Hist_{AUC}) between histograms derived from cGAN-generated and reference images. It is important to note that these histograms include all image voxels in 3D space and are not affected by subject motion. Moreover, the MI and Hist_{AUC} are complementary; MI is sensitive to the similarity in image patterns expressed in the 2 images, whereas Hist_{AUC} provides information with respect to scale relationship between voxel intensities in the 2 images (27,28).

Generation of Simulated Test Datasets

Given the low number of the original test datasets (6 scans), additional test datasets were generated on the basis of the original 6 test datasets. These simulated datasets were used to further investigate the potential of the cGAN method to address the problem of interframe motion.

Excessive interframe motion was simulated by adding to each dynamic frame (except the reference frame) an arbitrary translation (0, 1, or 2 voxels in each direction) and rotation (0°, 0.5°, or 1° for each Euler angle) vector (SimpleITK 1.2.4, Supplemental Fig. 3). Ten repetitions were performed for each dataset with different motion vectors added, resulting in a total of 60 synthetically created test datasets, each consisting of 37 dynamic frames. These datasets were then either

preprocessed using cGAN methodology or were directly coregistered to the reference frame (standard PET frame-based motion correction) using the normalized MI alignment routine as described above.

Moreover, to assess the potential of cGAN methodology to aid in the detection of intraframe motion in routine clinical static studies, we partitioned the list-mode data of the reference frames (#37 from 55–60 min after injection) into a series of short subframes (10 subframes of 30 s and 20 subframes of 15 s). cGAN was used to produce artificially generated high-count images from these subframes. This procedure was applied for each measurement of the test dataset (6 scans). Improvement in image quality was assessed on the basis of the increase in MI after cGAN processing. In addition, to further demonstrate the ability of cGAN processing in accurately accounting for intraframe motion, we selected a representative reference frame, which we partitioned into 15-s subframes and introduced random motion (translation 3–5 mm, rotation <1°) to the subframes. After motion correction either with (cGAN-aided) or without cGAN preprocessing, the coregistered subframes were summed and the resulting images were visually compared for image quality.

cGAN-Based IDIF

To assess the clinical performance of the cGAN method for motion compensation of dynamic PET frames, we extracted the IDIF from the test dataset (both original and simulated) and compared the IDIF with the AIF. For this, we replaced the MRI navigator-based motion correction in our previously developed IDIF pipeline with the developed cGAN-aided motion correction. This analysis pipeline was described in detail previously (9,10). In brief, it entails automated segmentation of the petrous region of the internal carotid arteries (ICA) from the corresponding TOF-MRA images followed by an automatic multiscale intermodal NMI coregistration (Greedy ITK 1.2.4) of the TOF-MRA volume and the reference frame (frame #37) for each study. The arterial blood-pool region was defined on the basis of the MR angiography image, clearly identifying the ICA region. This region was subsequently transferred into PET space where it was used to extract the time–activity curve. cGAN-aided motion vectors were applied during the extraction of the time–activity curve to adjust the blood-pool region for the computed displacements. Finally, an iterative regional partial volume correction procedure was applied in each PET frame to recover the true activity in the internal carotid arteries (10).

Postprocessing of IDIF

The motion- and partial volume-corrected IDIF was interpolated with a step length of 1 using a “Piecewise Cubic Hermite Interpolating Polynomial” to match the blood sampling times. All corrections were applied to the IDIF, with the AIF being considered as the reference (3,9). First, count rates from sampled arterial blood were scaled using the cross-calibration factor between the PET/MR and the on-site γ -counter to express the AIF in the same units as the PET data (Bq/mL). Second, a plasma IDIF was derived on the basis of the individual plasma-to-blood ratios obtained from sampled arterial blood of the study subjects. Third, the delay between the AIF and the IDIF was corrected by shifting the IDIF curve to match the sampling times of the AIF. Finally, due to the difference in sampling location (ICA for IDIF and radial arteries for AIF), a monoexponential dispersion function with a tau value of 5 s (29) was convolved with the IDIF to mimic the dispersion effects.

Quantification of CMRGlc

Calculation of cerebral metabolic rate of glucose (CMRGlc) for the test datasets was performed using a voxelwise Patlak graphical analysis (lumped constant = 0.65 (30)) using either the AIF or the IDIF. Analyses were performed using in-house-developed Matlab tools (Matlab R2018a; The MathWorks) that generate parametric images representing CMRGlc ($\mu\text{mol}/100 \text{ g}/\text{min}$). In particular, a linear function was fitted to the Patlak-transformed

data, including data from 25 min after injection until the end of the scan (8 data points). The resulting slope was then multiplied with the subject’s plasma glucose level ($\mu\text{mol}/\text{L}$) and divided by the lumped constant. By applying a gray matter (GM) mask derived from individually coregistered T1-weighted MR images, the average CMRGlc value in the GM was determined using either the AIF ($\text{CMRGlc}_{\text{AIF}}$) or the IDIF ($\text{CMRGlc}_{\text{IDIF}}$).

Assessment of cGAN Performance for Motion Compensation

The quality of cGAN-aided motion correction of the dynamic frame sequence was assessed in relation to the sampled AIF. Specifically, IDIFs were determined from the test datasets (both original and simulated) using cGAN-aided motion vectors and compared with the AIFs using the area under the curve (AUC). Differences in GM CMRGlc values derived from the IDIF and AIF were assessed using the absolute percentage difference ($|%\Delta|$) between CMRGlc values:

$$|\% \Delta| = \left| \frac{\text{CMRGlc}_{\text{IDIF}} - \text{CMRGlc}_{\text{AIF}}}{\text{CMRGlc}_{\text{AIF}}} \right| \times 100. \quad \text{Eq. 3}$$

cGAN performance was assessed separately for the original dataset ($n = 6$) and the simulated dataset ($n = 60$).

RESULTS

Figure 2 visualizes the results of cGAN processing of the dynamic frame sequence from approximately 100 s (1.7 min) after injection until the penultimate frame in the study (#36). The data indicate a visually excellent quality of the artificially generated images for frames of 60 s duration, as early as 2 min after injection of the tracer. In contrast, the quality of cGAN images appears suboptimal for very short frames (5 s) before 2 min after injection.

Quantitative assessment of cGAN performance based on MI is depicted in Figure 3. A substantial increase in MI of the individual frames after the application of cGANs, in frames as early as 1 min after injection, is clearly noted. Figure 4 indicates a substantial decrease in the $|%\Delta|$ between histogram AUCs characterizing cGAN-processed images and those characterizing the original images during the very early phase of the study (60–120 s). During that time, cGAN-processed images derived from the very short frames (5 s) decreased the difference in histogram AUC by approximately 80% relative to histogram AUCs obtained from the original images. Subsequent improvements were minor (<5%) for longer and later frames with better count statistics.

Supplemental Figure 4 demonstrates that cGAN-based IDIFs were closer to the reference standard in comparison to the IDIFs obtained without cGAN processing and using only standard frame-based motion correction (motion profile of the represented subjects in Supplemental Fig. 5). For the original dataset ($n = 6$), the $|%\Delta|$ between AUCs derived using the motion-corrected IDIF and the AIF was $1.2\% \pm 0.9\%$. The GM CMRGlc values determined using these 2 input functions differed by less than 5% ($2.4\% \pm 1.7\%$) (Fig. 5). The quantitative difference in AUC and GM CMRGlc values between AIF and IDIF (before and after cGAN preprocessing) for individual datasets ($n = 6$) with their respective augmentations (10 iterations) is depicted in Table 1. For the simulated datasets ($n = 6 \times 10$ iterations), the mean difference in AUC values between those obtained using the AIF and the IDIF using cGAN preprocessing was $0.9\% \pm 0.7\%$, whereas the difference in AUC values between AIF and the IDIF without cGAN preprocessing was $2.9\% \pm 3.1\%$. Moreover, IDIFs extracted from cGAN-preprocessed motion compensated data resulted in CMRGlc values closer to those obtained using the AIF, with an absolute difference of $2.2\% \pm 1.8\%$ as compared with CMRGlc values determined

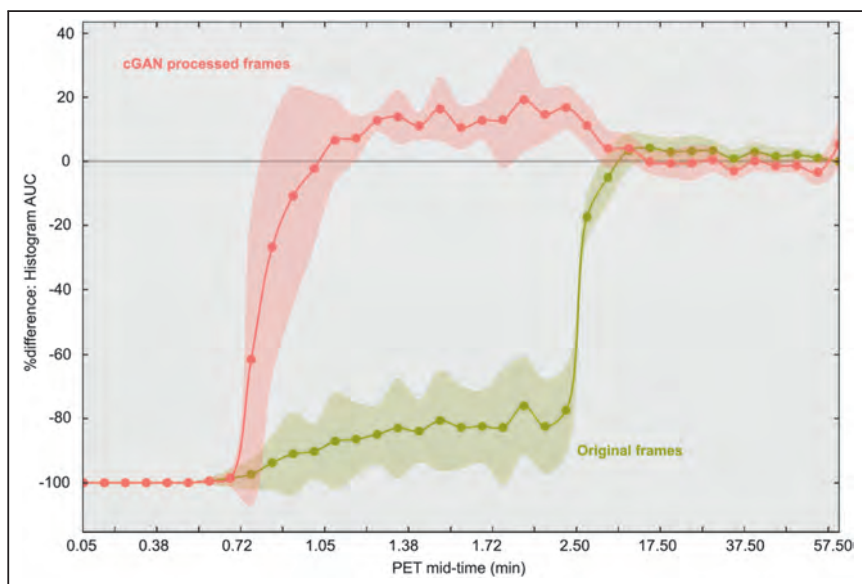


FIGURE 4. The $|\% \Delta|$ of the AUC between the reference image histogram and image histograms derived from cGAN-processed images (red) and original images (green) as a function of scan time. Note, images were not motion corrected because histograms are independent from motion. The percentage difference is substantially decreased for low-count (short) frames between 1 min and 2 min after injection, suggesting that an accurate motion vector can be determined even for early frames.

without cGAN preprocessing of $3.9\% \pm 3.5\%$. The improved performance of cGAN-aided as compared with non-cGAN-aided motion correction can be also inferred from the smaller variance of both AUC and GM CMRGlc values in the case of cGAN preprocessing.

Figure 6 shows representative images that were obtained by partitioning the reference image (55–60 min after injection) into 15-s subframes and the image quality of these subframes after cGAN processing. For the 10×30 s subframe dataset, the MI improved by 135% (from 0.030 ± 0.003 to 0.070 ± 0.001), whereas improvement was even greater for the 20×15 s dataset (improvement of 290%; from 0.002 ± 0.003 to 0.0700 ± 0.0001). Moreover, Figure 7 demonstrates the improvement in image quality of the reference image when 15-s subframes with artificially introduced random motion underwent standard frame-based motion correction and cGAN preprocessing before rigid-body motion correction as compared with non-motion-corrected summed subframes. As expected, motion correction improves image sharpness, and one can appreciate a slight improvement of images processed using cGAN methodology as compared with those processed with standard frame-based motion correction.

DISCUSSION

We present a fully automated motion-correction approach for dynamic ^{18}F -FDG PET studies of the brain that uses cGAN preprocessing of low-count images to improve the estimation of motion vectors derived using conventional rigid-body coregistration algorithms (Fig. 2). Our results suggest that cGAN methodology allows the creation of artificially generated high-count ^{18}F -FDG brain images from early low-count images that closely resemble the ^{18}F -FDG uptake pattern at late (~ 60 min after injection) scan times. The creation of artificially generated, high-count images allows then the reliable determination of a motion vector directly from the data, which was verified by the comparison of an IDIF with arterial blood samples. Thus, cGAN-aided

motion correction is likely to have a substantial impact on the quality of dynamic low-count ^{18}F -FDG PET brain studies and as a result might contribute to the expansion of absolute brain quantification into clinical routine. Especially in the context of clinical PET/CT imaging, cGAN preprocessing of low-count image frames could play an important role in improving the performance of established motion-correction approaches. The developed cGAN methodology also shows promise in addressing the problem of intraframe motion in long-duration (5–20 min) PET scans, by allowing the partitioning of a frame into subframes which, after cGAN preprocessing, can be accurately corrected for motion.

To prevent motion when imaging the brain, subjects are usually instructed to remain motionless, and their head is immobilized using bands that affix the skull to the head rest (31). This approach works reasonably well when imaging cooperative subjects, but frequently fails in the clinical population due to the subjects being either uncomfortable or claustrophobic within the PET gantry (31).

As a result, motion artifacts are frequently encountered in both static and dynamic PET imaging. The problem with motion artifacts is even more severe when an IDIF is extracted from the dynamic PET sequence, given that the magnitude of random displacements and the system resolution are typically larger than the small size of the arteries. Accordingly, accurate motion correction is an important prerequisite for absolute quantification in PET imaging (17).

It has been well recognized that the original low-count/high-noise images are poorly suited for alignment due to the poor

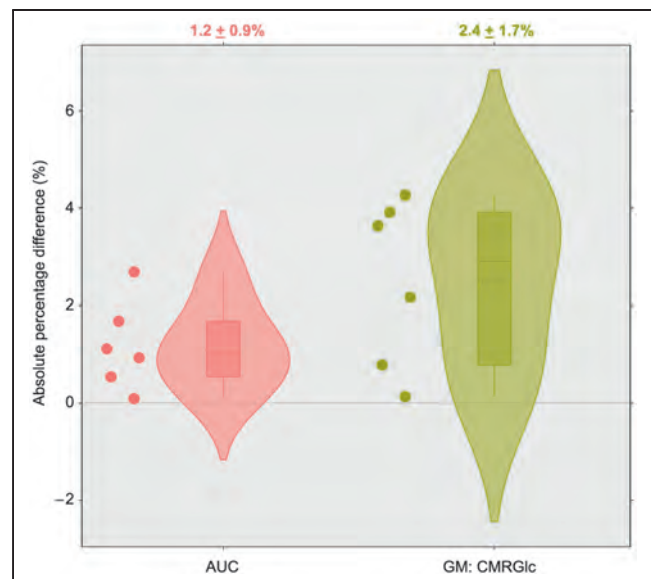


FIGURE 5. The $|\% \Delta|$ between AUC and GM CMRGlc values ($n = 6$) obtained using the cGAN-based IDIF and AIF. All differences were within 5% of the AIF standard.

TABLE 1

The $|\%Δ|$ Between AUC or GM CMRGlc Values ($n = 6 \times 10$ Synthetic Datasets) Using the IDIF (Motion Corrected With cGAN and Without cGAN Processing) and Values Obtained Using Arterial Blood Sampling

Patient ID	AUC original PET frames (mean \pm SD %)	AUC cGAN processed frames (mean \pm SD %)	GM CMRGlc original PET frames (mean \pm SD %)	GM CMRGlc cGAN processed frames (mean \pm SD %)
P-01	1.4 \pm 0.8	0.8 \pm 0.3	3.8 \pm 2.3	3.9 \pm 0.4
P-02	2.0 \pm 1.4	0.4 \pm 0.3	2.7 \pm 2.5	1.3 \pm 1.0
P-03	8.3 \pm 1.7	1.7 \pm 0.4	10.1 \pm 2.6	0.9 \pm 0.6
P-04	4.3 \pm 2.9	0.8 \pm 0.7	3.1 \pm 2.3	0.9 \pm 0.8
P-05	1.1 \pm 0.6	0.2 \pm 0.2	1.9 \pm 0.6	1.0 \pm 0.3
P-06	1.3 \pm 0.6	0.5 \pm 0.4	4.9 \pm 0.9	1.9 \pm 0.6

definition of image landmarks that could guide the registration procedure. As such, low-count images require some form of pre-processing to achieve a satisfactory performance of the subsequently applied coregistration routines (32). This preprocessing step could include various forms of smoothing or morphologic operations, but could also consist of more sophisticated forms of processing, such as the cGAN methodology. From a conceptual point of view, cGAN preprocessing might be superior to the previously applied methods, as cGAN processing is based on an automated (i.e., operator-independent) mapping of low-count images to their true high-count match. Stated differently, the calculated mapping is specific to the noise characteristics of the original low-count images, and the resulting artificially generated images represent the most likely prediction of the final (high-count) tracer distribution one could expect based on the training data. Overall, our data clearly highlight the strengths of cGAN processing, such as the autonomous optimized smoothing and “smart” inpainting, which substantially enhance the information content of low-count

images so that coregistration algorithms are provided with sufficient information to accurately estimate the motion parameters.

In practical terms, the functionality of cGANs consists in the ability to correctly predict the local distribution of measured data based on a statistically insufficient sample. More specifically, the cGAN algorithm extracts the most likely relationships between low-count images (where the underlying distribution is ambiguous) and high-count images (where the underlying distribution is well defined) from the training dataset and applies the extracted relationships to new images. As a result, cGAN methodology is able to accurately predict generic image features (such as brain contours) from low-count images. The improved definition of brain contours then allows improved performance of conventional MI coregistration routines that strongly depend on well-defined imaging features.

Images with dissimilar uptake pattern are typically encountered in dynamic studies when the tracer uptake pattern changes as a function of time during the frame sequence. Our results showed that structural information inherent to very early low-count images (<2 min after injection) is insufficient to generate an acceptable mapping with the reference frame, thus precluding the generation of a high-count image that could guide the derivation of an accurate motion vector. Conversely, ^{18}F -FDG brain uptake at times > 2 min after injection appears to be sufficient for adequate cGAN mapping if the frames are not too short (>30 s).

However, we acknowledge that the relevance of cGAN processing is strongly diminished in the case of high-count/low-noise images that are already characterized by well-defined features. Finally, despite the fact that histograms derived from cGAN-processed images have a similar overall shape with respect to the reference images (Supplemental Fig. 6), they tend to overrepresent high intensities and should not be used in lieu of the original low-count images for clinical diagnosis.

Data from our previous studies suggest that motion magnitude increases with time, and for very early time points (<2 min) the motion magnitude tends to be negligible (i.e., translation all axes < 1 mm, rotation <1° in all axes) (9,10). Moreover,

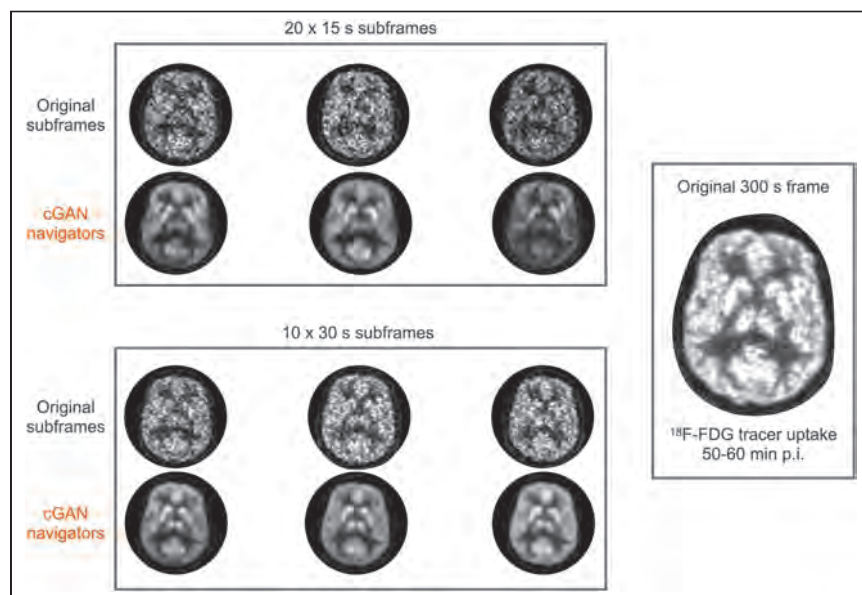


FIGURE 6. Performance of cGAN processing when applied to a subset of frames that were partitioned into frames of either 15-s duration (left upper panel) or 30-s duration (left lower panel) from an original 300-s static ^{18}F -FDG frame at 55 min after injection (right panel). The image quality of the processed subframes for both subsets is substantially improved when compared with the unprocessed subframes and resembles closely the original 300-s frame that includes all data.

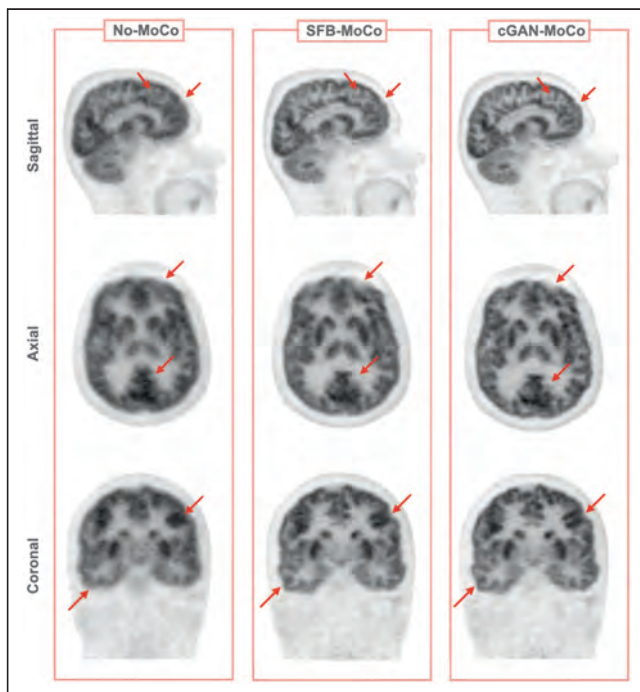


FIGURE 7. Summed images corresponding to 55–60 min p.i., after intra-frame motion correction using motion vectors obtained from 15-s subframes. (Left column) Summed images without correction for intraframe motion (No-MoCo). (Middle column) Summed images after standard frame-based motion correction without cGAN preprocessing (SFB-MoCo). (Right column) Summed images using cGAN-aided motion correction (cGAN-MoCo). Red arrows indicate the areas of improvement.

even in the case of subject movement in this very early phase of the study, the error accrued in the integral under the blood time–activity curve remains negligible. We demonstrated this accuracy in our own test dataset, showing a mean value of <1.5% for the absolute difference between the IDIF and the sampled arterial blood curve, which translated to an average difference of <3% for the calculated glucose metabolic rate in GM (Fig. 5).

An exciting application of cGAN-aided motion correction is the possibility to address intraframe motion in static clinical PET scans. Clinical ^{18}F -FDG brain scans are usually performed at times > 45 min with a typical duration of 10–20 min. Such relatively long frames are sometimes subject to considerable patient motion artifacts, which impair image resolution and reduce image contrast important for differential diagnosis. Our data suggest that due to the high tracer uptake in brain tissue at these late time points, these long frames can be partitioned into subframes as short as 15 s, which can be then processed with cGAN methodology to yield images of sufficient quality for accurate coregistration (Fig. 6). Thus, one can envision a reconstruction protocol in which list-mode data are sequentially divided into smaller and smaller subframes that are individually corrected for motion by taking advantage of enhanced image features generated by cGAN preprocessing, resulting in an overall improvement in image quality. We would like to point out that the short subframes (15 s) are only necessary to determine the exact time of displacement. Because realistic patient motion occurs in the form of a few distinct shifts in head position interspersed within a longer time frame, most motion vector parameters derived from the set of all short subframes will be negligible.

In this context, the question arises whether mappings are specific to one particular imaging system or whether they could be also applied to ^{18}F -FDG data obtained from other imaging systems. Our very preliminary data suggest that mappings might be transferrable to other imaging systems on the basis of the application of our mappings to a dynamic ^{18}F -FDG study (12 × 60 s, 4 × 120 s, 5 × 300 s) acquired using an external PET/CT system from a different vendor. The only requirement is that mappings should match their respective PET mid-times. Supplemental Figure 7 suggests that mappings might possibly be independent from the imaging system; however, this issue mandates further investigations that were not the focus of this work.

One of the main drawbacks of the study is the low number of test datasets. Although synthetic data with variable motion parameters were generated, they were still generated from the test datasets. Moreover, there are several other limitations that need to be considered when applying cGAN methodology in clinical applications. First, current implementations of cGAN processing are highly computationally intensive. The time to generate one (source-to-target) mapping pair is 17 h on a dedicated NVIDIA DGX Workstation with 1 × 32 GB Tesla V100 Volta GPU for a frame size of 344 × 344 × 127 voxels. However, once a mapping specific for a particular tracer is established via the training process, the time to apply this mapping to a low-count image of any individual subject is only 1 min. Another potential source of error might be intra-frame motion in the reference frame. In this study, we did not correct for such motion artifacts because neither visual inspection of image quality nor close monitoring of the subjects during the last frame indicated noticeable subject motion. Finally, our cGAN implementation requires a training set that consists of image pairs that are devoid of motion artifacts. Because our data were acquired on a fully integrated PET/MR system, simultaneously acquired MR navigators were used to correct the training set for motion. When translating these findings to other sites, the use of cycle GANs (33), which produce generic mappings from spatially non-corresponding data, may be a potential solution that voids the requirement of motion-corrected image pairs.

CONCLUSION

We present a data-driven motion-correction approach for dynamic ^{18}F -FDG brain studies that is based on cGAN methodology. The method allows the derivation of an accurate motion vector for low-count frames as early as 2 min after injection, thus facilitating the derivation of an IDIF void of motion artifacts. The developed methodology has the potential to improve the accuracy of noninvasive absolute quantification in the context of clinical PET and PET/CT studies. In addition, cGAN methodology might also facilitate correction for intraframe motion, thus improving image quality of clinical scans of long duration.

DISCLOSURE

This work was supported by the Austrian Science Fund KLI482-B31. David Iommi and Zacharias Chalampalakis are funded by a Marie Skłodowska-Curie grant (no. 764458, EU Horizon 2020 research and innovation program). Lucas Rischka is recipient of a DOC Fellowship of the Austrian Academy of Sciences at the Department of Psychiatry and Psychotherapy, Medical University of Vienna. Without relevance to this work, Rupert Lanzenberger received travel grants or conference speaker honoraria within the last 3 years from Bruker BioSpin MR, Heel, and support

from Siemens Healthcare regarding clinical research using PET/MR. He is shareholder of BM Health GmbH since 2019. No other potential conflict of interest relevant to this article was reported.

KEY POINTS

QUESTION: Can conditional generative adversarial networks facilitate ^{18}F -FDG PET brain motion correction by generating temporally activity invariant PET navigators?

PERTINENT FINDINGS: The proposed motion-correction approach allows accurate noninvasive determination of an IDIF. The developed noninvasive method yields CMRGlc values that are within 5% of those determined using arterial sampling.

IMPLICATIONS FOR PATIENT CARE: cGAN-aided motion correction of ^{18}F -FDG dynamic PET brain studies depends only on the acquired emission data and can be applied retrospectively without additional information. As such, it can be easily implemented in clinical routine and has the potential to facilitate noninvasive absolute quantification in the context of clinical ^{18}F -FDG PET/CT patient studies.

ACKNOWLEDGMENTS

We express our gratitude to Vivian Tseng from The University of Applied Arts Vienna for creating the graphical abstract for our article. To invite swift adoption of this novel approach by the research and clinical community, software codes developed for cGAN processing are free and available online: <https://github.com/LalithShiyam/QIMP-tools/tree/master/PANDA>. This repository contains all software code that has been used to perform analyses in our work.

REFERENCES

- Lammertsma AA. Forward to the past: the case for quantitative PET imaging. *J Nucl Med*. 2017;58:1019–1024.
- Subramaniam RM. Precision medicine and PET/computed tomography: emerging themes for future clinical practice. *PET Clin*. 2017;12:xi–xii.
- Sari H, Erlandsson K, Law I, et al. Estimation of an image derived input function with MR-defined carotid arteries in FDG-PET human studies using a novel partial volume correction method. *J Cereb Blood Flow Metab*. 2017;37:1398–1409.
- Jochimsen TH, Zeisig V, Schulz J, et al. Fully automated calculation of image-derived input function in simultaneous PET/MRI in a sheep model. *EJNMMI Phys*. 2016;3:2.
- Su Y, Vlassenko AG, Couture LE, et al. Quantitative hemodynamic PET imaging using image-derived arterial input function and a PET/MR hybrid scanner. *J Cereb Blood Flow Metab*. 2017;37:1435–1446.
- Khalighi MM, Deller TW, Fan AP, et al. Image-derived input function estimation on a TOF-enabled PET/MR for cerebral blood flow mapping. *J Cereb Blood Flow Metab*. 2018;38:126–135.
- Su Y, Shoghi KI. Single-input-dual-output modeling of image-based input function estimation. *Mol Imaging Biol*. 2010;12:286–294.
- Fung EK, Carson RE. Cerebral blood flow with $[^{15}\text{O}]$ water PET studies using an image-derived input function and MR-defined carotid centerlines. *Phys Med Biol*. 2013;58:1903–1923.
- Sundar LKS, Muzik O, Rischka L, et al. Towards quantitative $[^{18}\text{F}]$ FDG-PET/MRI of the brain: Automated MR-driven calculation of an image-derived input function for the non-invasive determination of cerebral glucose metabolic rates. *J Cereb Blood Flow Metab*. 2019;39:1516–1530.
- Shiyam Sundar LK, Muzik O, Rischka L, et al. Promise of fully integrated PET/MRI: noninvasive clinical quantification of cerebral glucose metabolism. *J Nucl Med*. 2020;61:276–284.
- Carson RE, Barker WC, Jeih-San Liow, Johnson CA. Design of a motion-compensation OSEM list-mode algorithm for resolution-recovery reconstruction for the HRRT. *IEEE Nucl Sci Symp Conf Rec*. 2003;5:3281–3285.
- Lu Y, Gallezot J-D, Naganawa M, et al. Data-driven voluntary body motion detection and non-rigid event-by-event correction for static and dynamic PET. *Phys Med Biol*. 2019;64:065002.
- Ren S, Jin X, Chan C, et al. Data-driven event-by-event respiratory motion correction using TOF PET list-mode centroid of distribution. *Phys Med Biol*. 2017;62:4741–4755.
- Feng T, Yang D, Zhu W, Dong Y, Li H. Real-time data-driven rigid motion detection and correction for brain scan with listmode PET. *IEEE Nucl Sci Symposium (MIC/RTSD)*. 2016;1:4.
- Huang C, Petibon Y, Normandin M, Li Q, El Fakhri G, Ouyang J. Fast head motion detection using PET list-mode data. *J Nucl Med*. 2015;56(suppl 3):1827.
- Thielemans K, Schleyer P, Dunn J, Marsden PK, Manjeshwar RM. Using PCA to detect head motion from PET list mode data. *IEEE Nucl Sci Symp (MIC)*. 2013;1:5.
- Lu Y, Naganawa M, Toyonaga T, et al. Data-driven motion detection and event-by-event correction for brain PET: comparison with Vicra. *J Nucl Med*. 2020;61:1397–1403.
- Costes N, Dagher A, Larcher K, Evans AC, Collins DL, Reilhac A. Motion correction of multi-frame PET data in neuroreceptor mapping: simulation based validation. *Neuroimage*. 2009;47:1496–1505.
- Picard Y, Thompson CJ. Motion correction of PET images using multiple acquisition frames. *IEEE Trans Med Imaging*. 1997;16:137–144.
- Kyme AZ, Se S, Meikle SR, Fulton RR. Markerless motion estimation for motion-compensated clinical brain imaging. *Phys Med Biol*. 2018;63:105018.
- Isola P, Zhu J-Y, Zhou T, Efros AA. Image-to-image translation with conditional adversarial networks. Research Gate website. https://www.researchgate.net/publication/310610633_Image-to-Image_Translation_with_Conditional_Adversarial_Networks. Published November 2016. Accessed March 17, 2021.
- Wang Y, Yu B, Wang L, et al. 3D conditional generative adversarial networks for high-quality PET image estimation at low dose. *Neuroimage*. 2018;174:550–562.
- Keller SH, Hansen C, Hansen C, et al. Motion correction in simultaneous PET/MR brain imaging using sparsely sampled MR navigators: a clinically feasible tool. *EJNMMI Phys*. 2015;2:14.
- Goodfellow I, Pouget-Abadie J, Mirza M, et al. Generative adversarial nets. In: Ghahramani Z, Welling M, Cortes C, Lawrence ND, Weinberger KQ, eds. *Advances in Neural Information Processing Systems 27*. Curran Associates, Inc.; 2014:2672–2680.
- Mirza M, Osindero S. Conditional generative adversarial nets. arXiv.org website (Cornell University). <https://arxiv.org/abs/1411.1784v1>. Published November 2014. Accessed March 17, 2021.
- Ronneberger O, Fischer P, Brox T. U-Net: convolutional networks for biomedical image segmentation. arXiv.org website (Cornell University). <https://arxiv.org/abs/1505.04597v1>. Published May 2015. Accessed March 17, 2021.
- Reza FM. *An Introduction to Information Theory*. Courier Corporation; 1994.
- Studholme C, Hill DLG, Hawkes DJ. Automated 3-D registration of MR and CT images of the head. *Med Image Anal*. 1996;1:163–175.
- Iida H, Law I, Pakkenberg B, et al. Quantitation of regional cerebral blood flow corrected for partial volume effect using O-15 water and PET: I. theory, error analysis, and stereologic comparison. *J Cereb Blood Flow Metab*. 2000;20:1237–1251.
- Wu HM. Measurement of the global lumped constant for 2-deoxy-2-[^{18}F]fluoro-D-glucose in normal human brain using $[^{15}\text{O}]$ water and 2-deoxy-2-[^{18}F]fluoro-D-glucose positron emission tomography imaging a method with validation based on multiple methodologies. *Mol Imaging Biol*. 2003;5:32–41.
- Huang C, Ackerman JL, Petibon Y, Brady TJ, El Fakhri G, Ouyang J. MR-based motion correction for PET imaging using wired active MR microcoils in simultaneous PET-MR: phantom study. *Med Phys*. 2014;41:041910.
- Mukherjee JM, Lindsay C, Mukherjee A, et al. Improved frame-based estimation of head motion in PET brain imaging. *Med Phys*. 2016;43:2443.
- Zhu J-Y, Park T, Isola P, Efros AA. Unpaired image-to-image translation using cycle-consistent adversarial networks. *IEEE Inter Conf Comp Vis*. 2017;2223–2232.

Titre : Modélisation et reconstruction de images paramétrique corps-entier en imagerie pharmacologique TEP-IRM.

Mots clés : TEP, reconstruction dynamique, TEP corps entier, imagerie paramétrique

Résumé : La tomographie par émission de positons (TEP) est fréquemment utilisée pour des applications cliniques, avec une majorité des pratiques reposant sur des mesures qualitatives et semi-quantitatives. Mais l'imagerie TEP a la capacité de fournir des informations fonctionnelles entièrement quantitatives sur les processus sous-jacents explorés, grâce à l'imagerie dynamique et à la modélisation cinétique. Ces informations quantitatives peuvent être utilisées comme biomarqueurs pour des applications cliniques, en particulier pour la médecine de précision. Des protocoles avec des positions du lit multiples, dédiés à l'imagerie dynamique du corps entier (DWB), ont été développés afin d'étendre le champ de vue effectif, au prix de restrictions dans le nombre de détections et la fréquence d'échantillonnage. L'objectif de cette thèse est d'améliorer la qualité de l'imagerie paramétrique du corps entier pour les applications d'imagerie DWB sur un système hybride TEP-IRM.

Dans notre première contribution, nous avons présenté le développement d'un protocole entièrement automatisé pour l'imagerie DWB sur un système TEP-IRM clinique, qui a permis de réduire les délais d'acquisition, ce qui se traduit par une augmentation du nombre de détections et de la fréquence d'échantillonnage. Le recours à l'automatisation complète a permis d'optimiser la planification des positions des lits, en utilisant au mieux le champ de vue effectif.

Pour la deuxième contribution, nous avons développé des algorithmes de reconstruction dynamique dans un logiciel ouvert, et évalué les avantages offerts par l'utilisation de divers modèles cinétiques dans la reconstruction de données TEP dynamiques simulées et réelles. Ces évaluations étaient focalisées sur les reconstructions de lits individuels des protocoles DWB. Dans le cas particulier de l'imagerie DWB, la reconstruction dynamique a montré des propriétés favorables pour l'exactitude et la précision des images paramétriques du corps entier, tout en fournissant des images dont

le bruit est comparable à celui des protocoles dynamiques standards à position de lit unique, reconstruits avec des techniques ordinaires.

Dans notre troisième contribution, nous présentons une extension des fonctionnalités développées précédemment: la reconstruction dynamique simultanée de toutes les données multi-lits. Cette méthodologie permet l'utilisation synchrone de toutes les données d'acquisition DWB dans une seule boucle de reconstruction. La méthode a été appliquée à une étude pharmacocinétique DWB réalisée sur un système TEP-IRM. Une comparaison a été faite avec des reconstructions statiques standards suivies d'une modélisation cinétique post reconstruction. Les résultats obtenus avec les deux méthodes étaient en bon accord, sans introduction de biais sur les métriques évaluées. En outre, l'utilisation de la reconstruction dynamique a entraîné une réduction notable du bruit dans les images d'émission et paramétriques.

Dans notre quatrième contribution, une méthode de détection et de correction des erreurs de modélisation utilisant la modélisation résiduelle adaptative a été appliquée et évaluée. Elle a montré des résultats prometteurs pour la réduction des erreurs de modélisation et leur propagation, tout en permettant la générnicité dans l'utilisation des algorithmes de reconstruction dynamique.

Nos résultats ont montré que la reconstruction dynamique est nécessaire en imagerie paramétrique corps-entier pour obtenir une quantification précise et stable. De nombreuses méthodes ont été proposées dans ce projet afin d'optimiser le processus de reconstruction TEP pour l'imagerie DWB, en utilisant au mieux les données dynamiques acquises sur plusieurs positions de lit. Pour généraliser son utilisation, certaines améliorations méthodologiques doivent encore être apportées pour garantir une imagerie paramétrique fiable et sans artefact, notamment en ce qui concerne les mouvements du patient.

Title : Modelling and Reconstruction of Whole Body parametric maps in PET-MRI Pharmacological imaging

Keywords : Positron Emission tomography, Dynamic imaging, dynamic reconstruction, Dynamic whole body PET, Parametric imaging, pharmacokinetic maps.

Abstract : Positron Emission Tomography (PET) is used extensively for clinical applications, with the majority of practices relying on qualitative and semi-quantitative measures. But PET imaging has the ability to deliver fully quantitative functional information of underlying imaged processes by use of dynamic imaging and kinetic modelling. That unique quantitative information can be utilised as biomarkers for clinical applications, especially in precision medicine. But clinical applications often require imaging over the whole body and the majority of clinical scanners provide a limited axial Field of View (FOV). Multiple bed position protocols for dynamic whole-body (DWB) imaging have been developed to extend the effective FOV, at the cost of considerable limitations in acquisition counts and sampling frequency. The objective of this thesis is to improve the quality of whole-body parametric imaging for DWB imaging applications on a hybrid PET/MR scanner.

In our first contribution we presented the development of a fully automated acquisition protocol for DWB imaging on a clinical PET/MR system, which resulted in reduced delays between whole body sweeps of the dynamic whole-body acquisition. These improvements can be used towards increasing acquisition counts and sampling frequency. Furthermore, the use of full automation enabled optimized planning of the individual bed positions for the best use of the effective FOV.

For the second contribution we developed dynamic reconstruction algorithms within an existing open source reconstruction software. We evaluated benefits offered by use of various dynamic models in reconstruction, using simulated and real dynamic PET data.

These evaluations were focused on reconstructions of individual beds from DWB acquisition protocols. Our results agreed with previous findings on the use of dynamic reconstruction. In the particular case of DWB imaging, dynamic reconstruction showed desirable properties for whole-body parametric image accuracy and precision, while providing

images of comparable image noise to regular single bed dynamic protocols processed with regular reconstruction techniques.

In our third contribution we present an extension of the developed functionalities on the reconstruction software for direct multi-bed dynamic reconstruction of DWB data. This methodology enables the synchronous use of all acquired DWB data within a single reconstruction loop. The method was applied on a DWB pharmacological study performed on a clinical PET/MR system and comparison was made with regular frame static reconstructions followed by post reconstruction parametric modelling. The results between the two methods were in good agreement, with no introduction of bias on the evaluated metrics. Furthermore, the use of dynamic reconstruction resulted in noticeable noise reduction in activity and parametric images.

In the fourth and final contribution, an adaptive residual modelling method was applied in reconstruction and evaluated on the DWB pharmacological study, to address modelling errors. This method showed promising results in reducing modelling errors and error propagation while also allowing for genericity in the use of dynamic reconstruction algorithms.

Overall, our findings showed that dynamic reconstruction is necessary in DWB parametric imaging to achieve accurate and stable quantification. Many methods have been proposed in this project that showed how reconstruction can be optimised for multi-bed DWB imaging, by making best use of all dynamic and bed PET raw data in the reconstruction process. But before widespread use of dynamic reconstruction, some methodological improvements need to be addressed further to guarantee artefact free and reliable parametric imaging. Most notably there is need for accurate estimation of underlying complex elastic motion in the dynamic datasets, followed by the correction of these motion types within the dynamic reconstruction process.